Remote sensing of laser- and sun-induced chlorophyll fluorescence for studying water and carbon functioning in terrestrial ecosystems

Hamadou Balde

Sorbonne Université

Ecole doctorale des sciences de l'environnement d'Ile de France N°129

L'Ecole Polytechnique, Laboratoire de Météorologie Dynamique (LMD) et Laboratoire Ecologie, Systématique, et Evolution (ESE, IDEEV), Université Paris-Saclay /Equipes de recherche ABC (t) au LMD et Ecophysiologie végétale à l'ESE

Remote sensing of laser- and sun-induced chlorophyll fluorescence for studying water and carbon functioning in terrestrial ecosystems

Presented by Hamadou BALDE

Doctoral thesis in Remote sensing and environmental sciences

Co-supervised by Dr. Yves Goulas and Prof. Kamel Soudani

Will be presented on December 13th, 2023 with a jury composed by:

Jean-Louis Roujean	DR (CNRS), CESBIO/Toulouse	Rapporteur
Jean-Philippe Mevy	MCF (HDR), IMBE/Marseille	Rapporteur
Hélène Chepfer	PR, Sorbonne Université/LMD/Palaiseau	Présidente
Valerie le Dantec	MCF (HDR), Université-Toulouse III/CESBIO	Examinatrice
Véronique Bruniquel	Directrice des opérations, ACRI-ST	Invitée
Fabienne Maignan	IGR, LSCE/Gif-sur-Yvette	Invitée
Yves Goulas	IGR (HDR), LMD/Palaiseau	Co-directeur
Kamel Soudani	PR, Université Paris-Saclay/ESE	Co-directeur

Thèse préparée au Laboratoire de Météorologie Dynamique, Institut Pierre-Simon Laplace, Ecole polytechnique et au Laboratoire Ecologie, Systématique et Evolution, Université Paris-Saclay.

Dedicated:

To my parents, brothers, sisters, and siblings for their endless love, care, emphahty, support and encouragement.

To my losses throughout this journey, my grandmother Dianambé Kandé, my brother and nephew Aliou and Bacary for their love and care. May your souls rest in peace!

"Nothing comes from nothing. There is always something to give before getting rewards from what is given." Hamadou BALDE.

Acknowledgements

A thesis is three years of discoveries, adventures and meetings. So, completing my Ph.D. research has been a very exciting and enriching experience of my life. It would have not been possible at all without the great supervision and advice of my co-supervisor Yves Goulas, research engineer at Laboratoire de Météorologie Dynamique (LMD), from day one. I would like to express my gratitude to you for your great supervision, availability, guidance, explanation and help in each of my steps throughout this amazing journey. I am very grateful to my co-supervisor Kamel Soudani, professor at Université Paris-Saclay, for his excellent supervision, advice, guidance, and fruitful discussions that we had throughout this journey. This work would have not been possible without your tremendous supervision. I want to address my special thanks to my encadrant Gabriel Hmimina for your supervision, guidance, tremendous technical support, and endless discussions that we have had throughout this journey. You were an inspiration for me. I am very grateful to Gwendal Latouche at Laboratoire Écology, Systématique et Évolution (ESE) for his supervision, guidance, technical intervention in the field and strictness.

My acknowledgements go to Centre National d'Études Spatiales (CNES) and ACRI-ST for funding my Ph.D. project. My thanks also go to the members of my "comité de suivi de thèse" for their follow-up during my thesis.

I am very thankful to my colleagues at LMD and ESE. I thank all of you for providing a very stimulating scientific and social environment that helped me to grow scientifically and personally. I would love to specifically thank the LMD "cake time" team and the Polytechnique foot team for providing a social environment. A special thanks to Abderrahmane Ounis and Riwal Plougonven at LMD for your fruitful discussions and advice. You have always been here to put me on the right track and I appreciate that. My warm thanks also go to Cécile Teissedre, Alexis Sanchez, and Yanis Grit at LMD for your positive humour and helps. I am very grateful also to Nicolas Delpierre, Daniel Berveiller, Alexandre Morfin, and Clotilde Pérot-Guillaume at ESE for their advices, data collection and technical supports at Barbeau/ICOS site and I warmly thank my mentor Christophe François at ESE for his advices and supports.

My special thanks to my childhood friends (Idrissa, Foulah and Ousmane) and my friends in Senegal and France with whom I shared many experiences, solidarity and living together. I would like to mention my friend Mamadou Lamine NDAW, Ibrahima Bella BA, Hamissou MOHAMAN, Ousmane BADJI, Moussa DIEDHIOU, Ousmane CISSE, Ndiouga

Sarr BADJI, Souleymane BA, Moussa BA, Abdoul BA, Zahra CISSE, Awa DIOP, Mamadou pathé DIALLO, Cheikh DIONE, Mbaye DIENG, Cheikh DIENE, Jean Mohamed SAWADOGOU, Abibou LÔ, Malick MBOUP, Salim, Naïla BACARY, Khadidiatou SY, Naïma MOHAMED.

Last but not least, I would love to express my sincere gratitude to my parents (Salimatou BALDE and Demba) for their love, care, positivity, trust, and supports. I also want to thank all my sisters, brothers and siblings for their love, care and empathy.

Contents

Table of contents

List of abbreviations

adj. R^2: the adjusted coefficient of determination

APAR: Absorbed Photosynthetically Active Radiation

ATP: Adenosine Triphosphate

BRDF: Bidirectional Reflectance Distribution Function

ChlF: Chlorophyll Fluorescence

CO_2: Carbon dioxide

DART: Discrete Anisotropic Radiative Transfer

DOY: day of year

EC: Eddy Covariance

ECOSTRESS: Ecosystem Spaceborne Thermal Radiometer Experiment on Space Station instrument

ESE: Laboratoire Écologie, Systématique et Évolution

EVI: Enhanced Vegetation Index

fAPAR: fraction of Absorbed Photosynthetically Active Radiation

FCVI: Fluorescence Correction Vegetation Index

f_{esc}: fraction of SIF that escapes from the canopy

FLD: Fraunhofer Line Depth

3FLD: three-band Fraunhofer Line Discrimination

FLEX: Fluorescence Explorer

F_m: Maximum dark-adapted chlorophyll fluorescence yield

F_m': Maximum light-adapted chlorophyll fluorescence yield

F_o: Minimum dark-adapted chlorophyll fluorescence yield

FOV: Field-of-View

Fs: Steady-state chlorophyll fluorescence yield

FWHM: Full Width at Half Maximum

$F_{yieldLIF}$: LED induced chlorophyll fluorescence yield

GLM: Generalized Linear Model

GOSAT: Greenhouse Gases Observing Satellite

GPP: Gross Primary Production

ICOS: Integrated Carbon Observation System

IPCC: Intergovernmental Panel on Climate Change

IT: Integration Time

LAI: Leaf Area Index

LED: Light-emitting Diode

LET: Linear Electron Transport chain

LIDAR: Light Detection and Ranging

LMD: Laboratoire de Météorologie Dynamique

LNIR: Reflected light in the NIR region

LUE: The efficiency of the absorbed light used in photosynthesis

mNDI: modified red-edge Normalized Difference Index

MODIS: Moderate resolution Imaging Spectroradiometer

NADPH: Adenine Dinucleotide Phosphate

NDVI: Normalized Difference Vegetation Index

NEE: Net Ecosystem Exchange

NIR: Near-infrared region

NIR_V: near-infrared reflectance of vegetation index

NPQ: Non-Photochemical Quenching

OCO-2: Orbiting Carbon Observatory-2

PAM: Pulse Amplitude Modulation

PFTs: Plant Functional Types

PQ: Photochemical Quenching

PRI: Photochemical Reflectance Index

PSI: Photosystem I

PSII: Photosystem II

PTFE: polytetrafluoroethylene

R: Surface spectral reflectance

R^2: The coefficient of determination

RF: Random Forest

RGB: Red, green and blue camera images

RMSE: Root Mean Squared Error

R-NIR: Reflectance in the NIR region

$rNIR_V$: Near-infrared radiance of vegetation index

RS: Remote Sensing

SAA: Solar Azimuth Angle

SAR: Synthetic Aperture Radars

SFM: Spectral Fitting Method

SIF: Sun-Induced chlorophyll Fluorescence

SIF_y: SIF normalized by the photosynthetically active radiation

SNR: Signal-to-noise ratio

SWC: Volumetric Soil Water Content

SWIR: shortwave infrared region

SZA: Solar Zenith Angle

Ta: Air temperature

Tc: Leaf canopy temperature

TROPOMI: TROPOspheric Monitoring Instrument

UTC: Coordinated Universal Time

VIs: Vegetation Indices

VIS: Visible region

VPD: Atmospheric vapor pressure deficit

Φ_D: Quantum yield of constitutive heat dissipation

Φ_F: Quantum yield of chlorophyll fluorescence

Φ_k: The ratio of SIF_y to $F_{yieldLIF}$

Φ_N: Quantum yield of NPQ,

Φ_P: Quantum yield of photochemistry

List of notations

RF-R: Random forest GPP prediction model using only MODIS surface spectral reflectance as inputs
RF-SIF-R: Random forest GPP prediction model using MODIS surface spectral reflectance plus TROPOMI SIF as inputs
RF-SIF-R-PFT: Random forest GPP prediction model using MODIS surface spectral reflectance plus TROPOMI SIF and the PFT as inputs
RF-SIF-VI: Random forest GPP prediction model using MODIS VIs plus TROPOMI SIF as inputs
FY-R: Random forest $F_{yieldLIF}$ prediction model using only surface spectral reflectance as inputs
FY-R-SIF: Random forest $F_{yieldLIF}$ prediction model using surface spectral reflectance plus far-red SIF as inputs
FY-R-SIF$_y$: Random forest $F_{yieldLIF}$ prediction model using surface spectral reflectance plus far-red SIF_y as inputs
FY-R-SIF$_y$-SA: Random forest $F_{yieldLIF}$ prediction model using surface spectral reflectance, far-red SIF_y and solar angles as inputs
Φ_k-R: Random forest Φ_k prediction model using only surface spectral reflectance
Φ_k-R-SA: Random forest Φ_k prediction model using surface spectral reflectance and solar angles as inputs
GPP-ENV-SA: Random forest GPP prediction model using environmental variables and solar angles as inputs
GPP-ENV-RS: Random forest GPP prediction model using environmental and remote sensing variables and solar angles as inputs
SIF-ENV-SA: Random forest SIF prediction model using environmental variables and solar angles as inputs
SIF-ENV-RS: Random forest SIF prediction model using environmental and remote sensing variables and solar angles as inputs

1. Chapter 1: Introduction

1.1. Context

In the context of increasingly changing climate conditions, understanding the role of terrestrial ecosystems in terms of exchanges of carbon, water, and energy is paramount in order to fill in the knowledge gap on climatic interactions between the biosphere and the atmosphere. The terrestrial ecosystems are one of the main carbon pools (among others pools: the ocean, the lithosphere, and the atmosphere carbon pools). It is complex and can store between 25% and 30% of the global anthropogenic carbon emissions (Wang et al., 2017). In addition, terrestrial ecosystems drive several ecosystem functions such as photosynthesis, evapotranspiration, respiration, and soil processes (He et al. 2013; Ryu et al., 2019; Wang et al., 2021; Hall et al., 2012). The Gross Primary Production (GPP) is the total amount of carbon dioxide (CO_2) taken up by the vegetation through photosynthesis per unit area and time. GPP represents the largest global CO_2 flux between the atmosphere and the terrestrial ecosystems and plays a crucial role in intra-annual and inter-annual variations of atmospheric CO_2 concentration (Friedlingstein et al., 2019; Cai and Prentice, 2020). It has also been considered as a key indicator in sustaining the global food and energy supplies (He et al., 2013). Therefore, an accurate quantification of GPP and its spatial and temporal variations is not only a crucial prerequisite for understanding atmosphere-biosphere interactions and ecosystem functioning and services, but also for assessing ecosystem responses and adaptations to climate change (Ryu et al. 2019; Xiao et al. 2019).

To date, the study of the terrestrial ecosystem's role as sink or source of atmospheric CO_2 remains difficult because obtaining direct measurements of GPP at a large scale is impossible (Baldocchi, 2014). The Net Ecosystem Exchange (NEE) of CO_2 between the terrestrial ecosystems and the atmosphere directly measured by the Eddy Covariance (EC) flux sites can be used to indirectly quantify GPP at the canopy scale, but also for calibrating and validating GPP models (Falge et al., 2002; Baldocchi, 2014; Baldocchi et al., 2018 ; Ryu et al., 2019 ; Jung et al., 2020; Burba, 2013). However, the EC techniques are applicable only within limited spatial range due to their restricted spatial coverage and distribution across ecosystems, notably in key areas such as Africa and South America, where GPP estimations are needed (Mengistu et al., 2021). GPP can also be estimated using process-based models and data-driven methods (Pei et al. 2022; Liao et al., 2023). Process-based models fully simulate ecological and

physiological processes of ecosystems (Beer et al. 2010). They are heavily based on assumptions and require large amounts of data, which are difficult to get at the ecosystem scale for their calibration and validation. For instance, remote sensing coupled with process-based models have been widely used for estimating GPP (Running et al., 2004; Pei et al. 2022). Data-driven models instead depend on statistical relations between in-situ carbon flux observations and remote sensing, pedological and meteorological data to quantify GPP. Statistical models usually reach high spatial and temporal predictability of GPP, but they lack a rigorous theoretical assumption on the underlying processes (Pierrat et al., 2022; Balde et al., 2023). The representativeness of these models depends on the data used for training and they are unadapted for future predictions. For instance, FLUXCOM (Jung et al. 2019) is a data-driven GPP estimation upscaled from tower observation sites to global scale.

Optical Remote Sensing (RS) of vegetation is based on the measurement of reflected or emitted radiance by plants canopies, which are affected by their biochemical, structural , and physiological properties (Ustin and Middleton, 2021). The fraction of reflected, transmitted, absorbed, and emitted radiation by canopies are optical signals that are directly related to plant structural, biochemical, and physiological activities. The main applications of RS in agriculture and terrestrial ecology include crop phenotyping (Wen et al., 2023), agricultural land use mapping and monitoring (Leroux et al., 2018), crop health and growth monitoring (Tunca et al., 2018; Weiss et al., 2020), crop yield forecasting (Tunca et al., 2018; Elders et al., 2022; Sarr and Sultan, 2023), evaluating ecosystem services related to soil and water resources or biodiversity loss (Bonannella et al., 2022 ; Farella et al., 2022), and notably monitoring vegetation photosynthesis (Zhao et al., 2022; Xiao et al., 2021). For monitoring vegetation photosynthesis and its spatial and temporal dynamics at the ecosystem scale, optical vegetation indices (VIs) derived from a combination of vegetation spectral signals at different wavelengths have been used (Ustin and Middleton, 2021). These VIs include the Normalized Difference Vegetation Index (NDVI) (Tucker, 1979), the Enhanced Vegetation Index (EVI) (Huete et al., 2002), more recently the near-infrared reflectance of vegetation index (NIR_v) (Badgley et al., 2017), and the modified red-edge Normalized Difference Index (mNDI) (Hmimina et al., 2014), which have been broadly and successfully used to estimate biophysical, phenological, and biochemical variables, including Leaf Area Index (LAI), fraction of Absorbed Photosynthetically Active Radiation (fAPAR), leaf chlorophyll content, etc., (Campbell et al., 2019; Zeng et al., 2022). The LAI and fAPAR mainly characterize canopy structure and vegetation biochemical properties, which are important for understanding energy and matter

allocations within the terrestrial ecosystems (Xiao et al., 2019; Lee et al., 2023). Therefore, VIs have been widely used in modelling crop yield and estimating canopy biophysical, phenological, and biochemical variables and GPP at the ecosystem scale (Zhang et al., 2006; Zhang et al., 2016; Wang et al., 2021). However, GPP estimates based on VIs as inputs are limited in dense canopies because VIs saturate. They are also less sensitive to variations in photosynthetic status resulting from physiological responses induced by rapid changes in abiotic conditions (Pabon-Moreno et al., 2022; Rhoul, 2018). Remote sensing also provides access to variables which are potentially related to canopy functioning such as the Photochemical Reflectance Index (PRI) and Sun-Induced chlorophyll Fluorescence (SIF).

PRI is a reflectance-based vegetation index dependent on changes in reflectance in the green part of the spectrum (Gamon et al., 1992). PRI is defined as the relative variation of reflectance at 531 nm compared to reflectance at 570 nm. The change in reflectance at 531 nm has been linked with two mechanisms involved in the energy heat dissipation of the light absorbed by the photosynthetic apparatus. First, an increase of the pH gradient across the thylakoid membrane directly induces rapid changes in the aggregation state of the chlorophyll protein complexes of the antennae that causes changes in absorbance centred around 531-535 nm range (Louis et al., 2005). Second, the change in the state of epoxidation of xanthophylls and their accumulation is accompanied by changes in absorbance centred around the 505-515 nm range (Ruban 2016). These absorbance variations induce a variation in reflectance in a wide band around 531 nm (Hmimina et al., 2014). Further, PRI has been used as a good indicator of stomatal conductance, excess heat dissipation or Non-Photochemical Quenching (NPQ) (Hmimina et al. 2015; Gitelson et al., 2017; Yang et al., 2020), and more recently as a tool for improving GPP prediction across vegetation types (Soudani et al. 2014;Wang et al., 2020). However, PRI diurnal and seasonal variations and its spatial and temporal dynamics are sensitive to canopy structure, sun-canopy geometry, and chlorophyll content changes (Hmimina et al., 2014; Merlier et al., 2017). These factors can lead to misinterpretation of PRI changes as being due to vegetation functioning (Gamon and Berry, 2012). Therefore, the foremost challenge to date is to find a remote sensing signal that can provide direct monitoring of physiological vegetation responses at the ecosystem scale.

Since the 1980s, vegetation Chlorophyll Fluorescence (ChlF) has been widely used to provide an effective, non-destructive, and direct proxy to monitor the changes in vegetation physiological state at leaf scale (Maxwell and Johnson, 2000; Porcar-Castell et al., 2014).

Indeed, the light energy absorbed by the vegetation chlorophyll pigments has three possible fates: photosynthesis, heat dissipation, or chlorophyll fluorescence emission. These three pathways compete with each other and their relations depend on the light intensity and other environmental conditions. For instance, Pulse Amplitude Modulation (PAM) and MoniPAM instruments allow the measurements of the steady-state fluorescence (Fs), the dark-adapted fluorescence (F_o) and the maximal fluorescence (dark-adapted: F_m, light-adapted: F_m'). The combination of these fluorescence parameters have been used to evaluate vegetation photochemistry quantum yield, non-photochemical quantum yield, and fluorescence quantum yield at the leaf scale (Baker, 2008; Yang et al., 2021). Therefore, variations in vegetation functioning with regard to environmental conditions can be detected through chlorophyll fluorescence changes because of the tight relations that exist between photosynthetic electron transport rate and chlorophyll fluorescence, and thus to carbon assimilation. However, the deployment of such measurements at the ecosystem scale are not fully feasible yet for technical limitations (Ounis et al., 2001).

RS of Sun-Induced chlorophyll Fluorescence (SIF) is a fast and growing field in terrestrial ecosystem science studies. SIF has emerged as a strong proxy for monitoring global vegetation photosynthesis activity (Frankenberg et al. 2011; Joiner et al., 2011; Guanter et al., 2014), spanning its structural and functional activities from canopy to ecosystem scales (Dechant et al., 2020; Mohammed et al., 2019; Sun et al., 2023). Measurements and predictions of SIF across different vegetation types, spatial and temporal scales, and from diverse RS platforms have considerably improved our understanding of what drives SIF and have opened up new opportunities to quantify, monitor, and model vegetation photosynthesis activities at the canopy level and beyond (Sun et al. 2017; Mohammed et al., 2019; Sun et al. 2023). However, previous studies showed that the link between GPP and SIF considerably depend on: the spatial and temporal scales (Mohammed et al., 2019; Wood et al., 2017; Yang et al. 2020), the vegetation types (Wang et al. 2020; Zhang et al., 2018; Kim et al., 2021; Balde et al., 2023) the photosynthetic pathways (Verma et al., 2017; Liu et al., 2017; He et al., 2020; Wu et al., 2022), the canopy structure and phenology (Yang et al., 2019; Dechant et al., 2020; Tagliabue et al., 2019), and also on the environmental conditions (Paul-Limoges et al., 2018 ; Magney et al., 2019; Hornero et al., 2021). Thus, it can be seen that at infra-daily timescales, which are necessary to characterize rapid changes in GPP due to changes in abiotic conditions, the relationship between GPP and SIF is not linear (Marrs et al., 2020; Kim et al., 2021). For instance, some studies report that the correlation between GPP and SIF is curvilinear or

hyperbolic at the infra-daily timescales (Damm et al., 2015; Paul-Limoges et al., 2018; Chen et al., 2020; Kim et al., 2021). This non-linearity is difficult to detect on broad timescales because of spatial and temporal aggregation that smooth out the effects of variations in canopy structure (LAI, angular leaf distribution, etc.), in canopy optical properties, and environmental conditions (Li et al., 2018; Dannenberg et al., 2020; Li et al., 2020; Jonard et al., 2020). Therefore, the mechanisms underlying the relation between GPP and SIF are not yet fully understood.

1.2. Research gaps and objectives

As previously mentioned, the inconclusive findings about GPP-SIF relations (linear and non-linear correlations) raise concerns to better understand the relationships between GPP, SIF, and the vegetation physiological state under changing environmental conditions and across different vegetation types. Therefore, we are still wondering about, on one hand, **what are the links between SIF and GPP across vegetation types and what are the factors and the mechanisms underlying the temporal and spatial variations of SIF signal, and on the other hand, how can we decouple physiological and structural information contained in SIF signal measured at canopy scale.** Over short periods (seconds, infra-daily), the factors affecting the canopy SIF signal are more dynamic. As a result, variations in chlorophyll fluorescence yield can be largely attributed to variations in Photochemical Quenching (PQ) or Non-Photochemical Quenching (NPQ). At low light, most of the photons absorbed are used for photosynthesis, thus increasing its efficiency. However, at high light intensity, biochemical carbon assimilation reactions and electron transport chain can saturate, leading to a reallocation of the excess energy into SIF emission and heat dissipation through NPQ (Porcar-Castell et al., 2014; Porcar-Castell et al., 2021). This behavior can modify the links between SIF and GPP, especially during abiotic stress conditions (droughts, heatwaves, etc.) (Martini et al., 2022). Over long periods (several days or months), structural components, canopy biochemical properties, sun-canopy-sensor geometry, and abiotic conditions are changing. These changes may affect the relations between GPP and SIF, leading to misunderstandings of their relationships. Therefore, to better understand these relationships at different spatial and temporal scales and the effects of the multiple factors on SIF signals, it is important to have reliable ChlF measurements at canopy scale using both passive techniques and active measurements, as the latter are currently the only onnes capable of providing the basis to study the relationships between fluorescence yield and photosynthetic functioning.

Active chlorophyll fluorescence measurements provide direct access to the vegetation physiological status at leaf and canopy scales. However, in-situ measurements of SIF at canopy scale are not only essential to understand the variations in fluorescence at infra-daily timescales and to study the effects of canopy structure and sun-canopy geometry on SIF signal, but are also essential to constraint the dynamics of SIF with GPP. In addition, these measurements can also serve as a "bridge" between EC, airborne, and satellite data (integration and validation of SIF signals in time and space) (Zhang et al., 2021). However, while the combination of active and passive in-situ measurements can allow us to study the relationship between chlorophyll fluorescence and photosynthesis at different timescales (from seconds to season), they do not allow to quantify the spatial variability of the link between SIF and GPP. Therefore, the use of readily accessible satellite timeseries data such as TROPOMI SIF and MODIS Aqua and Terra spectral reflectance, constitutes a complement to explore the synergistic use of chlorophyll fluorescence and reflectance to predict the spatial and temporal dynamics of GPP across different vegetation types and abiotic conditions. These different approaches are crucial for characterizing and understanding the radiative transfer of chlorophyll fluorescence, the relationship between chlorophyll fluorescence and photosynthesis from leaf-to-canopy scale and beyond.

The main objectives of this thesis are to understand what are the links between GPP and SIF across different vegetation types, how chlorophyll fluorescence yield is correlated to active chlorophyll fluorescence yield, and how canopy structure and sun-canopy geometry properties affect SIF signal and to provide a method to correct these structural effects on SIF signal using active chlorophyll fluorescence measurements. In order to do that a large variety of observations were used, including satellite TROPOMI SIF, MODIS Terra and Aqua reflectance, ground-based Integrated Carbon Observation System (ICOS) CO_2 flux sites, in-situ chlorophyll fluorescence measurements using both active and passive methods, and data-driven modelling methods. Specifically, the following questions are risen:

1. What is the strength and the nature of the links between SIF and GPP across diverse vegetation types and can we predict GPP using synergistic uses of chlorophyll fluorescence and reflectance (Chapter 3)?
2. How do canopy structure and sun-canopy-sensor geometry affect SIF and how to correct them and what is the relationship between SIF yield and active chlorophyll fluorescence observations (Chapter 4)?

3. How do abiotic variables influence the SIF and GPP dynamics and their relationships (Chapter 5)?

1.3. Thesis outlines

Spatial and temporal variations in SIF and its relationship to GPP as a function of functional vegetation types still remain a poorly documented area of research. To make our contribution to this scientific question, we first presented in Chapter 2 an introduction to remote sensing of vegetation functioning and in Chapter 3 the strength of the links between the spatial measurements of SIF (product TROPOMI SIF) and the GPP resulting from ground-based measurements at forty ICOS flux sites spanning different Plant Functional Types (PFTs). In this chapter, we also highlighted the synergy between SIF, spectral reflectance (MODIS Aqua and Terra) and Vegetation Indices (VIs), including PRI, NDVI and NIR_v for GPP predictions using a data-driven Random Forest (FR) method.

The conclusions of Chapter 3 allowed us to show that it is difficult to determine the most important factors and mechanisms explaining the wide variability in the relationship between GPP and SIF at the spatial and temporal scale of TROPOMI SIF (Sentinel-5P mission, daily 5-7 km / 3.5-14 km pixel size). In order to understand changes in the relationships between GPP and SIF regarding the timescale, we examined these relations at infra-daily and seasonal timescales. To achieve this, it was essential to simultaneously measure the temporal dynamics of environmental conditions (total solar radiation, diffuse/direct radiation, temperature, soil water content, vapor pressure deficit), biochemical and canopy structure properties (canopy temperature, chlorophyll content, and leaf area index), and canopy photosynthesis (GPP) at the timescales mentioned above. We have carried out continuous and simultaneous measurements at canopy scale of ChlF based on two techniques, one passive (SIF) and the other active ($F_{yieldLIF}$, using modulated excitation), GPP, and environmental variables in Fontainebleau-Barbeau in 2022. These data allow us to directly analyse SIF and GPP relationships at different timescales and under different environmental conditions.

In Chapter 4, based on top-of-canopy measurements above a mature deciduous forest in Fontainebleau-Barbeau, including, reflectance (R), SIF, SIF normalized by incoming Photosynthetically Active Radiation (PAR) (SIF_y), $F_{yieldLIF}$, and the ratio between SIF_y and $F_{yieldLIF}$ (named Φ_k), we studied the effects of canopy structure and shadows on the diurnal and

seasonal dynamics of SIF and proposed a method to predict $F_{yieldLIF}$ and Φ_k. In this chapter, we mainly highlighted the complexity of interpreting diurnal and seasonal dynamics of SIF in forest canopies because SIF measurements are highly dependent on the complex interactions between the structure and biochemical properties of the canopy, the illumination (SZA and SAA) and the light conditions (ratio of diffuse to direct solar radiation).

Far-red SIF is increasingly used as a remote and proximal-sensing tool, as it is able to track vegetation GPP across different ecosystems. However, the use of SIF to probe variations in GPP in forests is challenged by confounding factors such as canopy physiological, canopy structural and canopy biochemical properties, along with environmental conditions. In Chapter 5, we examined SIF and GPP seasonal variations and how canopy structure and environmental conditions affected GPP-SIF relationship in the Fontainebleau-Barbeau deciduous forest. To do so, we combined canopy scale SIF measurements, reflectance and VIs, environmental variables measurements, and GPP. In summary, this study provides insights into understanding the complex drivers of the relationship between GPP and SIF at different temporal resolutions and under different environmental conditions in a deciduous stand. Lastly, in Chapter 6, we synthesized and discussed our findings and proposed some outlooks for future research.

2. Chapter 2: Introduction to optical remote sensing of vegetation functioning

2.1. Spectral reflectance features and vegetation indices

RS has a high potential for vegetation characterization because it allows to characterize the properties and features of the earth surface using: 1) passive sensors based on solar radiation as light source (within 0.4-2.5 µm) with the emission mainly in thermal infrared bands, and 2) active systems such as SAR (Synthetic Aperture Radars, specifically in the microwave domain) or Light Detection and Ranging (LIDAR) (Ustin and Middleton, 2021; Zeng et al., 2022). The earth observation in the optical domain from passive satellite sensors such as multispectral and hyperspectral sensors, have a good potential for monitoring and mapping canopy structure and vegetation biochemical properties (Zeng et al., 2022; Grotti et al., 2020; Song et al., 2021). These sensors measure the fraction of the solar radiation that is reflected from the canopies. The measured radiance is normalized to reflectance using concomitant measurements of solar irradiance. The potential of optical remote sensing for applications on vegetation functioning is based on: firstly, satellite-based optical sensors that can track the optical reflectance of the vegetation with a high spatial and temporal resolutions, which enable a spatially continuous monitoring of vegetation canopies through time and space; secondly, the reflectance of vegetation canopies is directly linked to structural and biochemical variables (important for understanding ecosystem functions) (Ustin and Middleton, 2021). Optical data for vegetation monitoring is restricted to 0.4-2.5 µm (Figure 2.1). Below 0.4 µm solar irradiance (ultraviolet radiation) is strongly absorbed by ozone, whereas above 2.5 µm reflected radiance is hardly detectable (very low reflected radiation of natural surfaces above 2.5 µm). Vegetation presents specific reflectance patterns from 0.4 to 2.5 µm, which is shaped by the biochemical and structural constituents of the leaves. In the visible region (VIS, 0.4-0.7 µm) low reflectance is caused by pigments absorption (chlorophyll, carotenoids and anthocyanins), mainly in the blue and red bands, used for photosynthesis. However, in the near-infrared region (NIR, 0.7-1.3 µm) absorption by leaf components is low and thus a large part of the incident radiation is reflected by the canopies. In the shortwave infrared region (SWIR, 1.4-2.5 µm) light is absorbed by leaf dry matter components (proteins, lignin, carbohydrates and waxes) and leaf water. Leaf water absorption is strongest around 1.4-1.6 µm and 1.8-2.1 µm, making these regions less

exploitable for vegetation studies based on optical data, because the atmosphere is sensitive to short-term changes in water content (Zeng et al. 2022).

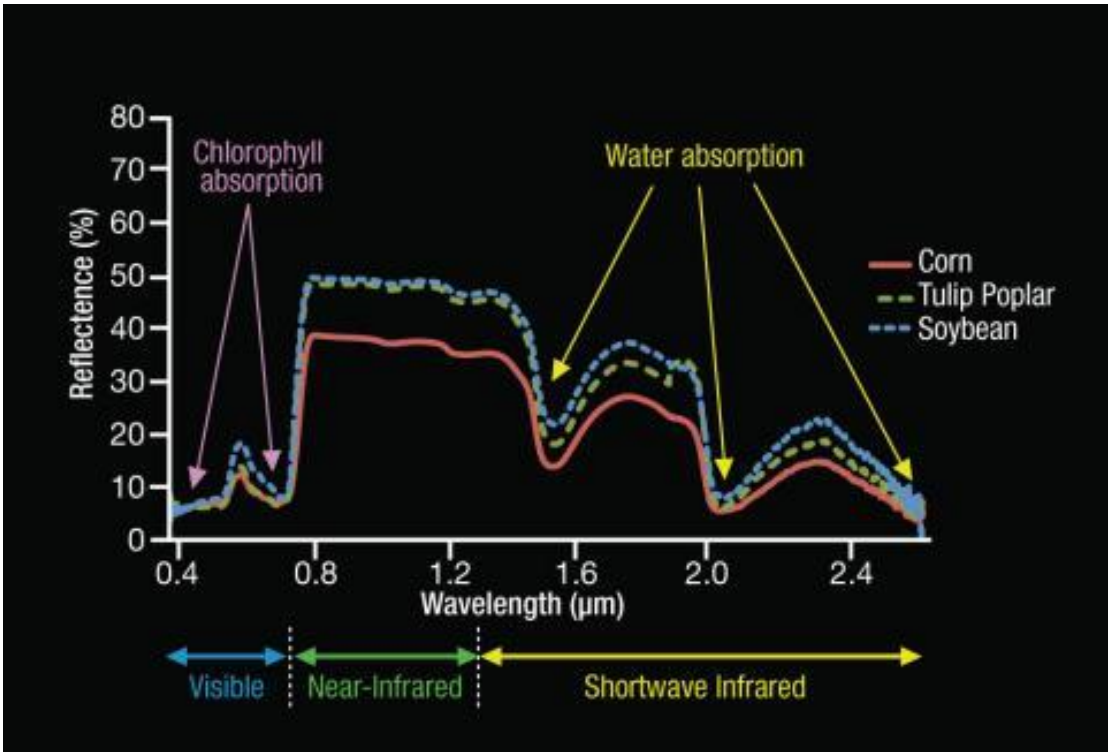

Figure 2.1. Typical reflectance curve for a leaf or plant canopy containing chlorophyll (credit: Eric Brown De Colstoun, NASA SCIENCE SHARE THE SCIENCE).

The characteristics of the canopy reflectance have been used to define vegetation indices (VIs). VIs are mathematical combinations of reflectance values acquired in different spectral bands, which are intended to describe vegetation structural and biochemical properties. The most used spectral bands in the optical domain for remote sensing of the vegetation are in the red, red-edge, near-infrared, and shortwave infrared bands. The most widely used VIs for characterizing vegetation greenness are currently NDVI, EVI, NIR_v, PRI, and various other VIs designed to estimate leaf chlorophyll content such as mNDI (Campbell et al., 2019; Hmimina et al., 2014; Zeng et al., 2022).

NDVI is based on the large difference in vegetation reflectance between the VIS and the NIR bands and is defined as the ratio of the difference to the sum of reflectance in the NIR and in red bands. In remote sensing, NDVI is specifically used for mapping vegetation cover and as a proxy of the green biomass. The value of NDVI varies between -1 and 1. For instance, for dense vegetation canopies, the values of NDVI are high (about 0.8 or even higher), while for bare soil values of NDVI will be close to zero, and negative over water bodies and dark shaded

areas. Note that when vegetation is in the active expansion and growth phases, the contribution of the soil to the measured global reflectance decreases in favour of the contribution of vegetation. During this phase, the measured spectral reflectance diminishes in the VIS and mid-infrared regions, while it increases in the near-infrared range. Therefore, NDVI reflects vegetation density, health, and cover. Indeed, it is worth noting that the saturation of spectral reflectance above a certain level of LAI observed in tropical forests or other vegetation types hinders the use of NDVI for monitoring and estimating vegetation carbon assimilation at canopy, regional, and global scales (Zhang et al. 2021).

Yet, NDVI is often used as an indicator of green biomass, Absorbed Photosynthetically Active Radiation (APAR) or photosynthetic capacity of the canopy depending on the interpretation that is made. However, this spectral vegetation index does not allow access to vegetation physiological responses (photosynthesis, transpiration, stomatal conductance, etc.) due to rapid changes of abiotic factors. This is why other spectral indices such as PRI and NIR_v, which are sensitive to short-term variations in photosynthetic activity and sun-canopy geometry, were introduced. NIR_v is the product of the reflectance in the NIR and NDVI (Badgley et al., 2017). This index has been recently used as a proxy of temporal changes in photosynthesis based on ground measurements and has also been used for correcting SIF from canopy structure and sun-canopy geometry effects (Wong et al. 2020; Hao et al. 2021).

SIF is a faint radiation re-emitted by the vegetation chlorophyll pigments, mainly chlorophyll *a*, upon sun exposure and absorption. Note that the chlorophyll fluorescence (and SIF) refers to chlorophyll *a* fluorescence within this manuscript as chlorophyll *b* and carotenoids also emit fluorescence, but their emissions are low and strongly re-absorbed by the canopy. SIF is one of the three possible fates of the absorbed energy by vegetation's photosystems, the other two being photochemistry and heat dissipation (NPQ) (Porcar-Castell et al. 2014) (see Figure 2.2). These three dissipation pathways compete with each other. SIF emission spectrum spans the spectral range from 650 to 800 nm. Therefore, SIF contains both visible radiation (red SIF, with its emission peak at 685 nm) and far-red radiation (far-red SIF, with its emission peak at 740 nm) (Figure 2.2).

SIF emission arises from both photosystem II (PSII) and photosystem I (PSI). PSII contributes to both red and far-red SIF emissions, and PSI notably to the far-red region (Mohammed et al. 2019). Compared to the vegetation reflected radiance, SIF is a small signal

(typically representing less than 3% of the absorbed solar radiation) (Krause, 1991) and is usually retrieved by exploiting telluric atmospheric oxygen absorption features or sun absorption bands (Meroni et al. 2009; Frankenberg and Berry 2018). Note that in healthy green vegetation the red peak is lower than the far-red one (Figure 2.2), because of the strong reabsorption of red fluorescence by chlorophyll pigments. SIF retrievals within atmospheric oxygen absorption features are determined with Fraunhofer Line Depth (FLD) methods (Plascyk, 1975) or through Spectral Fitting Method (SFM) (Cogliati et al. 2015). With these approaches, SIF retrievals require measurements of incoming irradiance and vegetation radiance using high resolution spectrometers (Cendrero-Mateo et al. 2019).

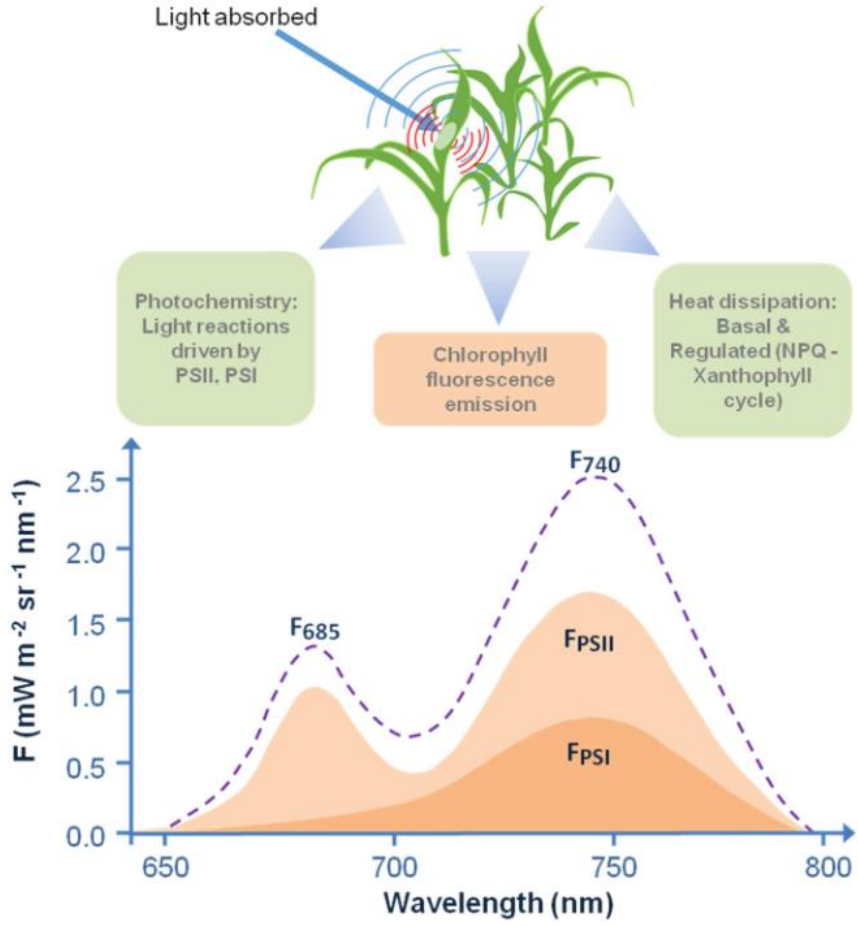

Figure 1.2. Repartition of leaves absorbed radiation and illustration of the spectral dependency of sun-induced fluorescence (F) under steady-state conditions (source: Mohammed et al. 2019).

2.2. Photochemistry, chlorophyll fluorescence, and non-photochemical quenching at photosystem scale

The main reason why chlorophyll fluorescence is used as a direct proxy of photosynthesis is that both mechanisms are triggered by absorption of light by chlorophyll pigments. The absorption of energy by PSII causes chlorophyll molecules in the antennae of PSII to reach an excited state. This energy can be partitioned into three main pathways: first, it can be used to drive photochemistry through Linear Electron Transport chain (LET); second, it can be dissipated as heat, a mechanism known as Non-Photochemical Quenching (NPQ); and third, it can be re-emitted as fluorescence in the red and far-red spectral regions (Porcar-Castell et al. 2014).

The LET chain transports electrons from PSII to PSI and injects protons into the lumen for producing Adenosine Triphosphate (ATP) and Nicotinamide Adenine Dinucleotide Phosphate (NADPH) to be used in the carbon fixation reactions of photosynthesis for synthetizing sugars. Through the LET chain, the excited reaction centre ($P_{680,}$ a chlorophyll dimer) (Figure 2.3) from PSII rapidly gives an electron to the quinone A (Q_A), which in turn donates it to an electron carrier, the plastoquinone (PQ) (Porcar-Castell et al. 2014). P_{680}^+ in PSII, which has just lost one electron, is positively charged and is reduced by the oxygen-evolving complex (OEC). The OEC divides a water molecule (H_2O) in the thylakoid lumen and releases protons (H^+) and oxygen (O_2). The protonated quinone (PQH_2) reduces the plastocyanin (PC), which passes an electron to PSI and additionally transfers protons in the thylakoid lumen. The cytochrome b6f has a double function: transferring protons from the chloroplast stroma to the thylakoid lumen and transporting electrons from the plastoquinone to the plastocyanin (PC) molecule. Simultaneously, energy absorbed in PSI by P_{700} is used to reduce the electron acceptor ferredoxin (F_d), which donates the electron to $NADP^+$ to release NADPH. The oxidized molecule (P_{700}^+) in PSI is reduced back to P_{700} by taking an electron from the PC. This series of reactions conclude the LET. Indeed, the proton gradient in the thylakoid lumen is used by ATP synthase to release ATP, ending the light reactions of photosynthesis.

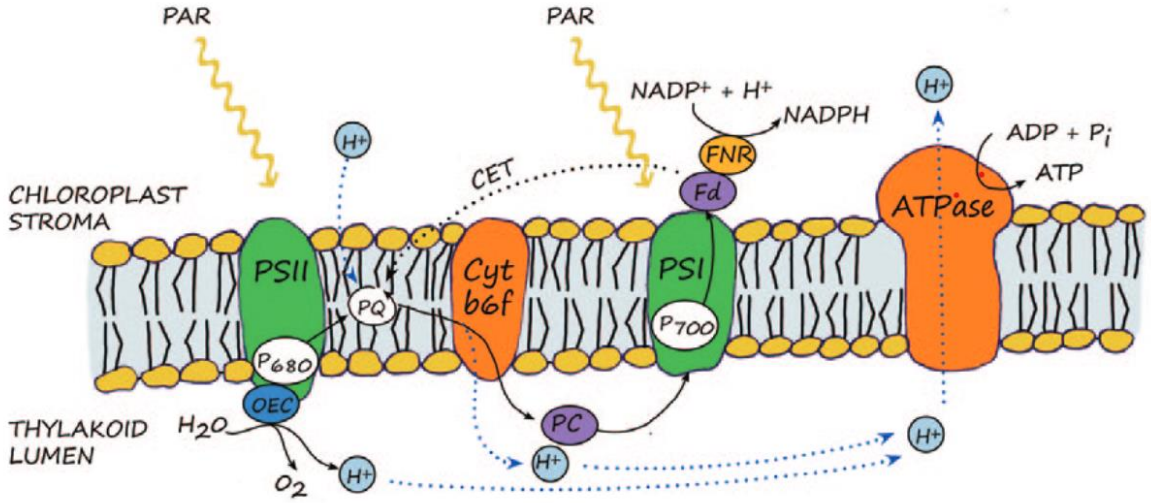

Figure 2.2. Illustration of linear electron transport and fluorescence emission (source: Porcar-castell et al., 2014).

When light intensity increases, the carbon fixation and electron transport chain can gradually become light saturated due to protons accumulation. This situation might lead to the formation of singlet oxygen, which is a reactive oxygen species that can harmfully affect the photosystem. Consequently, for their survival, plants have developed a number of photoprotection mechanisms that permit them to dissipate the excess absorbed energy as heat, which is mostly known as NPQ and that can induce a reduction in both the fraction of photon used in photosynthesis and in fluorescence emission. When the pH in the lumen decreases as a result of proton accumulation, it can act as a signal for NPQ mechanisms. Indeed, this drives the de-epoxidation of violaxanthin into zeaxanthin. The latter has a crucial role in triggering the NPQ mechanisms (Jahns and Holzwarth 2012).

The opening and functioning of the reaction's centres drive photochemistry, meaning that they are tightly paired with the oxidized Q_A. When a reaction centre is closed and a chlorophyll molecule is in an excited state, excess photons are mainly re-emitted as fluorescence. As a result, the fraction of open reaction centres (triggering photochemistry) is inversely correlated to the quantum yield of fluorescence (Kitajima and Butler, 1975). Plants control quenching mechanisms (i.e. Photochemical Quenching, PQ, and NPQ). Therefore, as PQ, NPQ, and fluorescence compete for the same excitation energy, each energy dissipation pathway can be quantitatively considered. Accordingly, the sum of all quantum yields is equal to unity (van der Tol et al. 2014).

$$\Phi_P + \Phi_F + \Phi_D + \Phi_N = 1 \quad (2.1)$$

where Φ_P is the quantum yield of photochemistry, which is the efficiency with which absorbed photons are used by the photochemistry process; Φ_F is the quantum yield of fluorescence emission, representing the total amount of absorbed light re-emitted as fluorescence; Φ_N is the quantum yield of NPQ, and Φ_D is the quantum yield of constitutive heat dissipation, which is the one observed upon dark adaptation and is assumed to be constant.

At low light conditions, NPQ is merely zero, PQ is the main energy dissipation pathway and Φ_P and Φ_F are negatively related because each reduction in Φ_P drives a further increase of the population of the excited states and consequently an increase in Φ_F. In contrast, at high light conditions, the NPQ mechanism can become the dominant process, leading directly to concomitant reduction in both Φ_P and Φ_F (Porcar-Castell et al. 2014). Therefore, NPQ controls directly the relationship between fluorescence and photosynthesis. It is worth noting that plants can use other mechanisms that can decouple the correlation between fluorescence and photosynthesis that operate at different temporal scales, including chloroplast movements (Sarvikas et al. 2010), photorespiration (Genty et al.,1990), and changes in the concentration in anthocyanins (Merzlyak et al. 2008).

2.3. Effect of leaf and canopy biochemical and structure properties on SIF

Leaf and canopy structure have a substantial effect on top-of-canopy SIF emission. At leaf scale, the chlorophyll pigment content not only significantly affects the amount of absorbed photosynthetically active radiation (APAR), and thus the magnitude of emitted SIF, but also the fraction of SIF that escapes the leaf. SIF is directly emitted from the chlorophyll molecules. However, SIF might also be scattered and re-absorbed by the same chlorophyll molecule in the red region, because SIF emission spectrum overlaps chlorophyll absorption (Porcar-Castell et al. 2014; Jonard et al. 2020). In addition, note that changes in leaf structure such as leaf pubescence and thickness and chloroplast movements, as well as wavelength-dependent light penetration can significantly influence SIF.

At the canopy scale, observed SIF is heavily affected by leaf area index, canopy chlorophyll content, leaf movements, distribution of leaf angle, clumping, roughness of upper canopy layers, and spatial and temporal distributions of sunlit and shaded leaves (Gao et al.,

2022; Morozumi et al., 2023), which in turn strongly influence the fraction of SIF that escapes from the canopy (f_{esc}) (Migliavacca et al. 2017; Yang and van der Tol, 2018). Further, ratio between diffuse and total light and sun-canopy-sensor geometry such as the sun zenith (SZA) and azimuth (SAA) angles all have also a substantial effect on canopy light distribution, interception, scattering and transmission (Zhang and Zhang, 2023). Therefore, these factors considerably influence SIF emission measured at the sensor level, and also the ability to retrieve SIF signal (Zhang et al., 2023). Because of these leaf and canopy effects, interpreting observed SIF data should be cautiously carried out and how we can derive vegetation physiological status from SIF is still challenging and an area of active research that we addressed in this thesis.

2.4. Light emitted diode (LED) chlorophyll fluorescence

Chlorophyll fluorescence can be measured using active or artificial light induction methods that allow direct evaluation of vegetation physiological state at the leaf and canopy scales (Porcar-Castell et al., 2014; Moya et al., 2019; Loayza et al., 2023). In active techniques, a modulated and spectrally designed source of light is used to excite chlorophyll that fluoresces in the spectral range between 650 and 800 nm. For instance, the development of pulse amplitude modulation (PAM) fluorimetry techniques, which use a weak and pulsed measuring light to induce fluorescence emission, has been widely and successfully used at the leaf scale to provide direct fluorescence yield measurements, allowing the evaluation of photosynthesis and vegetation responses to abiotic factors for decades (Baker, 2008; Magney et al., 2017). The theoretical bases linking fluorescence measured by active methods to photosynthesis at the leaf scale are well formulated and discussed in numerous publications (Schreiber, 2004). But, its applicability at canopy scale is hindered by technical limitations (Ounis et al., 2001). In the last decades, this gap was partially filled based on the use of a pulsed light, either lasers, laser diodes, and light emitting diode (LEDs) modulated with pulses of short duration (microsecond to picosecond) with a synchronized detection source for measuring fluorescence under daylight conditions at the canopy scale using ground-based or airborne remote sensing instruments (Moya et al., 2019; Ounis et al., 2016; Loayza et al., 2023). For instance, Moya et al, (2019) used fluorescence acquired by a micro-lidar instrument equipped with blue LEDs light excitation (LEDFLEX) to show that water stress can be detected in pea (*Pinus Sativum*), mint (*Mentha Spicata*), and sweet potatoes (*Ipomoea Batata*) crops at the canopy scale. Therefore, this breakthrough may be useful to gain a better understanding of terrestrial vegetation

functioning because active chlorophyll fluorescence measurements operate at constant excitation light intensity and direction. As a result, it is less affected by the temporal and spatial (horizontal and vertical) distribution of sunlit and shaded leaves on the upper surface and within the canopy compared to SIF.

3. Chapter 3: Synergy between TROPOMI sun-induced chlorophyll fluorescence and MODIS spectral reflectance for understanding the dynamics of gross primary productivity at Integrated Carbon Observatory System (ICOS) ecosystem flux sites

This Chapter is based on: Balde, H., Hmimina, G., Goulas, Y., Latouche, G., and Soudani, K.: Synergy between TROPOMI sun-induced chlorophyll fluorescence and MODIS spectral reflectance for understanding the dynamics of gross primary productivity at Integrated Carbon Observatory System (ICOS) ecosystem flux sites, Biogeosciences, 20, 1473–1490, https://doi.org/10.5194/bg-20-1473-2023, 2023.

NB: Supplementary materials are all in annexes (Annexe Chapter 3)

Abstract. An accurate estimation of vegetation Gross Primary Productivity (GPP), which is the amount of carbon taken up by vegetation through photosynthesis for a given time and area, is critical for understanding terrestrial atmosphere CO_2 exchange processes and ecosystem functioning, as well as ecosystem responses and adaptations to climate change. Prior studies, based on ground, airborne, and satellite Sun-Induced chlorophyll Fluorescence (SIF) observations, have recently revealed close relationships with GPP at different spatial and temporal scales and across different Plant Functional Types (PFTs). However, questions remain regarding whether there is a unique relationship between SIF and GPP across different sites and PFTs and how we can improve GPP estimates using solely remotely sensed data. Using concurrent measurements of daily TROPOspheric Monitoring Instrument (TROPOMI) SIF (daily SIF_d); daily MODIS Terra and Aqua spectral reflectance; Vegetation Indices (VIs, notably Normalized Difference Vegetation Index (NDVI), Near-Infrared Reflectance of vegetation (NIR_v), and Photochemical Reflectance Index (PRI)); and daily tower-based GPP across eight major different PFTs, including mixed forests, deciduous broadleaf forests, croplands, evergreen broadleaf forests, evergreen needleleaf forests, grasslands, open shrubland, and wetlands, the strength of the relationships between tower-based GPP and SIF_d at 40 Integrated Carbon Observation System (ICOS) flux sites was investigated. The synergy between SIF_d and MODIS-based reflectance (*R*) and VIs to improve GPP estimates using a data-driven modeling approach was also evaluated. The results revealed that the strength of the hyperbolic relationship between GPP and SIF_d was strongly site-specific and PFT-dependent. Furthermore, the Generalized Linear Model (GLM), fitted between SIF_d, GPP, and site and vegetation type as categorical variables, further supported this site- and PFT-dependent relationship between GPP and SIF_d. Using random forest (RF) regression models with GPP as output and the aforementioned variables as predictors (*R*, SIF_d, and VIs), this study also showed that the spectral reflectance bands (RF-*R*) and SIF_d plus spectral reflectance (RF-SIF-*R*) models explained over 80 % of the seasonal and interannual variations in GPP, whereas the SIF_d plus VI (RF-SIF-VI) model reproduced only 75 % of the tower-based GPP variance. In addition, the relative variable importance of predictors of GPP demonstrated that the spectral reflectance bands in the near-infrared, red, and SIF_d appeared as the most influential and dominant factors determining GPP predictions, indicating the importance of canopy structure, biochemical properties, and vegetation functioning on GPP estimates. Overall, this study provides insights into understanding the strength of the relationships between GPP and SIF and the use of spectral reflectance and SIF_d to improve estimates of GPP across sites and PFTs.

3.1. Introduction

In the context of climate change, understanding the role of terrestrial ecosystems in terms of exchanges of carbon, water, and energy is crucial in order to fill in the knowledge gap on climatic interactions between the biosphere and the atmosphere. Terrestrial ecosystems are one of the main components of the carbon cycle and are highly sensitive to abiotic stresses. Therefore, an accurate estimation of vegetation Gross Primary Productivity (GPP), which is the carbon flux taken up by vegetation through photosynthesis, is critical for understanding terrestrial–atmosphere CO_2 exchange processes and ecosystem functioning, as well as ecosystem responses and adaptations to climate change (Gamon et al., 2019). Eddy covariance (EC) techniques allow for the estimation of GPP locally (Falge et al., 2002; Moureaux et al., 2008; Chu et al., 2021). However, they have limitations when it comes to upscaling carbon flux estimates at larger scales due to their restricted spatial coverage, temporal dynamics of flux footprints, and limited distribution across different vegetation types, notably in key areas such as Africa and South America (Xiao, 2004; Gamon, 2015; Xiao et al., 2019). GPP can also be estimated based on physical and ecophysiological modeling approaches. However, for estimating GPP at larger scales, those methods are hampered by the lack of understanding of the underlying physiological processes (Jiang & Ryu, 2016; Zhang et al., 2017; Madani et al., 2020).

Remote sensing is widely used to upscale daily GPP to landscape, regional, and global scales using reflected sunlight measured by satellite sensors (Running et al., 2004; Baldocchi et al., 2020 ; Wu et al., 2020 ; Kong et al., 2022; Wang et al., 2022). These approaches are mainly based on reflectance-based Vegetation Indices (VIs) such as the Normalized Difference Vegetation Index (NDVI), Enhanced Vegetation Index (EVI), and more recently Near-Infrared Reflectance of vegetation (NIR_v) (Badgley et al., 2017; Baldocchi et al., 2020). VIs are mostly sensitive to spatial and temporal variability in structural Leaf Area Index (LAI) and biochemical canopy attributes (Dechant et al., 2020; Pabon-Moreno et al., 2022), but they suffer from saturation in canopy-dense ecosystems and are less sensitive to diurnal and daily variations in photosynthetic status resulting from physiological responses induced by rapid changes in abiotic stresses (Daumard et al., 2012; Guanter et al., 2014; Wieneke et al., 2016; Zhang, et al., 2021a). Remote sensing also provides access to variables which are related to canopy functioning such as the Photochemical Reflectance Index (PRI) (Gamon et al., 1992; Wang et

al., 2020) and Sun-Induced chlorophyll Fluorescence (SIF) (Porcar-Castell et al., 2014; Goulas et al., 2017; Yang et al., 2020; Zhang et al., 2022; Li & Xiao, 2022).

PRI is a reflectance-based vegetation index that has been shown to detect vegetation functioning activities under abiotic stress conditions that the abovementioned VIs cannot capture (Meroni et al., 2008). It is due to changes in the absorptance of leaves of around 510 nm or reflectance at 531 nm that are related to the interconversion of the xanthophyll pigment cycles, which represents an important photoprotection mechanism (Gamon et al., 1992; Meroni et al., 2008). Moreover, previous studies have pointed out that PRI can be used to improve canopy GPP estimates at the ecosystem level at daily timescales (Wang et al., 2020; Hmimina et al., 2015; Soudani et al., 2014), but how variations in PRI at long timescales with spatial variations in vegetation types affect the relationship between PRI and GPP remains unresolved and is an area of active research (Porcar-Castell et al., 2014; Chou et al., 2017; Gitelson et al., 2017).

In recent years, SIF has emerged as a promising remotely sensed tool for monitoring canopy GPP, which is functionally and fundamentally different from the aforementioned VIs (Damm et al., 2010; Yang et al., 2015; Köhler et al., 2018; Wang et al., 2021; Guanter et al., 2021). In fact, SIF does not rely on vegetation reflectance; instead it is a faint signal directly emitted by chlorophyll from the absorbed sunlight just before the occurrence of a photochemical reaction (Porcar-Castell et al., 2014; Gu et al., 2019b; Zhang et al., 2021a). SIF has a physical and physiological meaning, and hence SIF offers new opportunities for the global assessment of canopy GPP (Mohammed et al., 2019; Wieneke et al., 2018; Zhang et al., 2020; Kimm et al., 2021; Dechant et al., 2022). Earlier studies relying on ground-, airborne-, and satellite-based SIF data measurements at different temporal and spatial scales have indicated a strong linear site-specific and vegetation-type-dependent relationship between GPP and SIF (Frankenberg et al., 2011; Guanter et al., 2014; Yang et al., 2017; Wood et al., 2017; Li et al., 2018b; Paul-Limoges et al., 2018; Zhang et al., 2021b; Zhang et al., 2022). In contrast, at finer temporal scales such as diurnal and hourly, the relationship between GPP and SIF is not as strong as at longer timescales. Instead, it appears to be non-linear due to rapid changes in instantaneous variations in photosynthetically active radiation (PAR) and environmental conditions (Damm et al., 2015; Marrs et al., 2020; Kim et al., 2021). How and to what extent driving factors such as canopy structure, spatial heterogeneity, and abiotic stress conditions mediate the GPP and

SIF relationship remains a challenge and needs to be investigated (Smith et al., 2018; Wang et al., 2021; Li & Xiao, 2022). The main drawback, which relates to the use of SIF to predict GPP at regional and global scales, lies in the weak SIF signal retrieval that requires averaging over large timescales and spatial scales and thus hampers detecting fine-scale dynamics needed to explain underlying processes (Gamon et al., 2019; Köhler et al., 2021).Yet, the TROPOspheric Monitoring Instrument (TROPOMI) sensor, which is on board the Sentinel-5 Precursor (S-5P), represents a novel tool for understanding SIF variations as well as an opportunity to fully evaluate the potential of SIF to improve GPP estimates at the ecosystem scale, as it provides a high temporal resolution at a daily scale (Köhler et al., 2018). In addition, the future satellite mission Fluorescence Explorer (FLEX) will provide on a single platform SIF at an unprecedented spatial resolution (300 m) together with visible reflectance in the green, red, and far-red spectral windows (Drusch et al., 2017).

The surface spectral reflectance (*R*), VIs, and SIF can be used altogether to better characterize highly spatiotemporal dynamics in vegetation canopy structure, canopy biochemical properties, and vegetation functioning as a response to frequent changes in abiotic conditions at site and ecosystem scales. However, to the best of our knowledge, an attempt to study the synergy between those variables has not been comprehensively addressed due to the fact that the relationships between structural and functional components are not linear and have complex interactions over time and space (Hilker et al., 2007; Sippel et al., 2018; Yazbeck et al., 2021; Pabon-Moreno et al., 2022; Kong et al., 2022).Therefore, a series of observations of SIF, *R*, and VIs at site and ecosystem scales could give insights into how SIF is related to GPP and whether SIF, *R*, and VIs could provide additional information on understanding the dynamics of GPP at the ecosystem scale and beyond.

The overarching objective of this work is to study the potential of SIF, *R*, and VIs (namely NDVI, NIRv, and PRI) to estimate canopy GPP and the synergy between these predictive variables. Specifically, this study primarily intends to evaluate at a daily timescale the strength of the relationships between SIF and GPP at 40 Integrated Carbon Observation System (ICOS) flux sites, including several vegetation functional types (mixed forests (MFs), deciduous broadleaf forests (DBFs), croplands (CROs), evergreen broadleaf forests (EBFs), evergreen needleleaf forests (ENFs), grasslands (GRAs), open shrubland (OSH), and wetlands

(WETs)), and ultimately to examine the synergy between SIF, *R*, and VIs to improve canopy GPP estimates based on a data-driven modelling approach.

3.2. Materials and methods

In this current section, the site characteristics and eddy covariance (EC) flux data are presented. Then, the remote sensing data (TROPOMI, MODIS Aqua and Terra, and Copernicus Land Cover classification) used in the study are described. Lastly, data analysis methods used in this study are presented. Study sites and flux tower in-situ EC flux data were obtained through the ICOS Data Portal release in 2018 and 2021 (https://www.icos-cp.eu/data-services, last access: 21 December 2021). We screened over 70 ecosystem ICOS sites, relying on the availability of GPP data for each site with simultaneous TROPOMI SIF observations in the period from February 2018 to December 2020, and maintained 40 sites for analyses. The study sites encompass a latitude from 5.27° N to 67.75° N, including a diversity of plant functional types (PFTs) based on the IGBP vegetation-type classification given by ICOS PI sites: mixed forests (MFs, 2 sites), croplands (CROs, 9 sites), deciduous broadleaf forests (DBFs, 6 sites), evergreen broadleaf forests (EBFs, 2 sites), evergreen needleleaf forests (ENFs, 13 sites), grasslands (GRAs, 3 sites), open shrubland (OSH, 1 site, which is actually a young vineyard plantation), and wetlands (WETs, 4 sites). The PFT at each site was confirmed by photointerpretation of pictures found in the ICOS Data Portal database and Google Earth. Detailed information and references of these sites are provided in Table S3.1 in the Supplementary materials. Figure 3.1 presents the location of these study sites, except for the GF-Guy site, located in French Guiana. In the analyses, we used daily GPP values computed as the sum of the half-hourly values estimated from each site. GPP data previously gap-filled by ICOS PI, representing for a full year, which was the case for instance at CH-Dav, FR-Bil, IT-SR2, and SE-Deg, were filtered out and were not used in the analyses.

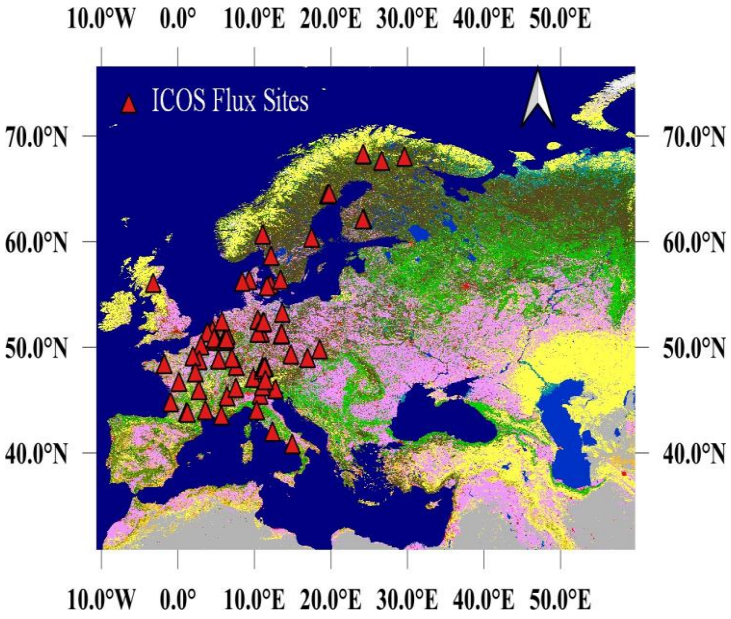

Figure 3.1. The study area and location of the EC ICOS flux sites, except for the GF-Guy site, located in French Guiana. The base map is the 100 m spatial resolution of the Copernicus Global Land Cover classification map. The triangles represent the locations of the flux sites used for investigating the relationships between tower-based GPP and TROPOMI SIF

3.2.1. Remote sensing data

3.2.1.1. MODIS Terra and Aqua data

Time series of daily MODIS Terra and Aqua surface reflectance products (MOD09GA, MODOCGA, MYD09GA, and MYDOCGA), centered at the location of each site, were downloaded from the Google Earth Engine database. The quality assurance (QA) flag (ideal quality, QA = 0) and the cloud mask (clear state) criteria were used. Both MODIS Terra and Aqua, used in this study, contain 16 spectral bands of which the spatial resolution from band 1 to band 7 is 500 m and 1 km for the remaining bands (8–16) (Vermote et al., 2015). Detailed information about the MODIS data products is given in Table S3.2. We used daily MODIS surface reflectance, NDVI, NIR_V, and PRI. These VIs are computed according to the equation given in Table 1. For the PRI computation, we used B_{13} as a reference band following Hilker et al. (2009).

Table 3.1. MODIS Terra and Aqua vegetation index computations. B2 (841–876 nm) denotes the surface spectral reflectance at band 2, B1 (620–670 nm) denotes the surface spectral reflectance at band 1, B11 (526–536 nm) represents the surface spectral reflectance at band 13.

Acronym	Full name	Formulation	Spatial resolution	References
NDVI	Normalized difference vegetation index	$(B_2 - B_1)/(B_2 + B_1)$	500 m	Tucker (1979)
PRI	Photochemical reflectance index	$(B_{11} - B_{13})/(B_{11} + B_{13})$	1 km	Drolet et al. (2008) Hilker et al. (2009)
NIRv	Near-infrared reflectance of vegetation	$B_2 \times$NDVI	500 m	Badgley et al. (2017)

3.2.1.2. TROPOMI SIF and Copernicus Global Land Cover data

TROPOMI, as a single payload of the Sentinel-5 Precursor (S-5P) satellite, was launched on 13 October 2017. TROPOMI has a near-sun-synchronous orbit with a repeat cycle of 16 days and an equatorial crossing time at around 13:30 local time (Köhler et al., 2018), which is comparable to those of Orbiting Carbon Observatory-2 (OCO-2) and the Greenhouse Gases Observing Satellite (GOSAT). However, the wide swath of TROPOMI (2600 km) is larger than that of OCO-2 (10 km), which enables TROPOMI to provide almost daily spatially continuous global coverage (Köhler et al., 2018). TROPOMI has a spatial resolution of 7 km along track (5 km since August 2019 owing to diminished integration time) and 3.5 to 14 km across track (based on the viewing angle) and covers the spectral range between 675–775 nm in the near-infrared with a spectral resolution of 0.5 nm, which allows for the retrieval of far-red SIF (Köhler et al., 2018). To decouple SIF emissions from the reflected incident sunlight, a statistical and data-driven approach is used; see Köhler et al. (2018), for more details. We used instantaneous and daily ungridded soundings of TROPOMI far-red SIF at 740 nm obtained from the Caltech dataset between February 2018 and December 2020 (https://data.caltech.edu/records/1347, last access: 14 June 2021). Instantaneous SIF data were reported in mW m^{-2} sr^{-1} nm^{-1}. Daily SIF (hereafter referred to as SIF_d) is computed by timing instantaneous SIF with a day-length correction factor included in the dataset.

The TROPOMI SIF observations corresponding to each site were determined by relying on the following criteria. Firstly, we extracted all pixels whose center locations are less than 5 km away from the flux tower sites for analyses. The latter choice was motivated by the fact that the relationship between TROPOMI SIF and tower-based GPP gradually weakened as the distance from site to the center of the pixel increased (data not shown). Secondly, to reduce the cloud effects on SIF data, SIF_d observations with a cloud fraction over 15 % were excluded, even though some findings reveal that TROPOMI SIF is less sensitive to cloud than surface

reflectance values (Guanter et al., 2012; Doughty et al., 2021). The 100 m spatial resolution of the Copernicus Global Land Cover classification map for the year 2019 (Buchhorn et al., 2020) was used as a base map of the study sites. This land cover classification map was obtained from the Coper- nicus Global Land Service website (https://lcviewer.vito.be/ download, last access: 25 May 2021).

3.3. Data analysis

In this study, the GPP and SIF_d relationship was evaluated at a daily timescale at different spatial scales. Before investigating the link between GPP and SIF_d, it was necessary to figure out a way to process outliers which were mostly associated with negative SIF_d values. It has been shown that excluding directly negative SIF values could have effects on studying the relationships between satellite SIF data and GPP (Köhler et al., 2018; Köhler et al., 2021). Thus, to handle the outliers, an exponential model was used to account for the structural relationship between the instantaneous SIF and the SIF error included in the dataset. A threshold of ±0.15 mW m^{-2} sr^{-1} nm^{-1} was then applied to the residual random error of the exponential model.

We used a hyperbolic model to relate GPP to SIF_d following (Damm et al., 2015; Kim et al., 2021) $GPP = \mathrm{a} \times \frac{SIF_d}{SIF_d + \mathrm{b}}$, where a and b are fitted parameters. It is worth noting that a linear model between GPP and SIF_d was also investigated, and the results are provided in the Supplementary materials. Before relating GPP to SIF_d using this hyperbolic model at each site, SIF values equal to or less than zero were discarded. Afterward, the same model was fitted on a PFT scale by pooling all data across all sites for the same PFT. To explore the generalizability of the relationship between GPP and SIF_d, first the hyperbolic model was adjusted on data pooled across all sites. Second, to further test how the year, site, and PFT, as categorical variables, and their interactions (year · GPP, site · GPP, and PFT · GPP) influence the GPP and SIF_d relationship, a Generalized Linear Model (GLM) was used. Within the GLM, SIF_d is considered a response variable, whereas site, PFT, year, and GPP are the explanatory variables. These aforementioned variables and their interaction effects may affect the changes or variations either in SIF_d or GPP and may consequently influence the slope and intercept of their relation- ships.

In order to study the synergy between SIF_d, R, and VIs to improve GPP estimates, a Random Forest (RF) regression model was used (Breiman, 2001). Briefly, an RF is a machine

learning algorithm which combines the results of several random ensemble decision trees to reach a final accurate output. Before setting up the RF model, the correlation matrix between all variables was computed. It has been shown that important features can be affected by the high correlation between feature predictors (Toloşi and Lengauer, 2011), suggesting that a decrease in importance values is observed when the level of correlation and the number of correlated variables increase. In practice, a strongly predictive variable belonging to a group of correlated variables can be considered less important than an independent and less informative variable. Based on remotely sensed data inputs and one categorical explanatory variable (PFT), the variables that are the most relevant for estimating GPP on daily data pooled altogether across all sites were evaluated. Four RF models were established by relying on the combination of the predictive variables to estimate GPP: (1) only surface spectral reflectance (RF-*R*), (2) surface spectral reflectance plus SIF_d (RF-SIF-*R*), (3) surface spectral reflectance plus SIF_d and the PFT as a categorical variable (RF-SIF-*R*-PFT), and (4) SIF_d plus VIs (RF-SIF-VI) (namely NDVI, NIRv, and PRI). A total of 80 % of the data were used for training and the remaining for testing the model. It is worth mentioning that a RandomizedSearchCV technique was used (scikit- learn library for Python) to tune the model, and it took the best parameters for each model to predict GPP and applied a 10-fold cross-validation and 20 iterations on the training set to avoid splitting the dataset into training, validating, and testing sets, which could affect the number of data allocated to the training and could easily lead to model overfitting. The ensemble of decision tree models includes 200 trees for all models, but the number of splits per tree and the maximum depth varied. The relative importance of each variable, based on the mean decrease in the impurity method, was used to evaluate the part of the contribution of each input variable in predicting the canopy GPP variability. For TROPOMI data extraction, MATLAB R2021a (MathWorks, Inc., USA) was used, and Python version 3.9.1 was used for data analysis and visualization (sklearn, SciPy, seaborn, matplotlib, pan- das, and NumPy libraries for Python).

Ultimately, the strength of the relationships between SIF_d and GPP was compared based on the coefficient of determination (R^2), root mean square error (RMSE), and the *p*-value metrics. The random forest models were evaluated and compared based on out-of-bag adjusted R^2 and RMSE. Last but not least, a paired *t* test was used to compare the performance of the RF models based on the method proposed by Nadeau and Bengio (2003). A 5 % significance level was used for all statistical inferences.

3.4. Results

3.4.1. GPP vs. SIF_d relationships

Site-specific relationships

The first aim was to evaluate the strength of the relationships between tower-based GPP and SIF_d encompassing different vegetation types at site level. To do so, a hyperbolic model was used to relate GPP to SIF_d at each site. Figure 3.2 shows the relationships between GPP and SIF_d at each site. Overall, the results revealed a hyperbolic relationship with relatively saturating GPP in the presence of moderate to high SIF_d. However, the relationships between GPP and SIF_d are site-dependent, suggesting that the difference in plant functional types and spatial heterogeneity across sites may significantly affect the relationships between GPP and SIF_d. The strongest relationships were found at DK-Sor, FR-Fon, DE-Tha, SE-Nor, and BE-Bra, which are the DBF, ENF, and MF vegetation-type sites, with R^2 values being between 0.64 and 0.87 ($p < 0.0001$). The weakest relationships were recorded at the FI-Var, FR-EM2, and DE-RuW sites, and no significant relationship was found at GF-Guy, IT-Cp2, and FR-Mej. For each fit, the number of data points was between 160 and 1510, depending on the data availability at each site. Detailed information and statistics on the relationships between GPP and SIF_d at each site are given in Table S3.3. Note that the independent assessment considering the linear model to relate SIF_d to GPP at each site and each PFT and data pooled across all sites revealed a relatively consistent lower goodness of fit, justifying the use of a hyperbolic model (see Tables S3.4 and S3.5 and Figs. S3.1, S3.2, and S3.3 in the Supplementary materials).

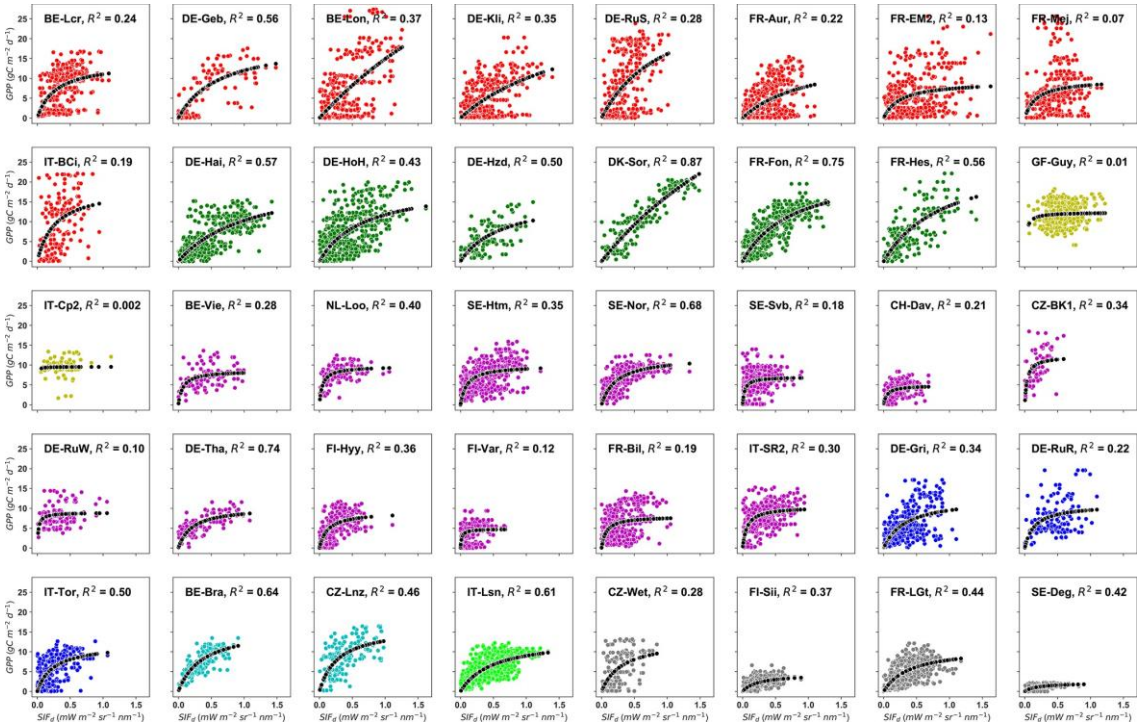

Figure 3.2. Site-specific tower-based GPP and SIFd relationships at daily timescales. R^2 represents the coefficient of determination of the relationship between GPP and SIF_d for each site. The color code represents the eight different plant functional types encountered at the study sites: red stands for croplands (CROs), green for deciduous broadleaf forests (DBFs), yellow for evergreen broadleaf forests (EBFs), magenta for evergreen needleleaf forests (ENFs), blue for grasslands (GRAs), cyan for mixed forests (MFs), lime for open shrubland (OSH), and dim-grey for wetland (WET). The dotted black line represents the hyperbolic fit between GPP and SIFd. Plant-functional-type-specific and overall site relationships.

To test the effects of the PFT on the relationship between GPP and SIF_d at the daily timescale, data were pooled across sites of the same PFT (MF, CRO, ENF, DBF, EBF, GRA, OSH, and WET), and the hyperbolic model was applied on each PFT. Figure 3.3 depicts the scatterplots of the relationships between GPP and SIF_d. The relationship between GPP and SIF_d was statistically significant for all PFTs (R^2 = 0.06–0.61, $p < 0.0001$), taken individually. Furthermore, the hyperbolic relationship between GPP and SIF_d was the strongest for OSH, DBF, and MF, with an R^2 of 0.61, 0.59, and 0.52, respectively, and the lowest for EBF with an R^2 of 0.06. This result suggests that the relationships between GPP and SIF_d were clearly PFT-specific, as shown in Table 3.2.

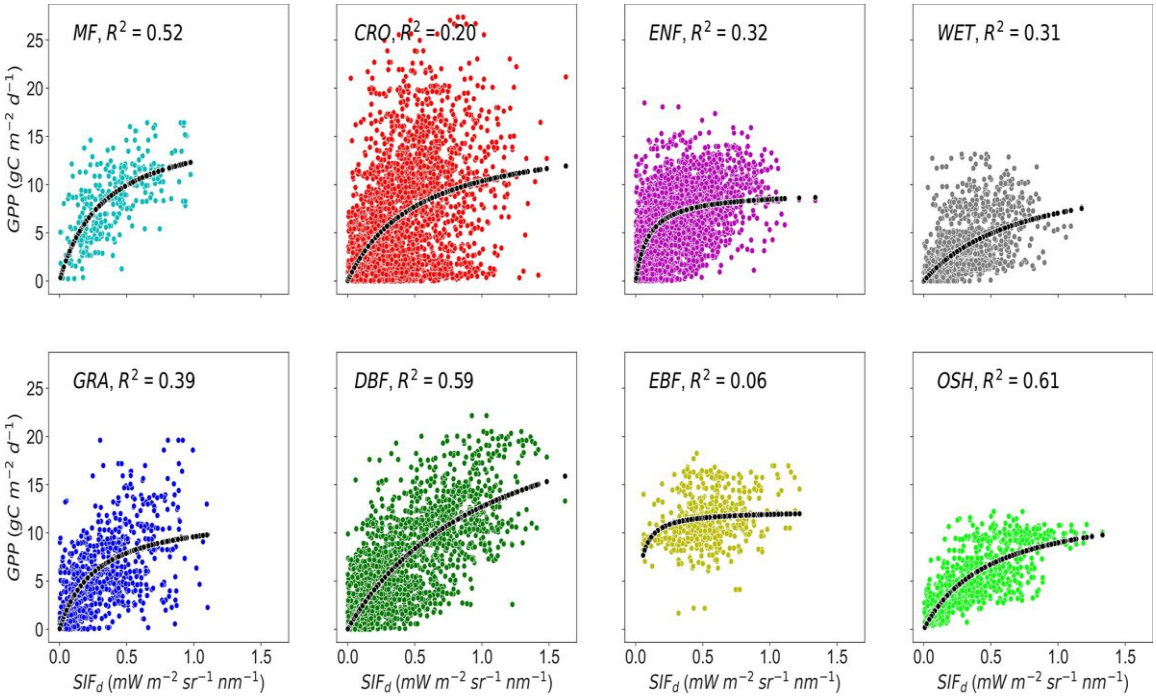

Figure 3.3. Relationships between tower-based GPP and SIFd in eight plant functional types: MF, CRO, ENF, DBF, EBF, GRA, OSH, and WET at daily timescales. R^2 represents the coefficient of determination of the relationship between GPP and SIF_d. All pairwise relationships between GPP vs. SIF_d were statistically significant with $p < 0.0001$. The dotted black line represents the hyperbolic fit between GPP and SIF_d.

Table 3.2. Summary statistics of the plant-functional-type-specific GPP and SIF_d relationship in eight major PFTs. All pairwise relationships between GPP and SIF_d were statistically significant with $p < 0.0001$. a and b denote the fitted parameters from the hyperbolic model. The unit of RMSE is in gC m^{-2} $d^{-1.}$

PFT	Site	R^2	a	b	RMSE	N
CRO	9	0.20	15.74	0.52	5.29	5538
DBF	6	0.59	26.59	1.09	3.61	3566
EBF	2	0.06	12.31	0.03	2.66	956
ENF	13	0.32	9.30	0.10	2.94	6440
GRA	3	0.39	12.21	0.27	3.32	1658
MF	2	0.52	16.46	0.33	2.79	620
OSH	1	0.61	13.44	0.50	2.10	1510
WET	4	0.31	12.35	0.75	2.50	2710
ALL	40	0.36	15.33	0.45	3.93	22998

Moreover, the generalizability of the relationship between GPP and SIF_d was first tested on data pooled together across all sites (Figure 3.4). A significant but weak relationship between GPP and SIF_d was found across all sites with an R^2 of 0.36 ($p < 0.0001$) and RMSE of 3.93 gC m^{-2} d^{-1}. However, when the variations between the year, site, and PFT as input variables were included in a GLM, along with GPP, the results showed a strong significant relationship between SIF_d, year, site, PFT, and GPP ($p < 0.001$). Furthermore, the interactions between the

year and GPP and PFT and GPP were found to have a statistically substantial effect on the SIF_d and GPP relationship, while the interaction between the site and GPP was not significant (see Table S3.5). These findings support that the GPP and SIF_d relationship is considerably influenced by the site PFT and the interannual variations in SIF_d.

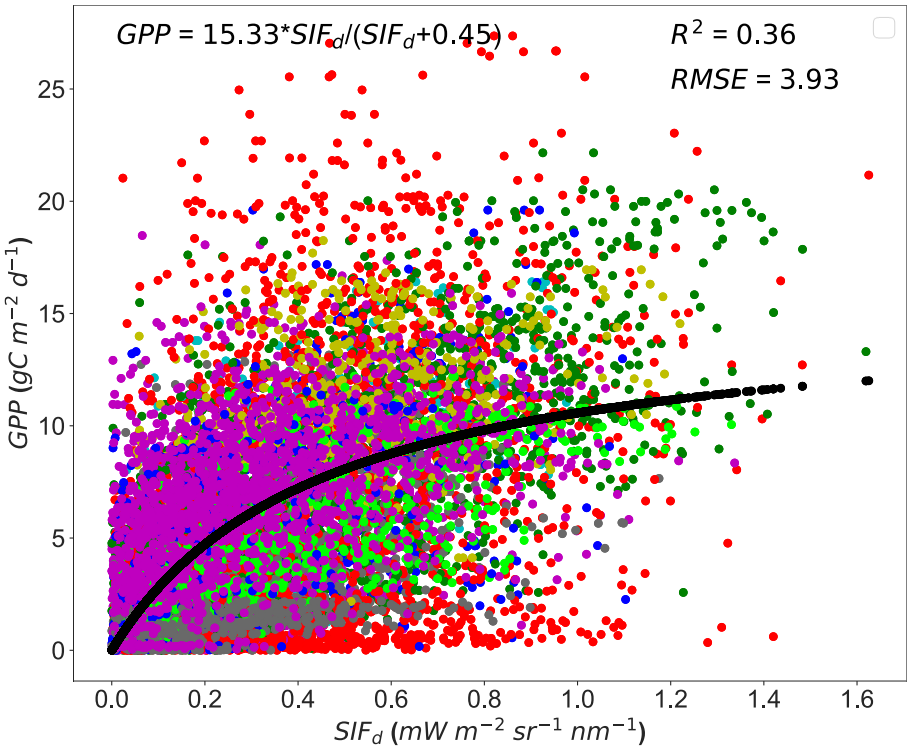

Figure 3.4. Scatterplots of the relationships between tower-based GPP and SIFd in eight PFTs pooled together across all sites. The dotted black line represents the hyperbolic fit between the GPP and SIF_d. The color code represents the plant functional types encountered in the study sites: red stands for croplands (CROs), green for deciduous broadleaf forests (DBFs), yellow for evergreen broadleaf forests (EBFs), magenta for evergreen needleleaf forests (ENFs), blue for grasslands (GRAs), cyan for mixed forests (MFs), lime for open shrubland (OSH), and dimgrey for wetland (WET).

3.4.2. Synergy between SIF_d, R, and VIs to quantify GPP

In order to optimize the inputs for the Random Forest (RF) regression and to avoid the effects of highly correlated explanatory variables on the model performance, the correlation matrix was computed. The correlation matrix (supplied in Supplementary materials Figure S3.4) revealed a strong dependency between predictive variables (notably B_9 vs B_{10}, B_{11} vs B_{12}, and B_{13} vs B_{14}), indicating that using an RF model built in these variables could be affected by those high correlations. Based on these observations, the R of B_{10}, B_{12}, and B_{14} was excluded from the explanatory variables of RF regression models.

3.4.3. Performance of GPP estimates using random forest regression

In Figure 3.5, tower-based GPP is represented against the four RF GPP models across all sites. Overall, all the RF-model-predicted GPP shows a high agreement with tower-based GPP. Yet, the RF-R model has the strongest relationship with tower-based GPP with an adjusted R^2 of 0.86 and RMSE of 1.72 gC m^{-2} d^{-1}, while the RF-SIF-VI model presents the lowest predictions of GPP, as the adjusted R^2 and RMSE were 0.75 and 2.29 gC m^{-2} d^{-1}, respectively. Furthermore, the RF-SIF-R and RF-SIF-R-PFT model performed similarly well at estimating GPP, as they could explain 82% and 83% of the variations in GPP across all sites, respectively. A paired t-test realized between the four models based on the adjusted R^2 performance revealed that the difference in adjusted R^2 between RF-R and RF-SIF-R, RF-R and RF-SIF-R-PFT, and RF-SIF-R and RF-SIF-R-PFT models was not statistically significant. In other words, these three RF models have statistically the same performance.

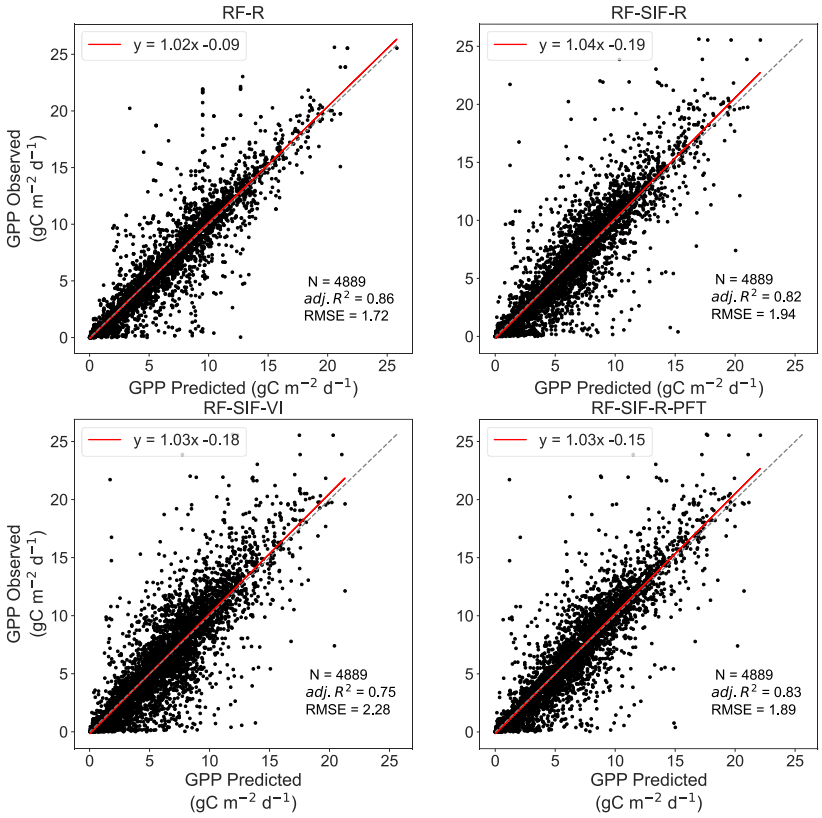

Figure 3.5. Scatterplots of the observed GPP against the RF-predicted GPP across all sites. N denotes the number of data points used for the RF model's testing, adj. R^2 represents the

adjusted coefficient of determination of the relationship between observed GPP and predicted GPP, and the RMSE is the root mean squared error between the observed GPP and RF-model-predicted GPP. The dashed diagonal line depicts the 1:1 line. RF-R denotes prediction using only surface spectral reflectance; RF-SIF-R includes R and SIFd as inputs to predict GPP; RF-SIF-VI integrates SIF_d and VIs to estimate GPP; and RF-SIF-R-PFT includes R, SIF_d, and plant functional type as categorical variables to predict GPP.

The RF regression model's GPP estimates and the observed GPP representing different vegetation types at the site level are depicted in Figures 3.6 and 3.7 for the RF-SIF-R model predictions as an example. The estimates for each site from the other models are presented in the Supplementary materials (Figures S3.6-a RF-R, S3.6-b RF-R, S3.7-a RF-SIF-VI, S3.7-b RF-SIF-VI, S3.8-a RF-SIF-R-PFT, and S3.8-b RF-SIF-R-PFT) and the summary statistic results in Tab S3.7 for all RF models. At the site level, the RF-SIF-R model predicted tower-based GPP with high accuracy (adj. R^2 = 0.54-0.95), except for three sites such as IT-BCi (adj. R^2 = 0.21), IT-Cp2 (adj. R^2 = 0.25), and *SE-Deg* (adj. R^2 = 0.41), where the RF-SIF-R model had difficulties in reproducing GPP, even if R^2 remained statistically significant at 5% probability level. It is worth noting that all other RF models have poor GPP predictions for these aforementioned sites. However, on data pooled across all sites of the same PFT, the RF-SIF-R model shows high performance in estimating GPP for all eight major PFTs with an adj. R^2 being between 0.68 and 0.90. The lowest predictions are encountered in the CRO and EBF sites, whereas the best tower-based GPP estimates were found in the DBF and OSH sites.

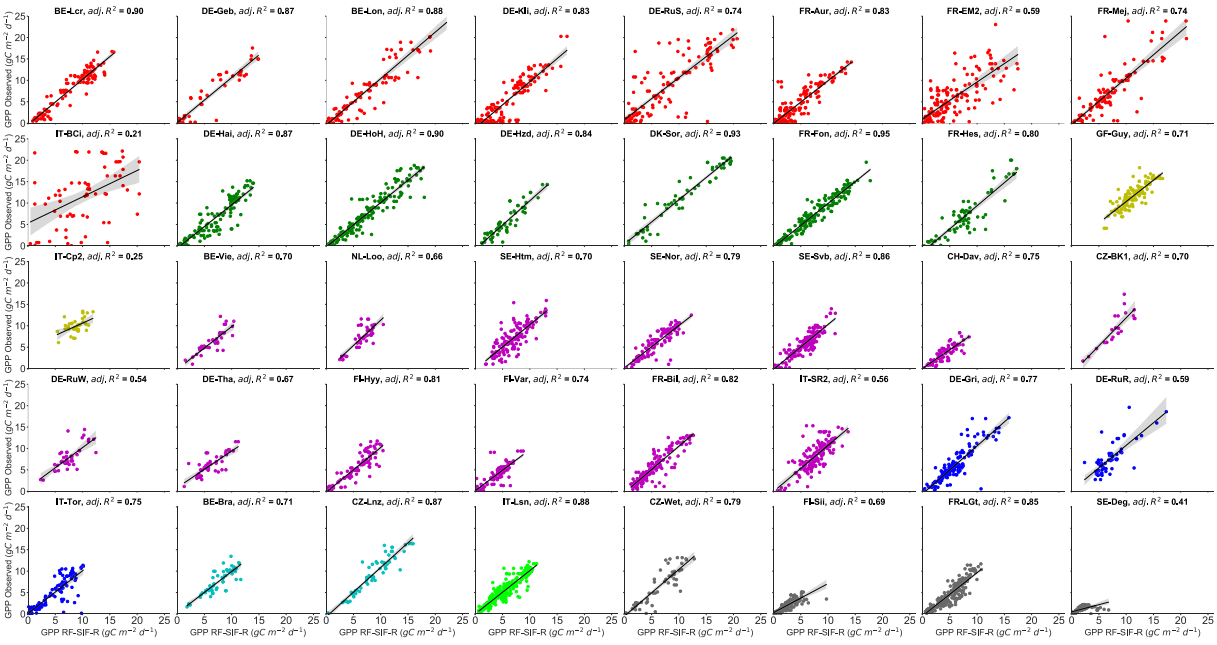

Figure 3.6. Site-specific scatterplots between observed GPP and RF-SIF-R-predicted GPP at daily timescales. The adj. R^2 represents the adjusted coefficient of determination of the

relationships between observed GPP and predicted GPP. All pairwise relationships between observed GPP vs. Predicted GPP were statistically significant at all sites (with $p < 0.0001$). The color code represents the eight different vegetation types encountered in the study sites: red stands for CRO, green for DBF, yellow for EBF, magenta for ENF, blue for GRA, can for MF, lime for OSH, and dim-grey for WET.

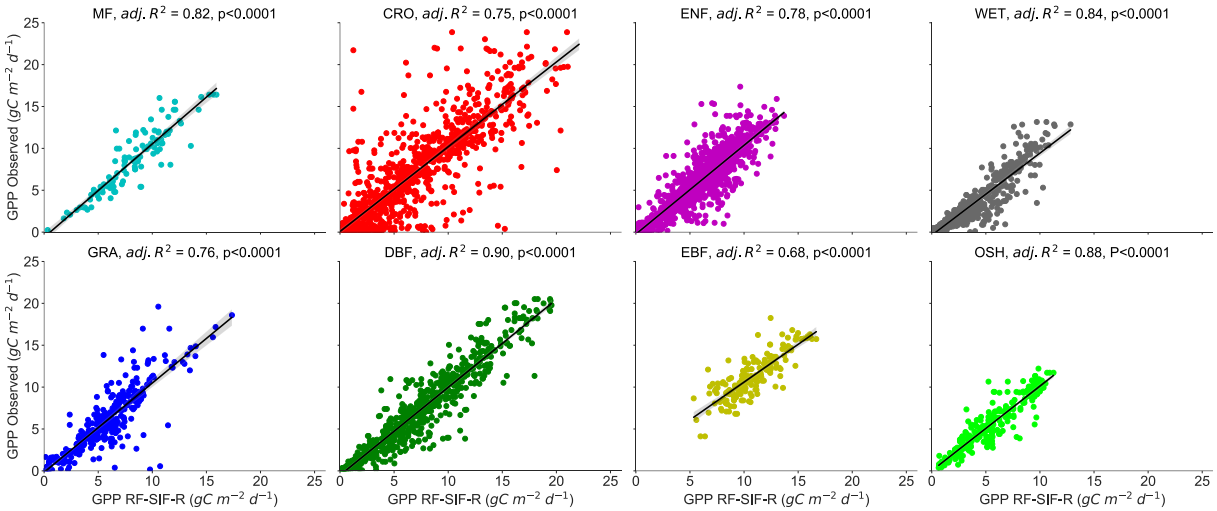

Figure 3.7. Scatterplots of observed GPP against RF-SIF-R-predicted GPP in eight PFTs at daily timescales. The adj. R^2 represents the adjusted coefficient of determination of the relationship between observed GPP and predicted GPP. p denotes the probability value of the relationships.

In Figure 3.8 and Table 3.3, the observed and estimated GPP representing different PFTs for all four RF models is depicted. The estimation for each site is given in Supplementary materials Figure S3.5. Overall, all RF models' GPP predictions capture the seasonal and interannual dynamics of the tower-based GPP very well. However, there are sites, years and vegetation types where observed GPP cannot be estimated with high accuracy. For instance, the RF models tend to underestimate GPP maxima in GRA, WET, and EBF vegetation types. These underestimates are mostly marked by the slope of the relationships between the observed GPP and predicted GPP in Table 3.3.

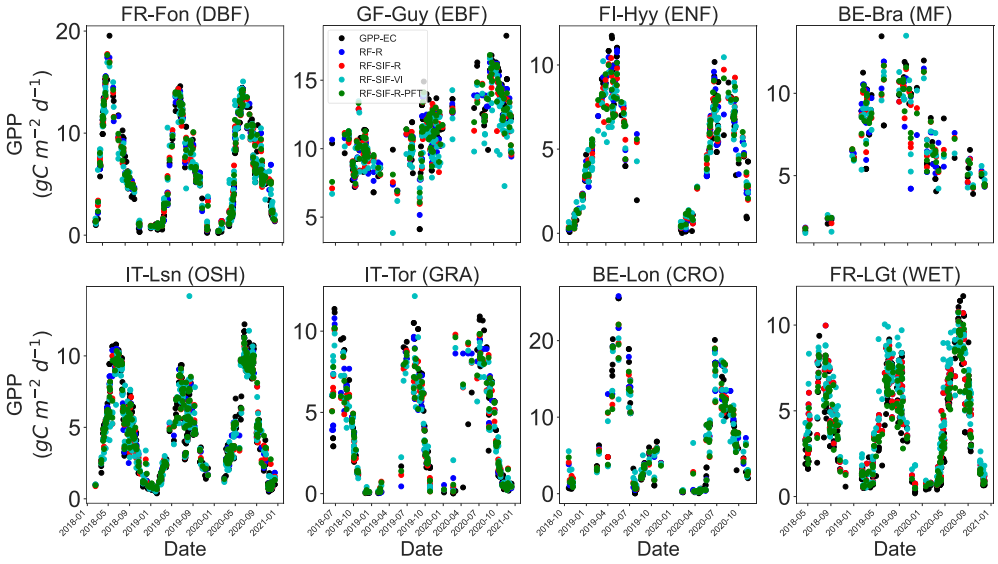

Figure 3.8. Comparison between observed GPP and RF-regression-model-estimated GPP at selected ICOS flux sites representing different PFTs: DBF, EBF, ENF, MF, CRO, GRA, OSH, and WET. The color code represents the different RF GPP predictions and the observed GPP: red stands for RF-SIF-R, green for RF-SIF-R-PFT, blue for RF-R, cyan for RF-SIF-VI, and black for observed GPP.

Table 3.3. Summary statistics of plant-functional-type-specific observed GPP against RF-model-predicted GPP relationships in eight major PFTs: MF, CRO, ENF, DBF, EBF, GRA, OSH, and WET. All pairwise relationships between observed GPP and predicted GPP were statistically significant with $p < 0.0001$. The sign ± denotes the 95 % confidence interval on the slope and intercept of the relationships between observed GPP and predicted GPP.

			RF-R				RF-SIF-R			
PFT	Site	N	Adj. R^2	Slope	Intercept	RMSE	Adj. R^2	Slope	Intercept	RMSE
CRO	9	1171	0.78	1.03±0.03	0.00±0.24	2.67	0.75	1.01±0.03	0.08±0.26	2.89
DBF	6	748	0.92	1.02±0.02	-0.23±0.18	1.41	0.90	1.05±0.02	-0.52±0.21	1.61
EBF	2	188	0.77	0.93±0.07	1.01±0.83	1.23	0.68	0.90±0.09	1.58±0.99	1.45
ENF	13	1385	0.85	1.01±0.02	-0.01±15	1.29	0.78	1.06±0.03	-0.23±0.19	1.54
GRA	3	364	0.81	1.02±0.05	-0.02±32	1.64	0.76	1.07±0.06	-0.17±0.38	1.87
MF	2	117	0.84	1.05±0.08	-0.15±0.76	1.49	0.82	1.12±0.10	-0.62±0.83	1.56
OSH	1	317	0.91	1.02±0.04	-0.09±0.22	0.99	0.88	1.01±0.04	0.01±0.24	1.10
WET	4	599	0.92	0.98±0.02	-0.15±0.10	0.85	0.84	0.98±0.03	-0.37±0.15	1.17
All	40	4889	0.86	1.02±0.01	-0.09±0.08	1.72	0.82	1.04±0.01	-0.19±0.10	1.94
			RF-SIF-VI				RF-SIF-R-PFT			
PFT	Site	N	Adj. R^2	Slope	Intercept	RMSE	Adj. R^2	Slope	Intercept	RMSE
CRO	9	1171	0.70	1.03±0.04	0.01±0.29	3.14	0.75	1.00±0.03	0.12±0.26	2.87
DBF	6	748	0.84	1.05±0.03	-0.58±0.28	2.06	0.91	1.04±0.02	-0.40±0.21	1.56
EBF	2	188	0.51	0.77±0.11	3.42±1.14	1.80	0.72	0.96±0.09	0.74±0.98	1.37

ENF	13	1385	0.66	1.02±0.04	0.10±0.24	1.92	0.79	1.08±0.03	-0.39±0.19	1.5
GRA	3	364	0.69	0.98±0.07	0.02±0.43	2.11	0.77	1.07±0.06	-0.29±0.38	1.84
MF	2	117	0.71	1.04±0.12	0.04±1.07	2.00	0.82	1.12±0.09	-0.73±0.84	1.56
OSH	1	317	0.83	0.98±0.05	0.21±0.29	1.33	0.89	1.02±0.04	-0.06±0.24	1.08
WET	4	599	0.72	0.88±0.04	-0.39±0.21	1.54	0.88	1.05±0.03	-0.29±0.12	0.99
All	40	4889	0.75	1.03±0.02	-0.18±0.12	2.28	0.83	1.03±0.01	-0.15±0.09	1.89

3.4.4. Relative importance of the predictive variables for predicting GPP

Figure 3.9 shows the relative importance (or mean decrease in impurity) of the predictive variables of the RF models for predicting GPP across all sites pooled together. Figure 3.9 indicates that for the RF-R model, R in the near-infrared (NIR) band (B_2 :841-876 nm) and R in the red band (B_1: 620-670 nm) were found as the most important input variables for GPP estimates. Moreover, it can be seen that the contribution of the far-red R (B_{13}) in predicting GPP is also important, whereas the contribution of the other R bands was on a similar level. For the RF-SIF-R model, SIF_d (>23%), R in the NIR (B_2 = 17%), and the R in the red band (B_1= 9%) are by far the most relevant variables for GPP prediction, while the other variables contribute less to GPP estimates. The RF-SIF-R-PFT model differs from the previous model (RF-SIF-R) only on the plant functional-type categorical variable and its results underline that the plant functional-type variable is still important for predicting GPP. Ultimately, reflectance-based vegetation indices are widely used for predicting GPP at larger scales. Hence, it is worthwhile investigating what the contributions of these interesting variables jointly with SIF_d in predicting canopy GPP are. The relative importance derived from the RF-SIF-VI model reveals that SIF_d (36%) is substantially the most relevant variable for predicting GPP. The contributions of NIR_v and NDVI to the model are comparable, whereas PRI has a lower contribution in estimating GPP.

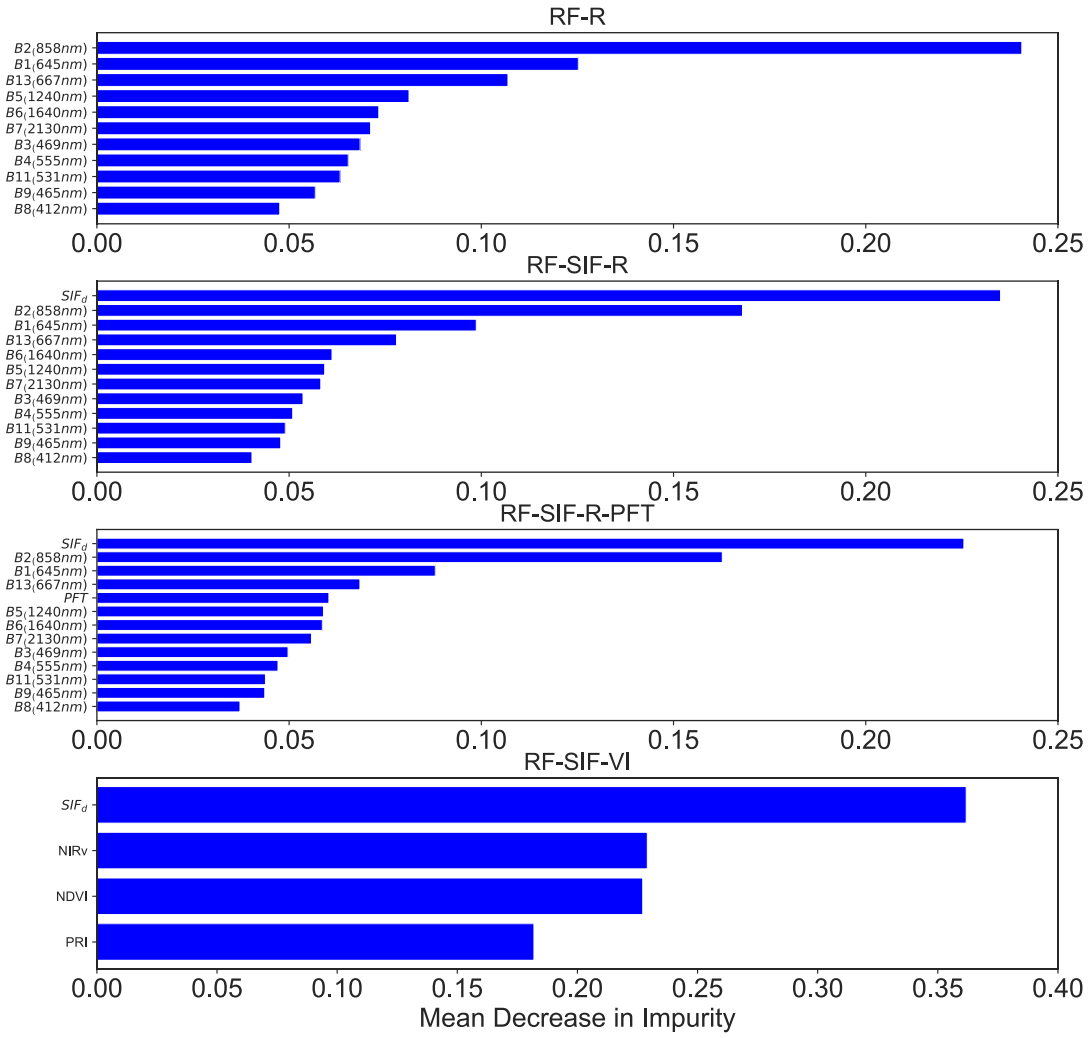

Figure 3.9. Relative importance of predictive variables of the RF models based only on remote sensing data for estimating GPP, except for the RF-SIF-R-PFT model. The RF-R model is based only on MODIS surface spectral reflectance; the RF-SIF-R model uses SIF_d and surface reflectance as input variables; the RF-SIF-R-PFT model integrates SIF_d, surface reflectance, and PFT as explanatory variables; and the RF-SIF-VI model combines SIF_d and reflectance-based indices, notably NDVI, NIR_v, and PRI, as input variables for predicting GPP across all sites. The wavelengths depicted on the spectral bands denote the central wavelength.

3.5. Discussion

3.5.1. Strength of the relationship between GPP and SIF_d at site and PFT levels

In this study, the first aim was to evaluate the strength of the relationship between tower-based GPP and SIF_d at daily timescales and at different spatial scales (at site and plant functional type levels).

At the site level, the results demonstrate that there were strong and statistically significant relationships between GPP and SIF_d. However, the hyperbolic fit between tower-based GPP and SIF_d varies significantly across sites, which suggests a site-specific relationship. In other words, at these scales the differential variations in plant physiology and vegetation structure across sites and years and the spatiotemporal dynamics of the flux tower footprints (depending mainly on the height of the tower and wind direction), along with spatial heterogeneity and environmental conditions across sites may strongly affect first of all the SIF emissions, scattering and reabsorption across sites, and consequently the relationship between GPP and SIF_d (Fournier et al., 2012; Paul-Limoges et al., 2018; Tagliabue et al., 2019; Li et al., 2020; Chu et al., 2021; Zhang, et al., 2021b). These results are consistent with previous studies based on ground-based and satellite measurements which found evidence that canopy structure, as well as PFT, have substantial effects on the relationships between GPP and SIF across multiple sites (Dechant et al., 2020; Lu et al., 2020; Li et al., 2018b; Sun et al., 2018; Wang et al., 2020; Hao et al., 2021; Wang et al., 2022). For instance, Wang et al. (2020) found that the relationship between OCO-2 SIF observed at 757 nm and 771 nm and at tower-based GPP across eight vegetation types at 61 flux sites all over the world relies on canopy structure, and Lu et al. (2020) reported a better relationship between canopy GPP and SIF corrected from reabsorption and scattering effects than top-of-canopy SIF based on ground-based measurements, underlying the importance of canopy structure on SIF and GPP relationships.

Furthermore, these results are also in good agreement with several studies carried out with instantaneous ground-based measurements at different vegetation types, sites, and locations (Kim et al., 2021, Damm et al., 2015; He et al., 2020, Gu et al., 2019). For instance, Kim et al. (2021) pointed out that a hyperbolic model could better explain the relationships between GPP and SIF in an evergreen needle forest, and Damm et al. (2015) showed similar results in cropland, mixed temperate forest and grassland vegetation types. One of the most

plausible explanations is that GPP might reach saturation in high sunlight, while SIF tends to keep increasing with PAR. It is also paramount to mention that the saturation of optical signals is a common issue in remote sensing, which can explain part of the weaker relationships found in the EBF sites.

The relationship between tower-based GPP and SIF_d considering the PFT was also examined. The results revealed a significant PFT-specific GPP and SIF_d relationships across all eight major vegetation types. Yet, the hyperbolic relationship between GPP and SIF_d varies considerably across PFTs, suggesting a PFT-specific relationship. The relationship between GPP and SIF_d is driven by the ratio between canopy photosynthesis light use efficiency and fluorescence yield, along with the canopy escape probability fraction of SIF photons from the canopy to sensor (Porcar-Castell et al., 2014; Zhang et al., 2018; Zeng et al., 2019). The major drivers affecting the canopy photosynthesis and SIF yield include among others leaf morphology and orientation, plant physiology, canopy structure (leaf area index, chlorophyll contents, etc.), rapid changes in incident radiation and illuminated canopy surface, different contributions from photosystem I and II, as well as rapid abiotic responses (Porcar-Castell et al., 2014; Mohammed et al., 2019; Gamon et al., 2019; Yang et al., 2021; Chu et al., 2021; Wang et al., 2022). These explanations altogether sustained the PFT-specific GPP vs SIF relationship, as those factors can differ considerably across PFTs. Additionally, the results showed that the MF, DBF and OSH sites have the strongest GPP and SIF_d relationship, which indicates that SIF may easily capture the seasonal, interannual, and phenological variations in GPP within this vegetation type. In other words, in the MF, DBF and OSH (one sample of vineyard plantation) biomes, there are explicitly marked seasonal and phenological changes compared to the EBF or ENF forest where there is greenness all the time. Thus, in the DBF, MF and OSH biomes the SIF signal may easily capture the variations in LAI and absorbed PAR and consequently display a high correlation between GPP and SIF_d. On the other hand, the lower observed relations between GPP and SIF_d in the EBF (GF-Guy and IT-Cp2) sites could be partly explained by a lower spatiotemporal variability in SIF emissions in tropical forests coupled to dispersed and lower GPP values observed on the datasets, as well as challenges in detecting or decoupling the understory vegetation effects from all vegetation canopy contributions to SIF emissions and uncertainties related to GPP estimates in tropical forests, while in CRO (FR-Mej) the difference in photosynthetic pathways (C3, C4 or a mix of both) and different management practices may be the reasons why SIF_d could not capture the

variations in GPP, as reported in earlier studies (Li et al., 2018; Hayek et al., 2018; Mengistu et al., 2021; He et al., 2020; Hornero et al., 2021; Li & Xiao, 2022). Previous studies have also reported weak relationships between GPP and SIF in the EBF vegetation-type (Li et al., 2018b; Wang et al., 2020). Moreover, it is worth mentioning that the biases related to cloudless and cloudy skies in space-based SIF retrieval, complicate the use of SIF to estimate GPP at the PFT scale because cloudless-sky SIF and cloudless-sky GPP are completely different from cloudy-sky SIF and cloudy-sky GPP, and consequently, their relationship may also differ (Miao et al., 2018). Investigating GPP and SIF relationships based only on clear-sky data and only on cloudy-sky data, without the mix of both, is justified to better understand their links. Ultimately, the PFT-dependent relationships between GPP and SIF_d in this study was confirmed by the weak and statistically significant relationship reported for all biomes on data pooled together across all sites. This hypothesis was further supported by significant effects of the year, site, and PFT on the relationship between SIF_d and GPP reported in the GLM. Exploring the newly launched satellite instruments such as OCO-3 and ECOSTRESS and the upcoming FLEX and GeoCarb satellite missions, which are planned to have diurnal sampling or fine-spatial resolution (for instance 300 m for FLEX), along with ongoing ground-based, and airborne-based SIF and GPP data altogether will improve the ability not only to better understand the GPP and SIF relationship, but also to completely decouple the effects of driving factors such as vegetation physiology, canopy structure, and abiotic stress conditions that mediate their relationships at the ecosystem scale.

3.5.2. Synergy between SIF_d, R, and VIs for estimating GPP using random forest

The second main goal in this paper was to explore the synergy between SIF_d from the TROPOMI instrument and MODIS R and VIs namely NDVI, NIR_v, and PRI for predicting GPP on data pooled across all sites. To achieve this purpose, four RF regression models were established: RF-R, RF-SIF-R, RF-SIF-R-PFT, and RF-SIF-VI. Except for the RF-SIF-R-PFT model, the main advantage of using solely remotely sensed data for estimating GPP is that we do not need to rely on land cover type, land cover change, and meteorological data (Xiao et al., 2019).

The current results show that the RF-R (surface spectral reflectance alone), RF-SIF-R (SIF_d plus surface spectral reflectance) and RF-SIF-R-PFT (SIF_d plus surface spectral reflectance plus PFT) models, statistically explain the same variance of GPP at the daily

timescale (82~86%), whereas the RF-SIF-VI (SIF_d plus reflectance-based indices) explains the lowest part, about 75% of GPP across all sites. It is well known that at the seasonal scale spectral reflectance captures the variations in canopy structure. The seasonal variations in canopy structure, especially LAI, are strongly correlated with variations in GPP (Dechant et al., 2022). This could justify the strong relationship found between tower-based GPP and the predicted GPP by the RF-R model. On the other hand, SIF is an integrative variable at the seasonal and interannual scales as shown in Figure 3.9 and the correlation matrix results (a strong contribution of SIF to GPP estimates and a high correlation between GPP and SIF_d compared to each R band taken alone). However, SIF, while exhibiting the highest relative importance, fails to improve the GPP estimate. Hence, while being limited by its spatial resolution (7 km x 3.5 km), at which SIF may lose its physiological information and most likely may reflect phenological, structural, and illumination information (Jonard et al., 2020; Kimm et al., 2021), SIF remains a better predictor of GPP than each reflectance band individually. These results also revealed that the RF-SIF-VI has the poorest performance in predicting GPP. This lower performance could be partly due to the well-known saturation of VIs over dense canopies. In addition, the paired t-test did not show any statistically significant difference between RF-R and RF-SIF-R models, which confirms the above hypothesis, which suggests that SIF represents the variations in absorbed PAR at these scales. Recently, Pabon-Moreno et al. (2022) used solely Sentinel-2 satellite-derived red-edge-based and near-infrared-based vegetation indices and all spectral bands to predict GPP at daily time scale across 54 EC flux sites using a data-driven approach (random forest). The authors reported that spectral bands jointly with VIs can inform only 66% of the variance in GPP, which is far less than the here worse-performing model (i.e., RF-SIF-VI) in predicting GPP. The daily scale and solely remotely-sensed-driven RF-R and RF-SIF-R models outperform previous GPP products derived based on data-driven methods (Wolanin et al., 2019; Tramontana et al., 2016; Jung et al., 2019) and process-based models (Jiang & Ryu, 2016; Zhang et al., 2017; Lin et al., 2019), which included even more inputs as predictive variables such as meteorological data, land-cover-type data, and land-cover-change data and were conducted mostly at longer timescales (8-day or monthly timescale) compared to this study. Furthermore, these results are in strong agreement to two recent studies (Cho et al., 2021; Li et al., 2021). More specifically, Cho et al. (2021) found that remotely sensed data alone can explain 81% of GPP variability across four vegetation types, including ENF, EBF, DBF, and MF, in South Korea at 8-day timescales, and Li et al. (2021) pointed out that instantaneous GPP estimates across 56 flux tower sites could be achieved with an R^2 of 0.88 and RMSE of

2.42 µmol CO_2 m^{-2} s^{-1} using ECOSTRESS land surface temperature, daily MODIS satellite data, and meteorological data from ERA5 reanalysis. This study also revealed that GPP prediction can be achieved with high accuracy based on solely remotely sensed data that are widely and publicly available for all.

The RF models could clearly capture the GPP variations at each site, encompassing different vegetation types as shown in Figures 3.6 and 3.8. Indeed, there are sites, years, and vegetation types where tower-based GPP was underestimated, which were the cases for WET and EBF vegetation types. Furthermore, all RF models struggle to accurately estimate tower-based GPP at the IT-BCi, IT-Cp2 and SE-Deg sites, owing most likely to SIF pixel heterogeneities and lower GPP values observed in these sites, along with previously explained issues associated with estimating GPP in crops and tropical stands. Similar results were reported recently in Pabon-Moreno et al. (2022), including eight vegetation types (ENF, CRO, DBF, GRA, WET, MF, savannah (SAV), and OSH). The reason behind these poor performances may also be related to difficulties in detecting abiotic stress conditions (Bodesheim et al., 2018), underscoring need for more research on predicting GPP during extreme abiotic conditions.

Furthermore, in this study, it is determined what the main variables contributing to GPP prediction are using the four RF models based on the relative importance metric of each model. Yet, it is found that SIF_d, the R in the NIR band (B_2), the red band (B_1), and the far-red band (B_{13}), as well as the vegetation type, NDVI, and NIR_v, seem to provide useful information for the predictions of GPP as shown in Figure 3.9. B_2 and B_1 are well-known spectral bands for characterizing vegetation canopy structure, seasonal phenology, canopy scattering, and reabsorption due to chlorophyll content within leaves, and consequently have a dominant role in estimating GPP across all sites. The high contribution of SIF_d is presumably due to its integrative role at the seasonal and interannual scales as explained previously (Maguire et al., 2020; Dechant et al., 2022). PRI is known to be involved in the xanthophyll cycle, which is an important photoprotection mechanism and as driver of GPP (Wang et al., 2020; Hmimina et al., 2015; Soudani et al., 2014). However, in this study, the findings evidenced that the contribution of PRI in predicting GPP was weak, which could be explained by the spatial and temporal aggregation of the rapid responses in plant physiological and functional activities, observable at the finer scales (diurnal). Ultimately, the findings in this study suggest that using

R bands and SIF for estimating GPP is an important approach for improving GPP predictions compared to GPP products that include meteorological and land-cover-type information.

3.6. Conclusion

In this study, the strength of the relationships between tower-based GPP and SIF_d encompassing eight major plant functional types (PFTs) at the site and interannual scales was evaluated, and the synergy between SIF_d, surface spectral reflectance, and reflectance-based indices namely NDVI, NIR_v, and PRI to improve GPP estimates using a data-driven modeling approach was examined.

At the site scale, the results showed a strong and statistically significant hyperbolic relationship between GPP and SIF_d ($p<0.0001$). However, these relationships were site-dependent, indicating that canopy structure and environmental conditions affect the relationship between GPP and SIF_d. The GPP and SIF_d relationships across all sites of the same PFT were considerably significant and were PFT-specific. Furthermore, it was also found that the relationships between GPP and SIF_d on data pooled across all sites were moderately weak but statistically significant, confirming the PFT dependence of the relationship between GPP and SIF_d. The GLM results supported this PFT-dependent relationship between GPP and SIF_d as the site, year, and PFT have meaningful effects on the slope of the relationship between GPP and SIF_d.

This study also demonstrated that the spectral reflectance bands and SIF_d plus reflectance explained over 80% of the tower-based GPP variance. The RF models were able to represent the GPP seasonal and interannual variabilities across all sites. In addition, from the mean decrease in impurity results obtained from the RF models, it is inferred that the spectral reflectance bands in the near-infrared, red, and SIF_d appeared as the most influential and dominant factors determining GPP predictions. In summary, this study provides insights into understanding the strength of the relationships between GPP and SIF across different ICOS flux sites and the use of daily MODIS R and SIF_d TROPOMI in predicting GPP across different vegetation types.

4. Chapter 4: Data-based investigation of the effects of canopy structure and shadows on chlorophyll fluorescence in a deciduous oak forest

This Chapter is based on: Balde, H., Hmimina, G., Goulas, Y., Latouche, G., Ounis, A., and Soudani, K.: Data-based investigation of the effects of canopy structure and shadows on chlorophyll fluorescence in a deciduous oak forest, Biogeosciences, 21, 1259–1276, https://doi.org/10.5194/bg-21-1259-2024, 2024.

NB: Supplementary materials are all in annexes (Annexe Chapter 4)

Abstract. Data from satellite, aircraft, drone, and ground-based measurements have already shown that canopy scale sun-induced chlorophyll fluorescence (SIF) is tightly related to photosynthesis, which is linked to vegetation carbon assimilation. However, our ability to effectively use those findings are hindered by confounding factors, including canopy structure, fluctuations in solar radiation and in sun-canopy-geometry that highly affect the SIF signal. Thus, disentangling these factors has become paramount in order to use SIF for monitoring vegetation functioning at canopy scale and beyond. Active chlorophyll fluorescence measurements ($F_{yieldLIF}$), which directly measures the apparent fluorescence yield, have been widely used to detect physiological variation of the vegetation at leaf scale. Recently, the measurement of $F_{yieldLIF}$ has become feasible at the canopy scale, opening up new opportunities to decouple structural, biophysical, and physiological components of SIF at the canopy scale. In this study, based on top-of-canopy measurements above a mature deciduous forest, reflectance (R), SIF, SIF normalized by incoming photosynthetically active radiation (SIF_y), $F_{yieldLIF}$, and the ratio between SIF_y and $F_{yieldLIF}$ (named Φ_k) were used to investigate the effects of canopy structure and shadows on the diurnal and seasonal dynamics of SIF. Further, random forest (RF) models were also used to not only predict $F_{yieldLIF}$ and Φ_k, but also provide an interpretation framework by considering additional variables, including the R in the blue, red, green, red-edge, and near-infrared bands, SIF, SIF_y, and sun zenith (SZA) and azimuth (SAA) angles. Results revealed that the SIF signal is highly affected by the canopy structure and sun-canopy geometry effects compared to $F_{yieldLIF}$. This was evidenced by the weak correlations obtained between SIFy and FyieldLIF at the diurnal timescale. Furthermore, the daily mean $\overline{SIF_y}$ captured the seasonal dynamics of daily mean $\overline{F_{yieldLIF}}$ and explained 58% of its variability. The findings also revealed that reflectance in the near-infrared (R-NIR) and the NIR_v (the product of NIR by the normalized difference vegetation index) are good proxies of Φ_k at the diurnal timescale, while their correlations with Φ_k decrease at the seasonal timescale. With $F_{yieldLIF}$ and Φ_k as outputs and the abovementioned variables as predictors, this study also showed that the RF models can explain between 86% and 90% of $F_{yieldLIF}$, and 60% and 70% of Φ_k variations under clear sky conditions. In addition, the predictor importance estimates for $F_{yieldLIF}$ RF models revealed that R at 410, 665, 740, and 830 nm, SIF, SIF_y, SZA, and SAA emerged as the most useful and influential factors for predicting FyieldLIF, while R at 410, 665, 705, and 740 nm, SZA, and SAA are crucial for predicting Φ_k. This study highlighted the complexity of interpreting diurnal and seasonal dynamics of SIF in forest canopies. These

dynamics are highly dependent on the complex interactions between the structure of the canopy, the vegetation biochemical properties, the illumination angles (SZA and SAA) and the light conditions (ratio of diffuse to direct solar radiation). However, such measurements are necessary to better separate the variability in SIF attributable to radiation and measurement conditions from the subtler variability attributable to plant physiological processes.

4.1. Introduction

Spatial and temporal information on vegetation status are crucial to gain a better understanding of vegetation functioning and productivity. Remotely sensed data mostly from satellite and airborne platforms have provided such information for decades now (Ustin and Middleton, 2021). However, most of the remote sensing methods used for detecting and monitoring the dynamics of vegetation properties were exclusively based on vegetation greenness derived from optical vegetation indices (VIs) such as the Normalized Difference Vegetation Index (NDVI), and more recently the Near-Infrared Reflectance of vegetation index (NIR_V), which have been broadly and successfully used to estimate some biophysical and biochemical attributes, including leaf area index (LAI), fraction of Absorbed Photosynthetically Active Radiation (fAPAR), and leaf chlorophyll content (Campbell et al., 2019; Zeng et al., 2022b).

Sun-Induced chlorophyll Fluorescence (SIF) is a direct indicator of the vegetation photosynthetic activity that responds to abiotic stresses such as heatwaves and droughts, earlier than VIs (Frankenberg et al., 2011; Guanter et al., 2014; Rascher et al., 2015; Jonard et al., 2020). Further, SIF is not directly impacted by soil background as green vegetation is the only source of chlorophyll fluorescence in the red and far-red. The potential carried by SIF is currently used for estimating and monitoring terrestrial Gross Primary Productivity (GPP) across different vegetation types, including, crops, deciduous forests, evergreen forests, tropical forests, wetlands, etc. (Li and Xiao, 2022; Verma et al., 2017; Wood et al., 2017; Balde et al., 2023), for assessing vegetation structural changes, and estimating crop productivity (He et al., 2020; Liu et al., 2022).

However, because of the coarse spatial scale of the satellite products used in these above mentioned studies, the results are inconclusive and it is still questioned whether SIF can provide reliable estimates of GPP at different spatial scales and temporal resolutions across different

vegetation types, and more particularly under various abiotic stress conditions (Paul-Limoges et al., 2018; Yazbeck et al., 2021; Lin et al., 2022; Balde et al., 2023; Sun et al., 2023b). Further, satellite SIF signals are also subject to the effects of the interactions between the roughness of upper canopy layers (tree forms, gaps), and the Solar Zenith (SZA) and Azimuth (SAA) Angles. These interactions modulate the spatial and temporal distributions of sunlit and shaded leaves, the light distribution within the canopy and the main physiological processes such as photosynthesis, evapotranspiration, and stomatal conductance (Gao et al., 2022; Morozumi et al., 2023).

The recent increased availability of diurnal and seasonal time series of SIF data from airborne, drone, and ground-based measurements was crucial for gaining a better understanding of what drives SIF at various spatial and temporal scales and across biomes (Damm et al., 2015; Rascher et al., 2015; Yang et al., 2017; Goulas et al., 2017; Wang et al., 2021; Zhang et al., 2021; Wang et al., 2022; Xu et al., 2021; De Cannière et al., 2022). However, interpretation of locally measured SIF data should be cautiously carried out. In fact, rapid variations in fluorescence may be due to local effects linked to the conditions of illumination and to the light absorption by the canopy. These effects may lead to significant variations in SIF without substantial variations in photosynthesis of the entire canopy. Therefore, distinguishing the effects of endogenous factors related to canopy structure from the effects of photosynthesis changes on SIF signal is warranted.

At the top-of-canopy, the radiative transfer of SIF can be resumed within Equation. (4.1):

$$SIF = PAR \times fAPAR \times \Phi_F \times f_{esc} \quad (4.1)$$

where *PAR* is the incoming Photosynthetically Active Radiation (400-700 nm), which is the first driver of canopy SIF signal (Miao et al., 2020). *fAPAR* is the fraction of Absorbed *PAR* by the vegetation, and f_{esc} is the fraction of all chlorophyll fluorescence photons emitted from all leaves and escaped from the canopy, also known as fluorescence escape probability fraction, which is dependent on the biophysical and biochemical properties of the canopy and on the sun and view geometry. Φ_F is the chlorophyll fluorescence quantum yield (the ratio of the total amount of photons emitted to the total amount of photons absorbed by the chlorophyll pigments) and hence it is a direct indicator of the photosynthetic efficiency. From Equation (1), it is explicit that in order to interpret top-of-canopy *SIF* and use it as a proxy of Φ_F and

photosynthesis, it is necessary to understand and disentangle Φ_F from the *SIF* canopy structure dependent variations (due to the spatiotemporal effect's variations in sunlit and shaded leaves and to the light distribution and attenuation within the canopy) that are contained in *fAPAR* and f_{esc}.

Disentangling the photosynthetically dependent variations from the canopy dependent ones in SIF signal is critical to use SIF as a proxy of vegetation response to changing environmental conditions and to abiotic stresses at large scales. It is especially needed for the upcoming Fluorescence Explorer (FLEX) satellite mission that aims at providing measurements of SIF at its full spectral emission (670-780 nm) and with unprecedented spatial resolution (300 m) and repeated global coverage (Drusch et al., 2017). Therefore, the top-of-canopy SIF measured together with GPP at the carbon flux sites can play a substantial role for calibrating and validating FLEX products and airborne campaigns measurements.

Recent studies have developed novel approaches based on theoretical insights to correct SIF signal for multiple scattering and reabsorption effects (Zeng et al., 2019; Yang and van der Tol, 2018; Yang et al., 2020) by determining the f_{esc} and allowing the downscaling of SIF emission from canopy to fluorescence emission yield (Lu et al., 2020). This assumes that the entire canopy acts like a big leaf, with unique absorption, fluorescence, and photosynthetic properties. In this situation, f_{esc} is the ratio of top-of-canopy SIF to SIF total and it is closely related to canopy structural variations, including LAI, leaf angle distribution, reabsorption, and sun-canopy geometry, and varies across time and space (Zeng et al., 2019). Recently, f_{esc} has been estimated using NIR_v or the Fluorescence Correction Vegetation Index (FCVI). The former considers soil background effects and is the product of NDVI and the reflectance in the near-infrared (NIR) (Badgley et al., 2017) and it has successfully been used to assess photosynthesis productivity (Mengistu et al., 2021). The latter, FCVI, is framed as the difference between the NIR and the broadband visible reflectance (400-700 nm), considering that the reflectance is measured in the same direction as the SIF observations (Yang et al., 2020). Both approaches have shortcomings, as they cannot be universally applied, because some steps in the estimation of f_{esc} using NIR_v are inconsistent with the radiative transfer theory (Yang et al., 2020) and their effectiveness might be greatly compromised for SIF at the red band where the scattering is much weaker than in the near-infrared. The use of FCVI is also limited as it is

not suitable in sparse vegetation canopies and its computation requires hyperspectral data in the visible spectral range.

If one would like to disentangle the radiation and vegetation structure dependent SIF variations from the physiological information in the SIF signal, determining Φ_F is required. Φ_F can be defined at the leaf scale, or even at lower scales (chloroplasts) where the absorbed light energy is dissipated following three pathways: photosynthesis, fluorescence, and heat dissipation. Estimating leaf-scale Φ_F from canopy SIF measurements is an ongoing work that is under exploration. In addition, the computation of total absorbed photosynthetically active radiation (APAR) requires measurements of the incident, transmitted, and reflected PAR, which cannot be measured at satellite and airborne platforms, and are not always available for all ground sites even those belonging to major carbon flux observation networks such as the Integrated Carbon Observation System (ICOS). This is the reason why for decades the apparent Φ_F was estimated by normalizing the top-of-canopy SIF signal converted in quanta energy by the incident PAR (Daumard et al., 2012; Goulas et al., 2017). Recently, two promising approaches have been used by Zeng et al. (2022a) and Loayza et al. (2023) to estimate Φ_F. To determine Φ_F over cropped fields, including, rapeseed, barley, corn, wheat, and sugar beet, Zeng et al. (2022a) normalized canopy SIF by the near-infrared radiance of vegetation index ($rNIR_v$, the product of NDVI and the reflected vegetation radiance in the near-infrared), while Loayza et al. (2023) used the integrated vegetation reflected radiance between 500 and 700 nm on potato crop. These approaches have advantages because the effects of canopy structure and sun-canopy geometry on Φ_F estimates may be fully cancelled out, the PAR is not needed as an input, and their applicability at the satellite scale is highly feasible. However, how much these methods are reliable and effective on estimating Φ_F under varying environmental conditions and across diverse spatiotemporal scales and vegetation types is not well explored yet.

Luckily, chlorophyll fluorescence can be measured using active methods that allow direct evaluation of the physiological status of the vegetation at the leaf and canopy scales (Porcar-Castell et al., 2014; Moya et al., 2019; Loayza et al., 2023). In active techniques, a modulated source of light is used to excite the chlorophyll that fluoresces in the spectral range between 650 and 800 nm. For instance, the pulse amplitude-modulated techniques, which use a measuring pulsed light and an actinic continuous light, has been widely used at the leaf scale to provide direct chlorophyll fluorescence yield measurements, allowing the evaluation of

photosynthesis and vegetation responses to abiotic factors for decades (Baker, 2008; Magney et al., 2017). But, its applicability at canopy and ecosystem scales were hindered by the techniques limitations (Ounis et al., 2001). In the last decades, this gap was filled based on the use of either lasers (or laser diodes), or Light Emitting Diodes (LED) providing short pulses of light (microsecond to even picosecond), together with a synchronized detection to measure chlorophyll fluorescence under daylight conditions at the canopy scale with in-situ or airborne remote sensing instruments (Moya et al., 2019; Ounis et al., 2016; Loayza et al., 2023). Therefore, the fluorescence efficiency can be directly observed at the canopy and landscape scales, which is useful to gain a better understanding of terrestrial vegetation functioning. Indeed, LED induced chlorophyll fluorescence ($F_{yieldLIF}$) is less affected by the temporal and spatial (horizontal and vertical) distribution of sunlit and shaded leaves on the upper surface and within the canopy compared to SIF, but it may be highly sensitive to environmental conditions such as heavy wind speeds (Lopez Gonzalez, 2015).

In forest stands such as temperate deciduous forests, when the vegetation green-up and senescence phases are excluded, LAI is merely constant. However, the spatial dynamics in LAI may be large from one plot to another. Thus, the canopy structural effect correction on SIF signal is all the more crucial from a spatial view point. Further, SIF signal is subject to diurnal variations due to the complex interactions between lighting conditions (diffuse/total radiation, solar and viewing angles) and canopy structure (Aasen et al., 2019; Xu et al., 2021). Therefore, correcting SIF from these effects, which are very local, is warranted for (i) interpreting and upscaling SIF signal spatially and temporally across diverse vegetation types, (ii) disentangling the physiological response from variations due to exogenous effects on SIF, (iii) assessing how SIF responds to extreme environmental conditions (heatwaves, drought, etc.), and ultimately (iv) gaining a better understanding of the relationships between SIF and GPP. Nevertheless, to the best of our knowledge, an attempt to use active fluorescence measurements at the canopy scale to correct SIF from canopy structure, incident sunlight, and sun-canopy geometry effects has not been addressed yet.

The main objective of this work is to use active chlorophyll fluorescence ($F_{yieldLIF}$) as a reference measurement and to compare it to SIF yield (SIF_y = SIF/PAR) in order to analyse and correct the effects of canopy structure and sun-canopy geometry on top-of-canopy SIF at diurnal and seasonal timescales in a temperate deciduous forest, considering diverse environmental

conditions. More specifically, this study intended to (i) evaluate the relationship between $F_{yieldLIF}$ and SIF_y and evidence the effects of canopy structure and sun-canopy geometry on top-of-canopy SIF through their influence over this relationship; (ii) examine these effects with the aim of developing a correction method based on reflectance measurements and lightning conditions (solar angles, ratio of diffuse to total radiation, etc.).

4.2. Materials and Methods

4.2.1. Study site description

This study was conducted at the Fontainebleau-Barbeau forest site (FR-Fon), which is an Eddy Covariance (EC) flux observation site belonging to the ICOS network (Delpierre et al., 2016). The site is located 53 km southeast of Paris, France. It is occupied by a temperate deciduous broad-leaf forest type. The dominant forest overstory consisted of mature sessile oak trees (*Quercus petraea (Matt.) Liebl*), accounting for 79% of the basal area (Maysonnave et al., 2022), with an understory of hornbeam (*Carpinus betulus L.*) (for more details: http://www.barbeau.universite-paris-saclay.fr/). The stand height is around 25 m. The soil is an endostagnic luvisol, covered by an oligo-mull humus (Maysonnave et al., 2022). The climate is temperate and characterized by an annual average rainfall of approximately 680 mm and an average air temperature of approximately 11°C (Soudani et al., 2014). The LAI is approximately 5.8 $m^2.m^{-2}$ using the litter collection method over the 2012-2018 period (Soudani et al., 2021). At the Fontainebleau-Barbeau site, carbon and water fluxes have been continuously monitored at 35 m height using the EC method. The main micrometeorological variables, including incident and reflected radiations, are measured at high frequency (1 min), while vapor pressure deficit, precipitation, air and soil temperature, water table depth, soil moisture, and wind speed are either recorded or estimated at a half-hourly timescale.

4.2.2. Sun-induced and light-emitting diode induced chlorophyll fluorescence, and reflectance measurements

4.2.2.1. Sun-induced chlorophyll fluorescence measurement system

In the framework of the ECOFLUO project, a passive in-situ spectral measurement automated instrument (named SIF3) was developed based on a collaboration between the

"Laboratoire de Météorologie Dynamique (LMD), École Polytechnique, France et Laboratoire Écologie, Systématique et Évolution (ESE), Université Paris-Saclay, France". SIF3 acquires continuous measurements of incident and reflected radiation above the canopy. It was installed at the top of the 35 m height tower of Fontainebleau-Barbeau site above the canopy in July 2021 (Supplementary materials Figure S4.1). To avoid artificial shading of the measured area, SIF3 was set to the southern part of the tower.

The SIF3 measurement system includes a control computer (LattePanda V1, LattePanda Shanghai, China and two Arduino microcontrollers), two spectrometers with coolers, shutter controllers, a general cooler with temperature controller inside the box, two optical fibers, a reference panel, a servo motor, a PAR sensor, a GPS, temperature and relative humidity sensors, and a camera. The two spectrometers are a high-resolution spectrometer (ASEQ instruments, Vancouver, Canada, HR1-T model with thermoelectric cooling) and a broad band spectrometer (ASEQ, LR1-T model with thermoelectric cooling). The high-resolution spectrometer (HR1-T) has a spectral range between 650 and 800 nm, a high spectral resolution with full width at half maximum (FWHM) of approximately 0.3 nm. The HR1-T was used to determine sun-induced chlorophyll fluorescence. The broad band spectrometer (LR1-T) has a spectral range between 400 and 1000 nm and a FWHM of approximately 1.5 nm. It was used to measure canopy reflectance and the optical vegetation indices (VIs).

In order to reduce the noise and dark current, both spectrometers were contained within a dry and thermoregulated box system that maintained the temperature at 19 ± 0.61 °C. SIF3 performs sequential vegetation reflected radiance measurements and irradiance measurements on a polytetrafluoroethylene (PTFE) reference panel (PMR10P1, Thorlabs, Maisons-Laffitte, France). The sequential measurements of SIF3 were: first to measure the reference PTFE with LR1-T and HR1-T spectrometers, and second to measure vegetation reflected radiance with both spectrometers. Within one measurement of the target canopy or the reference, each spectrometer performed the following steps: (i) optimizing the integration time (IT) for measurement, (ii) measurement, and (iii) measurement of the dark current. The date and time at the start and end of each measurement were recorded. Two 15 m long optical fibers (FT1000EMT and FT1000UMT, Thorlabs, Maison-Laffitte, France, for HR1-T and LR1-T spectrometers, respectively) with a 1000 µm core diameter and a numerical aperture of 0.39 NA were used to measure the irradiance of the reference and the radiance of the canopy, at the

nadir position. The field-of-view (FOV) of each measuring channel is adjusted to 25° with the use of a Gershun tube to ensure a flatter spatial response and covers approximately 6 m^2 of the canopy area. Long-pass optical filters (5CGA-550, cut-off wavelength 550 nm and 5CGA-375, cut-off wavelength 375 nm, Newport, Irvine, CA, USA, for the HR1-T and LR1-T channels, respectively) were placed in front of each tube to avoid second order detection and to protect fiber ends. The dark current measurements were subtracted from the reference and canopy measurements before SIF retrieval. The IT of each spectra was automatically optimized to achieve values that are as high as possible, but unsaturated to improve as much as possible the signal-to-noise ratio (SNR). Note that SIF3 integrates a quantum sensor to measure the PAR at high frequency and a camera that allows taking RGB images of the canopy in the FOV. Before the installation of SIF3 in the field, we performed lens alignment, radiometric and spectral calibrations of the instrument using a calibrated light source (4P-GPS-060-SF and EHLS-100-075R, Labsphere, North Sutton, NH, USA).

4.2.2.2. Light-emitting diode chlorophyll fluorescence measurement system

$F_{yieldLIF}$ measurements were acquired with an active fluorometer instrument, named LIF, developed in the LMD laboratory, which was installed at the top of the 35 m height tower next to SIF3 above the canopy. This instrument is very similar to the one described by Moya et al. (2019). It uses a blue LED array (ENFIS Ltd, Swansea, UK; peak wavelength 455 nm, FWHM 21 nm, radiant power 6 W) as an excitation source. To separate the chlorophyll fluorescence emission induced by the LED from that induced by daylight and from the reflected sunlight in the filter bandwidth, the LED light is pulsed at a variable frequency with a pulse duration of about 5 µs. Note that the instrument uses a bimodal excitation conditioned by the PAR: for PAR < 90 µmol m^{-2} s^{-1} (night time), the frequency is set at 30 Hz, while it is set at 200 Hz (daytime) for PAR > 100 µmol m^{-2} s^{-1}. This bimodal excitation scheme helps to avoid variable fluorescence induction during night and to increase SNR during daytime. The instrument optical head consisted of two main parts: (i) the source module that includes the blue LED array, its electronic driver, a heat dissipation module and a Fresnel lens (diameter 180 mm) to collimate the excitation light, and (ii) a detection module that includes a second Fresnel lens of the same diameter, a set of optical filters, a large area PIN photodiode (10x10 mm^2, S3590, Hamamatsu Photonic, Japan) and a laboratory designed amplifier that selects the LED induced fluorescence signal ($F_{yieldLIF}$) from the reflected sunlight in the same wavelengths band (LNIR). This

amplifier uses a sample and hold circuit (AD585, Analog Devices, Wilmington, MA, USA) to deliver the peak value of the fluorescence signal to the digital analog (AD) conversion card (USB 6212, NI, Austin, Texas, USA) and a lowpass electronic filter to deliver LNIR to the same card. The set of optical filters includes a highpass interferential filter with a cut-off wavelength at 400 nm to reject UV light, a second highpass interferential filter with a cut-off wavelength at 650 nm to reject the excitation light and a 3 mm thick RG9 filter (Schott, Germany) to select the far-red fluorescence emission over 725 nm. The FOV can be controlled thanks to an onboard camera (RLC-520A, Reolink, Hong-Kong). We selected a top of the canopy area in the FOV of the SIF instrument, resulting in a 9 m measuring distance with a viewing zenith angle of 30°. However, as the FOV of the instrument is about 100 mrad, the measured area was about 0.4 m^2, which is much smaller than the FOV of SIF3 (approximately 6 m^2). Power supplies as well as synchronisation and acquisition electronics are enclosed in a separate box, connected to the optical head by a 5 meters long cable. $F_{yieldLIF}$ and LNIR are stored on disk with an acquisition and control program written in LabVIEW (NI, Austin, Texas, USA) that runs on a LattePanda V1 microcomputer. Other variables such as PAR and LED, photodiode and box temperatures are also continuously monitored.

4.2.2.3. Canopy sun-induced chlorophyll fluorescence retrieval

As spectral measurements are recorded in digital counts, they were converted into radiometric units before SIF retrieval. SIF was retrieved at the far-red oxygen observation band (O_2-A) from the HR1-T canopy reflectance measurements. Data quality control is performed prior to SIF retrieval following the protocol proposed by Cogliati et al. (2015) to put aside abnormal data caused by abrupt changes in incident radiation. SIF retrieval was performed using the classical three-band Fraunhofer Line Discrimination (3FLD) method at O_2-A band (Meroni et al., 2009; Daumard et al., 2012).

The 3FLD approach is rooted in the FLD principle, which requires measurements in two channels, one inside and one outside a Fraunhofer or absorption line (Meroni et al., 2009). The FLD hypothesis is based on the consistency of reflectance and SIF at both bands. However, studies have found evidence that the two variables are not constant (Meroni et al. 2009). The 3FLD method rather assumes that reflectance and SIF vary linearly around the absorption band considered, which solves the limitation given by the FLD hypothesis, and uses three spectral

bands per absorption line to retrieve SIF (Zhang et al., 2021). The 3FLD SIF retrieval at 760 nm (O_2-A band) can be derived as follows:

$$SIF_{760} = \frac{(E_l \times w_l + E_r \times w_r) \times L_{in} - (L_l \times w_l + L_r \times E_r) \times E_{in}}{(E_l \times w_l + E_r \times w_r) - E_{in}} \quad (4.2)$$

$$w_l = \frac{\lambda_r - \lambda_{in}}{\lambda_r - \lambda_l},\ w_r = \frac{\lambda_{in} - \lambda_l}{\lambda_r - \lambda_l}$$

where *L* is the upwelling radiance. *E* is the downwelling irradiance measured on the reference panel. Indices '*r*', '*l*' and 'in' represent the reference bands at the left, right, and inside the absorption band, respectively. *wl* and *wr* denote the weighting factors depending on the wavelength λ on the left, inside, and on the right of the absorption band. Within this study, the left, inside and right bands were set at 757.86, 760.51, and 770.46 nm, respectively.

4.2.3. Theoretical derivations of Φ_k, vegetation indices, and SIF yield

NIR_v has been used to isolate vegetation signal properties from soil background and to correct canopy-scale far-red SIF for scattering effects (Badgley et al., 2017). NIR_v can be computed according to (Badgley et al., 2017) and (Zeng et al., 2019) using the following equations:

$$NDVI = \frac{R_{[780-800]} - R_{[670-680]}}{R_{[780-800]} + R_{[670-680]}} \quad (4.3)$$

$$NIR_v = R - NIR_{850} \times NDVI \quad (4.4)$$

where *R* represents the spectral reflectance and the index number denotes the wavelength range or wavelength at which the reflectance was derived. In equation (4), NIR_v is largely dependent on the LAI, the leaf angle distribution, and the geometry of the sun-canopy, as well as on the influence of fluctuations in incident radiation at the diurnal and seasonal timescale.

$F_{yieldLIF}$ is an active measurement and is not directly dependent on the ambient light conditions. Thus, it is not impacted by ambient radiation changes, because the measured LED induced chlorophyll fluorescence is directly and only emitted by the leaves targeted by the LED. Variations in $F_{yieldLIF}$ are then presumably only induced by changes in the photosynthetic pigment concentrations, in the leaf area inside the FOV, and in the vegetation functioning that

modulates the chlorophyll fluorescence quantum yield. As no significant phenological changes occurred during the study period, we assumed that the $F_{yieldLIF}$ is free from the vegetation structure and sun-canopy geometry effects and can be used as a reference measurement in this respect. The blue LED light can be considered as constant and therefore, from Equation (4.1) we can assume that Φ_F is equal to $F_{yieldLIF}$ and then Equation (4.1) becomes:

$$SIF = PAR \times fAPAR \times F_{yieldLIF} \times f_{esc} \quad (4.5)$$

$$\frac{SIF}{(PAR \times F_{yieldLIF})} = fAPAR \times f_{esc} \quad (4.6)$$

From equation (6), we defined Φ_k as following:

$$\Phi_k = \frac{SIF}{(PAR \times F_{yieldLIF})} = \frac{SIF_y}{F_{yieldLIF}} \quad (4.7)$$

Note that this is a simplification of the complex relation that does exist between SIF_y and $F_{yieldLIF}$, as SIF yield and $F_{yieldLIF}$ respond differently to canopy structure effects. At the diurnal timescale, Φ_k is subjective to variations in leaf angle distribution, incident sunlight or atmosphere conditions (clear or cloudy sky conditions), and to the effects of sun-canopy geometry (including SZA and SAA).

In remote sensing, the total amount of light absorbed by the canopy cannot be directly measured. This quantity is highly dependent on the solar angle and canopy structure (distribution of light and shaded areas at the top and inside the canopy). Hence, by normalizing the canopy emitted SIF by the incident PAR, it is possible, as a first approximation and empirically, to partially disentangle the SIF signal from its dependence to incident radiation and thus to detect some changes in the vegetation properties or the plant physiological responses to abiotic factors. Therefore, the SIF_y was calculated using the PAR measured at the top of the EC tower site. Note that the SIF fluxes were converted into quanta units following (Daumard et al., 2012) prior to SIF_y calculation.

$$SIF_y = SIF/PAR \quad (4.8)$$

4.3. Data analysis

In this study, we used data measurements from June to August 2022. As radiation-limited photosynthesis is expected in early morning and late afternoon, due to lower incoming irradiance, only the data recorded between 9:00 am and 16:00 pm (UTC) were considered in this study. The negative SIF values, the SIF_y values higher than mean ± 3 standard deviation, and the PAR data less than 200 µmol m^{-2} s^{-1} were excluded in the analysis. First, we applied a linear model to analyse at the daily and seasonal timescales the strength of the relationships: i) between SIF_y and $F_{yieldLIF}$, and ii) between NIR_v and Φ_k. Note that daily means of SIF_y, $F_{yieldLIF}$, NIR_v, and Φ_k are hereafter noted $\overline{SIF_y}$ and $\overline{F_{yieldLIF}}$, $\overline{NIR_v}$ and $\overline{\Phi_k}$. The coefficient of determination (R^2) and the p-value are used to assess the strength of the correlations. These relations are examined at instantaneous (seconds to minutes) and daily (averaged data from 9 am to 16 pm) timescales. Second, we used random forest (RF) models as a tool to understand $F_{yieldLIF}$ and Φ_k dynamics by comparing their predictions based on a combination of remote sensing metrics. We chose RF models because they are non-parametric models and are well adapted for predicting nonlinear and multi-parameters relationships in complex situations and foremostly highly interpretable by using metrics such as the importance of predictor variables and partial dependence (Breiman, 2001). Several types of RF models were designed for estimating $F_{yieldLIF}$ and Φ_k. The expression of each model and its purpose are given in Table 1. We used the clear sky condition (the fraction of diffuse PAR over total PAR < 0.3) data to train the models. It is worth noting that for $F_{yieldLIF}$ predictions using all data (clear sky and cloudy conditions) or clear sky condition data alone yielded the same results (data not shown), while for Φ_k, which was defined to represent the effects of canopy structure and sun-canopy geometry, only clear sky conditions were used with respect to satellite conditions of data acquisition. To avoid the impact of correlations of predictors on the RF models' predictions, the correlations matrix between predictors was computed (Supplementary materials Figure S4.2 and S4.3) and then the least correlated predictors were selected to train our models. All RF models were established using 200 trees and sampled with replacement based on bag fraction of 80% (80% of the data for training and 20% for testing). The out-of-bag (OOB) predictor importance estimates were determined to evaluate the contribution of each predictor. Model performance was evaluated using the OOB coefficient of determination (OOB R^2) score and the adjusted coefficient of determination (adj. R^2) of the correlations between the test dataset and the

predictions, as well as the Root Mean Squared Error (RMSE). The closest the OOB R^2 and adj. R^2 are, the better the model is able to be generalized. All RF models were run using instantaneous measurements. For SIF and reflectance data extraction, MATLAB R2021a (MathWorks, Inc., USA) was used, and Python version 3.9.1 was used for data analysis and visualization (Sklearn, Scipy, Seaborn, Matplotlib, Pandas, and Numpy libraries).

Table 4.1. Random forest models for $F_{yieldLIF}$ and Φ_k predictions. R denotes spectral reflectance in blue (410 nm), red (530 nm and 560 nm), green (665 nm), red-edge (705 and 740 nm), and near-infrared (830 nm). SIF is the far-red sun-induced chlorophyll fluorescence at 760 nm, SIF_y is the ratio of SIF over PAR, SA stands for solar angles, including solar zenith (SZA) and azimuth (SAA) angles. $F_{yieldLIF}$ is the LED induced chlorophyll fluorescence, and Φ_k is the ratio between SIF_y and $F_{yieldLIF}$.

Model name	**Inputs**	**Outputs**	**Purpose**
FY-R	R_{410}, R_{530}, R_{560}, R_{665}, R_{705}, R_{740}, R_{830}	$F_{yieldLIF}$	To test the ability of reflectances to predict $F_{yieldLIF}$.
FY-R-SIF	R_{410}, R_{530}, R_{560}, R_{665}, R_{705}, R_{740}, R_{830}, SIF	$F_{yieldLIF}$	To test the ability of reflectances and SIF to predict $F_{yieldLIF}$.
FY-R-SIFy	R_{410}, R_{530}, R_{560}, R_{665}, R_{705}, R_{740}, R_{830}, SIF_y	$F_{yieldLIF}$	To test the effect of apparent SIF yield (SIF normalized by PAR) to predict $F_{yieldLIF}$.
FY-R-SA	R_{410}, R_{530}, R_{560}, R_{665}, R_{705}, R_{740}, R_{830}, SZA, SAA	$F_{yieldLIF}$	To test the ability of reflectances and solar angles to predict $F_{yieldLIF}$.
FY-R-SIFy-SA	R_{410}, R_{530}, R_{560}, R_{665}, R_{705}, R_{740}, R_{830}, SIF_y, SZA, SAA	$F_{yieldLIF}$	To test the ability of reflectances, SIF yield, and solar angles to predict $F_{yieldLIF}$.
Φ_k-R	R_{410}, R_{530}, R_{560}, R_{665}, R_{705}, R_{740}, R_{830}.	Φ_k	To test the ability of reflectances to predict Φ_k.

	R_{410}, R_{530}, R_{560}, R_{665}, R_{705}, R_{740}, R_{830}, SZA, SAA		To test the synergy between reflectances and solar angles to predict Φ_k.
Φ_k-R-SA		Φ_k	

4.4. Results

4.4.1. Relationships between canopy SIF_y and $F_{yieldLIF}$ and their seasonal variations

The results, in Figure 4.1a, show that the coefficients of determination of the relationships between SIF_y and $F_{yieldLIF}$ were low and varied highly across the season and that the ratio between diffuse PAR and total PAR cannot entirely explain this inter-daily variability. This indicates that at the diurnal scale SIF_y was weakly correlated to $F_{yieldLIF}$. Note that relations between SIF_y and $F_{yieldLIF}$ analysed at hourly timescale (hourly averages) relatively improved their correlation (Supplementary materials Figure S4.4). At the seasonal scale (daily averages), in Figure 4.1b, the results show that the R^2 between $\overline{SIF_y}$ and $\overline{F_{yieldLIF}}$ was 0.58, indicating that $\overline{SIF_y}$ and $\overline{F_{yieldLIF}}$ were better correlated at the seasonal timescale. The fraction of diffuse to total PAR cannot explain this correlation. Similarly, the seasonal dynamics in $\overline{SIF_y}$ and $\overline{F_{yieldLIF}}$, in Figure 4.1c, shows a good correspondence. Although, their agreements tend to diverge at some period of the season. Additionally, note that, overall, the magnitude of both variables has considerably decreased from the starting to the end of the given period.

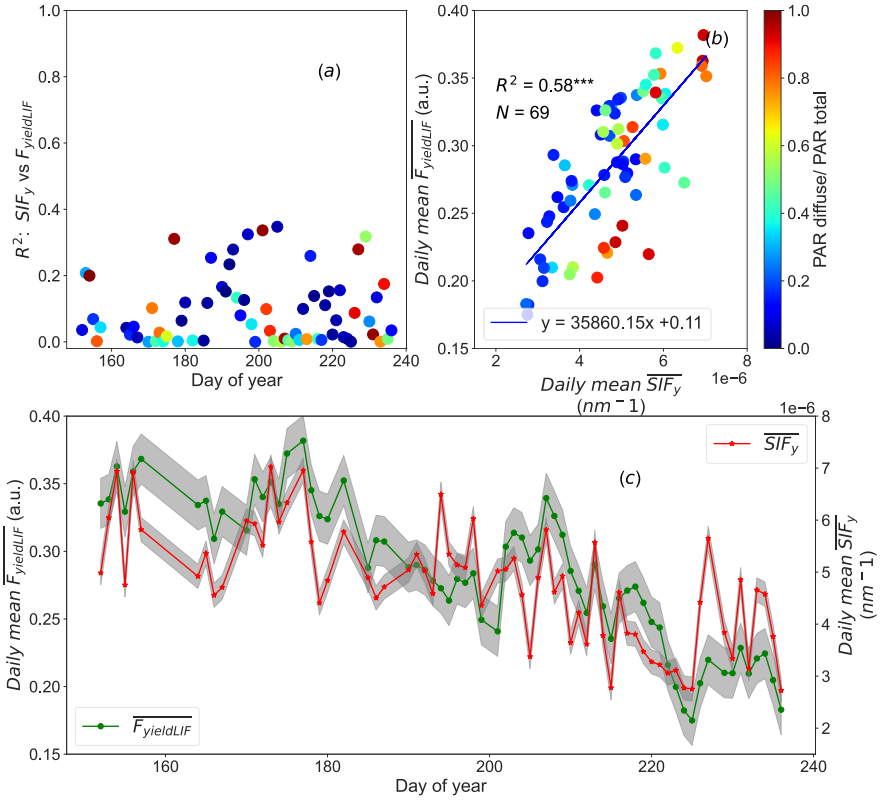

Figure 4.1. Figure 4.1a shows the inter-daily variations in the coefficient of determination (R^2) of the relationship between SIF_y and $F_{yieldLIF}$ and Figure 4.1b the relationship between daily mean $\overline{SIF_y}$ and $\overline{F_{yieldLIF}}$. In Figures 4.1a and 4.1b the colour of the points shows the fraction of diffuse and total PAR with the colour scale on the left of Figure 4.1b. While Figure 4.1c depicts seasonal dynamics of $\overline{SIF_y}$ and $\overline{F_{yieldLIF}}$. The shading around the lines indicates the 95% confidence interval. The asterisks stand for the statistical significance level (*** = P≤0.001).

4.4.2. Diurnal variations in PAR, NIR_v, Reflectance NIR, Φ_k, SIF, SIF_y, and $F_{yieldLIF}$

Figure 4.2 shows the diurnal cycles (from 9 am to 16 pm) of PAR, NIR_v, R-NIR, Φ_k, SIF, SIF_y, and $F_{yieldLIF}$. It shows three sunny and steady weather days and so the PAR constantly increased in the morning to a maximum around noon and decreased in the afternoon for all days. Its values were between 1000 and almost 2000 µmol m^{-2} s^{-1}.

The diurnal variations in NIR_v and R-NIR exhibited similar patterns, with the lowest values recorded at noon. The depression observed in NIR_v and R-NIR patterns from 10 am to around 12 pm is attributed to shadows observed within the FOV of the SIF3 instrument as has shown by the sunlit leaves fraction determined from RGB images (Supplementary materials Figure S4.5 and S4.6).

Φ_k surged in the early morning hours (not shown) and then declined from 10 am up to around 12 pm, afterwards, it increased in the afternoon for all days. The depression observed in Φ_k between 10 am and 12 pm is simultaneous to the decline in NIR_v and in R-NIR. This implies that diurnal dynamics in Φ_k may be due to the intra-daily pattern in the distribution of sunlit and shaded leaf fraction caused by the geometric relationships between canopy structure and sun's geometry.

It is well-known that diurnal SIF cycles are tightly linked with dynamics in PAR. Conversely, on Figure 4.2 SIF exhibited different diurnal dynamics for all days than the incident PAR ones. The pattern in SIF declined from 10 am to around 12 pm and was afterwards dominated by dynamics in PAR. It can also be observed that the magnitude of SIF markedly decreased from July, 10^{th} to August, 6^{th}, being from 2.06 to 1.33 $mWm^{-2}\ sr^{-1}nm^{-1}$ (approximately 35% relative decrease in SIF emission).

The diurnal variations in SIF_y surged in the early morning (not shown) and then decreased from 10 am to noon and afterwards increased in the afternoon for the three considered days. Similarly, to SIF, the magnitude of SIF_y also shows an overall decreased from July, 10^{th} to August, 6^{th}. In contrast, the diurnal pattern in $F_{yieldLIF}$ shows a continuous and significant decrease during the day, with a 10% loss. Note that the range of $F_{yieldLIF}$ have also decreased over the given period. $F_{yieldLIF}$ appears insensitive to the canopy structure and sun-canopy geometry changes, compared to the dynamics in SIF and SIF_y, which showed a significant decline in the morning. Besides, it is worth noting that $F_{yieldLIF}$ measurements are continuously recorded (day and night), the full diurnal cycles are presented in Supplementary materials Figure S4.7.

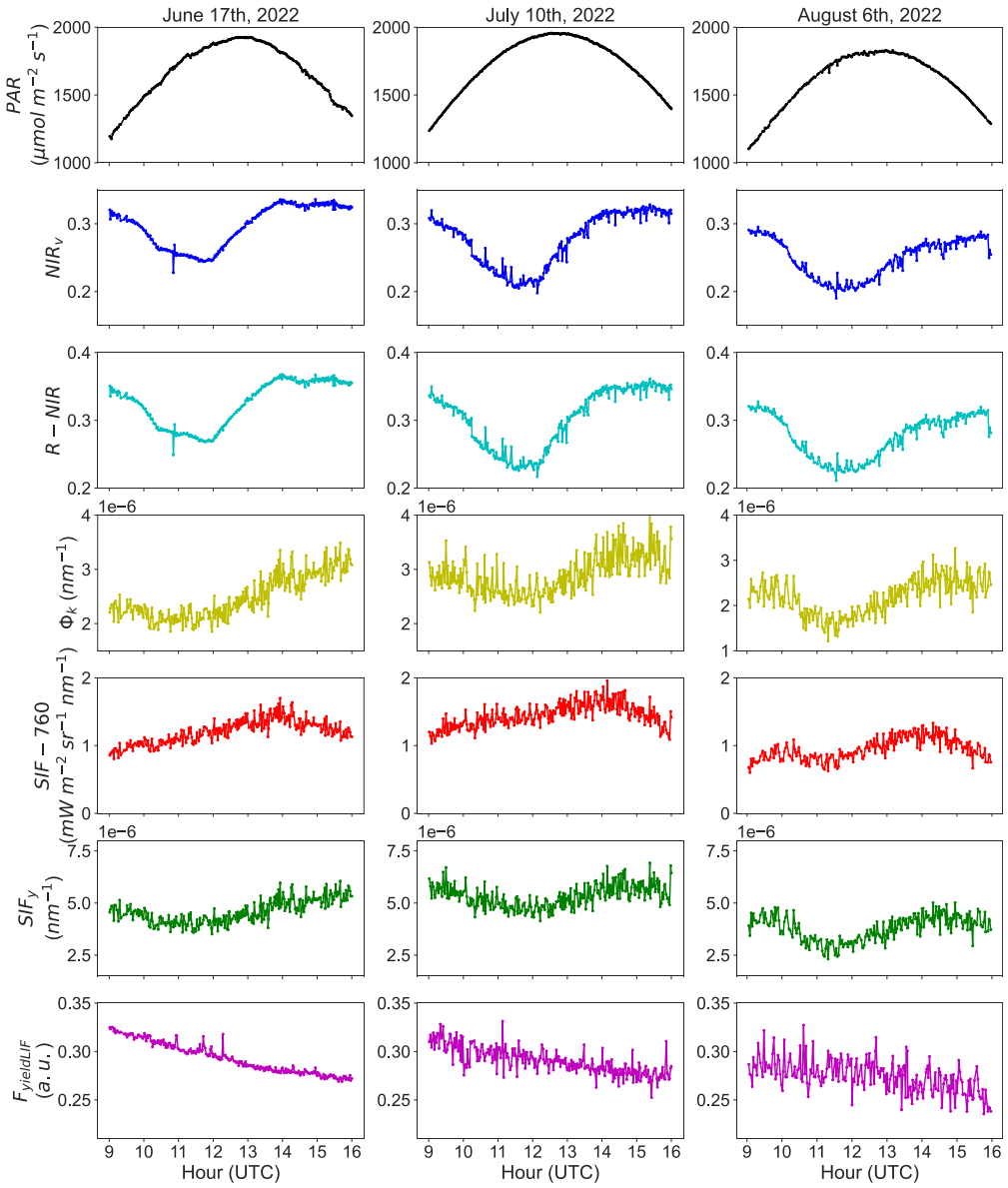

Figure 4.2. Presents the diurnal patterns acquired during three clear sky days of: the photosynthetically active radiation (PAR, *in black*), the near infrared reflectance of vegetation index (NIR_V, *in blue*), the reflectance in the near infrared (R-NIR, *in cyan*), the ratio between SIF_y and $F_{yieldLIF}$ (Φ_k, *in yellow*), the SIF (SIF-760, *in red*), the ratio of SIF over PAR (SIF_y, *in green*), and the active chlorophyll fluorescence ($F_{yieldLIF}$, *in magenta*), respectively. The data correspond to June 17th, July 10th, and August 6th, 2022. The noisy signals observed on July 10th and August 6th, 2022 are due to high wind speed with an average value of 2.39 and 3.27 m s-1, respectively.

4.4.3. Relationships between Φk and NIR_V and its seasonal variations

Figure 4.3a shows the R^2 of the relationship between NIR_V and Φ_k at instantaneous scale (acquisition time-step) as a function of the fraction between diffuse and total PAR, while Figure

4.3b depicts the relationships between Φ_k and NIR_v at seasonal scale, and Figure 4.3c underlines their seasonal dynamics.

Conversely, to the weak correlation found between SIF_y and $F_{yieldLIF}$ seen in Figure 1a, the results in Figure 4.3a show that there are relatively moderate and substantially good relationships between NIR_v and Φ_k over the season. Thus, for most of the clear sky conditions (ratio diffuse PAR to total PAR < 0.3), NIR_v may explain more than 50% of the instantaneous variations in Φ_k at the diurnal scale, but the strength of the relationship between these two variables under clear skies remains variable. The lowest values of R^2 are mostly related to diffuse sky conditions.

The results in Figure 4.3b show a weak, but statistically significant relationship between the daily mean $\overline{NIR_v}$ and $\overline{\Phi_k}$ with an R^2 of 0.16 at the seasonal scale. This indicates that $\overline{NIR_v}$ is a weak proxy of $\overline{\Phi_k}$ at the seasonal scale. Furthermore, we can also infer that the fraction of diffuse to total PAR explains this correlation, as lower correlation values of $\overline{NIR_v}$ and $\overline{\Phi_k}$ are closely related to clear sky conditions and high correlation values to diffuse sky conditions. In addition, the seasonal dynamics in $\overline{NIR_v}$ and $\overline{\Phi_k}$ (Figure 4.3c) exhibited a good match for some days at the seasonal scale. The magnitude of $\overline{NIR_v}$ and $\overline{\Phi_k}$ also varied significantly over the season, which can be caused by rapid changes in ambient environmental conditions and in leaf and canopy biochemical and structural properties. Note that an independent analysis, identical to the one presented here on the relationship between NIR_v and Φ_k, was realised on the relationships between R-NIR and Φ_k. The results shown in Supplementary materials Figure S4.8 suggest that the NIR reflectance alone can also be a good proxy of Φ_k at diurnal timescale. This is paramount for implementing this approach at the satellite scale.

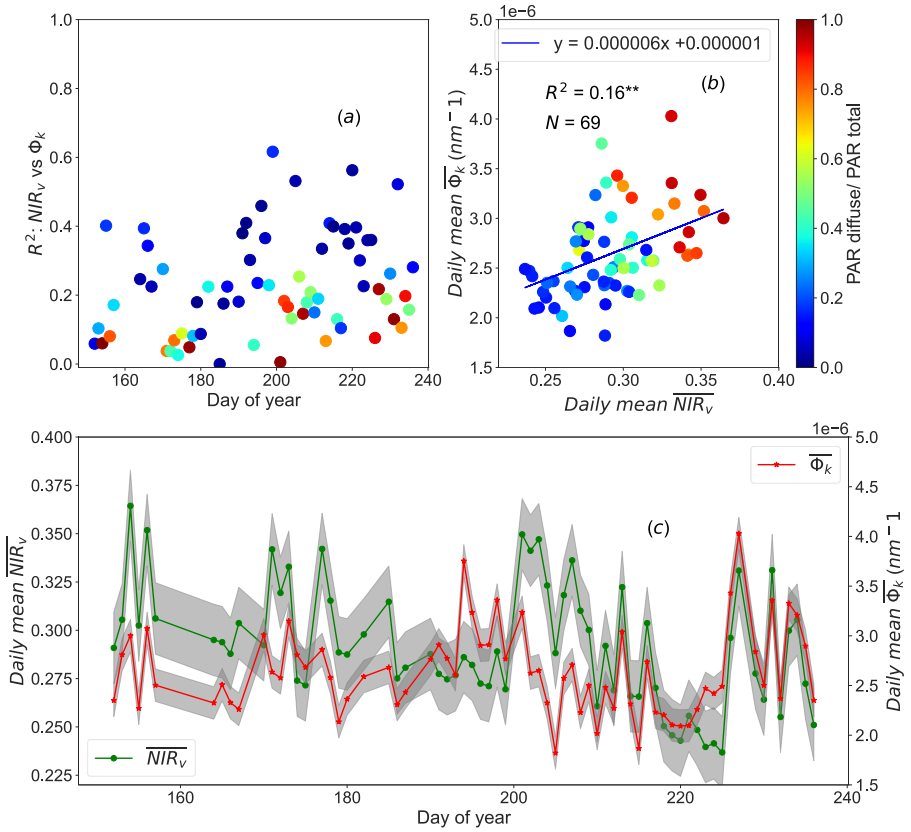

Figure 4.3. Figure 4.3a exhibits the inter-daily variations of the coefficient of determination (R^2) of the relationships between the near-infrared reflectance of vegetation index (NIR_v) and the canopy Φ_k at instantaneous scale, as a function of the fraction between diffuse and total PAR. Figure 4.3b presents the seasonal relationship between the daily means $\overline{NIR_v}$ and $\overline{\Phi_k}$, as a function of the fraction between diffuse and total PAR. And Figure 4.3c shows the seasonal dynamics in $\overline{NIR_v}$ and $\overline{\Phi_k}$. The shaded area indicates the 95% confidence interval. The asterisks stand for the statistical significance level (** = $P \leq 0.01$).

4.4.4. Random forest models for predicting $F_{yieldLIF}$ and Φ_k in temperate deciduous forest

We tested the potential of RF modelling approach to predict $F_{yieldLIF}$ and Φ_k based on remotely sensed products. We intended to show FY-R-SIF_y-SA and FY-R-SA models' results for $F_{yieldLIF}$, and Φ_k-R and Φ_k-R-SA for Φ_k estimates. The other RF models' results for $F_{yieldLIF}$ are given in Supplementary materials Figure S4.9.

The results show that all random forest models had a strong performance on the prediction of $F_{yieldLIF}$ (Table 4.2), with OOB R^2 varying between 0.86 and 0.90 and adj. R^2 between 0.87 and 0.90. In figure 4.4, the RF models' residuals between observed and predicted $F_{yieldLIF}$ are randomly distributed and $F_{yieldLIF}$ is not over-or under-estimated. Note that adding SIF (FY-R-SIF, OOB R^2 = 0.87 and adj. R^2 = 0.88) or SIF_y (FY-R-SIF_y, OOB R^2 = 0.88 and adj. R^2 = 0.89) relatively increases the model performance compared to the FY-R model (FY-

R, OOB R^2 = 0.86 and adj. R^2 = 0.87), but the difference between R^2 is not statistically significant. Thus, the use of reflectance bands only allows to predict $F_{yieldLIF}$ and SIF or SIF_y did not provide an additional improvement for predicting $F_{yieldLIF}$ at the acquisition-time step. Substituting SIF for SZA and SAA also showed good model performance (FY-R-SA, OOB R^2 = 0.90 and adj. R^2 = 0.90). The FY-R-SIF_y-SA model revealed a performance similar to the FY-R-SA model's one (FY-R-SIF_y-SA, OOB R^2 = 0.90 and adj. R^2 = 0.90). The predictor importance estimates for FY-R-SA model showed that SZA, SAA, and R410 contribute the most in determining $F_{yieldLIF}$ (Figure 4.4d), while for FY-R-SIFy-SA model, SZA, R830, SAA, R410, and R740 (Figure 4.4b) provide the most useful information for $F_{yieldLIF}$ predictions.

Table 4.2. Random forest (RF) model's statistical results for predicting $F_{yieldLIF}$. N denotes the number of data points used for the RF model's testing, adj. R^2 represents the adjusted coefficient of determination of the relationship between the test dataset $F_{yieldLIF}$ and the predicted $F_{yieldLIF}$, OOB R^2 is the model accuracy on the validation data set (1/3 of the training set), and the RMSE is the root mean square error between observed $F_{yieldLIF}$ and RF model predicted $F_{yieldLIF}$.

Model	OOB R^2	adj. R^2	RMSE	N
FY-R	0.86	0.87	0.016	1802
FY-R-SIF	0.87	0.88	0.016	1802
FY-R-SIFy	0.88	0.89	0.015	1802
FY-R-SA	0.90	0.90	0.014	1802
FY-R-SA-SIFY	0.90	0.90	0.014	1802

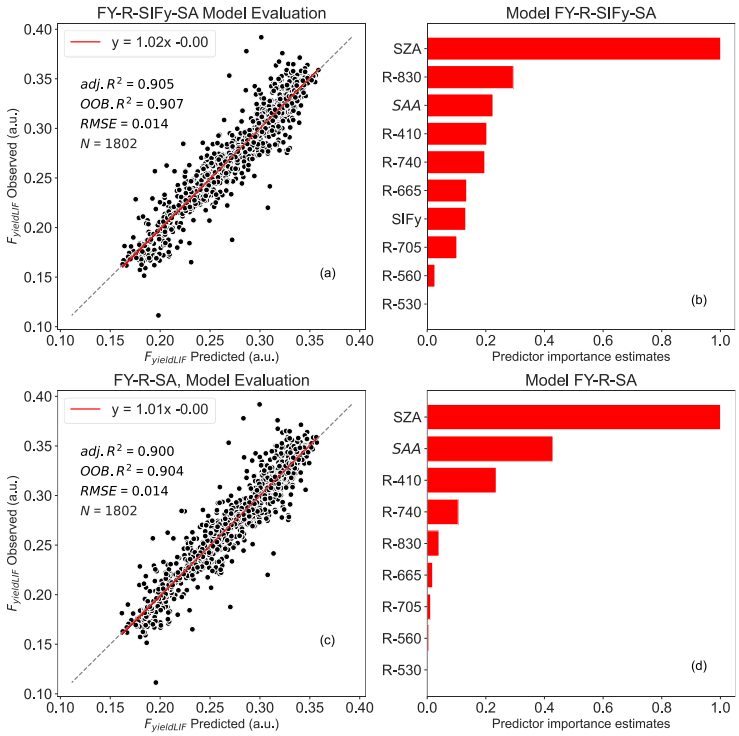

Figure 4.4. Random forest (RF) model outputs: Figure 4.4a depicts the FY-R-SIF$_y$-SA model performance between observed and predicted F$_{yieldLIF}$, Figure 4.4b represents the predictor importance estimates for FY-R-SIF$_y$-SA model, Figure 4.4c represents the FY-R-SA model performance between observed and predicted F$_{yieldLIF}$, and Figure 4.4d represents the predictor importance estimates for FY-R-SA model. N denotes the number of data points used for the RF model's testing, adj. R^2 represents the adjusted coefficient of determination of the relationship between the test dataset F$_{yieldLIF}$ and the predicted F$_{yieldLIF}$, OOB R^2 is the model accuracy on the validation data set (1/3 of the training set), and the RMSE is the root mean square error between observed F$_{yieldLIF}$ and RF model predicted F$_{yieldLIF}$. The dashed diagonal line depicts the 1:1 line. FY-R-SIF$_y$-SA denotes F$_{yieldLIF}$ prediction using R, SIF$_y$ and solar angles as inputs; and FY-R-SA includes R, SZA, and SAA to predict F$_{yieldLIF}$.

The results reveal that RF models had good performance in predicting Φ_k (Figure 4.5). The best performing model was achieved using R and sun angles as inputs (Φ_k-R-SA, OOB R^2 = 0.69 and adj. R^2 = 0.70), while R alone explained 58% of Φ_k on the validation dataset and 62% on the test dataset (Φ_k-R, OOB R^2 = 0.58 and adj. R^2 = 0.62). The predictor importance estimates (Figures 4.5b & 4.5d) show that R410, R740, R665, R705, SZA, and SAA are the main predictors for estimating Φ_k, underlining the dependency of Φ_k to shadow effects.

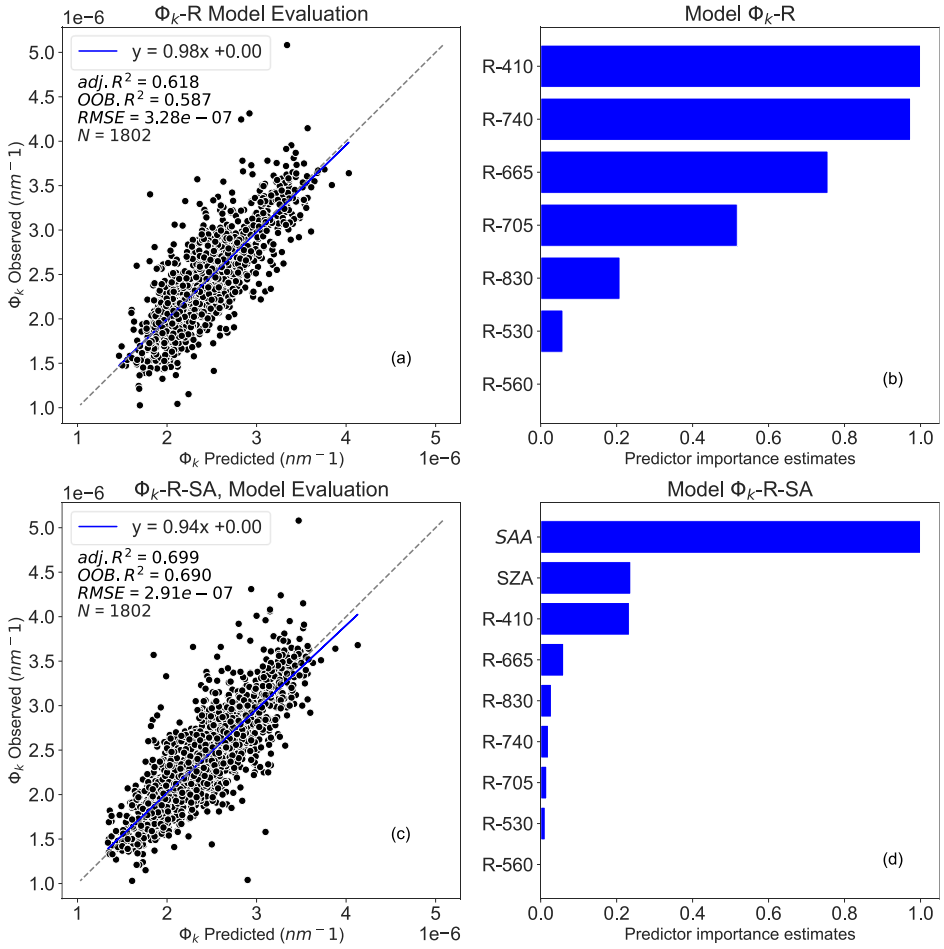

Figure 4.5. Random forest (RF) model outputs: Figure 4.5a depicts the Φ_k-R model performance between observed and predicted Φ_k, Figure 4.5b presents the predictor importance estimates for Φ_k-R model, Figure 4.5c represents the Φ_k-R-SA model performance between observed and predicted Φ_k, and Figure 4.5d presents the predictor importance estimates for Φ_k-R-SA model. N denotes the number of data points used for the RF model's testing, adj. R^2 represents the adjusted coefficient of determination of the relationship between observed and predicted Φ_k, OOB R^2 is the model accuracy on the validation dataset (1/3 of the training set), and the RMSE is the root mean square error between observed and RF model predicted Φ_k. The dashed diagonal line depicts the 1:1 line. Φ_k-R denotes Φ_k prediction using only R; and Φ_k-R-SA integrates R, SZA, and SAA to estimate Φ_k.

4.5. Discussion

4.5.1. Relationships between SIF_y and $F_{yieldLIF}$ at instantaneous and daily timescales

The first objective of this study was to show the effects of canopy structure on SIF signal. The relationship between SIF_y and $F_{yieldLIF}$ was investigated at the daily and seasonal timescales during the growing season from June to August. The results demonstrated that SIF_y and $F_{yieldLIF}$ were more correlated at the seasonal timescale than at the diurnal timescale. Passive SIF is highly dependent on both the structural and physiological properties of the leaf and canopy (Biriukova et al., 2021; Dechant et al., 2022). At the diurnal timescale, far-red SIF is strongly affected by canopy scattering and by the distribution of sunlit and shaded areas at the top and within the canopy (Dechant et al., 2020; Zhang and Zhang, 2023). This study showed that those factors strongly affected SIF_y (SIF normalized by PAR). Further, as SIF_y was estimated using PAR, but not absorbed radiations, SIF_y estimation did not consider the conditions of radiation extinction within the canopy. Therefore, the canopy structural effects can strongly blur the information on the physiological functioning of the vegetation provided by SIF_y, and hence lead to low correlations between SIF_y and $F_{yieldLIF}$. Thus, interpreting SIF_y signal for inferring vegetation physiology at the diurnal scale should be carried out with great care, considering the effects of canopy structure and the complex interactions between structure and illumination geometry. The development of new methods and models are warranted to better explore the possibility to use SIF as a proxy for vegetation functioning at high frequency (seconds to minutes), especially when the vegetation structure is complex and heterogeneous such as in forest stands. On the other hand, the better correlation found at the seasonal timescale can be explained by a potential removal of short-term changes in illumination conditions, canopy structure, and sun-canopy geometry. Note that the seasonal variability of $\overline{SIF_y}$ is also

driven by the seasonal changes in leaf biochemical properties and solar zenith and azimuth angles. These factors can also drive the seasonal dynamics in $\overline{F_{yieldLIF}}$, leading to a better correlation. This may explain why the fraction of the diffuse to total PAR could not entirely explain the relation between $\overline{SIF_y}$ and $\overline{F_{yieldLIF}}$ (Figure 4.1b). In summary, our results underlined that it is difficult to decouple vegetation structural and physiological effects in SIF, owing to fluctuations of sun-canopy geometry throughout the day at the diurnal timescale and the difficulties link to the accurate estimation of total SIF and the fraction of absorbed PAR at the canopy scale (Chang et al., 2021).

4.5.2. Effects of canopy structure and sun-canopy geometry on diurnal dynamics in SIF, NIR_v, R-NIR, Φ_k, SIF_y, and $F_{yieldLIF}$

The fraction of absorbed radiation by the canopy (fAPAR) and the fraction of emitted chlorophyll fluorescence that reach the sensor heavily impact SIF. The results obtained during clear sky days revealed that NIR_v, R-NIR, and Φ_k exhibited similar diurnal patterns. This suggests that the diurnal variations in NIR_v that is the product of NDVI and R-NIR, and Φ_k that represents the product of fAPAR and f_{esc}, were dominated by the bidirectional NIR reflectance effect as it has been shown in (Chang et al., 2021). These authors pointed out that the diurnal dynamics in NIR_v was determined by the diurnal pattern of the reflectance in the NIR within maize crop rows that were under shadow conditions at midday. Sun et al. (Sun et al., 2023a) clearly stated that the dynamics of the fluorescence escape fraction (f_{esc}) in homogeneous C3 crop canopy appears to exhibit a diurnal pattern similar to directional reflectance. Further, at intra-daily timescale, Φ_k is likely to be driven by canopy structure (shadow, leaf angle distribution, etc.) and sun-canopy geometry (SZA and SAA) effects, in particular the distribution of fractions of sunlit and shaded leaves. This situation can lead to large variability of the diurnal patterns in NIR_v and Φ_k as has been shown in Figure 4.2.

The results also highlighted that, at diurnal timescale, the peaks in SIF and PAR do not match (Figure 4.2), which is probably due to the effects of sun-canopy geometry. Indeed, directionality effects can induce variations in the fraction of sunlit and shaded leaves within the FOV, modulating the actual amount of radiation reaching the leaves (different from the incident radiation measured at the sensor, unaffected by shading) and therefore affecting canopy total SIF emission. This finding is in contradiction with several studies that showed that the diurnal

patterns in SIF is mainly dominated by PAR (Campbell et al., 2019; Wang et al., 2021), but in agreement with (Nichol et al., 2019), who showed that the peaks of PAR and SIF did not match in a Boreal Scots pine canopy. Further, note that at high incident PAR, the light energy might exceed the capacity of photosynthesis. In this case, the plant photoprotective mechanism known as non-photochemical heat dissipation is activated, leading first to stomatal closure, and hence to SIF emission reduction (Jonard et al., 2020; De Cannière et al., 2022).

The results also showed that the diurnal dynamics in SIF_y and $F_{yieldLIF}$ did not match (Figure 4.2). This is probably due to both physiological and canopy structure effects. The early decline of SIF_y before noon could be likely due not only to shadow effects, but also to the fact that the PAR was high. These findings corroborate with previous studies (Loayza et al., 2023; Li et al., 2020; Moya et al., 2019). For instance, Loayza et al. (2023) found that under clear sky conditions, at the diurnal timescale, within potato plants, firstly the chlorophyll fluorescence yield declined drastically when the PAR reached values higher than 1000 µmol m^{-2} s^{-1}, and secondly $F_{yieldLIF}$ continuously decreased for PAR > 600 µmol m^{-2} s^{-1}. Thus, the continuous decline of $F_{yieldLIF}$ observed here (Figure 4.2) is likely caused by the fact that the PAR was higher than 1250 µmol photon m^{-2} s^{-1} for the chosen days. Within this situation, the vegetation photosynthetic capacity could be overwhelmed and the energy-dependent and non-energy-dependent non-photochemical heat dissipation can be triggered. Note that energy-dependent heat dissipation can last from a few seconds to a few minutes, while non-energy-dependent heat dissipation can lead to photoinhibition or photobleaching and can last longer (hours to weeks) (Porcar-Castell et al., 2014). Both mechanisms can induce a decrease in SIF_y and $F_{yieldLIF}$ at the diurnal timescale.

4.5.3. Relationships between NIR_v and Φ_k at daily and seasonal timescales

Strong correlations were found between NIR_v and Φ_k at the diurnal timescale. However, their correlations varied largely depending on the ratio of diffuse to total PAR, with high correlation corresponding to clear sky conditions and low correlation to diffuse sky conditions. This result suggests that under clear sky conditions NIR_v is relatively a good proxy of Φ_k and hence can be used to take canopy structure and sun-canopy geometry (i.e. crown shadow, reabsorption, and scattering within leaves and canopies) effects on SIF at the diurnal timescale into account. Indeed, with diffuse sky conditions, canopy structure, shadows and sun-canopy geometry play a minor role in the variations in NIR_v and Φ_k, even though there are still strong

fluctuations in incident light; justifying the low correlations observed between NIR_v and Φ_k during diffuse sky conditions. On the other hand, the positive weak but statistically significant correlation found between daily mean $\overline{NIR_v}$ and daily mean $\overline{\Phi_k}$ at the seasonal timescale indicates that $\overline{NIR_v}$ and $\overline{\Phi_k}$ relations were driven by the fraction between diffuse and total PAR. Indeed, this underlined well NIR_v usage because it was meant to correct reabsorption and scattering effects on SIF at daily and seasonal timescales (Badgley et al., 2017).

4.5.4. Random forest models for $F_{yieldLIF}$ and Φ_k predictions

How we can determine and properly disentangle the confounding factors, including structural, biophysical, and physiological canopy components that all contribute to remotely sensed SIF remains a challenging task. SIF has emerged as a promising tool for determining and characterizing structural and physiological vegetation traits. However, the relationships between these confounding factors and SIF are often complex and site-specific and thus require a model with a set of parameters incorporating these complexities. Therefore, in this study, we examined the potential of RF modelling approaches to predict $F_{yieldLIF}$ and Φ_k based on different remotely sensed input variables under clear sky conditions.

For $F_{yieldLIF}$, the RF models can explain between 86 and 90% of the variability in $F_{yieldLIF}$ (see Table 4.2 and Figure 4.4), sustaining that directional reflectance, chlorophyll fluorescence, and sun-canopy geometry (SZA and SAA) can effectively capture relevant variations in $F_{yieldLIF}$. For instance, FY-R-SA and FY-R-SIF_y-SA models' predictor importance estimates showed that SZA, SAA, R410, R740, and R830 provide the most useful information for $F_{yieldLIF}$ predictions (Figure 4.4). The reflectance in the blue spectral band (R410) is largely affected by the strong blue light absorption by the chlorophyll pigments and it is highly subjective to leaves or canopy shadow conditions, while reflectance in the red-edge (R740) and near-infrared bands characterize the leaf area index and the chlorophyll content of the entire forest (Zeng et al., 2022b). The red-edge region is mainly used to determine leaf and canopy chlorophyll contents. Because of these abovementioned characteristics of R, it is not surprising that the combination of reflectance at specific spectral bands can be used to infer effective and relevant information that allow capturing $F_{yieldLIF}$ variations. The data also revealed that adding SIF or SIF_y as predictors did not significantly improve the model performance estimates as it has been shown in (Balde et al., 2023). This result indicates that even at high temporal resolution the

contribution of SIF or SIF_y is important compared to each reflectance band individually, but the combined effect of reflectance bands could mitigate or hide the use of SIF as vegetation physiological proxy. The results showed that SZA and SAA significantly improved the model prediction for $F_{yieldLIF}$ (FY-R-SA). First, the contribution of SZA can be attributed to the illumination conditions because incoming radiations are tightly related to SZA. Second, the effect of SAA is attributable to the anisotropy in reflectance and canopy structure in the azimuthal plane.

For Φ_k, results indicate that RF models can explain between 60 and 70% of the variability in Φ_k (Figure 4.5a and 4.5b). The unexplained 30 or 40% in Φ_k variance evidenced that the ratio SIF_y over $F_{yieldLIF}$ strongly varies and depends on several factors, including canopy structure, sun geometry, and illumination conditions. Therefore, this suggests that mechanistic models that used NIR_v to approximate the product of fAPAR and f_{esc} are simplistic and do no fully account for the complex interactions between incident radiation and canopy structure, notably due to the distribution of light and shaded leaves at the top and inside of the forest canopy.

4.6. Conclusion

In this work, the simultaneous and continuous active and passive measurements of chlorophyll fluorescence at the canopy scale in a sessile oak mature forest allowed to analyse the diurnal cycles of key variables, including SIF, SIF_y, NIR_v, and $F_{yieldLIF}$. A novel remote sensing indicator, Φ_k, the ratio between SIF_y and $F_{yieldLIF}$, which is also theoretically the product of fAPAR and f_{esc}, was introduced. On one hand, the relationship between SIF_y and $F_{yieldLIF}$ was evaluated, and on the other hand, the relation between NIR_v and Φ_k was examined at daily and seasonal scales. Further, several random forest models with reflectances, SIF, and sun angles as inputs were also used to not only predict $F_{yieldLIF}$ and Φ_k, but also to provide sensitivity analysis and interpretation of the model outputs.

The results showed that SIF signal is highly impacted by the canopy structure and the sun-canopy geometry effects, as evidenced by the weak correlations found between SIF_y and $F_{yieldLIF}$ at diurnal timescale using instantaneous measurements. However, SIF_y captured the seasonal dynamics of $F_{yieldLIF}$ by explaining 58% of the variations in $F_{yieldLIF}$. The results also

revealed that NIR_v and reflectance at near-infrared (R-NIR) are good proxies of Φ_k at the diurnal timescale, while their correlations diverged at the seasonal scale.

Based on random forest models, the combination of reflectance, chlorophyll fluorescence, and sun geometry (SZA and SAA) allow to predict $F_{yieldLIF}$ and Φ_k at the diurnal timescale under clear sky conditions. For instance, the RF models were able to explain 86-90% of $F_{yieldLIF}$ variability, and 60-70% of Φ_k variations were explained. Furthermore, the data also revealed that adding SIF or SIF_y as predictors did not improve much the model performance compared to the reflectance-based model. But the predictor importance estimates showed that SIF and SIF_y provide useful and impactful information in determining $F_{yieldLIF}$. This result indicates that even at high temporal resolution the contribution of SIF or SIF_y is important compared to each reflectance band individually, but the combined effect of reflectance bands could mitigate or hide the use of SIF as vegetation functioning proxy.

Overall, this study provides insights into understanding the complex and difficult relationship that exists between passive SIF and active chlorophyll fluorescence, and into the use of remote sensing data that are readily accessible at satellite scale (spectral reflectance at 10 nm resolution, sun geometry, and chlorophyll fluorescence) to predict $F_{yieldLIF}$ and Φ_k at canopy scale.

5. Chapter 5: Investigating the responses of sun-induced chlorophyll fluorescence, gross primary production and their inter-relationship to abiotic factors changes in a temperate deciduous forest

This chapter is based on: Balde, H., Hmimina, G., Goulas, Y., Latouche, G., Ounis, A., Berveiller D., and Soudani, K.: Investigating the responses of sun-induced chlorophyll fluorescence, gross primary production and their inter-relationship to abiotic factors changes in a temperate deciduous forest, preprint [https://doi.org/10.5194/egusphere-2024-657]

NB: Supplementary materials are all in annexes (Annexe Chapter 5)

Abstract. Far-red Sun-Induced chlorophyll Fluorescence (SIF) is increasingly used as a proxy of vegetation Gross Primary Production (GPP) across different ecosystems and at spatiotemporal resolutions going from proximal and continuous to satellite-based remote sensing measurements. However, the use of SIF to probe variations in GPP in forests is challenged by confounding factors such as leaf physiological and biochemical properties and canopy structure along with abiotic factors (light intensity, temperature, soil water content, atmospheric vapour pressure deficit, etc.). To provide insights into understanding the complex drivers of GPP and SIF variations and their relationships, we examined SIF and GPP seasonal and diurnal changes and how canopy structure and environmental conditions affected SIF and GPP relationships in an oak deciduous forest. To do so, we combined canopy scale SIF measurements, spectral vegetation indices, environmental variables measurements including diffuse and direct radiation in the spectral range of the photosynthetically active radiation (PAR), air and canopy temperature, soil water content (SWC), atmospheric vapour pressure deficit (VPD), and GPP estimated from measurements of an eddy covariance flux tower. Further, Random Forest (RF) models were used to predict SIF and GPP and to analyse the responses of SIF and GPP to environmental drivers. The results show that both SIF and GPP variations and their relationships were dependent on the temporal scale considered. At the seasonal scale, the data show that leaves phenological and canopy biochemical properties variations, seasonal cycle of solar radiation, and other abiotic factors such as atmospheric Vapor Pressure Deficit (VPD) and Soil Water Content (SWC) control not only SIF and GPP variations, but also the relationship between GPP and SIF. Further, during the extreme weather conditions (heatwaves observed in 2022 in: mid-June (DOY: 166-169), mid-July (DOY: 196-199), and early August (DOY: 218-224), we observed that SIF and reflectance-based Vegetation Indices (VIs) such as Normalizd Difference Vegetation Index (NDVI) and near-infrared reflectance of vegetation index (NIR_v), and SIF and PAR are uncorrelated, while GPP, SIF, passive SIF yield (SIF_y) and active fluorescence yield ($F_{yieldLIF}$) strongly decreased. This indicates that SIF can capture GPP activity and VIs cannot be used to track changes in vegetation physiology during severe abiotic conditions. This specific response of SIF compared to VIs underlined the interest of SIF to track GPP under severe abiotic conditions. At the diurnal timescale, the also revealed that the light saturation of the relationship between GPP and SIF was not only dependent on PAR, but also relied upon the fraction of diffuse to total PAR, as well as upon VPD, SWC, and

air and canopy temperature. The other key finding was that sun zenith and azimuth angles had strong and inverse effects on GPP and SIF variations. This result highlights that using passive in-situ SIF measurements to validate satellite measurements at coarse spatial and temporal resolutions can therefore be very difficult because obtained results will not be reproducible from one site to another, specifically in forest stands.

5.1. Introduction

Uncertainty related to future climate forecasts are highly dependent on the terrestrial ecosystem feedback on the global carbon cycle. Vegetation carbon sequestration through photosynthesis is a main contributor to terrestrial ecosystem feedbacks (IPCC, 2022) and hence its monitoring can play a key role in global climate changes estimations. Gross primary production (GPP) is an indicator of vegetation carbon sequestration. GPP can be determined locally from measurements or from models (Xiao et al. 2019). However, Remote Sensing (RS) has been widely and successfully used as an unprecedented tool for upscaling, monitoring, and understanding vegetation carbon exchange across space and time (Xiao et al., 2021; Pierrat et al. 2022a).

The main success of RS observations can be attributed to their capacity in capturing valuable information on vegetation characteristics (leaf area index, chlorophyll content, fraction of absorbed radiation, surface temperature, etc.) that significantly affect or are linked to GPP. However, the relationships between RS observations and GPP are often site-, and vegetation type-specific and can considerably be affected by local abiotic factors, thereby hindering the potential of this technique. Improvements in how we associate RS observations to GPP are warranted to better understand and monitor global carbon dynamics, specifically in forest ecosystems.

GPP can be described using the light-use efficiency model at canopy scale (Monteith, 1972)

$$GPP = PAR \times fAPAR \times LUE \quad (5.1)$$

where PAR is the flux of photosynthetically active radiation (400-700 nm), fAPAR is the fraction of absorbed PAR by the canopies, and LUE is the efficiency of the absorbed light used in photosynthesis (the fraction of absorbed light energy converted into chemical energy).

Sun-Induced chlorophyll Fluorescence (SIF) is a remotely sensed optical signal emitted during the light reaction of photosynthesis, which is tightly related to photosynthesis and vegetation carbon assimilations. SIF has emerged as an unprecedented tool for monitoring and understanding GPP over a wide variety of terrestrial ecosystems (Frankenberg et al., 2011; Balde et al. 2023; Wang et al. 2020) and across diverse spatial and temporal scales (Goulas et al. 2017; Zhang et al. 2022; Pierrat et al. 2022b; Xu et al. 2021; Sun et al. 2023a) because of its links with both the structural (i.e. fAPAR and PAR) and physiological components of GPP (i.e. LUE). So, SIF can also analogously be written as:

$$SIF = PAR \times fAPAR \times \Phi_F \times f_{esc} \quad (5.2)$$

where Φ_F is the quantum fluorescence yield (ratio of photons emitted to photons absorbed) and f_{esc} is the fraction of emitted SIF photons, which escape the canopy. Equations (5.1) and (5.2) showed that GPP and SIF share the same driver (i.e. absorbed photosynthetically active radiation, APAR = incident PAR x fAPAR), which have been found to explain the relationship between GPP and SIF in maize (Miao et al. 2020) and in an evergreen needleleaf forest (Kim et al. 2021). From the combination of equations (5.1) and (5.2), we obtain:

$$GPP = SIF \times \frac{LUE}{\Phi_F \times f_{esc}} \quad (5.3)$$

This is the main evidence of using SIF as a proxy of GPP, notably when observations are averaged over large spatial and temporal scales (Sun et al. 2023b). However, these conditions are not always met (Damm et al. 2015; Marrs et al. 2020; Kim et al. 2021), typically at high temporal resolutions (diurnal level: half-hourly, hourly, etc.) and under water and light limited conditions (heatwaves, drought, etc.) (Berger et al. 2022; Martini et al. 2022; Pierrat et al. 2022a). Therefore, considering a more complex relationship between SIF and GPP as discrepancies between variations in Φ_F, LUE, f_{esc}, and the fraction between diffuse sky and clear sky conditions may further improve the usefulness of SIF as a proxy of GPP. Besides, reflectance-based remotely sensed metrics (i.e. vegetation indices) such as the Normalized Difference Vegetation Index (NDVI), the near-infrared reflectance of vegetation index (NIR_v),

and the Photochemical Reflectance Index (PRI), can provide information on both structural and functional processes affecting GPP.

Both SIF and GPP are physically affected by canopy structure (i.e. vertical distribution of LAI, canopy roughness, leaf angle distribution, etc.) and radiation conditions that mediate in time and space fAPAR and f_{esc}. At a given constant LAI, both GPP and SIF can increase under cloudy conditions as a result of increasing fAPAR because diffuse light can penetrate deeper into the canopy (Durand et al. 2021). If changes of GPP under diffuse sky conditions have been studied, it is not always considered when estimating GPP with remote sensing metrics such as SIF, and reflectance-based vegetation indices (VIs).

VIs are sensitive to canopy traits such as LAI, leaf chlorophyll content, leaf angles, and clumping. They are also good proxies of fAPAR and hence they have been successfully used to describe canopy structure. For instance, NDVI and NIR_v provide crucial information on the structural determinants of GPP and SIF (Zeng et al. 2022). However, how sensitive these variables are to changes in SIF and GPP, which are heavily affected by PAR, fAPAR, changes in ratio between LUE and Φ_F, and abiotic conditions is still unclear and need to be investigated.

The non-photochemical quenching (NPQ), a photoprotection mechanism that plants activate to avoid damage from excess light, regulates the efficiency with which fluorescence and photosynthesis use APAR. The extent to which plants can avoid photodamage from excess light depends heavily on the abiotic conditions and on plant photosynthetic capacity and types (Cannière et al. 2022). This is particularly important in respect to vegetation sensitivity to extreme weather conditions such as heatwaves and drought. For instance, heatwaves can create stress conditions which will affect photosynthesis and fluorescence efficiencies (Wang et al. 2022; Zanotelli et al. 2023). Thus, determining and monitoring NPQ can be useful to provide insight into photosynthesis efficiency, and presumably also into fluorescence efficiency, even though such a relation has not been established yet. The reversible heat dissipation is the most common NPQ. It happens under short-term extreme light stress conditions and can be detected using the Photochemical Reflectance Index (PRI), which was found to track changes in photosynthesis efficiency over diurnal scales (Sukhova et al. 2022).

For instance, including information on SIF and heat dissipation using PRI as a proxy was shown to improve GPP predictions across different vegetation types at daily scale (Wang

et al. 2020). Further, Lu et al. (2020) have revealed that correcting SIF for canopy structural effects using f_{esc} derived from NIR_V and fAPAR can also improve the relationship between SIF and GPP, underlining the relevance of disentangling structural and physiological components of SIF. It is well documented and mechanistically explained why spectral reflectance and VIs are related to changes in canopy structure at broad scales, but there is no clear evidence that there are robust relationships among them at high temporal resolutions. To establish such relationships, the effects from canopy architecture, leaf physiology, sun-canopy geometry, and sky conditions (i.e. cloudy and sunny) have to be accounted for. Thus, the ability for VIs or reflectance-based metrics to inform SIF and GPP will be limited to quantitative correlations at site- and vegetation type-specific, unless we are able to accurately incorporate the aforementioned effects in mechanistic models.

Recently, advances in machine learning have provided opportunities for predictive modelling, data analysis, and foremostly for model output interpretation. In this context, random forest (RF) models are of particular interest. RF models are non-parametric models and are well adapted for predicting nonlinear and multi-parameters relationships in complex situations (Breiman, 2001). RF models have already been successfully used to understand how canopy structure and functions affect the dynamics of GPP and SIF either with satellite (Balde et al. 2023) or ground-based observations (Pierrat et al. 2022a). We hypothesized that using RF models can help to understand SIF and GPP dynamics and improve their predictions based on a combination of RS metrics, sun-canopy geometry, and abiotic variables.

Therefore, the main concerns of this study are: 1) to understand dynamics of GPP and SIF and their responses to abiotic factors and 2) to predict GPP and SIF by using RF models as a quantitative and interpretative tool that can associate structural and physiological information provided by VIs, SIF, and abiotic variables. To do so, we studied one full growing season of ground-based remote sensing data acquired in a temperate deciduous oak forest. We first assessed the seasonal dynamics of abiotic variables, VIs, fluorescence, and GPP. Secondly, we examined how abiotic factors affect the relations between GPP and SIF considering different temporal resolutions. Thirdly, we combined RS metrics and abiotic variables to predict GPP and SIF, and to quantify and interpret their contributions to GPP and SIF estimates.

5.2. Materials and Methods

5.2.1. Study site description

We collected data at the Fontainebleau-Barbeau forest site, an Eddy Covariance (EC) observation site belonging to the ICOS Ecosystem network (FR-Fon) (Delpierre et al. 2016). The site is located 53 km southeast of Paris, France. It is a mixed temperate deciduous broadleaf forest stand with stem density predominantly (79%) of mature sessile oak trees (*Quercus petraea (*Matt.) Liebl) (Maysonnave et al., 2022) with an understory of hornbeam (*Carpinus betulus* L.) (for more details see: http://www.barbeau.universite-paris-saclay.fr/). The climate is temperate and characterized by an annual average rainfall of approximately 680 mm and an average air temperature of approximately 11°C (Soudani et al., 2014). The LAI is approximately 5.8 $m^2.m^{-2}$ using the litter collection method over the 2012-2018 period (Soudani et al., 2021). At the Fontainebleau-Barbeau site, carbon and water fluxes have been continuously monitored at 35 m height using the EC method.

5.2.2. Data collection: ground-based remote sensing, GPP, and environmental variables

Ground-based remotely sensed observations (far-red SIF, NDVI, NIR_v, PRI, mNDI, and spectral reflectance) were collected using an automated SIF3 instrument developed at the Laboratory of the Meteorology Dynamic (LMD), Ecole Polytechnique and the Laboratory of Ecology, Systematic and Evolution (ESE). The automated SIF3 instrument was installed at the top of a 35 m height tower of Fontainebleau-Barbeau site, above the canopy. To avoid artificial shading from the tower on the measured area, SIF3 was set to the southern part of the tower. It has 25° field of view (FOV) and measures alternatively sun irradiance and vegetation radiance at a high spectral resolution to deduce SIF, spectral reflectance, and VIs. In this study, observations run from April 2022 to mid-September 2022. Remotely sensed observations were averaged over a 30 min window and synchronized with GPP and abiotic variables. Far-red SIF (i.e. at 760 nm) was retrieved using a Fraunhofer-line based retrieval method (Daumard et al. 2012). Note that daily mean SIF data were used to understand the seasonal dynamics. The Fraunhofer-line based method has been widely used for SIF retrieval because of its less insensitivity to atmospheric scattering and reliability even under cloudy sky conditions (Mohammed et al. 2019; Cendrero-Mateo et al. 2019). Low quality retrieval and retrieval with unstable illumination conditions were filtered out from SIF observations. The VIs, including

the Normalized Difference Vegetation Index (NDVI) (Tucker 1979) and near-infrared reflectance of vegetation index (NIR_v) (Badgley et al., 2017) as indicators of vegetation structure, modified red-edge Normalized Difference Index (mNDI) (Hmimina et al., 2014) as an indicator of leaf chlorophyll content, and Photochemical Reflectance Index (PRI) (Gamon et al., 1997) as indicator of extreme heat dissipation, were calculated as follows:

$$NDVI = \frac{R_{[780-800]} - R_{[670-680]}}{R_{[780-800]} + R_{[670-680]}} \quad (5.4)$$

$$NIR_v = R_{[780-800]} \times NDVI \quad (5.5)$$

$$mNDI_{705} = \frac{R_{750} - R_{705}}{R_{750} + R_{705} - 2 \times R_{445}} \quad (5.6)$$

$$PRI = \frac{R_{[569-571]} - R_{[520-532]}}{R_{[569-571]} + R_{[520-532]}} \quad (5.7)$$

with R being the reflectance at a given wavelength or the average across a wavelength range in nm.

To consider the functional component of SIF, an apparent fluorescence yield was calculated by normalizing SIF by PAR. We used half-hourly GPP data estimated from net ecosystem exchanges measurements. GPP and SIF data were also aggregated at daily timescale and used to study the seasonal dynamics. The main micrometeorological variables, including incident, reflected, direct, and diffuse radiations in the PAR spectral range, are measured at high frequency (1 min) and were aggregated at the half-hourly and the daily temporal resolutions. Atmospheric vapor pressure deficit (VPD), precipitation, air, canopy and soil temperature, soil water content, relative humidity, and wind speed are recorded half-hourly and were averaged at daily scale. Note that the soil water contents are averaged values in cm^3 water per cm^3 soil. The averaged values are calculated between 0 and 150 cm depth.

To consider the effects of sky, the fraction of diffuse radiation over the total incoming radiation was determined. This fraction varies with respect to variations in sun zenith angle and with the sky conditions. It is worth noting that values of the fraction <0.3 are considered as sunny days, while values of the fraction >0.70 are cloudy days.

5.3. Data analysis: seasonal dynamics, relationships, and random forest models

The influence of environmental variables on the links between GPP and SIF was examined at half-hourly and daily timescales using a non-linear curve fitting of GPP vs SIF (Kim et al. 2021). The coefficient of determination (R^2) is used to assess the strength of the correlations.

We examined the significance of remote sensing metrics (reflectance and VIs), sun-canopy geometry, and abiotic variables as predictors for SIF and GPP at diurnal scale using random forest regression models. Various types of RF models were established for estimating SIF and GP (Table 5.1). All RF models were created using 200 trees and sampled with replacement based on bag fraction of 80% (80% of the data for training and 20% for testing). All RF models were run with only sunny days data at a half-hourly temporal resolution. The out-of-bag (OOB) predictor importance estimates were determined to evaluate the contribution of each predictor to the predicted output. Note that, we also used the partial dependence plot to study the relationship between inputs and estimated variables (i.e. GPP and SIF). Model performance was evaluated using the OOB R^2 score and the adjusted R^2 between the testing dataset and the predictions, as well as the RMSE. The closest the OOB R^2 and adjusted R^2 are, the better the model is able to be generalized.

Table 5.1. Random forest models set up for SIF and GPP predictions using environmental and remote sensing variables as inputs and only sunny days data: vapor pressure deficit (VPD), volumetric soil water content (SWC), sun zenith (SZA) and azimuth (SAA) angles, far-red sun-induced chlorophyll fluorescence (SIF) at 760 nm, photochemical reflectance index (PRI), near-infrared reflectance of vegetation index (NIR_v), normalized difference vegetation index (NDVI), and modified red-edge normalized difference index (mNDI).

Model name	Inputs	Outputs	Purpose
GPP-ENV-SA	VPD, SWC, SZA, SAA	GPP	To test the synergy between environmental variables and sun angles to predict GPP.
GPP-ENV-RS	SIF, PRI, NIR_v, NDVI, mNDI, VPD, SWC, SZA, SAA	GPP	To test the synergy between remote sensing and environmental variables and sung angles to predict GPP.
SIF-ENV-SA	VPD, SWC, SZA, SAA	SIF	To test the synergy between environmental variables and sun angles to predict far-red SIF.
SIF-ENV-RS	PRI, NIR_v, NDVI, mNDI, VPD, SWC, SZA, SAA	SIF	To test the synergy between remote sensing and environmental variables and sun angles to predict far-red SIF.

5.4. Results

5.4.1. Seasonal variations in GPP, SIF, VIs and environmental variables

The variations in GPP, SIF, $F_{yieldLIF}$, SIF_y, vegetation indices (VIs), and abiotic variables at Fontainebleau-Barbeau forest site during the period of measurements (growing season 2022) are illustrated in Figure 5.1.

The GPP of the deciduous oak trees started to raise gradually in April and until the end of May following the development of the leaves (Figure 5.1A). Seasonal variations in GPP were characterized by sharp fluctuations across the season reflecting PAR, air temperature (Ta), and atmospheric Vapour Pressure Deficit (VPD) changes. The dynamics in Ta and VPD showed contrasted and marked weather conditions, i.e. in 2022 in Barbeau, heat waves in: mid-June (DOY: 166-169), mid-July (DOY: 196-199), and early August (DOY: 218-224), coinciding to the peak values of Ta and VPD. Note that during these heatwaves' periods, GPP substantially decreased and the values of Ta and VPD showed obvious air drought conditions. The seasonal variations in SWC revealed an overall steady decline, meaning that the soil was constantly drying from an SWC > 0.4 cm^3 cm^{-3} at the beginning of the season to an SWC < 0.27 cm^3 cm^{-3} in the end.

The seasonal variations in NDVI and mNDI exhibited similar patterns, which represent the seasonality changes of canopy attributes in deciduous forests (E and G). PRI values showed a rapid increase during the budburst and the leaf expansion phases until it reached its maximum in early June. Afterwards, PRI is stable and slightly decreased during the leaf maturation phase. This PRI temporal pattern was consistent with the temporal pattern of NDVI and mNDI throughout the season. The within-day PRI changes are attributable to the activity of the xanthophyll cycle and to fluctuations in the PAR intensity, while the seasonal dynamic of NIR_v was due to day-to-day changes in light intensity and sun-canopy geometry, and also to changes in canopy attributes throughout the season.

Far-red SIF followed the same temporal pattern as the other variables, reflecting the phenological dynamics of the canopy. Like GPP, far-red SIF reached its maximal values soon after the new leaves were fully developed in early June. SIF then gradually declined following the decrease in GPP. $F_{yieldLIF}$ showed a steady decrease over the season, while variations in SIF_y

were driven by the changes in light intensity and indicated the onset of the growing season. The dynamics in SIF_y also showed a similar trend of decrease across the season like GPP and SIF. Note that both $F_{yieldLIF}$ and SIF_y significantly declined during the heat waves periods, as it has been observed in GPP and SIF dynamics.

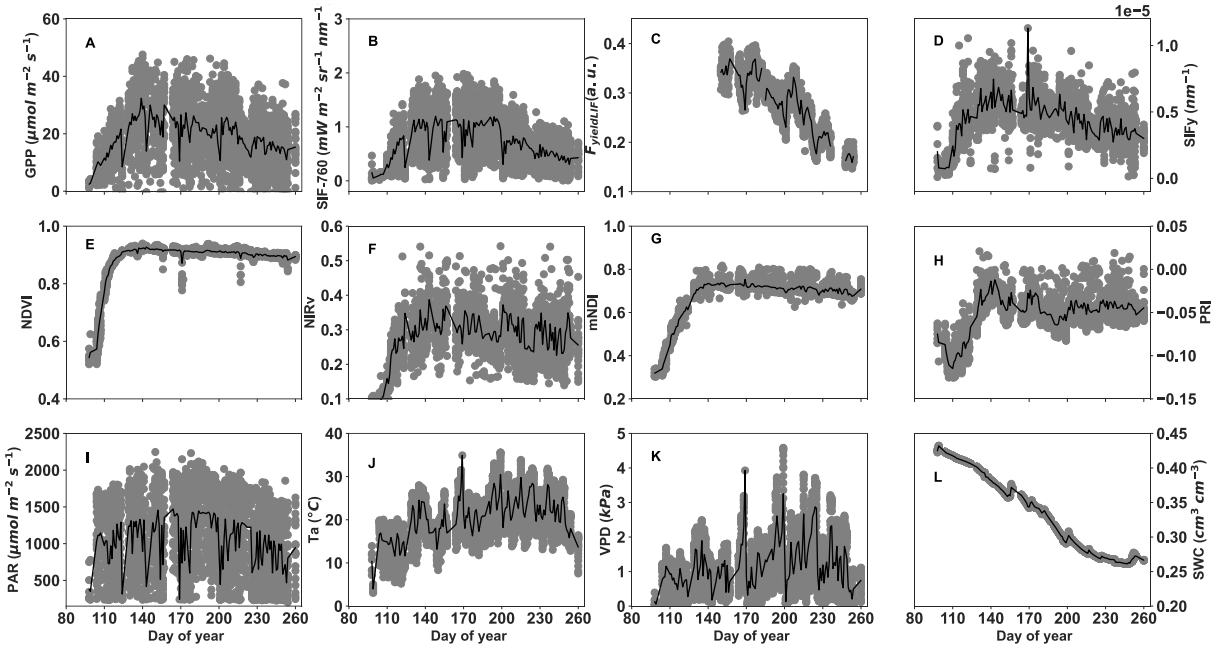

Figure 5.1. Variations in Gross Primary Production (GPP) (Figure 5.1A), far-red Sun-Induced chlorophyll Fluorescence (SIF) of the whole canopy (Figure 5.1B), active chlorophyll fluorescence yield ($F_{yieldLIF}$) (Figure 5.1C), apparent SIF yield (SIF_y) (Figure 5.1D), Normalized Difference Vegetation Index (NDVI) (Figure 5.1E), near-infrared reflectance of vegetation index (NIR_v) (Figure 5.1F), modified red-edge Normalized Vegetation Index (mNDI) (Figure 5.1G), Photochemical Reflectance Vegetation Index (PRI) (Figure 5.1H), Photosynthetically Active Radiation (PAR) (Figure 5.1I), air temperature (Ta) (Figure 5.1J), Vapor Pressure Deficit (VPD) (Figure 5.1K), and volumetric Soil Water Content (SWC) (Figure 5.1L) under all sky conditions during the 2022 growing season. Gray points indicate the data at half-hourly timescale and the black line represents daily mean values.

5.4.2. Influence of abiotic variables on the daily and seasonal variations of the relationship between GPP and SIF

The relationship between GPP and SIF was non-linear (Figure 5.2). The hyperbolic regression shows that GPP saturated with increasing SIF values (i.e. SIF> 1 mW m^{-2} sr^{-1} nm^{-1}) and yields a significantly higher R^2 = 0.53 than a linear regression (data not shown) at half-hourly time resolution. The results also reveal that the relation between GPP and SIF is

significantly stronger for cloudy days than for sunny days, with R^2 of 0.66 and 0.59, respectively.

The relationship between SIF and GPP exhibits gradual changes with the day of year (DOY), the Photosynthetically Active Radiation (PAR), the fraction of diffuse to total PAR, the atmospheric Vapour Pressure Deficit (VPD), the leaf canopy temperature (Tc), and the Soil Water Content (SWC). It can be seen that the saturation of GPP with increasing SIF happened for high PAR, and that for high VPD and very high Tc the GPP stayed low, when far-red SIF kept increasing. In other words, the ratio GPP over SIF decreases with increasing PAR, VPD, and Tc. The temporal dynamic (DOY) has strong impact on the relationship between SIF and GPP, with both GPP and SIF increasing linearly from the start of the season until around DOY 140, and afterward GPP starts saturating until around DOY 215 and then both GPP and SIF linearly decrease, underlining the fact that seasonal variations in leaves and canopy have a large influence on the relationship between SIF and GPP. The gradual changes in the fraction of diffuse to total PAR reveals that SIF and GPP linearly increased during cloudy days. However, on sunny days, GPP shows saturation, when SIF continues to increase. Finally, the soil water content has also a strong influence on the relationship between GPP and SIF, with drier conditions corresponding to the lowest GPP values and the highest GPP values observed when water availability was not a limiting factor.

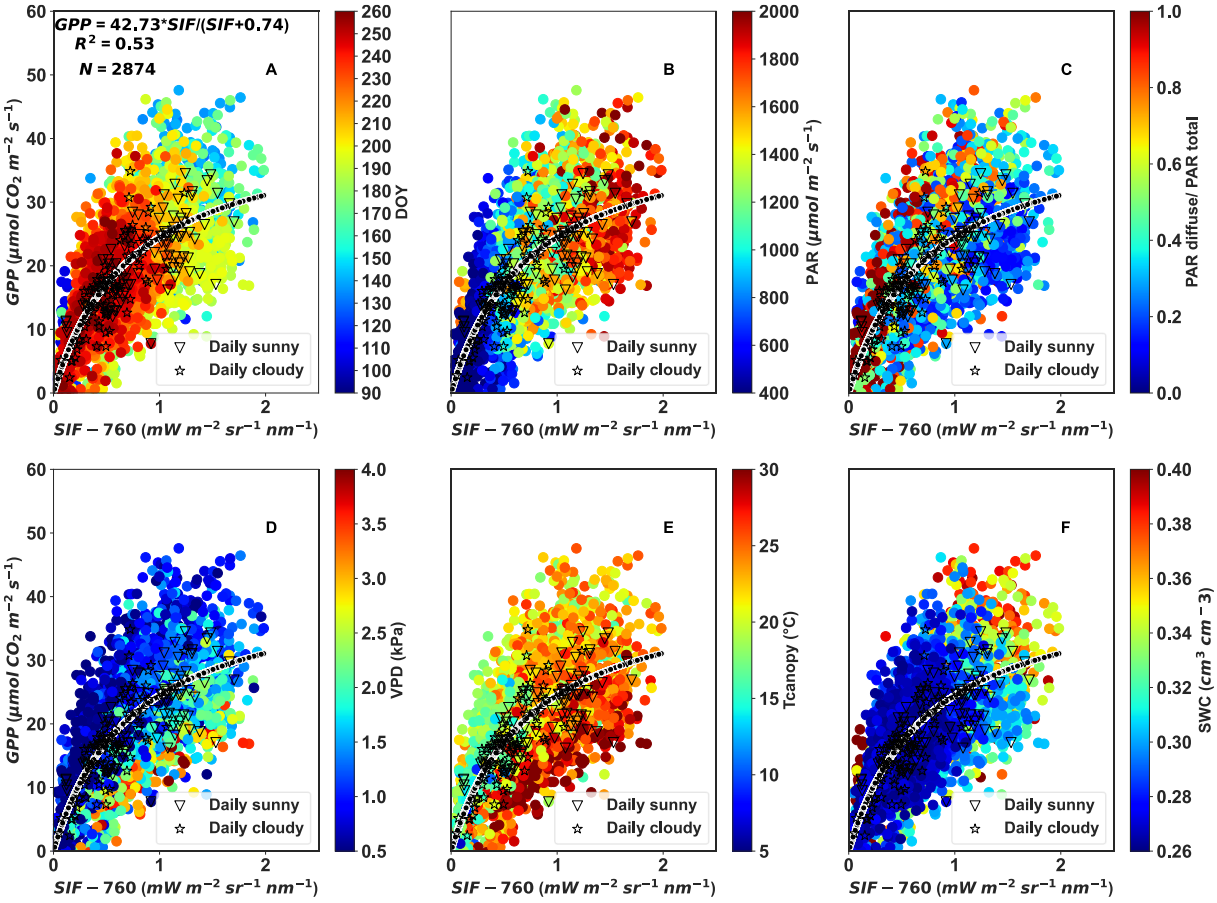

Figure 5.2. The hyperbolic relationship between gross primary production (GPP) and far-red sun-induced chlorophyll fluorescence (SIF) at half-hourly timescale seen with color scaled dots for: day of year (DOY, Figure 5.2A), photosynthetically active radiation (PAR, Figure 5.2B), ratio of diffuse to total PAR (Figure 5.2C), vapor pressure deficit (VPD, Figure 5.2C), leaf canopy temperature (Tcanopy, Figure 5.2D), and mean soil water content at 150 cm depth (SWC, Figure 5.2E), except triangles and stars points.

In Figure 5.3 the coefficient of determination (R^2) of the relation between daily GPP and daily SIF shows strong inter-daily variability. R^2 significantly decreases when VPD (Figure 5.3C) and PAR (Figure 5.3A) are high. The highest correlations were obtained for relatively low VPD and moderate PAR, and during cloudy days (Figure 5.3B). Note that also the correlation between GPP and SIF substantially declines during the drier period of the season, corresponding exactly to the peaks of VPD. This suggests that inter-daily variations in GPP and SIF relations were significantly affected by the abiotic conditions, as well as by the intermittence between cloudy and sunny days.

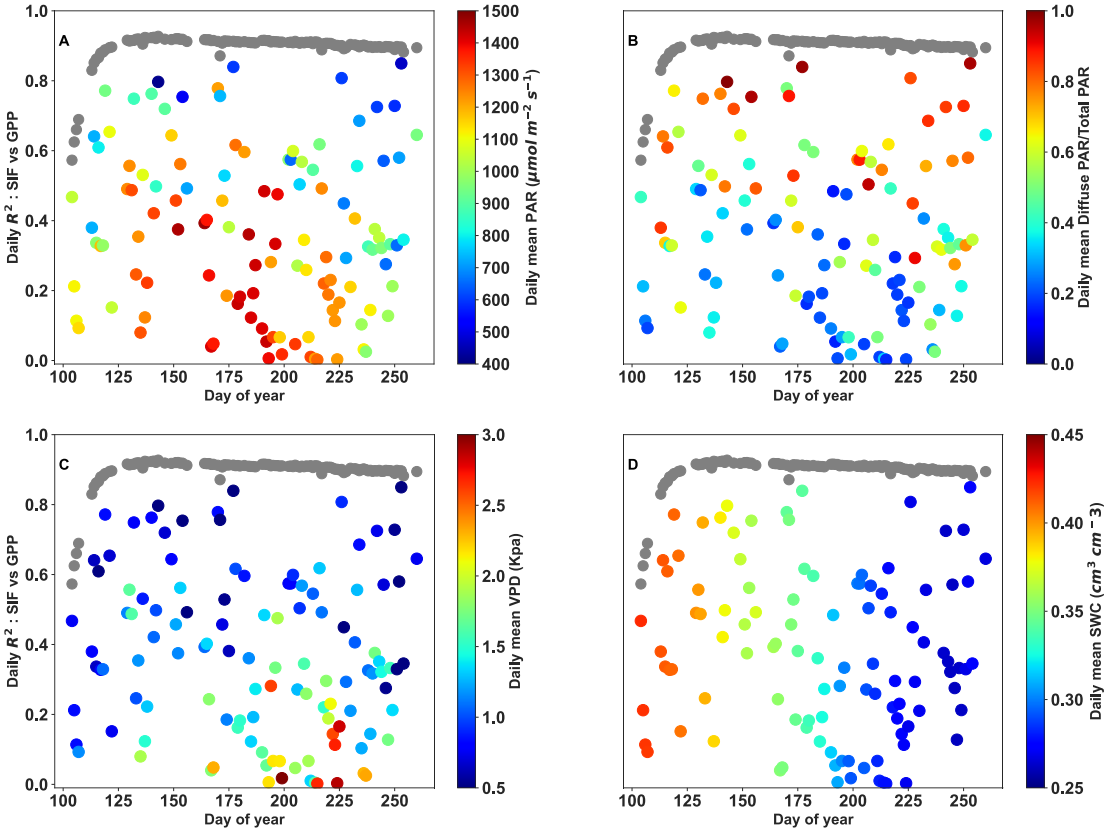

Figure 5.3. Inter-daily variations of the coefficient of determination between GPP vs far-red SIF seen with color scaled dots for: photosynthetically active radiation (PAR, Figure 5.3A), ratio of diffuse to total PAR (Figure 5.3B), vapour pressure deficit (VPD, Figure 5.3C), and mean soil water content at 150 cm depth (SWC, Figure 5.5D). The grey line represents the seasonal dynamic of the normalized difference vegetation index (NDVI). The number of data points per day varied between 20 and 23, representing more than 87% of the total data points.

How GPP is related to SIF at satellite overpass times is a crucial question. Hence, we investigated the relationship between GPP and SIF at satellite overpass times using only data acquired at 10H30 am and 13H30 pm under on sunny days (Figure 5.4). A substantial hyperbolic relation was found between GPP and far-red SIF at satellite overpass times. The results presented in Figure 5.4 showed that the non-linear correlation was stronger in the afternoon (13h30 pm) than in the morning (10h30 am) with R^2 of 0.79 and 0.57, respectively. This suggests that the GPP-SIF relation depends strongly on the vegetation physiological state and on the conditions of illumination.

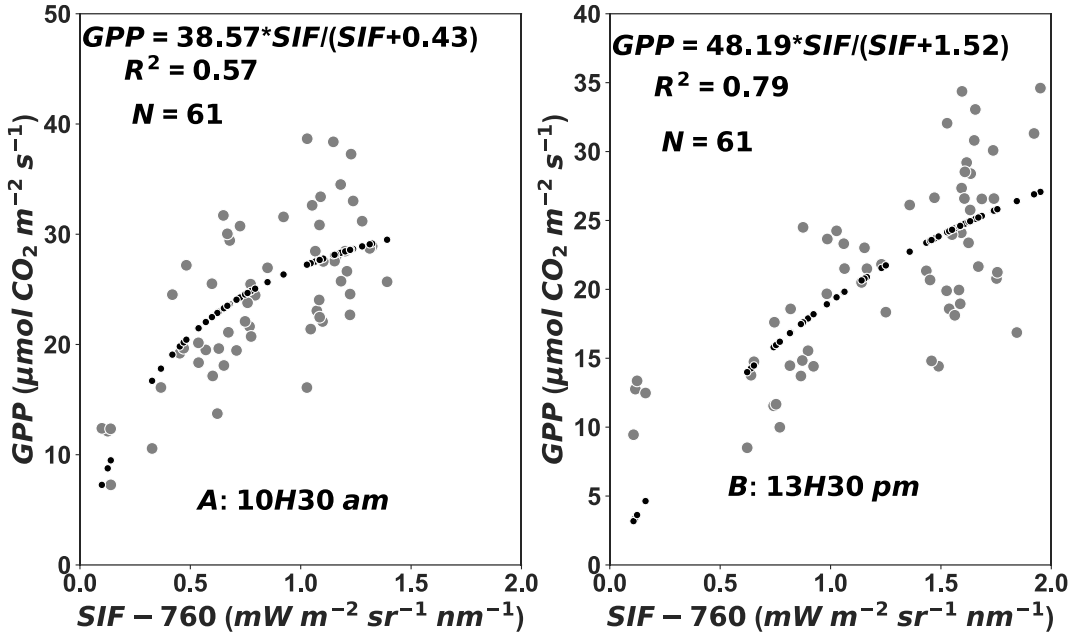

Figure 5.4. Relationship between daily GPP and canopy far-red SIF (SIF-760) at satellite overpass times on sunny days. R^2 represents the coefficient of determination, and the hyperbolic regression line is the black dotted line.

5.4.3. Main drivers of SIF and GPP variations and predictions for sunny days

To predict GPP and SIF using environmental and remote sensing variables and assess the contribution of these variables to their variations, several RF regression analyses were performed and the main results are presented in Figures 5.5, 5.6, and 5.7 (the other model results are given in Supplementary materials Figure S5.1, S5.2 and S5.3). The predictor importance estimates for SIF-ENV-RS model is exhibited in Figure 5.5B. This model explains approximately 94% of the total variance of far-red SIF (Figure 5.5A). SWC appears to be the most important variable, followed by SZA and SAA, and the contribution of mNDI, PRI, and VPD play lesser roles for SIF prediction (Figure 5.5B). For GPP, the RF model represented in Figure 5.5D captures between 70% and 72% of the variability in GPP (Figure 5.5C). VPD and SZA appear to be the most determinant variables, followed by SWC and far-red SIF, and the contribution of all other variables was relatively minor for GPP prediction.

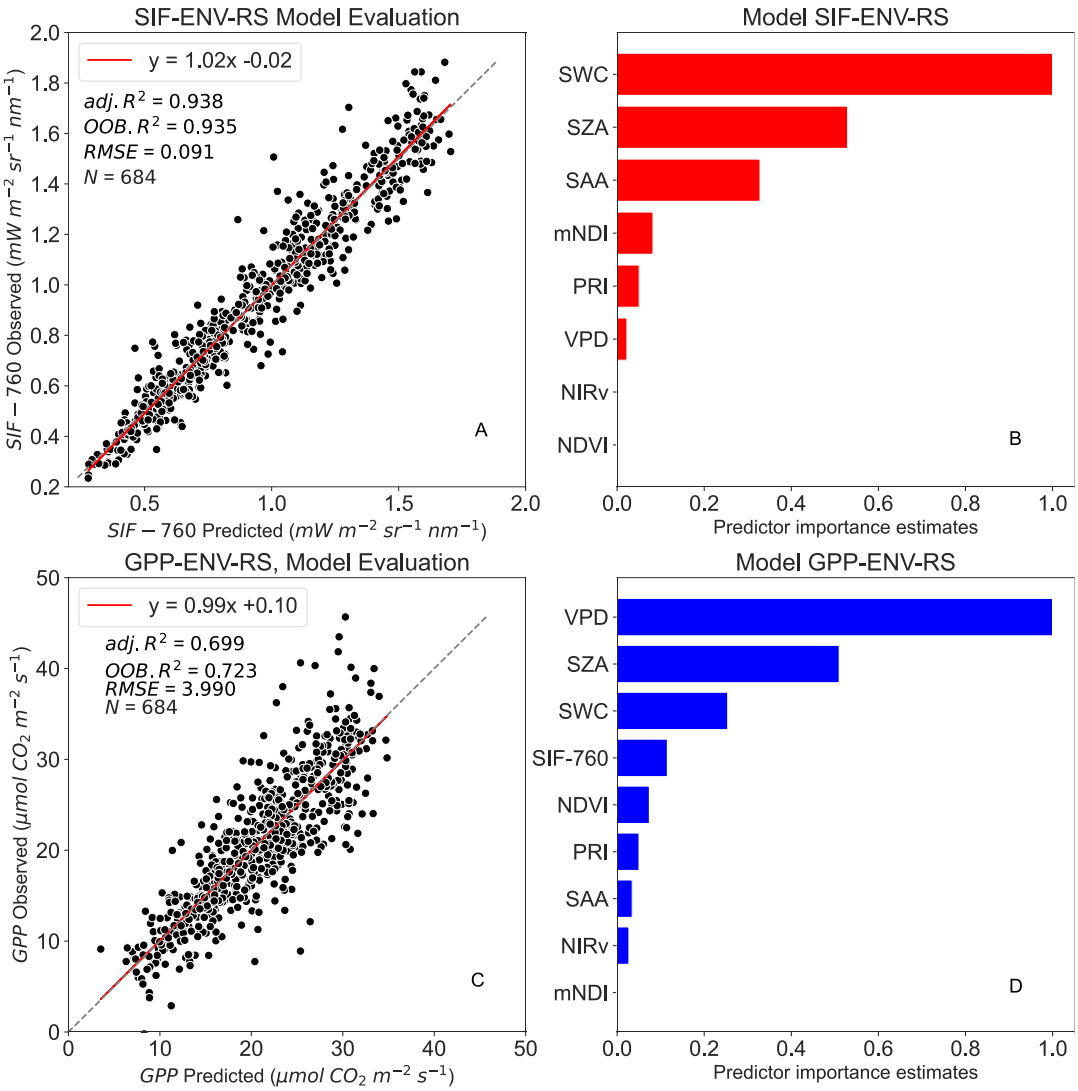

Figure 5.5. Figure 5.5A presents SIF-ENV-RS model performance between observed and predicted SIF (SIF-760), Figure 5.5B shows predictor importance estimates for SIF-ENV-RS model, Figure 5.5C presents GPP-ENV-RS model performance between observed and predicted GPP, Figure 5.5D shows predictor importance estimates for GPP-ENV-RS model. N denotes the number of observations used for the RF model evaluation, adj. R^2 represents the adjusted coefficient of determination of the relationship between test data and predicted SIF or GPP, OOB R^2 is the model accuracy on the validation data, and the RMSE is the root mean square error between observed SIF or GPP and RF model predicted SIF or GPP. The dashed diagonal line depicts the 1:1 line. Data at half-hourly timescale on only sunny days were used.

The results in Figure 5.6 reveal a monotonic positive relationship between SIF and low values of SWC (SWC < 0.3 $cm^3\ cm^{-3}$) and a saturation pattern at high SWC values (SWC > 0.3 $cm^3\ cm^{-3}$). The relationship between SIF and SAA is also positive for values of SAA < 200 degrees. For values of SAA between 200 and 250 degrees, the relation SIF-SAA slightly saturates, and afterward it becomes negative. SZA and VPD are negatively related to SIF, but note that SIF saturates for VPD > 2 kPa and for SZA > 60 degrees. The relationships between

SIF and PRI and between SIF and mNDI are first positive, but remain constant and afterward become negative at high values of PRI (PRI> -0.05) and mNDI (mNDI > 0.70); the response of mNDI is faster than the PRI one. The other variables (NDVI and NIR_v) have insignificant effects on the SIF variations.

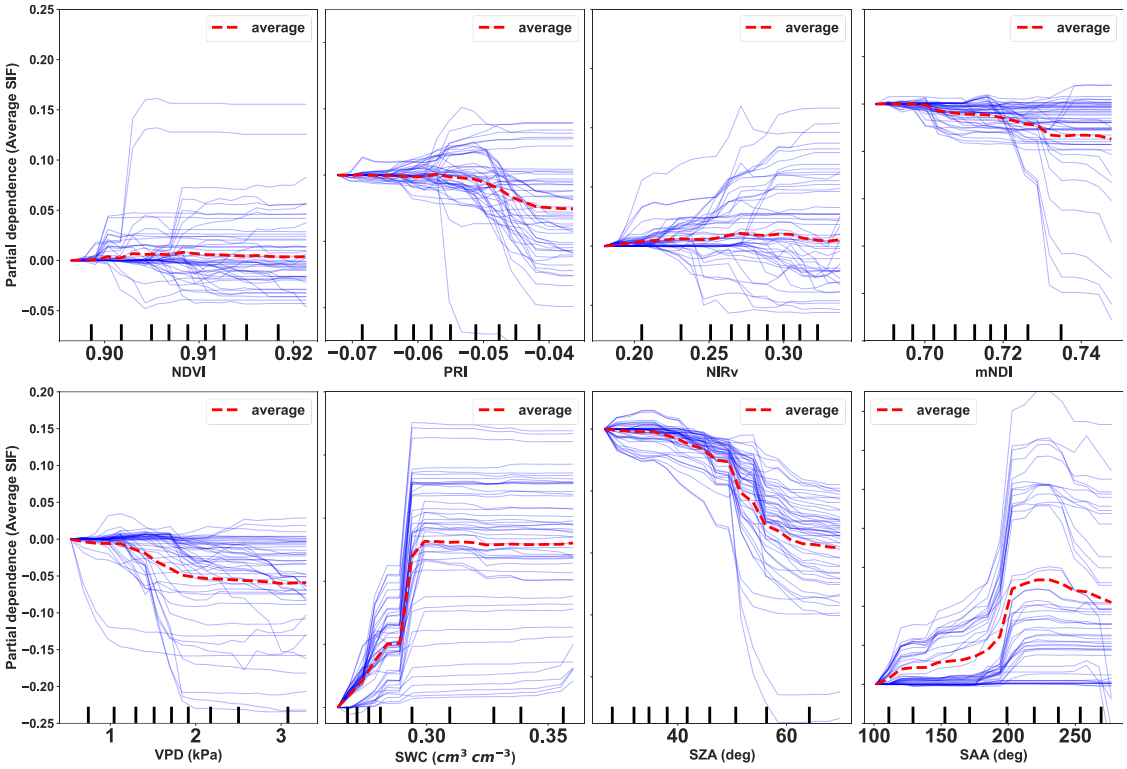

Figure 5.6. Partial dependence describing the marginal effect of each variable on far-red SIF variations under clear sky days at half-hourly timescale.

The results in Figure 5.7 show that NDVI, mNDI, PRI, SIF, and SWC have a positive relationship with GPP, but with a saturation pattern at high values, typically for NDVI > 0.915, mNDI > 0.72, PRI > -0.042, SIF > 1 mW m^{-2} sr^{-1} nm^{-1}, and SWC > 0.33 cm^3 cm^{-3}. The relations between GPP and NIR_v are positive and present high variabilities. The relationships between GPP and VPD, between GPP and SZA and between GPP and SAA are strongly negative. However, these correlations show strong variability for VPD > 2.5 kPa and SZA >50 degrees. The wide range of the partial dependence values for VPD >2.5 kPa suggests that VPD significantly impacts GPP variations.

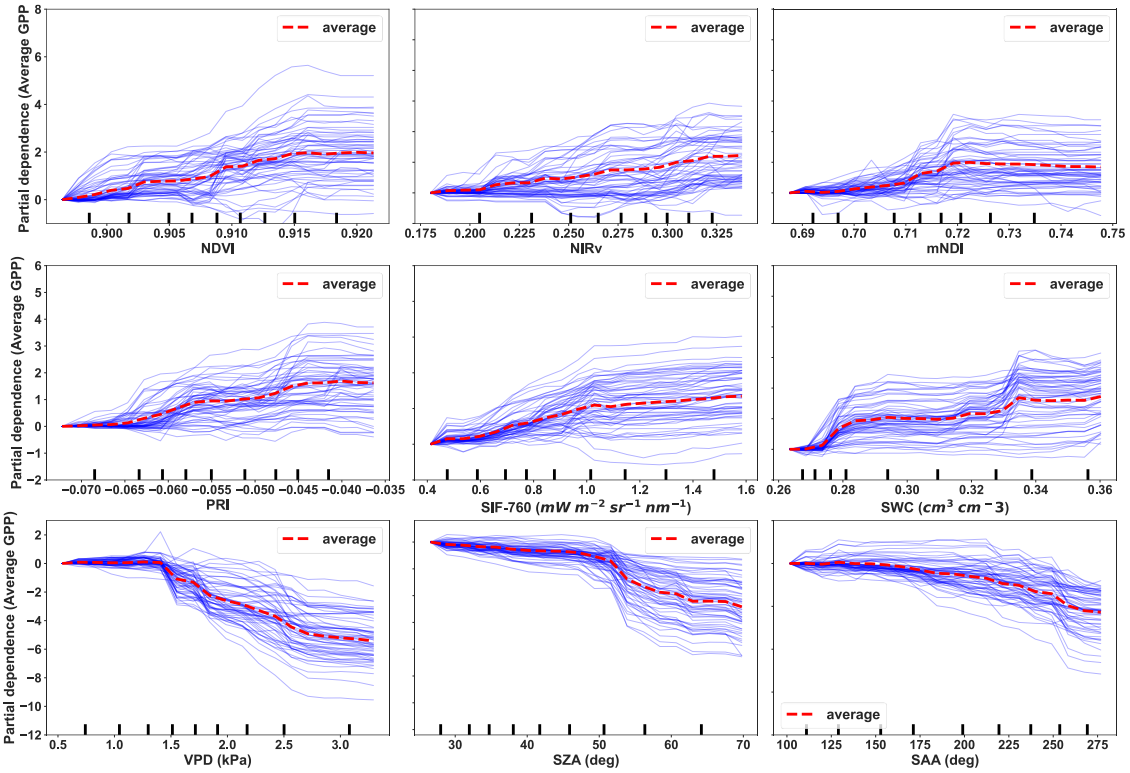

Figure 5.7. Partial dependence describing the marginal effect of each variable on GPP variations under only sunny days at half-hourly timescale.

5.5. Discussion

The results highlight that the seasonal patterns of SIF and GPP are similar (Figure 5.1), indicating that the temporal changes of both SIF and GPP are primarily driven by the seasonal changes in canopy structure and radiation conditions. Variations in vertical distribution of LAI, leaf angle distribution and clumping, and light intensity strongly determine the amount of absorbed photosynthetically active radiation (APAR). The seasonal changes also affect leaf biochemical properties and the distribution of sunlit and shaded leaves from which SIF and GPP depend on (Lu et al., 2020; Zhang et al., 2023). Besides, leaf physiology and abiotic factors (mainly leaf canopy temperature, VPD, and SWC) considerably affected the seasonal dynamics in $F_{yieldLIF}$ and SIF_y, and consequently the dynamics of SIF and GPP. These results are consistent with previous studies at both leaf and canopy scales (Lu et al. 2020; Kováč et al. 2022; Hu et al. 2023). The analyses in Figure 5.1 also demonstrated that seasonal changes in PRI and NIR_v were consistent with the dynamics of NDVI and mNDI throughout the season, indicating their dependence on leaf phenological, structural, and biochemical properties. Note that short-terms variations in PRI and NIR_v were greater than those in NDVI and mNDI, suggesting that these

indices are relatively independent. In fact, day-to-day variations in PRI may be related to the activity of xanthophyll cycle and to fluctuations in light intensity and leaf chlorophyll content as it has been shown in previous studies (Hmimina et al. 2014; Soudani et al. 2014; Sukhova et al. 2022). However, the seasonal dynamic in NIR_v is substantially affected by canopy structure and sun-canopy geometry changes that determine the fraction of sunlit and shaded leaves (Zhang et al. 2022; Zeng et al. 2022). Finally, during the extreme weather conditions (heatwaves in 2022 in: mid-June (DOY: 166-169), mid-July (DOY: 196-199), and early August (DOY: 218-224), we observed that SIF and VIs (NDVI, NIRv, mNDI, and PRI) and SIF and PAR are uncorrelated, while both GPP and SIF strongly decreased. This indicates that SIF can capture the vegetation functioning activity and VIs cannot be used to track changes in vegetation physiology during severe abiotic conditions. This specific response of SIF compared to VIs underlined the interest of SIF to track GPP under severe abiotic conditions. Note that $F_{yieldLIF}$ and SIFy also significantly dropped during the heatwaves periods, underlining the ability of FyieldLIF and SIF to reflect variations in vegetation physiology functioning under extreme weather conditions.

At the half-hourly temporal resolution, when SIF and GPP were considerably affected by variations in PAR (Figure 5.2), the relationship between GPP and SIF was strongly non-linear. This result suggests that the chlorophyll fluorescence does not linearly co-vary with photosynthesis because GPP saturates at a high PAR, while fluorescence continues to increase with PAR, which is consistent with several previous studies (Helm et al. 2020; Cheng et al. 2022; Sun et al. 2023b). This study also underlines that the hyperbolic relations between GPP and SIF was better on cloudy days ($R^2 = 0.66$) than on sunny days ($R^2 = 0.59$), indicating that light intermittence within and over the canopy and sun-canopy geometry significantly affected the link between GPP and SIF. These findings are in good agreement with previous studies in cork oak forest (Cheng et al. 2022). Clouds may reduce the total sun radiation received over the canopy and increase the diffuse radiations. Canopy SIF is mainly affected by direct radiation and is less impacted by diffuse radiation than GPP. Further, diffuse radiations can penetrate deeper in the canopy, presumably inducing more SIF emission due to exciting shaded leaves emission's and greatly reducing sun-canopy geometry effects. However, under high light intensity, which is clearly more frequent on sunny days, the excess absorbed light is dissipated as heat inducing both a decrease in the photosynthetic activity and the SIF emission. This is because when light intensity increases, the carbon assimilation and the electron transport chain

gradually become light saturated (Porcar-Castell et al. 2014). This explains why the link between GPP and SIF at satellite overpass times evidenced that GPP and SIF were hyperbolically more related in the afternoon (13H30 pm) than in the morning (10H30 am) (Figure 5.4). Further, under changing high radiation conditions, GPP is substantially sensitive to circadian rhythms, meaning that photosynthesis light saturation is more important in the afternoon than in the morning (Li et al., 2023).

If the light saturation of GPP is the primary widely known driver in the discrepancy between GPP and SIF, there are other ecosystems and abiotic stressors that vary intra-daily, daily, and seasonally. These stressors may have significant effects on fluorescence efficiency and vegetation photosynthesis activity and consequently they can affect the relationship between GPP and SIF. Thus, the results presented here (Figures 5.2, 5.3 and 5.5) evidenced that canopy temperature (Tc), soil water content, vapor pressure deficit, and sun-canopy geometry (SZA and SAA) are all influencing GPP and SIF and therefore may be responsible for intra-daily and seasonal divergence in the GPP and SIF relation. More specifically, strong discrepancies between GPP and SIF were associated with high PAR, Tc, and VPD (Figures 5.2 and 5.3). Those variables are regulated by the light intensity and the environmental conditions. Previous studies have also identified PAR and VPD as other potential causes for the non-linearity between GPP and SIF (Kim et al. 2021; Hu et al. 2023). In addition, abiotic stressors can impact SIF and GPP at several levels. First, the amount of light energy absorbed by the leaves can be strongly altered by high light intensity. The latter can affect the amount of SIF emitted and hence the relations between GPP and SIF. Second, the abiotic stressors can also affect the light partitioning in the chlorophyll molecules, leading to NPQ activation. VPD as a proxy of air temperature and relative humidity is associated with the variations in fAPAR and in the fraction of chlorophyll fluorescence that escaped (Li et al. 2023). Further, VPD is an indicator of atmospheric water demand and in this study VPD reached values that corresponded to severe air drought. VPD can affect stomatal closure. Stomatal closure can lead to decrease in plant water use efficiency and can prevent carbon assimilation by inhibiting the electron transport chain activity (Jonard et al. 2020; Magney et al., 2020), affecting hence photosynthesis and fluorescence emission and consequently the relationship between GPP and SIF (Figures 5.3 and 5.5). This behavior was observed in our results (Figures 5.2, 5.3 and 5.5). Previous research has also demonstrated that the influence of the VPD on the SIF-GPP relationship had a critical effect (Cheng et al. 2022). More specifically, we observed that a high VPD had a negative effect

on GPP and SIF (Figures 5.6 and 5.7). The same was also observed with high SZA. SZA can change the fraction of sunlit and shaded leaves, thus varying the canopy optical properties, which subsequently affect GPP and SIF. We also observed that both GPP and SIF saturate or decrease at high SWC, SAA, PRI and mNDI (Figures 5.6 and 5.7). One possible explanation is that both SIF and GPP are controlled by leaf physiology, leaf chlorophyll content, and the vegetation status under changing light conditions. The SWC is an indicator of plant water stress that also affects stomatal closure and hence the light reaction of photosynthesis and the fluorescence. The SWC was shown to have fluctuating responses to SIF and GPP in cork oak and poplar trees (Cheng et al. 2022), suggesting the response of GPP and SIF to SWC may be vegetation type-specific. The slight decrease of SIF at a high value of PRI and mNDI can be a consequence of NPQ and of the leaf chlorophyll fluorescence reabsorption, indicating that PRI could reflect the role of NPQ on sunny days. Whereas, the saturation of GPP with increasing PRI and mNDI is associated with the saturation of carbon assimilation in leaves under high light intensity. Therefore, this study supports that field measurements of remote sensing metrics, ecosystems and abiotic variables are needed to better understand the dynamics of GPP and SIF and their relationship.

5.6. Conclusion

In this study, the concomitant and continuous measurements of Sun-Induced chlorophyll Fluorescence (SIF), Gross Primary Production (GPP), reflectance-based vegetation indices (VIs), and abiotic variables of a sessile oak canopy allowed to analyse the main drivers of SIF and GPP variations. On one hand, the seasonal variations in SIF, GPP, VIs, and some abiotic variables (including PAR, air and canopy temperature, soil water content and vapor pressure deficit) were examined, and on the other hand, the relationship between GPP and SIF was evaluated considering different temporal resolutions. Further, random forest (RF) models were also used to not only predict SIF and GPP, but also to analyse the responses of SIF and GPP to abiotic drivers.

The results showed that both SIF and GPP had similar seasonal patterns, which were primarily controlled by the vegetation phenology that drives canopy structure and leaf biochemical and physiological attributes and diurnal and seasonal changes of incoming solar radiation. The analyses also demonstrated that the light saturation of the relationship between

GPP and SIF was not only dependent on PAR, but also on the fraction of diffuse to total PAR and on other abiotic variables such as VPD, SWC, and canopy temperature. The other key finding was that sun zenith and azimuth angles had strong and inverse effects on GPP and SIF, suggesting that sun-canopy geometry effects impact heavily the relationship between GPP and SIF. This last result may be specific to our study site consisting of a mature forest with an understorey, but it clearly highlights that the use of passive SIF measurements acquired at the canopy scale with a narrow field of view must be conducted with great care, as the measurements are strongly impacted by the distribution of sunlit and shaded leaves at the top of the canopy. Using passive in situ SIF measurements to validate satellite measurements at coarse spatial and temporal resolutions can therefore be very difficult, since obtained results will not be reproducible from one site to another, particularly in forest canopies where the structure is highly heterogeneous. Alternative solutions based on active measurements of SIF at canopy scale, or airborne measurements that take account of canopy heterogeneity, need to be considered.

6. Chapter 6: General conclusions, discussion, and perspectives

6.1. Synergy between TROPOMI SIF, R MODIS, and tower-based GPP

SIF is a faint radiation re-emitted by the vegetation chlorophyll pigments and its detection has emerged as a promising tool for monitoring vegetation carbon uptake via photosynthesis (Frankenberg and Berry, 2018; Porcar-Castell et al., 2021). Over coarse spatial and temporal scales, the emitted chlorophyll fluorescence and photosynthesis co-vary, leading to a strong correlation between GPP and SIF, as the absorbed PAR becomes the main driver of GPP and SIF (Guanter et al., 2012; Li and Xiao, 2022; Sun et al., 2023). Yet, earlier studies on GPP and SIF made at broad spatial and temporal scales evidenced that the relations between tower-based GPP and satellite SIF data depend on vegetation types (Damm et al., 2015; Balde et al., 2023), photosynthetic pathways (He et al., 2020), as well as on abiotic conditions (Verma et al., 2017; Li et al., 2018; Paul-Limoges et al., 2018).

Therefore, spatial and temporal variations in SIF and its relationship to GPP as functions of plant functional types (PFTs) and spatial and temporal scales still remain a poorly documented area of research. To make our contribution to this scientific question, we first investigated in Chapter 3 the strength and the nature of the links between SIF at coarse spatial resolution based on sentinel-5P (TROPOMI mission) and GPP from ground-based measurements at forty ICOS flux sites spanning different PFTs. We also highlighted the synergy between SIF, spectral reflectance (MODIS Aqua and Terra), and vegetation indices (VIs) such as PRI, NDVI and NIR_v for GPP predictions using data-driven Random Forest (RF) methods. The results evidenced that the strength and the nature of the relationships between GPP and SIF depend on site and vegetation type, which is consistent with the previous studies. The parameters of SIF and GPP regressions appear to be site-dependent, most likely reflecting the spatial and temporal heterogeneity of the vegetation cover and environmental conditions of the TROPOMI pixel, as well as differences in vegetation types. This also highlights the strong influence of the seasonal cycle of structural and biochemical properties of the canopy and the seasonal cycle of solar radiation, which all vary across different vegetation types (Tagliabue et al., 2019; Cho et al., 2021; Zhang et al., 2023a).

Further, the RF models established using remote sensing observations as inputs explained more than 80% of tower-based GPP inter-daily variations. However, we observed that daily surface spectral reflectance at different bands of MODIS sensor when taken as a whole outperformed daily TROPOMI SIF in predicting GPP. These reflectances include the reflectance in the red, the far-red and the NIR bands. Reflectance in the red, the far-red and the NIR bands are widely used for characterizing variations in canopy structure and in vegetation biochemical properties such as leaf area index and chlorophyll pigments content (Noda et al., 2021). These vegetation attributes, as well as the solar radiation, follow a seasonal cycle and explain to a large extent the observed correlation between reflectance and GPP at the seasonal scale. In addition, the strong contribution of the spectral reflectance in the inter-daily variations in GPP highlights that at these temporal and spatial scales, the interest of SIF as a proxy of GPP remains limited, compared to the reflectance. However, analysis of the relative importance of variables in the RF model using SIF and VIs (NDVI, PRI and NIR_v) as inputs to predict GPP shows that SIF is the most important variable for predicting GPP. It can be noted that this RF model using SIF combined with VIs (without adding reflectances as explanatory variables) resulted in good GPP prediction ($R^2 = 0.75$). This suggests that SIF is an integrating variable that can include the effects of the factors contained in the reflectances in the different bands. Remotely-sensed SIF observations alone are therefore capable of reproducing phenological cycle of the absorbed radiation (resulting from the seasonal cycle of "green" canopy and solar radiation) and presumably physiological responses (Zhang et al., 2023; Zhang et al., 2023), but the latter are difficult to evidence at broad spatial and temporal scales (Magney et al., 2020). This result also indicates that at a broad spatial scale, surface spectral reflectances could be used for estimating GPP and the use of SIF as a proxy of GPP raises question of whether the physiological information directly related to photosynthetic activity contained in SIF could be detected at this scale. With the upcoming satellite Fluorescence Explorer mission (FLEX), which will be launched in 2025 by ESA (Drusch et al., 2017) and which aims to measure fluorescence at a spatial resolution of 300 m, this result also raises the question about the "added value" of FLEX for GPP estimation compared with the current satellites such as TROPOMI. However, this result should not be misinterpreted because the spatial mismatch between the tower-based GPP footprints (around 300 m) and the TROPOMI SIF pixel size (7 km x 3.5 km) could limit the ability of TROPOMI SIF to capture any subtle variations in GPP linked to very local abiotic constraints such as water stress, which depends on local soil conditions. It should be noted that soil properties can vary greatly even at the scale of a few hundred m^2, particularly

in forests. The strong GPP and SIF relationship observed despite this mismatch implies that at a broad spatial scale: i) these relationships are explained by canopy phenological changes, as well as by the seasonal cycle of solar radiation and ii) the physiological information linked to abiotic conditions contained on the SIF signal is very subtle, and may be masked by temporal changes in canopy properties and rapid changes in abiotic factors such as solar irradiance and air temperature (Zhang et al., 2023; Wang et al., 2023). However, at fine spatial and temporal scales, the GPP and SIF link is not easy to establish because at these scales other factors can intervene and can cause high signal changes and consequently can lead to divergence between GPP and SIF (Kim et al., 2021). This high variability raises other questions about the exploitation of SIF signal as a proxy of the ecophysiological functioning of the vegetation cover in response to variations in abiotic conditions (Paul-Limoges et al., 2018; Magney et al., 2019; Sun et al., 2023a).

6.2. Effects of canopy structure on SIF and links between SIF_y and $F_{yieldLIF}$

The conclusions based on Chapter 3 allowed us to show that it is difficult to determine the most important factors and mechanisms explaining the wide variability in the relationship between GPP and SIF at the spatial and temporal scale of TROPOMI SIF (Sentinel-5P mission, daily 5-7 km / 3.5-14 km pixel size). In order to understand changes in the relationships between GPP and SIF regarding the temporal timescale, we have carried out continuous and simultaneous measurements of chlorophyll fluorescence at the canopy scale based on two techniques, one passive (SIF) and the other active ($F_{yieldLIF}$, using modulated excitation which allows the measurements of the chlorophyll fluorescence yield), GPP, and environmental variables in Fontainebleau-Barbeau in 2022.

How to disentangle the confounding factors, including canopy structure, fluctuations in solar radiation and canopy physiology information contained in the SIF signal is an important research question that hinders the use of SIF to probe photosynthetic activity and detect water stress/drought at the canopy scale and beyond (Wang et al., 2023; Kimm et al., 2021; Berger et al., 2022). Active chlorophyll fluorescence measurements ($F_{yieldLIF}$), which directly measures the apparent fluorescence yield, have been widely used to detect physiological variation of the vegetation at leaf scale (Porcar-Castell et al., 2021; Yang et al., 2021). Recently, the measurement of $F_{yieldLIF}$ has become feasible at the canopy scale (Loayza et al., 2023; Moya et

al., 2019), opening up new opportunities to decouple structural, biochemical, and physiological components of SIF at the canopy scale.

In Chapter 4, based on top-of-canopy measurements above a mature deciduous forest in Fontainebleau-Barbeau of reflectance (R), SIF, SIF normalized by incoming photosynthetically active radiation (SIF_y), $F_{yieldLIF}$, and the ratio between SIF_y and $F_{yieldLIF}$ (named Φ_k), we studied the effects of canopy structure and shadows on the diurnal and seasonal dynamics of SIF and proposed a method to predict $F_{yieldLIF}$ and Φ_k using RF models. Our analyses show that active $F_{yieldLIF}$ was not correlated with passive SIF_y at the diurnal timescale due to sun-canopy geometry effects. We also observed that the diurnal patterns in SIF and PAR did not match under clear sky conditions, underlining the effects of shadows on the measured canopy SIF signal in the Fontainebleau-Barbeau forest. The dynamics of the sunlit and shaded areas were characterized using continuous RGB images measurements in the field-of-view (FOV) of SIF measurements. This may explain the absence of correlation observed between SIF or SIF_y and $F_{yieldLIF}$. Further, as SIF_y was estimated from normalization by incident PAR, and not from normalization by the radiation absorbed by green vegetation elements, SIF_y does not consider the conditions of radiation extinction by the canopy. Indeed, the incident PAR measured above the canopy does not reflect what is happening locally at the upper layers of the canopies (cast shadows caused by high roughness of the top of the canopy) and within the canopy (distribution of gaps and clumping effects). Therefore, the high complexity of interactions between canopy structure and solar radiation can strongly blur the information on the physiological functioning of the canopy provided by SIF_y. For this reason, the development of new methods and models are warranted to better explore the possibility to use SIF as a proxy for vegetation functioning at high temporal frequency (intra-daily), especially when the vegetation structure is complex and heterogeneous such as in forest stands.

A novel remote sensing indicator, Φ_k, which is the ratio between SIF_y and $F_{yieldLIF}$, was introduced to characterize the effects of canopy structure and sun-canopy geometry interactions. SIF_y and $F_{yieldLIF}$ correspond to the chlorophyll fluorescence yield from passive and active measurements, respectively (the active measurement being considered as the "true" measure of canopy fluorescence yield). Therefore, changes in Φ_k used here reflect the effects of exogenous confounding factors that cause variations of the "apparent" fluorescence yield (SIF_y), while the "true" fluorescence yield related to photosynthetic functioning remains unchanged.

Φ_k diurnal pattern follows the pattern of the distribution of light and shadow spots. The latters were assessed from the RGB images of the FOV of SIF3, through the temporal variations

of reflectance in the near-infrared bands and of NIR_v, and from statistical analysis of the importance of the variable used in the random forest model (RF, Φ_k-R-SA). The results underlined that Φ_k was sensitive to the sun-canopy geometry and to the distribution of sunlit and shaded leaves on the upper canopy layers. RF regressions show that in addition to the significant effects of solar angle, Φ_k is also an indicator of local illumination conditions in the FOV, since Φ_k is strongly correlated to surface reflectance in different bands used as explanatory variables in the RF model (Φ_k-R). The spectral reflectances used are not corrected for Bidirectional Reflectance Distribution Function (BRDF) effects, therefore they contain useful information to improve the predictive power of SIF. This result, even if not for the same reasons, confirms the importance of using SIF and reflectance synergy in GPP prediction models.

$F_{yieldLIF}$ was more sensitive to surface reflectance and radiation than SIF and SIF_y, corroborating our previous conclusions based on TROPOMI and MODIS satellite measurements across the ICOS carbon flux sites. However, note that the contribution of SIF or SIF_y is important compared to each reflectance band taken individually, but the combined effect of reflectance bands could mitigate or hide the use of SIF as a vegetation physiological proxy. Therefore, in order to disentangle the structural and physiological information contained in SIF and to use SIF as a proxy of photosynthetic carbon uptake at the ecosystem scale, the synergy between SIF and reflectance at the canopy scale needs to be studied in other vegetation types and with different canopy structures.

In this chapter, we mainly highlighted the complexity of interpreting diurnal variations of SIF in forest canopies because in this type of ecosystems, SIF measurements are highly dependent on the complex interactions between the canopy properties (structure and biochemical properties), solar illumination geometry (SZA and SAA) and light (ratio of diffuse to direct solar radiation) conditions. However, how abiotic conditions and canopy structure at the seasonal scale, and specifically under various stress conditions affect SIF and GPP and their relationships is an active area of research that we addressed in the next chapter.

6.3. Abiotic variables effects on SIF and GPP variations and on their relationships

Airborne, drone and tower-based SIF data have shed light on what drives SIF at the canopy scale and illuminated the mechanisms affecting the relationship between GPP and SIF. Previous studies showed that SIF is able to track GPP across both diurnal and seasonal timescales (Yang et al., 2015; Goulas et al., 2017 ; Rossini et al., 2015 ; Lu et al., 2020 ; Campbell et al., 2019 ; Rascher et al., 2015). SIF has also been used to detect early stress due to its link with the photosynthetic activity (Ač et al., 2015; Jonard et al., 2020; Berger et al., 2022). SIF has been used to understand the correlations between vegetation carbon assimilation and energy dissipation variations under light stress (Miao et al., 2018; Kim et al., 2021), cold-stress (Magney et al., 2019; Pierrat et al., 2022), and between vegetation carbon assimilation and induced stomatal closure (Marrs et al., 2020). SIF was able to identify divergence between SIF and GPP during periods of heat-stress (Wieneke et al., 2018; Wohlfahrt et al., 2018; Martini et al., 2022), and during periods of drought or water-stress (De Cannière et al., 2022; Pinto et al., 2020). Because of its sensitivity to the light reactions of photosynthesis, SIF has the potential to be used in estimating and modeling transpiration (Damm et al., 2021; Maes et al., 2020; Lu et al., 2018) and as an alternative to partition Net Ecosystem Exchange (NEE) into GPP and Ecosystem Respiration (Kira et al., 2021;(Zhan et al., 2022).

Therefore, the use of SIF to probe variations in GPP in forests is challenged by confounding factors such as canopy physiological, canopy structural and canopy biochemical properties, along with abiotic conditions. The results presented in Chapter 5 also showed that the tower-based SIF data measured in Fontainebleau-Barbeau during the 2022 growing season tracked the variations in GPP. The strength and the nature of the relations between GPP and SIF were dependent on the temporal scale considered.

At the seasonal scale, we observed that the trees' phenological dynamics, solar radiation, and other abiotic factors such as atmospheric vapor pressure deficit (VPD) and soil water content (SWC) control the relationship between GPP and SIF. More, specifically, we observed that the seasonal dynamics in GPP, SIF, $F_{yieldLIF}$ and SIF_y responded to the leaf physiology and to the fluctuation in abiotic conditions, specifically during the heatwaves in the summer 2022. During the extreme weather conditions (heatwaves in 2022 in Barbeau in: mid-June (DOY: 166-169), mid-July (DOY: 196-199), and early August (DOY: 218-224), we observed that SIF and VIs (NDVI, NIRv, mNDI, and PRI) and SIF and PAR are uncorrelated, while GPP, SIF

and $F_{yieldLIF}$ strongly decreased. This indicates that SIF can capture the vegetation functioning activity, while VIs cannot be used to track changes in vegetation physiology during such severe abiotic conditions. This specific response of SIF and $F_{yieldLIF}$ compared to VIs underlined the interest of SIF to track GPP under severe abiotic conditions. Both VPD as an indicator of atmospheric water demand, and SWC as an indicator of plant water stress, can indicate stomatal closure. Stomatal closure can affect plant water use efficiency and prevent carbon uptake by blocking the electron transport chain and therefore affect the photosynthetic activity and chlorophyll fluorescence emission and hence affect the relations between GPP and SIF (Wu et al., 2022; Pierrat et al., 2022). However, further studies are warranted to better understand GPP, SIF and reflectance variations and correlations under severe abiotic conditions such as heatwaves. This is an ongoing work that we are currently performing.

In our studies, at the diurnal timescale, the interactions between the canopy structure and the sun-canopy geometry (solar zenith and azimuth angles) control the distribution of light and shadow spots. The SIF response at the infra-daily timescale suggests that SIF heavily depends on what is happening at the top of the canopy (Gu et al., 2019; Pierrat et al., 2022). Therefore, in forest canopies which can be highly heterogeneous the relations between GPP and SIF may be controlled by the canopy structure and the sun-canopy geometry effects at the diurnal timescale. Note that the estimated fluorescence yield (SIF_y) based on incident radiation measured above the canopy could not alleviate this issue because the radiation actually intercepted and absorbed by the canopy must be considered (Wang et al., 2023; Ač et al., 2015). This technical aspect should be taken into consideration when discussing the relevance of local measurements of SIF for calibrating/validating satellite measurements. This result also highlights that the use of passive SIF measurements acquired at the canopy scale with a narrow FOV must be conducted with great care, as the measurements are strongly impacted by the distribution of sunlit and shaded leaves at the top of the canopy. Using passive in-situ SIF measurements to validate satellite measurements at coarse spatial and temporal resolutions can therefore be very difficult, since obtained results will not be reproducible from one site to another, particularly in forest canopies. Therefore, alternative technical solutions based on active measurements of SIF at canopy scale or airborne measurements that take into account the canopy heterogeneity need to be considered in order to obtain reliable data to calibrate/validate satellite-based SIF products such as the future FLEX products.

Further, to better interpret SIF data, there is a critical need to gather detailed ancillary data. Top-of-canopy SIF variations cannot be directly interpreted as physiological changes

because of the confounding effects, which could be better disentangled by measuring visible and near-infrared hyperspectral reflectance data. Therefore, the analysis of the SIF and reflectance synergy to study the photosynthetic functioning of ecosystems requires further study, particularly at fine spatial and temporal scales under various environmental conditions and specifically in plant canopies characterized by complex structures.

Hyperspectral reflectance sensors detect the light reflected from the canopies within narrow wavelengths (Zeng et al., 2022). This information can be used to derive estimates of the escape ratio of canopy SIF (Yang et al., 2019; Zeng et al., 2019), of canopy pigment concentrations (Feng et al., 2008; Zeng et al., 2022), and other variables critical in regulating ecosystem functioning (including LAI, fAPAR and canopy water content) (Pasqualotto et al., 2018; le Maire et al., 2008). Further, active Light Detection and Ranging (LIDAR) data instead can be useful by providing an accurate representation of the spatial arrangement of canopy elements. This can be useful for assessing the horizontal and vertical distribution of sunlit and shaded leaves, as well as the leaf aggregation, which appear to play an important role in SIF variations and SIF and GPP relationships (Grotti et al., 2020; Song et al., 2021; Man et al., 2014). In addition, as the incident radiation is the primary driver of SIF, characterizing the light environment by precise measurements of incident, reflected and transmitted PAR (the prerequisite for an accurate estimate of the absorbed PAR) and using in-situ RGB camera images taken within the FOV of the canopy sensor (necessary to track temporal changes of the proportion of sunlit and shaded leaves) could give insight to better interpret the retrieved SIF at the canopy scale (Chen et al., 2020; Wu et al., 2020; Yang et al., 2021). The development and use of radiative transfer models where the 3D architecture of the vegetation is explicitly taken into account such as the Discrete Anisotropic Radiative Transfer (DART) model (Gastellu-Etchegorry et al., 2004; Regaieg et al., 2020), must inevitably be exploited to better understand the radiative transfer of chlorophyll fluorescence in plant canopies and for a better characterization of the fluorescence escape probability factor (f_{esc}) used in some equations of the SIF and GPP relationship as a first approximation of fluorescence attenuation in the canopy-sensor direction (Lu et al., 2020).

Co-located continuous active and passive measurements of canopy chlorophyll fluorescence could also provide additional insight into the physiological component of SIF (Chang et al., 2021; Helm et al., 2020; Martini et al., 2022; De Cannière et al., 2022). These data can be used to gather variables needed to establish SIF-driven mechanistic models of

photosynthesis at the ecosystem scale (Gu et al., 2019; Liu et al., 2022). Further, co-located continuous measurements of canopy SIF and canopy temperatures are more likely to improve evapotranspiration estimates at the ecosystem scale (Damm et al., 2021; Maes et al., 2020; Jonard et al., 2020) and hence to contribute to assess ecosystem water use and water stress. Therefore, future studies should look toward this direction. Finally, due to the multitude of confounding factors, the potential of SIF as a proxy for photosynthesis at the canopy scale and particularly under stress conditions in complex structures such as forests remains to be evaluated. Due to different sources of variations in the SIF signal and in GPP and SIF relationships (vegetation properties, biotic and abiotic conditions, spatial and temporal scales considered, instrumentation, SIF retrieval algorithms, etc.), there is an urgent need to develop a SIF and LIF measurement network according to standardized protocols and taking advantage of the carbon and water fluxes and ancillary data measurement networks where measurements are taken according to standardized protocols such as the ICOS ecosystem network.

References

References Chapter 1: Introduction

Badgley, G., Field, C. B., and Berry, J. A.: Canopy near-infrared reflectance and terrestrial photosynthesis, Science Advances, 3, e1602244, https://doi.org/10.1126/sciadv.1602244, 2017.

Baker, N. R.: Chlorophyll Fluorescence: A Probe of Photosynthesis In Vivo, Annual Review of Plant Biology, 59, 89–113, https://doi.org/10.1146/annurev.arplant.59.032607.092759, 2008.

Balde, H., Hmimina, G., Goulas, Y., Latouche, G., and Soudani, K.: Synergy between TROPOMI sun-induced chlorophyll fluorescence and MODIS spectral reflectance for understanding the dynamics of gross primary productivity at Integrated Carbon Observatory System (ICOS) ecosystem flux sites, Biogeosciences, 20, 1473–1490, https://doi.org/10.5194/bg-20-1473-2023, 2023.

Baldocchi, D.: Measuring fluxes of trace gases and energy between ecosystems and the atmosphere - the state and future of the eddy covariance method, Global Change Biology, 20, 3600–3609, https://doi.org/10.1111/gcb.12649, 2014.

Baldocchi, D., Chu, H., and Reichstein, M.: Inter-annual variability of net and gross ecosystem carbon fluxes: A review, Agricultural and Forest Meteorology, 249, 520–533, https://doi.org/10.1016/j.agrformet.2017.05.015, 2018.

Beer, C., Reichstein, M., Tomelleri, E., Ciais, P., Jung, M., Carvalhais, N., Rödenbeck, C., Arain, M. A., Baldocchi, D., Bonan, G. B., Bondeau, A., Cescatti, A., Lasslop, G., Lindroth, A., Lomas, M., Luyssaert, S., Margolis, H., Oleson, K. W., Roupsard, O., Veenendaal, E., Viovy, N., Williams, C., Woodward, F. I., and Papale, D.: Terrestrial Gross Carbon Dioxide Uptake: Global Distribution and Covariation with Climate, Science, 329, 834–838, https://doi.org/10.1126/science.1184984, 2010.

Bonannella, C., Hengl, T., Heisig, J., Parente, L., Wright, M. N., Herold, M., and de Bruin, S.: Forest tree species distribution for Europe 2000-2020: mapping potential and realized distributions using spatiotemporal Machine Learning, In Review, https://doi.org/10.21203/rs.3.rs-1252972/v1, 2022.

Burba, G.: Eddy covariance method for scientific, industrial, agricultural, and regulatory applications: a field book on measuring ecosystem gas exchange and areal emission rates, LI-COR Biosciences, Lincoln, Nebraska, 331 pp., 2013.

Cai, W. and Prentice, I. C.: Recent trends in gross primary production and their drivers: analysis and modelling at flux-site and global scales, Environ. Res. Lett., 15, 124050, https://doi.org/10.1088/1748-9326/abc64e, 2020.

Campbell, P., Huemmrich, K., Middleton, E., Ward, L., Julitta, T., Daughtry, C., Burkart, A., Russ, A., and Kustas, W.: Diurnal and Seasonal Variations in Chlorophyll Fluorescence Associated with Photosynthesis at Leaf and Canopy Scales, Remote Sensing, 11, 488, https://doi.org/10.3390/rs11050488, 2019.

Chen, J., Liu, X., Du, S., Ma, Y., and Liu, L.: Integrating SIF and Clearness Index to Improve Maize GPP Estimation Using Continuous Tower-Based Observations, Sensors, 20, 2493, https://doi.org/10.3390/s20092493, 2020.

Damm, A., Guanter, L., Paul-Limoges, E., van der Tol, C., Hueni, A., Buchmann, N., Eugster, W., Ammann, C., and Schaepman, M. E.: Far-red sun-induced chlorophyll fluorescence shows ecosystem-specific relationships to gross primary production: An assessment based on observational and modeling approaches, Remote Sensing of Environment, 166, 91–105, http://dx.doi.org/10.1016/j.rse.2015.06.004, 2015.

Dannenberg, M., Wang, X., Yan, D., and Smith, W.: Phenological Characteristics of Global Ecosystems Based on Optical, Fluorescence, and Microwave Remote Sensing, Remote Sensing, 12, 671, https://doi.org/10.3390/rs12040671, 2020.

Dechant, B., Ryu, Y., Badgley, G., Zeng, Y., Berry, J. A., Zhang, Y., Goulas, Y., Li, Z., Zhang, Q., Kang, M., Li, J., and Moya, I.: Canopy structure explains the relationship between photosynthesis and sun-induced chlorophyll fluorescence in crops, Remote Sensing of Environment, 241, 111733, https://doi.org/10.1016/j.rse.2020.111733, 2020.

Elders, A., Carroll, M. L., Neigh, C. S. R., D'Agostino, A. L., Ksoll, C., Wooten, M. R., and Brown, M. E.: Estimating crop type and yield of small holder fields in Burkina Faso using multi-day Sentinel-2, Remote Sensing Applications: Society and Environment, 27, 100820, https://doi.org/10.1016/j.rsase.2022.100820, 2022.

Falge, E., Baldocchi, D., Tenhunen, J., Aubinet, M., Bakwin, P., Berbigier, P., Bernhofer, C., Burba, G., Clement, R., Davis, K. J., Elbers, J. A., Goldstein, A. H., Grelle, A., Granier, A., Guðmundsson, J., Hollinger, D., Kowalski, A. S., Katul, G., Law, B. E., Malhi, Y., Meyers, T., Monson, R. K., Munger, J. W., Oechel, W., Paw U, K. T., Pilegaard, K., Rannik, Ü., Rebmann, C., Suyker, A., Valentini, R., Wilson, K., and Wofsy, S.: Seasonality of ecosystem respiration and gross primary production as derived from FLUXNET measurements, Agricultural and Forest Meteorology, 113, 53–74, https://doi.org/10.1016/S0168-1923(02)00102-8, 2002.

Farella, M. M., Fisher, J. B., Jiao, W., Key, K. B., and Barnes, M. L.: Thermal remote sensing for plant ecology from leaf to globe, Journal of Ecology, 110, 1996–2014, https://doi.org/10.1111/1365-2745.13957, 2022.

Frankenberg, C., Fisher, J. B., Worden, J., Badgley, G., Saatchi, S. S., Lee, J.-E., Toon, G. C., Butz, A., Jung, M., Kuze, A., and Yokota, T.: New global observations of the terrestrial carbon cycle from GOSAT: Patterns of plant fluorescence with gross primary productivity: CHLOROPHYLL FLUORESCENCE FROM SPACE, Geophysical Research Letters, 38, n/a-n/a, https://doi.org/10.1029/2011GL048738, 2011.

Friedlingstein, P., Jones, M. W., O'Sullivan, M., Andrew, R. M., Hauck, J., Peters, G. P., Peters, W., Pongratz, J., Sitch, S., Le Quéré, C., Bakker, D. C. E., Canadell, J. G., Ciais, P.,

Jackson, R. B., Anthoni, P., Barbero, L., Bastos, A., Bastrikov, V., Becker, M., Bopp, L., Buitenhuis, E., Chandra, N., Chevallier, F., Chini, L. P., Currie, K. I., Feely, R. A., Gehlen, M., Gilfillan, D., Gkritzalis, T., Goll, D. S., Gruber, N., Gutekunst, S., Harris, I., Haverd, V., Houghton, R. A., Hurtt, G., Ilyina, T., Jain, A. K., Joetzjer, E., Kaplan, J. O., Kato, E., Klein Goldewijk, K., Korsbakken, J. I., Landschützer, P., Lauvset, S. K., Lefèvre, N., Lenton, A., Lienert, S., Lombardozzi, D., Marland, G., McGuire, P. C., Melton, J. R., Metzl, N., Munro, D. R., Nabel, J. E. M. S., Nakaoka, S.-I., Neill, C., Omar, A. M., Ono, T., Peregon, A., Pierrot, D., Poulter, B., Rehder, G., Resplandy, L., Robertson, E., Rödenbeck, C., Séférian, R., Schwinger, J., Smith, N., Tans, P. P., Tian, H., Tilbrook, B., Tubiello, F. N., van der Werf, G. R., Wiltshire, A. J., and Zaehle, S.: Global Carbon Budget 2019, Earth System Science Data, 11, 1783–1838, https://doi.org/10.5194/essd-11-1783-2019, 2019.

Gamon, J. A. and Berry, J. A.: Facultative and constitutive pigment effects on the Photochemical Reflectance Index (PRI) in sun and shade conifer needles, Israel Journal of Plant Sciences, 60, 85–95, https://doi.org/10.1560/IJPS.60.1-2.85, 2012.

Gamon, J. A., Peñuelas, J., and Field, C. B.: A narrow-waveband spectral index that tracks diurnal changes in photosynthetic efficiency, Remote Sensing of Environment, 41, 35–44, https://doi.org/10.1016/0034-4257(92)90059-S, 1992.

Gitelson, A. A., Gamon, J. A., and Solovchenko, A.: Multiple drivers of seasonal change in PRI: Implications for photosynthesis 2. Stand level, Remote Sensing of Environment, 190, 198–206, https://doi.org/10.1016/j.rse.2016.12.015, 2017.

Guanter, L., Zhang, Y., Jung, M., Joiner, J., Voigt, M., Berry, J. A., Frankenberg, C., Huete, A. R., Zarco-Tejada, P., Lee, J.-E., Moran, M. S., Ponce-Campos, G., Beer, C., Camps-Valls, G., Buchmann, N., Gianelle, D., Klumpp, K., Cescatti, A., Baker, J. M., and Griffis, T. J.: Global and time-resolved monitoring of crop photosynthesis with chlorophyll fluorescence, Proceedings of the National Academy of Sciences, 111, E1327–E1333, https://doi.org/10.1073/pnas.1320008111, 2014.

Hall, F. G., Hilker, T., and Coops, N. C.: Data assimilation of photosynthetic light-use efficiency using multi-angular satellite data: I. Model formulation, Remote Sensing of Environment, 121, 301–308, 2012.

He, L., Magney, T., Dutta, D., Yin, Y., Köhler, P., Grossmann, K., Stutz, J., Dold, C., Hatfield, J., Guan, K., Peng, B., and Frankenberg, C.: From the Ground to Space: Using Solar-Induced Chlorophyll Fluorescence to Estimate Crop Productivity, Geophysical Research Letters, 47, https://doi.org/10.1029/2020GL087474, 2020.

He, M., Ju, W., Zhou, Y., Chen, J., He, H., Wang, S., Wang, H., Guan, D., Yan, J., Li, Y., Hao, Y., and Zhao, F.: Development of a two-leaf light use efficiency model for improving the calculation of terrestrial gross primary productivity, Agricultural and Forest Meteorology, 173, 28–39, https://doi.org/10.1016/j.agrformet.2013.01.003, 2013.

Hmimina, G., Dufrêne, E., and Soudani, K.: Relationship between photochemical reflectance index and leaf ecophysiological and biochemical parameters under two different water statuses: towards a rapid and efficient correction method using real-time measurements:

Disentangling PRI variability, Plant Cell Environ, 37, 473–487, https://doi.org/10.1111/pce.12171, 2014.

Hmimina, G., Merlier, E., Dufrêne, E., and Soudani, K.: Deconvolution of pigment and physiologically related photochemical reflectance index variability at the canopy scale over an entire growing season: Towards an understanding of canopy PRI variability, Plant Cell Environ, 38, 1578–1590, https://doi.org/10.1111/pce.12509, 2015.

Hornero, A., North, P. R. J., Zarco-Tejada, P. J., Rascher, U., Martín, M. P., Migliavacca, M., and Hernandez-Clemente, R.: Assessing the contribution of understory sun-induced chlorophyll fluorescence through 3-D radiative transfer modelling and field data, Remote Sensing of Environment, 253, 112195, https://doi.org/10.1016/j.rse.2020.112195, 2021.

Huete, A., Didan, K., Miura, T., Rodriguez, E. P., Gao, X., and Ferreira, L. G.: Overview of the radiometric and biophysical performance of the MODIS vegetation indices, Remote Sensing of Environment, 83, 195–213, https://doi.org/10.1016/S0034-4257(02)00096-2, 2002.

Joiner, J., Yoshida, Y., Vasilkov, A. P., Yoshida, Y., Corp, L. A., and Middleton, E. M.: First observations of global and seasonal terrestrial chlorophyll fluorescence from space, Biogeosciences, 8, 637–651, https://doi.org/10.5194/bg-8-637-2011, 2011.

Jonard, F., De Cannière, S., Brüggemann, N., Gentine, P., Short Gianotti, D. J., Lobet, G., Miralles, D. G., Montzka, C., Pagán, B. R., Rascher, U., and Vereecken, H.: Value of sun-induced chlorophyll fluorescence for quantifying hydrological states and fluxes: Current status and challenges, Agricultural and Forest Meteorology, 291, 108088, https://doi.org/10.1016/j.agrformet.2020.108088, 2020.

Jung, M., Koirala, S., Weber, U., Ichii, K., Gans, F., Camps-Valls, G., Papale, D., Schwalm, C., Tramontana, G., and Reichstein, M.: The FLUXCOM ensemble of global land-atmosphere energy fluxes, Sci Data, 6, 74, https://doi.org/10.1038/s41597-019-0076-8, 2019.

Jung, M., Schwalm, C., Migliavacca, M., Walther, S., Camps-Valls, G., Koirala, S., Anthoni, P., Besnard, S., Bodesheim, P., Carvalhais, N., Chevallier, F., Gans, F., Goll, D. S., Haverd, V., Köhler, P., Ichii, K., Jain, A. K., Liu, J., Lombardozzi, D., Nabel, J. E. M. S., Nelson, J. A., O'Sullivan, M., Pallandt, M., Papale, D., Peters, W., Pongratz, J., Rödenbeck, C., Sitch, S., Tramontana, G., Walker, A., Weber, U., and Reichstein, M.: Scaling carbon fluxes from eddy covariance sites to globe: synthesis and evaluation of the FLUXCOM approach, Biogeosciences, 17, 1343–1365, https://doi.org/10.5194/bg-17-1343-2020, 2020.

Kim, J., Ryu, Y., Dechant, B., Lee, H., Kim, H. S., Kornfeld, A., and Berry, J. A.: Solar-induced chlorophyll fluorescence is non-linearly related to canopy photosynthesis in a temperate evergreen needleleaf forest during the fall transition, Remote Sensing of Environment, 258, 112362, https://doi.org/10.1016/j.rse.2021.112362, 2021.

Lee, L. X., Whitby, T. G., Munger, J. W., Stonebrook, S. J., and Friedl, M. A.: Remote sensing of seasonal variation of LAI and fAPAR in a deciduous broadleaf forest, Agricultural

and Forest Meteorology, 333, 109389, https://doi.org/10.1016/j.agrformet.2023.109389, 2023.

Leroux, L., Congedo, L., Bellón, B., Gaetano, R., and Bégué, A.: Land Cover Mapping Using Sentinel-2 Images and the Semi-Automatic Classification Plugin: A Northern Burkina Faso Case Study, in: QGIS and Applications in Agriculture and Forest, John Wiley & Sons, Ltd, 119–151, https://doi.org/10.1002/9781119457107.ch4, 2018.

Li, X., Xiao, J., He, B., Altaf Arain, M., Beringer, J., Desai, A. R., Emmel, C., Hollinger, D. Y., Krasnova, A., Mammarella, I., Noe, S. M., Ortiz, P. S., Rey-Sanchez, A. C., Rocha, A. V., and Varlagin, A.: Solar-induced chlorophyll fluorescence is strongly correlated with terrestrial photosynthesis for a wide variety of biomes: First global analysis based on OCO-2 and flux tower observations, Global Change Biology, 24, 3990–4008, https://doi.org/10.1111/gcb.14297, 2018.

Li, Z., Zhang, Q., Li, J., Yang, X., Wu, Y., Zhang, Z., Wang, S., Wang, H., and Zhang, Y.: Solar-induced chlorophyll fluorescence and its link to canopy photosynthesis in maize from continuous ground measurements, Remote Sensing of Environment, 236, 111420, https://doi.org/10.1016/j.rse.2019.111420, 2020.

Liao, Z., Zhou, B., Zhu, J., Jia, H., and Fei, X.: A critical review of methods, principles and progress for estimating the gross primary productivity of terrestrial ecosystems, Frontiers in Environmental Science, 11, 2023.

Liu, L., Guan, L., and Liu, X.: Directly estimating diurnal changes in GPP for C3 and C4 crops using far-red sun-induced chlorophyll fluorescence, Agricultural and Forest Meteorology, 232, 1–9, https://doi.org/10.1016/j.agrformet.2016.06.014, 2017.

Louis, J., Ounis, A., Ducruet, J.-M., Evain, S., Laurila, T., Thum, T., Aurela, M., Wingsle, G., Alonso, L., Pedros, R., and Moya, I.: Remote sensing of sunlight-induced chlorophyll fluorescence and reflectance of Scots pine in the boreal forest during spring recovery, Remote Sensing of Environment, 96, 37–48, https://doi.org/10.1016/j.rse.2005.01.013, 2005.

Magney, T. S., Bowling, D. R., Logan, B. A., Grossmann, K., Stutz, J., Blanken, P. D., Burns, S. P., Cheng, R., Garcia, M. A., Köhler, P., Lopez, S., Parazoo, N. C., Raczka, B., Schimel, D., and Frankenberg, C.: Mechanistic evidence for tracking the seasonality of photosynthesis with solar-induced fluorescence, Proceedings of the National Academy of Sciences, 201900278, https://doi.org/10.1073/pnas.1900278116, 2019.

Marrs, J. K., Reblin, J. S., Logan, B. A., Allen, D. W., Reinmann, A. B., Bombard, D. M., Tabachnik, D., and Hutyra, L. R.: Solar-Induced Fluorescence Does Not Track Photosynthetic Carbon Assimilation Following Induced Stomatal Closure, Geophys. Res. Lett., 47, https://doi.org/10.1029/2020GL087956, 2020.

Martini, D., Sakowska, K., Wohlfahrt, G., Pacheco-Labrador, J., van der Tol, C., Porcar-Castell, A., Magney, T. S., Carrara, A., Colombo, R., El-Madany, T. S., Gonzalez-Cascon, R., Martín, M. P., Julitta, T., Moreno, G., Rascher, U., Reichstein, M., Rossini, M., and Migliavacca, M.: Heatwave breaks down the linearity between sun-induced

fluorescence and gross primary production, New Phytologist, 233, 2415–2428, https://doi.org/10.1111/nph.17920, 2022.

Maxwell, K. and Johnson, G. N.: Chlorophyll fluorescence - a practical guide, Journal of Experimental Botany, 51, 659–668, https://doi.org/10.1093/jexbot/51.345.659, 2000.

Mengistu, A. G., Mengistu Tsidu, G., Koren, G., Kooreman, M. L., Boersma, K. F., Tagesson, T., Ardö, J., Nouvellon, Y., and Peters, W.: Sun-induced fluorescence and near-infrared reflectance of vegetation track the seasonal dynamics of gross primary production over Africa, Biogeosciences, 18, 2843–2857, https://doi.org/10.5194/bg-18-2843-2021, 2021.

Merlier, E., Hmimina, G., Bagard, M., Dufrêne, E., and Soudani, K.: Potential use of the PRI and active fluorescence for the diagnosis of the physiological state of plants under ozone exposure and high atmospheric vapor pressure deficit, Photochem Photobiol Sci, 16, 1238–1251, https://doi.org/10.1039/c6pp00416d, 2017.

Mohammed, G. H., Colombo, R., Middleton, E. M., Rascher, U., van der Tol, C., Nedbal, L., Goulas, Y., Pérez-Priego, O., Damm, A., Meroni, M., Joiner, J., Cogliati, S., Verhoef, W., Malenovský, Z., Gastellu-Etchegorry, J.-P., Miller, J. R., Guanter, L., Moreno, J., Moya, I., Berry, J. A., Frankenberg, C., and Zarco-Tejada, P. J.: Remote sensing of solar-induced chlorophyll fluorescence (SIF) in vegetation: 50 years of progress, Remote Sensing of Environment, 231, 111177, https://doi.org/10.1016/j.rse.2019.04.030, 2019a.

Mohammed, G. H., Colombo, R., Middleton, E. M., Rascher, U., van der Tol, C., Nedbal, L., Goulas, Y., Pérez-Priego, O., Damm, A., Meroni, M., Joiner, J., Cogliati, S., Verhoef, W., Malenovský, Z., Gastellu-Etchegorry, J.-P., Miller, J. R., Guanter, L., Moreno, J., Moya, I., Berry, J. A., Frankenberg, C., and Zarco-Tejada, P. J.: Remote sensing of solar-induced chlorophyll fluorescence (SIF) in vegetation: 50 years of progress, Remote Sensing of Environment, 231, 111177, https://doi.org/10.1016/j.rse.2019.04.030, 2019b.

Ounis, A., Evain, S., Flexas, J., Tosti, S., and Moya, I.: Adaptation of a PAM-fluorometer for remote sensing of chlorophyll fluorescence, 8, n.d.

Pabon-Moreno, D. E., Migliavacca, M., Reichstein, M., and Mahecha, M. D.: On the potential of Sentinel-2 for estimating Gross Primary Production, IEEE Trans. Geosci. Remote Sensing, 1–1, https://doi.org/10.1109/TGRS.2022.3152272, 2022.

Paul-Limoges, E., Damm, A., Hueni, A., Liebisch, F., Eugster, W., Schaepman, M. E., and Buchmann, N.: Effect of environmental conditions on sun-induced fluorescence in a mixed forest and a cropland, Remote Sensing of Environment, 219, 310–323, https://doi.org/10.1016/j.rse.2018.10.018, 2018.

Pei, Y., Dong, J., Zhang, Y., Yuan, W., Doughty, R., Yang, J., Zhou, D., Zhang, L., and Xiao, X.: Evolution of light use efficiency models: Improvement, uncertainties, and implications, Agricultural and Forest Meteorology, 317, 108905, https://doi.org/10.1016/j.agrformet.2022.108905, 2022.

Pierrat, Z. A., Bortnik, J., Johnson, B., Barr, A., Magney, T., Bowling, D. R., Parazoo, N., Frankenberg, C., Seibt, U., and Stutz, J.: Forests for forests: combining vegetation indices with solar-induced chlorophyll fluorescence in random forest models improves gross primary productivity prediction in the boreal forest, Environ. Res. Lett., 17, 125006, https://doi.org/10.1088/1748-9326/aca5a0, 2022.

Porcar-Castell, A., Tyystjärvi, E., Atherton, J., van der Tol, C., Flexas, J., Pfündel, E. E., Moreno, J., Frankenberg, C., and Berry, J. A.: Linking chlorophyll a fluorescence to photosynthesis for remote sensing applications: mechanisms and challenges, Journal of Experimental Botany, 65, 4065–4095, https://doi.org/10.1093/jxb/eru191, 2014a.

Porcar-Castell, A., Tyystjärvi, E., Atherton, J., van der Tol, C., Flexas, J., Pfündel, E. E., Moreno, J., Frankenberg, C., and Berry, J. A.: Linking chlorophyll a fluorescence to photosynthesis for remote sensing applications: mechanisms and challenges, Journal of Experimental Botany, 65, 4065–4095, https://doi.org/10.1093/jxb/eru191, 2014b.

Porcar-Castell, A., Malenovský, Z., Magney, T., Van Wittenberghe, S., Fernández-Marín, B., Maignan, F., Zhang, Y., Maseyk, K., Atherton, J., Albert, L. P., Robson, T. M., Zhao, F., Garcia-Plazaola, J.-I., Ensminger, I., Rajewicz, P. A., Grebe, S., Tikkanen, M., Kellner, J. R., Ihalainen, J. A., Rascher, U., and Logan, B.: Chlorophyll a fluorescence illuminates a path connecting plant molecular biology to Earth-system science, Nat. Plants, 7, 998–1009, https://doi.org/10.1038/s41477-021-00980-4, 2021.

Rhoul, C.: Simulation de la fluorescence de la végétation mesurée depuis une orbite géostationnaire, 151, n.d.

Ruban, A. V.: Nonphotochemical Chlorophyll Fluorescence Quenching: Mechanism and Effectiveness in Protecting Plants from Photodamage, Plant Physiology, 170, 1903–1916, https://doi.org/10.1104/pp.15.01935, 2016.

Running, S. W., Nemani, R. R., Heinsch, F. A., Zhao, M., Reeves, M., and Hashimoto, H.: A Continuous Satellite-Derived Measure of Global Terrestrial Primary Production, BioScience, 54, 547, https://doi.org/10.1641/0006-3568(2004)054[0547:ACSMOG]2.0.CO;2, 2004.

Ryu, Y., Berry, J. A., and Baldocchi, D. D.: What is global photosynthesis? History, uncertainties and opportunities, Remote Sensing of Environment, 223, 95–114, https://doi.org/10.1016/j.rse.2019.01.016, 2019.

Sarr, A. B. and Sultan, B.: Predicting crop yields in Senegal using machine learning methods, International Journal of Climatology, 43, 1817–1838, https://doi.org/10.1002/joc.7947, 2023.

Soudani, K., Hmimina, G., Dufrêne, E., Berveiller, D., Delpierre, N., Ourcival, J.-M., Rambal, S., and Joffre, R.: Relationships between photochemical reflectance index and light-use efficiency in deciduous and evergreen broadleaf forests, Remote Sensing of Environment, 144, 73–84, https://doi.org/10.1016/j.rse.2014.01.017, 2014.

Sun, Y., Frankenberg, C., Wood, J. D., Schimel, D. S., Jung, M., Guanter, L., Drewry, D. T., Verma, M., Porcar-Castell, A., Griffis, T. J., Gu, L., Magney, T. S., Kohler, P., Evans,

B., and Yuen, K.: OCO-2 advances photosynthesis observation from space via solar-induced chlorophyll fluorescence, Science, 358, 189-+, https://doi.org/10.1126/science.aam5747, 2017.

Sun, Y., Wen, J., Gu, L., Joiner, J., Chang, C. Y., van der Tol, C., Porcar-Castell, A., Magney, T., Wang, L., Hu, L., Rascher, U., Zarco-Tejada, P., Barrett, C. B., Lai, J., Han, J., and Luo, Z.: From remotely-sensed solar-induced chlorophyll fluorescence to ecosystem structure, function, and service: Part II—Harnessing data, Global Change Biology, 29, 2893–2925, https://doi.org/10.1111/gcb.16646, 2023.

Tagliabue, G., Panigada, C., Dechant, B., Baret, F., Cogliati, S., Colombo, R., Migliavacca, M., Rademske, P., Schickling, A., Schüttemeyer, D., Verrelst, J., Rascher, U., Ryu, Y., and Rossini, M.: Exploring the spatial relationship between airborne-derived red and far-red sun-induced fluorescence and process-based GPP estimates in a forest ecosystem, Remote Sensing of Environment, 231, 111272, https://doi.org/10.1016/j.rse.2019.111272, 2019.

Tucker, C. J.: Red and photographic infrared linear combinations for monitoring vegetation, Remote Sensing of Environment, 8, 127–150, https://doi.org/10.1016/0034-4257(79)90013-0, 1979.

Tunca, E., Köksal, E. S., Çetin, S., Ekiz, N. M., and Balde, H.: Yield and leaf area index estimations for sunflower plants using unmanned aerial vehicle images, Environ Monit Assess, 190, 682, https://doi.org/10.1007/s10661-018-7064-x, 2018.

Ustin, S. L. and Middleton, E. M.: Current and near-term advances in Earth observation for ecological applications, Ecol Process, 10, 1, https://doi.org/10.1186/s13717-020-00255-4, 2021.

Verma, M., Schimel, D., Evans, B., Frankenberg, C., Beringer, J., Drewry, D. T., Magney, T., Marang, I., Hutley, L., Moore, C., and Eldering, A.: Effect of environmental conditions on the relationship between solar-induced fluorescence and gross primary productivity at an OzFlux grassland site: OCO SIF, MODIS, and GPP, Journal of Geophysical Research: Biogeosciences, 122, 716–733, https://doi.org/10.1002/2016JG003580, 2017.

Wang, K.-Q., Wang, H.-S., and Sun, O. J.: Application and comparison of remote sensing GPP models with multi-site data in China, Chinese Journal of Plant Ecology, 41, 337, https://doi.org/10.17521/cjpe.2016.0182, 2017.

Wang, S., Zhang, Y., Ju, W., Qiu, B., and Zhang, Z.: Tracking the seasonal and inter-annual variations of global gross primary production during last four decades using satellite near-infrared reflectance data, Science of The Total Environment, 755, 142569, https://doi.org/10.1016/j.scitotenv.2020.142569, 2021.

Wang, X., Chen, J. M., and Ju, W.: Photochemical reflectance index (PRI) can be used to improve the relationship between gross primary productivity (GPP) and sun-induced chlorophyll fluorescence (SIF), Remote Sensing of Environment, 246, 111888, https://doi.org/10.1016/j.rse.2020.111888, 2020a.

Wang, X., Chen, J. M., and Ju, W.: Photochemical reflectance index (PRI) can be used to improve the relationship between gross primary productivity (GPP) and sun-induced chlorophyll fluorescence (SIF), Remote Sensing of Environment, 246, 111888, https://doi.org/10.1016/j.rse.2020.111888, 2020b.

Weiss, M., Jacob, F., and Duveiller, G.: Remote sensing for agricultural applications: A meta-review, Remote Sensing of Environment, 236, 111402, https://doi.org/10.1016/j.rse.2019.111402, 2020.

Wen, T., Li, J.-H., Wang, Q., Gao, Y.-Y., Hao, G.-F., and Song, B.-A.: Thermal imaging: The digital eye facilitates high-throughput phenotyping traits of plant growth and stress responses, Science of The Total Environment, 899, 165626, https://doi.org/10.1016/j.scitotenv.2023.165626, 2023.

Wood, J. D., Griffis, T. J., Baker, J. M., Frankenberg, C., Verma, M., and Yuen, K.: Multiscale analyses of solar-induced florescence and gross primary production, Geophysical Research Letters, 44, 533–541, https://doi.org/10.1002/2016gl070775, 2017.

Wu, G., Guan, K., Jiang, C., Kimm, H., Miao, G., Bernacchi, C. J., Moore, C. E., Ainsworth, E. A., Yang, X., Berry, J. A., Frankenberg, C., and Chen, M.: Attributing differences of solar-induced chlorophyll fluorescence (SIF)-gross primary production (GPP) relationships between two C4 crops: corn and miscanthus, Agricultural and Forest Meteorology, 323, 109046, https://doi.org/10.1016/j.agrformet.2022.109046, 2022.

Xiao, J., Chevallier, F., Gomez, C., Guanter, L., Hicke, J. A., Huete, A. R., Ichii, K., Ni, W., Pang, Y., Rahman, A. F., Sun, G., Yuan, W., Zhang, L., and Zhang, X.: Remote sensing of the terrestrial carbon cycle: A review of advances over 50 years, Remote Sensing of Environment, 233, 111383, https://doi.org/10.1016/j.rse.2019.111383, 2019.

Xiao, J., Fisher, J. B., Hashimoto, H., Ichii, K., and Parazoo, N. C.: Emerging satellite observations for diurnal cycling of ecosystem processes, Nat. Plants, 7, 877–887, https://doi.org/10.1038/s41477-021-00952-8, 2021.

Yang, J. C., Magney, T. S., Yan, D., Knowles, J. F., Smith, W. K., Scott, R. L., and Barron-Gafford, G. A.: The Photochemical Reflectance Index (PRI) Captures the Ecohydrologic Sensitivity of a Semiarid Mixed Conifer Forest, Journal of Geophysical Research: Biogeosciences, 125, e2019JG005624, https://doi.org/10.1029/2019JG005624, 2020a.

Yang, P., van der Tol, C., Verhoef, W., Damm, A., Schickling, A., Kraska, T., Muller, O., and Rascher, U.: Using reflectance to explain vegetation biochemical and structural effects on sun-induced chlorophyll fluorescence, Remote Sensing of Environment, 231, 110996, https://doi.org/10.1016/j.rse.2018.11.039, 2019.

Yang, P., Van der Tol, C., Campbell, P. K. E., and Middleton, E. M.: Unravelling the physical and physiological basis for the solar-inducedchlorophyll fluorescence and photosynthesis relationship, Biodiversity and Ecosystem Function: Terrestrial, https://doi.org/10.5194/bg-2020-323, 2020b.

Yang, P., van der Tol, C., Campbell, P. K. E., and Middleton, E. M.: Unraveling the physical and physiological basis for the solar- induced chlorophyll fluorescence and photosynthesis relationship using continuous leaf and canopy measurements of a corn crop, Biogeosciences, 18, 441–465, https://doi.org/10.5194/bg-18-441-2021, 2021.

Zeng, Y., Hao, D., Huete, A., Dechant, B., Berry, J., Chen, J. M., Joiner, J., Frankenberg, C., Bond-Lamberty, B., Ryu, Y., Xiao, J., Asrar, G. R., and Chen, M.: Optical vegetation indices for monitoring terrestrial ecosystems globally, Nat Rev Earth Environ, 3, 477–493, https://doi.org/10.1038/s43017-022-00298-5, 2022.

Zhang, L., Guo, C. L., Zhao, L. Y., Zhu, Y., Cao, W. X., Tian, Y. C., Cheng, T., and Wang, X.: Estimating wheat yield by integrating the WheatGrow and PROSAIL models, Field Crops Research, 192, 55–66, https://doi.org/10.1016/j.fcr.2016.04.014, 2016.

Zhang, Q., Xiao, X., Braswell, B., Linder, E., Ollinger, S., Smith, M.-L., Jenkins, J. P., Baret, F., Richardson, A. D., Moore, B., and Minocha, R.: Characterization of seasonal variation of forest canopy in a temperate deciduous broadleaf forest, using daily MODIS data, Remote Sensing of Environment, 105, 189–203, https://doi.org/10.1016/j.rse.2006.06.013, 2006.

Zhang, Y., Joiner, J., Alemohammad, S. H., Zhou, S., and Gentine, P.: A global spatially Continuous Solar Induced Fluorescence (CSIF) dataset using neural networks, Biogeochemistry: Land, https://doi.org/10.5194/bg-2018-255, 2018.

Zhang, Y., Zhang, Q., Liu, L., Zhang, Y., Wang, S., Ju, W., Zhou, G., Zhou, L., Tang, J., Zhu, X., Wang, F., Huang, Y., Zhang, Z., Qiu, B., Zhang, X., Wang, S., Huang, C., Tang, X., and Zhang, J.: ChinaSpec: a Network for Long-term Ground-based Measurements of Solar-induced Fluorescence in China, J Geophys Res Biogeosci, https://doi.org/10.1029/2020JG006042, 2021.

Zhao, W., Wu, J., Shen, Q., Liu, L., Lin, J., and Yang, J.: Estimation of the Net Primary Productivity of Winter Wheat Based on the Near-Infrared Radiance of Vegetation, SSRN Journal, https://doi.org/10.2139/ssrn.4016083, 2022.

References Chapter 2: Introduction to optical remote sensing of vegetation functioning

Badgley, G., Field, C. B., and Berry, J. A.: Canopy near-infrared reflectance and terrestrial photosynthesis, Science Advances, 3, e1602244, https://doi.org/10.1126/sciadv.1602244, 2017.

Baker, N. R.: Chlorophyll Fluorescence: A Probe of Photosynthesis In Vivo, Annual Review of Plant Biology, 59, 89–113, https://doi.org/10.1146/annurev.arplant.59.032607.092759, 2008.

Campbell, P., Huemmrich, K., Middleton, E., Ward, L., Julitta, T., Daughtry, C., Burkart, A., Russ, A., and Kustas, W.: Diurnal and Seasonal Variations in Chlorophyll Fluorescence Associated with Photosynthesis at Leaf and Canopy Scales, Remote Sensing, 11, 488, https://doi.org/10.3390/rs11050488, 2019.

Cendrero-Mateo, Wieneke, Damm, Alonso, Pinto, Moreno, Guanter, Celesti, Rossini, Sabater, Cogliati, Julitta, Rascher, Goulas, Aasen, Pacheco-Labrador, and Arthur: Sun-Induced Chlorophyll Fluorescence III: Benchmarking Retrieval Methods and Sensor Characteristics for Proximal Sensing, Remote Sensing, 11, 962, https://doi.org/10.3390/rs11080962, 2019.

Cogliati, S., Verhoef, W., Kraft, S., Sabater, N., Alonso, L., Vicent, J., Moreno, J., Drusch, M., and Colombo, R.: Retrieval of sun-induced fluorescence using advanced spectral fitting methods, Remote Sensing of Environment, 169, 344–357, https://doi.org/10.1016/j.rse.2015.08.022, 2015.

Frankenberg, C. and Berry, J.: Solar Induced Chlorophyll Fluorescence: Origins, Relation to Photosynthesis and Retrieval, in: Comprehensive Remote Sensing, Elsevier, 143–162, https://doi.org/10.1016/B978-0-12-409548-9.10632-3, 2018.

Gao, S., Huete, A., Kobayashi, H., Doody, T. M., Liu, W., Wang, Y., Zhang, Y., and Lu, X.: Simulation of solar-induced chlorophyll fluorescence in a heterogeneous forest using 3-D radiative transfer modelling and airborne LiDAR, ISPRS Journal of Photogrammetry and Remote Sensing, 191, 1–17, https://doi.org/10.1016/j.isprsjprs.2022.07.004, 2022.

Genty, B., Harbinson, J., and Baker, N. R.: Relative quantum efficiencies of the two photosystems of leaves in photorespiratory and non-respiratory conditions., Plant Physiology and Biochemistry (Paris), 28, 1–10, 1990.

Grotti, M., Calders, K., Origo, N., Puletti, N., Alivernini, A., Ferrara, C., and Chianucci, F.: An intensity, image-based method to estimate gap fraction, canopy openness and effective leaf area index from phase-shift terrestrial laser scanning, Agricultural and Forest Meteorology, 280, 107766, https://doi.org/10.1016/j.agrformet.2019.107766, 2020.

Hao, D., Zeng, Y., Qiu, H., Biriukova, K., Celesti, M., Migliavacca, M., Rossini, M., Asrar, G. R., and Chen, M.: Practical approaches for normalizing directional solar-induced fluorescence to a standard viewing geometry, Remote Sensing of Environment, 255, 112171, https://doi.org/10.1016/j.rse.2020.112171, 2021.

Hmimina, G., Dufrêne, E., and Soudani, K.: Relationship between photochemical reflectance index and leaf ecophysiological and biochemical parameters under two different water statuses: towards a rapid and efficient correction method using real-time measurements: Disentangling PRI variability, Plant Cell Environ, 37, 473–487, https://doi.org/10.1111/pce.12171, 2014.

Jahns, P. and Holzwarth, A. R.: The role of the xanthophyll cycle and of lutein in photoprotection of photosystem II, Biochimica et Biophysica Acta (BBA) - Bioenergetics, 1817, 182–193, https://doi.org/10.1016/j.bbabio.2011.04.012, 2012.

Jonard, F., De Cannière, S., Brüggemann, N., Gentine, P., Short Gianotti, D. J., Lobet, G., Miralles, D. G., Montzka, C., Pagán, B. R., Rascher, U., and Vereecken, H.: Value of sun-induced chlorophyll fluorescence for quantifying hydrological states and fluxes: Current status and challenges, Agricultural and Forest Meteorology, 291, 108088, https://doi.org/10.1016/j.agrformet.2020.108088, 2020.

Kitajima, M. and Butler, W. L.: Quenching of chlorophyll fluorescence and primary photochemistry in chloroplasts by dibromothymoquinone, Biochimica et Biophysica Acta (BBA) - Bioenergetics, 376, 105–115, https://doi.org/10.1016/0005-2728(75)90209-1, 1975.

Krause, G.: Chlorophyll Fluorescence And Photosynthesis: The Basics, Annual review of plant physiology and plant molecular biology, https://doi.org/10.1146/annurev.arplant.42.1.313, 1991.

Loayza, H., Moya, I., Quiroz, R., Ounis, A., and Goulas, Y.: Active and passive chlorophyll fluorescence measurements at canopy level on potato crops. Evidence of similitude of diurnal cycles of apparent fluorescence yields, Photosynth Res, 155, 271–288, https://doi.org/10.1007/s11120-022-00995-8, 2023.

Magney, T. S., Frankenberg, C., Fisher, J. B., Sun, Y., North, G. B., Davis, T. S., Kornfeld, A., and Siebke, K.: Connecting active to passive fluorescence with photosynthesis: a method for evaluating remote sensing measurements of Chl fluorescence, New Phytologist, 215, 1594–1608, https://doi.org/10.1111/nph.14662, 2017.

Meroni, M., Rossini, M., Guanter, L., Alonso, L., Rascher, U., Colombo, R., and Moreno, J.: Remote sensing of solar-induced chlorophyll fluorescence: Review of methods and applications, Remote Sensing of Environment, 113, 2037–2051, https://doi.org/10.1016/j.rse.2009.05.003, 2009.

Merzlyak, M. N., Chivkunova, O. B., Solovchenko, A. E., and Naqvi, K. R.: Light absorption by anthocyanins in juvenile, stressed, and senescing leaves, Journal of Experimental Botany, 59, 3903–3911, https://doi.org/10.1093/jxb/ern230, 2008.

Migliavacca, M., Perez-Priego, O., Rossini, M., El-Madany, T. S., Moreno, G., van der Tol, C., Rascher, U., Berninger, A., Bessenbacher, V., Burkart, A., Carrara, A., Fava, F., Guan, J.-H., Hammer, T. W., Henkel, K., Juarez-Alcalde, E., Julitta, T., Kolle, O., Martín, M. P., Musavi, T., Pacheco-Labrador, J., Pérez-Burgueño, A., Wutzler, T., Zaehle, S., and Reichstein, M.: Plant functional traits and canopy structure control the relationship between photosynthetic CO_2 uptake and far-red sun-induced fluorescence in a Mediterranean grassland under different nutrient availability, New Phytologist, 214, 1078–1091, https://doi.org/10.1111/nph.14437, 2017.

Mohammed, G. H., Colombo, R., Middleton, E. M., Rascher, U., van der Tol, C., Nedbal, L., Goulas, Y., Pérez-Priego, O., Damm, A., Meroni, M., Joiner, J., Cogliati, S., Verhoef, W., Malenovský, Z., Gastellu-Etchegorry, J.-P., Miller, J. R., Guanter, L., Moreno, J., Moya, I., Berry, J. A., Frankenberg, C., and Zarco-Tejada, P. J.: Remote sensing of solar-induced chlorophyll fluorescence (SIF) in vegetation: 50 years of progress, Remote Sensing of Environment, 231, 111177, https://doi.org/10.1016/j.rse.2019.04.030, 2019.

Morozumi, T., Kato, T., Kobayashi, H., Sakai, Y., Tsujimoto, K., Nakashima, N., Buareal, K., Lan, W., and Ninomiya, H.: Row orientation influences the diurnal cycle of solar-induced chlorophyll fluorescence emission from wheat canopy, as demonstrated by radiative transfer modeling, Agricultural and Forest Meteorology, 339, 109576, https://doi.org/10.1016/j.agrformet.2023.109576, 2023.

Moya, I., Loayza, H., López, M. L., Quiroz, R., Ounis, A., and Goulas, Y.: Canopy chlorophyll fluorescence applied to stress detection using an easy-to-build micro-lidar, Photosynthesis Research, 142, 1–15, https://doi.org/10.1007/s11120-019-00642-9, 2019.

Ounis, A., Bach, J., Mahjoub, A., Daumard, F., Moya, I., and Goulas, Y.: Combined use of LIDAR and hyperspectral measurements for remote sensing of fluorescence and vertical profile of canopies, Rev. Teledetec., 87, https://doi.org/10.4995/raet.2015.3982, 2016.

Ounis, A., Evain, S., Flexas, J., Tosti, S., and Moya, I.: Adaptation of a PAM-fluorometer for remote sensing of chlorophyll fluorescence, 8, n.d.

Plascyk, J. A.: The MK II Fraunhofer line discriminator (FLD-II) for airborne and orbital remote sensing of solar-stimulated luminescence, Optical Eng., 14, 339–346, 1975.

Porcar-Castell, A., Tyystjärvi, E., Atherton, J., van der Tol, C., Flexas, J., Pfündel, E. E., Moreno, J., Frankenberg, C., and Berry, J. A.: Linking chlorophyll a fluorescence to photosynthesis for remote sensing applications: mechanisms and challenges, Journal of Experimental Botany, 65, 4065–4095, https://doi.org/10.1093/jxb/eru191, 2014.

Sarvikas, P., Hakala-Yatkin, M., Dönmez, S., and Tyystjärvi, E.: Short flashes and continuous light have similar photoinhibitory efficiency in intact leaves, J Exp Bot, 61, 4239–4247, https://doi.org/10.1093/jxb/erq224, 2010.

Schreiber, U.: Pulse-Amplitude-Modulation (PAM) Fluorometry and Saturation Pulse Method: An Overview, in: Chlorophyll a Fluorescence: A Signature of Photosynthesis, edited by: Papageorgiou, G. C. and Govindjee, Springer Netherlands, Dordrecht, 279–319, https://doi.org/10.1007/978-1-4020-3218-9_11, 2004.

Song, J., Zhu, X., Qi, J., Pang, Y., Yang, L., and Yu, L.: A Method for Quantifying Understory Leaf Area Index in a Temperate Forest through Combining Small Footprint Full-Waveform and Point Cloud LiDAR Data, Remote Sensing, 13, 3036, https://doi.org/10.3390/rs13153036, 2021.

van der Tol, C., Berry, J. A., Campbell, P. K. E., and Rascher, U.: Models of fluorescence and photosynthesis for interpreting measurements of solar-induced chlorophyll fluorescence, Journal of Geophysical Research-Biogeosciences, 119, 2312–2327, https://doi.org/10.1002/2014jg002713, 2014.

Ustin, S. L. and Middleton, E. M.: Current and near-term advances in Earth observation for ecological applications, Ecol Process, 10, 1, https://doi.org/10.1186/s13717-020-00255-4, 2021.

Wong, C. Y. S., D'Odorico, P., Arain, M. A., and Ensminger, I.: Tracking the phenology of photosynthesis using carotenoid-sensitive and near-infrared reflectance vegetation indices in a temperate evergreen and mixed deciduous forest, New Phytologist, 226, 1682–1695, https://doi.org/10.1111/nph.16479, 2020.

Yang, P. and van der Tol, C.: Linking canopy scattering of far-red sun-induced chlorophyll fluorescence with reflectance, Remote Sensing of Environment, 209, 456–467, https://doi.org/10.1016/j.rse.2018.02.029, 2018.

Zeng, Y., Hao, D., Huete, A., Dechant, B., Berry, J., Chen, J. M., Joiner, J., Frankenberg, C., Bond-Lamberty, B., Ryu, Y., Xiao, J., Asrar, G. R., and Chen, M.: Optical vegetation indices for monitoring terrestrial ecosystems globally, Nat Rev Earth Environ, 3, 477–493, https://doi.org/10.1038/s43017-022-00298-5, 2022.

Zhang, Y., Migliavacca, M., Penuelas, J., and Ju, W.: Advances in hyperspectral remote sensing of vegetation traits and functions, Remote Sensing of Environment, 252, 112121, https://doi.org/10.1016/j.rse.2020.112121, 2021.

Zhang, Z. and Zhang, Y.: Solar angle matters: Diurnal pattern of solar-induced chlorophyll fluorescence from OCO-3 and TROPOMI, Remote Sensing of Environment, 285, 113380, https://doi.org/10.1016/j.rse.2022.113380, 2023.

References Chpater 3: Synergy between TROPOMI sun-induced chlorophyll fluorescence and MODIS spectral reflectance for understanding the dynamics of gross primary productivity at Integrated Carbon Observatory System (ICOS) ecosystem flux sites

Badgley, G., Field, C. B., and Berry, J. A.: Canopy near-infrared reflectance and terrestrial photosynthesis, Science Advances, 3, e1602244, https://doi.org/10.1126/sciadv.1602244, 2017.

Baldocchi, D. D., Ryu, Y., Dechant, B., Eichelmann, E., Hemes, K., Ma, S., Sanchez, C. R., Shortt, R., Szutu, D., Valach, A., Verfaillie, J., Badgley, G., Zeng, Y., and Berry, J. A.: Outgoing Near-Infrared Radiation From Vegetation Scales With Canopy Photosynthesis Across a Spectrum of Function, Structure, Physiological Capacity, and Weather, Journal of Geophysical Research: Biogeosciences, 125, https://doi.org/10.1029/2019JG005534, 2020.

Bodesheim, P., Jung, M., Gans, F., Mahecha, M. D., and Reichstein, M.: Upscaled diurnal cycles of land–atmosphere fluxes: a new global half-hourly data product, Earth System Science Data, 10, 1327–1365, https://doi.org/10.5194/essd-10-1327-2018, 2018.

Breiman, L.: Random Forests, Machine Learning, 45, 5–32, https://doi.org/10.1023/A:1010933404324, 2001.

Buchhorn, M., Smets, B., Bertels, L., Roo, B. D., Lesiv, M., Tsendbazar, N.-E., Li, L., and Tarko, A.: Copernicus Global Land Service: Land Cover 100m: version 3 Globe 2015-2019: Product User Manual, Zenodo, https://doi.org/10.5281/ZENODO.3938963, 2020.

Cho, S., Kang, M., Ichii, K., Kim, J., Lim, J.-H., Chun, J.-H., Park, C.-W., Kim, H. S., Choi, S.-W., Lee, S.-H., Indrawati, Y. M., and Kim, J.: Evaluation of forest carbon uptake in South Korea using the national flux tower network, remote sensing, and data-driven technology, Agricultural and Forest Meteorology, 311, 108653, https://doi.org/10.1016/j.agrformet.2021.108653, 2021.

Chou, S., Chen, J., Yu, H., Chen, B., Zhang, X., Croft, H., Khalid, S., Li, M., and Shi, Q.: Canopy-Level Photochemical Reflectance Index from Hyperspectral Remote Sensing and Leaf-Level Non-Photochemical Quenching as Early Indicators of Water Stress in Maize, Remote Sensing, 9, 794, https://doi.org/10.3390/rs9080794, 2017.

Chu, H., Luo, X., Ouyang, Z., Chan, W. S., Dengel, S., Biraud, S. C., Torn, M. S., Metzger, S., Kumar, J., Arain, M. A., Arkebauer, T. J., Baldocchi, D., Bernacchi, C., Billesbach, D., Black, T. A., Blanken, P. D., Bohrer, G., Bracho, R., Brown, S., Brunsell, N. A., Chen, J., Chen, X., Clark, K., Desai, A. R., Duman, T., Durden, D., Fares, S., Forbrich, I., Gamon, J. A., Gough, C. M., Griffis, T., Helbig, M., Hollinger, D., Humphreys, E., Ikawa, H., Iwata, H., Ju, Y., Knowles, J. F., Knox, S. H., Kobayashi, H., Kolb, T., Law, B., Lee, X., Litvak, M., Liu, H., Munger, J. W., Noormets, A., Novick, K., Oberbauer, S. F., Oechel, W., Oikawa, P., Papuga, S. A., Pendall, E., Prajapati, P., Prueger, J., Quinton, W. L., Richardson, A. D., Russell, E. S., Scott, R. L., Starr, G., Staebler, R., Stoy, P. C., Stuart-Haëntjens, E., Sonnentag, O., Sullivan, R. C., Suyker, A., Ueyama, M., Vargas, R., Wood, J. D., and Zona, D.: Representativeness of Eddy-Covariance flux footprints for areas surrounding AmeriFlux sites, Agricultural and Forest Meteorology, 301–302, 108350, https://doi.org/10.1016/j.agrformet.2021.108350, 2021.

Damm, A., Elbers, J., Erler, A., Gioli, B., Hamdi, K., Hutjes, R., Kosvancova, M., Meroni, M., Miglietta, F., Moersch, A., Moreno, J., Schickling, A., Sonnenschein, R., Udelhoven, T., Van Der LINDEN, S., Hostert, P., and Rascher, U.: Remote sensing of sun-induced fluorescence to improve modeling of diurnal courses of gross primary production (GPP): RS OF SUN-INDUCED FLUORESCENCE TO IMPROVE MODELING OF GPP, Global Change Biology, 16, 171–186, https://doi.org/10.1111/j.1365-2486.2009.01908.x, 2010.

Damm, A., Guanter, L., Paul-Limoges, E., van der Tol, C., Hueni, A., Buchmann, N., Eugster, W., Ammann, C., and Schaepman, M. E.: Far-red sun-induced chlorophyll fluorescence shows ecosystem-specific relationships to gross primary production: An assessment based on observational and modeling approaches, Remote Sensing of Environment, 166, 91–105, https://doi.org/10.1016/j.rse.2015.06.004, 2015.

Daumard, F., Goulas, Y., Champagne, S., Fournier, A., Ounis, A., Olioso, A., and Moya, I.: Continuous Monitoring of Canopy Level Sun-Induced Chlorophyll Fluorescence During the Growth of a Sorghum Field, IEEE Transactions on Geoscience and Remote Sensing, 50, 4292–4300, https://doi.org/10.1109/TGRS.2012.2193131, 2012.

Dechant, B., Ryu, Y., Badgley, G., Zeng, Y., Berry, J. A., Zhang, Y., Goulas, Y., Li, Z., Zhang, Q., Kang, M., Li, J., and Moya, I.: Canopy structure explains the relationship between photosynthesis and sun-induced chlorophyll fluorescence in crops, Remote Sensing of Environment, 241, 111733, https://doi.org/10.1016/j.rse.2020.111733, 2020.

Dechant, B., Ryu, Y., Badgley, G., Köhler, P., Rascher, U., Migliavacca, M., Zhang, Y., Tagliabue, G., Guan, K., Rossini, M., Goulas, Y., Zeng, Y., Frankenberg, C., and Berry, J. A.: NIRVP: A robust structural proxy for sun-induced chlorophyll fluorescence and photosynthesis across scales, Remote Sensing of Environment, 268, 112763, https://doi.org/10.1016/j.rse.2021.112763, 2022.

Doughty, R., Xiao, X., Köhler, P., Frankenberg, C., Qin, Y., Wu, X., Ma, S., and Moore, B.: Global-scale consistency of spaceborne vegetation indices, chlorophyll fluorescence, and photosynthesis, J Geophys Res Biogeosci, https://doi.org/10.1029/2020JG006136, 2021.

Drolet, G. G., Middleton, E. M., Huemmrich, K. F., Hall, F. G., Amiro, B. D., Barr, A. G., Black, T. A., McCaughey, J. H., and Margolis, H. A.: Regional mapping of gross light-use efficiency using MODIS spectral indices, Remote Sensing of Environment, 112, 3064–3078, 2008.

Drusch, M., Moreno, J., Del Bello, U., Franco, R., Goulas, Y., Huth, A., Kraft, S., Middleton, E. M., Miglietta, F., Mohammed, G., Nedbal, L., Rascher, U., Schuttemeyer, D., and Verhoef, W.: The FLuorescence EXplorer Mission Concept—ESA's Earth Explorer 8, IEEE Trans. Geosci. Remote Sensing, 55, 1273–1284, https://doi.org/10.1109/TGRS.2016.2621820, 2017.

Falge, E., Baldocchi, D., Tenhunen, J., Aubinet, M., Bakwin, P., Berbigier, P., Bernhofer, C., Burba, G., Clement, R., Davis, K. J., Elbers, J. A., Goldstein, A. H., Grelle, A., Granier, A., Guðmundsson, J., Hollinger, D., Kowalski, A. S., Katul, G., Law, B. E., Malhi, Y., Meyers, T., Monson, R. K., Munger, J. W., Oechel, W., Paw U, K. T., Pilegaard, K., Rannik, Ü., Rebmann, C., Suyker, A., Valentini, R., Wilson, K., and Wofsy, S.: Seasonality of ecosystem respiration and gross primary production as derived from FLUXNET measurements, Agricultural and Forest Meteorology, 113, 53–74, https://doi.org/10.1016/S0168-1923(02)00102-8, 2002.

Fournier, A., Daumard, F., Champagne, S., Ounis, A., Goulas, Y., and Moya, I.: Effect of canopy structure on sun-induced chlorophyll fluorescence, ISPRS Journal of Photogrammetry and Remote Sensing, 68, 112–120, https://doi.org/10.1016/j.isprsjprs.2012.01.003, 2012.

Frankenberg, C., Fisher, J. B., Worden, J., Badgley, G., Saatchi, S. S., Lee, J.-E., Toon, G. C., Butz, A., Jung, M., Kuze, A., and Yokota, T.: New global observations of the terrestrial carbon cycle from GOSAT: Patterns of plant fluorescence with gross primary

productivity: CHLOROPHYLL FLUORESCENCE FROM SPACE, Geophysical Research Letters, 38, n/a-n/a, https://doi.org/10.1029/2011GL048738, 2011.

Gamon, J. A.: Reviews and Syntheses: optical sampling of the flux tower footprint, Biogeosciences, 12, 4509–4523, https://doi.org/10.5194/bg-12-4509-2015, 2015.

Gamon, J. A., Peñuelas, J., and Field, C. B.: A narrow-waveband spectral index that tracks diurnal changes in photosynthetic efficiency, Remote Sensing of Environment, 41, 35–44, https://doi.org/10.1016/0034-4257(92)90059-S, 1992.

Gamon, J. A., Somers, B., Malenovský, Z., Middleton, E. M., Rascher, U., and Schaepman, M. E.: Assessing Vegetation Function with Imaging Spectroscopy, Surv Geophys, 40, 489–513, https://doi.org/10.1007/s10712-019-09511-5, 2019.

Gitelson, A. A., Gamon, J. A., and Solovchenko, A.: Multiple drivers of seasonal change in PRI: Implications for photosynthesis 2. Stand level, Remote Sensing of Environment, 190, 198–206, https://doi.org/10.1016/j.rse.2016.12.015, 2017.

Goulas, Y., Fournier, A., Daumard, F., Champagne, S., Ounis, A., Marloie, O., and Moya, I.: Gross Primary Production of a Wheat Canopy Relates Stronger to Far Red Than to Red Solar-Induced Chlorophyll Fluorescence, Remote Sensing, 9, 97, https://doi.org/10.3390/rs9010097, 2017.

Gu, L., Wood, J. D., Chang, C. Y. -Y., Sun, Y., and Riggs, J. S.: Advancing Terrestrial Ecosystem Science With a Novel Automated Measurement System for Sun-Induced Chlorophyll Fluorescence for Integration With Eddy Covariance Flux Networks, Journal of Geophysical Research: Biogeosciences, 124, 127–146, https://doi.org/10.1029/2018JG004742, 2019a.

Gu, L., Han, J., Wood, J. D., Chang, C. Y., and Sun, Y.: Sun-induced Chl fluorescence and its importance for biophysical modeling of photosynthesis based on light reactions, New Phytologist, 223, 1179–1191, https://doi.org/10.1111/nph.15796, 2019b.

Guanter, L., Frankenberg, C., Dudhia, A., Lewis, P. E., Gómez-Dans, J., Kuze, A., Suto, H., and Grainger, R. G.: Retrieval and global assessment of terrestrial chlorophyll fluorescence from GOSAT space measurements, Remote Sensing of Environment, 121, 236–251, https://doi.org/10.1016/j.rse.2012.02.006, 2012.

Guanter, L., Zhang, Y., Jung, M., Joiner, J., Voigt, M., Berry, J. A., Frankenberg, C., Huete, A. R., Zarco-Tejada, P., Lee, J.-E., Moran, M. S., Ponce-Campos, G., Beer, C., Camps-Valls, G., Buchmann, N., Gianelle, D., Klumpp, K., Cescatti, A., Baker, J. M., and Griffis, T. J.: Global and time-resolved monitoring of crop photosynthesis with chlorophyll fluorescence, Proceedings of the National Academy of Sciences, 111, E1327–E1333, https://doi.org/10.1073/pnas.1320008111, 2014.

Guanter, L., Bacour, C., Schneider, A., Aben, I., van Kempen, T. A., Maignan, F., Retscher, C., Köhler, P., Frankenberg, C., Joiner, J., and Zhang, Y.: The TROPOSIF global sun-induced fluorescence dataset from the Sentinel-5P TROPOMI mission, Earth System Science Data, 13, 5423–5440, https://doi.org/10.5194/essd-13-5423-2021, 2021.

Hao, D., Asrar, G. R., Zeng, Y., Yang, X., Li, X., Xiao, J., Guan, K., Wen, J., Xiao, Q., Berry, J. A., and Chen, M.: Potential of hotspot solar-induced chlorophyll fluorescence for better tracking terrestrial photosynthesis, Glob Change Biol, gcb.15554, https://doi.org/10.1111/gcb.15554, 2021.

Hayek, M. N., Longo, M., Wu, J., Smith, M. N., Restrepo-Coupe, N., Tapajós, R., da Silva, R., Fitzjarrald, D. R., Camargo, P. B., Hutyra, L. R., Alves, L. F., Daube, B., Munger, J. W., Wiedemann, K. T., Saleska, S. R., and Wofsy, S. C.: Carbon exchange in an Amazon forest: from hours to years, Biogeosciences, 15, 4833–4848, https://doi.org/10.5194/bg-15-4833-2018, 2018.

He, L., Magney, T., Dutta, D., Yin, Y., Köhler, P., Grossmann, K., Stutz, J., Dold, C., Hatfield, J., Guan, K., Peng, B., and Frankenberg, C.: From the Ground to Space: Using Solar-Induced Chlorophyll Fluorescence to Estimate Crop Productivity, Geophysical Research Letters, 47, https://doi.org/10.1029/2020GL087474, 2020.

Hilker, T., Coops, N. C., Nesic, Z., Wulder, M. A., and Black, A. T.: Instrumentation and approach for unattended year-round tower-based measurements of spectral reflectance, Computers and Electronics in Agriculture, 56, 72–84, https://doi.org/10.1016/j.compag.2007.01.003, 2007.

Hilker, T., Lyapustin, A., Hall, F. G., Wang, Y., Coops, N. C., Drolet, G., and Black, T. A.: An assessment of photosynthetic light use efficiency from space: Modeling the atmospheric and directional impacts on PRI reflectance, Remote Sensing of Environment, 113, 2463–2475, https://doi.org/10.1016/j.rse.2009.07.012, 2009a.

Hilker, T., Lyapustin, A., Hall, F. G., Wang, Y., Coops, N. C., Drolet, G., and Black, T. A.: An assessment of photosynthetic light use efficiency from space: Modeling the atmospheric and directional impacts on PRI reflectance, Remote Sensing of Environment, 13, 2009b.

Hmimina, G., Merlier, E., Dufrêne, E., and Soudani, K.: Deconvolution of pigment and physiologically related photochemical reflectance index variability at the canopy scale over an entire growing season: Towards an understanding of canopy PRI variability, Plant Cell Environ, 38, 1578–1590, https://doi.org/10.1111/pce.12509, 2015.

Hornero, A., North, P. R. J., Zarco-Tejada, P. J., Rascher, U., Martín, M. P., Migliavacca, M., and Hernandez-Clemente, R.: Assessing the contribution of understory sun-induced chlorophyll fluorescence through 3-D radiative transfer modelling and field data, Remote Sensing of Environment, 253, 112195, https://doi.org/10.1016/j.rse.2020.112195, 2021.

Jiang, C. and Ryu, Y.: Multi-scale evaluation of global gross primary productivity and evapotranspiration products derived from Breathing Earth System Simulator (BESS), Remote Sensing of Environment, 186, 528–547, https://doi.org/10.1016/j.rse.2016.08.030, 2016.

Jonard, F., De Cannière, S., Brüggemann, N., Gentine, P., Short Gianotti, D. J., Lobet, G., Miralles, D. G., Montzka, C., Pagán, B. R., Rascher, U., and Vereecken, H.: Value of sun-induced chlorophyll fluorescence for quantifying hydrological states and fluxes:

Current status and challenges, Agricultural and Forest Meteorology, 291, 108088, https://doi.org/10.1016/j.agrformet.2020.108088, 2020.

Jung, M., Koirala, S., Weber, U., Ichii, K., Gans, F., Camps-Valls, G., Papale, D., Schwalm, C., Tramontana, G., and Reichstein, M.: The FLUXCOM ensemble of global land-atmosphere energy fluxes, Sci Data, 6, 74, https://doi.org/10.1038/s41597-019-0076-8, 2019.

Kim, J., Ryu, Y., Dechant, B., Lee, H., Kim, H. S., Kornfeld, A., and Berry, J. A.: Solar-induced chlorophyll fluorescence is non-linearly related to canopy photosynthesis in a temperate evergreen needleleaf forest during the fall transition, Remote Sensing of Environment, 258, 112362, https://doi.org/10.1016/j.rse.2021.112362, 2021.

Kimm, H., Guan, K., Jiang, C., Miao, G., Wu, G., Suyker, A. E., Ainsworth, E. A., Bernacchi, C. J., Montes, C. M., Berry, J. A., Yang, X., Frankenberg, C., Chen, M., and Köhler, P.: A physiological signal derived from sun-induced chlorophyll fluorescence quantifies crop physiological response to environmental stresses in the U.S. Corn Belt, Environ. Res. Lett., 16, 124051, https://doi.org/10.1088/1748-9326/ac3b16, 2021.

Köhler, P., Frankenberg, C., Magney, T. S., Guanter, L., Joiner, J., and Landgraf, J.: Global Retrievals of Solar-Induced Chlorophyll Fluorescence With TROPOMI: First Results and Intersensor Comparison to OCO-2, Geophysical Research Letters, 45, 10,456-10,463, https://doi.org/10.1029/2018GL079031, 2018.

Köhler, P., Fischer, W. W., Rossman, G. R., Grotzinger, J. P., Doughty, R., Wang, Y., Yin, Y., and Frankenberg, C.: Mineral Luminescence Observed from Space, Geophys Res Lett, 48, https://doi.org/10.1029/2021GL095227, 2021.

Kong, J., Ryu, Y., Liu, J., Dechant, B., Rey-Sanchez, C., Shortt, R., Szutu, D., Verfaillie, J., Houborg, R., and Baldocchi, D. D.: Matching high-resolution satellite data and flux tower footprints improves their agreement in photosynthesis estimates, Agricultural and Forest Meteorology, 316, 108878, https://doi.org/10.1016/j.agrformet.2022.108878, 2022.

Li, J., Zhang, Y., Gu, L., Li, Z., Li, J., Zhang, Q., Zhang, Z., and Song, L.: Seasonal variations in the relationship between sun-induced chlorophyll fluorescence and photosynthetic capacity from the leaf to canopy level in a rice crop, Journal of Experimental Botany, 71, 7179–7197, https://doi.org/10.1093/jxb/eraa408, 2020.

Li, X. and Xiao, J.: TROPOMI observations allow for robust exploration of the relationship between solar-induced chlorophyll fluorescence and terrestrial gross primary production, Remote Sensing of Environment, 268, 112748, https://doi.org/10.1016/j.rse.2021.112748, 2022.

Li, X., Xiao, J., and He, B.: Chlorophyll fluorescence observed by OCO-2 is strongly related to gross primary productivity estimated from flux towers in temperate forests, Remote Sensing of Environment, 204, 659–671, https://doi.org/10.1016/j.rse.2017.09.034, 2018a.

Li, X., Xiao, J., He, B., Altaf Arain, M., Beringer, J., Desai, A. R., Emmel, C., Hollinger, D. Y., Krasnova, A., Mammarella, I., Noe, S. M., Ortiz, P. S., Rey-Sanchez, A. C., Rocha, A. V., and Varlagin, A.: Solar-induced chlorophyll fluorescence is strongly correlated with terrestrial photosynthesis for a wide variety of biomes: First global analysis based on OCO-2 and flux tower observations, Global Change Biology, 24, 3990–4008, https://doi.org/10.1111/gcb.14297, 2018b.

Li, X., Xiao, J., Fisher, J. B., and Baldocchi, D. D.: ECOSTRESS estimates gross primary production with fine spatial resolution for different times of day from the International Space Station, Remote Sensing of Environment, 258, 112360, https://doi.org/10.1016/j.rse.2021.112360, 2021.

Lin, S., Li, J., Liu, Q., Li, L., Zhao, J., and Yu, W.: Evaluating the Effectiveness of Using Vegetation Indices Based on Red-Edge Reflectance from Sentinel-2 to Estimate Gross Primary Productivity, Remote Sensing, 11, 1303, https://doi.org/10.3390/rs11111303, 2019.

Lu, X., Liu, Z., Zhao, F., and Tang, J.: Comparison of total emitted solar-induced chlorophyll fluorescence (SIF) and top-of-canopy (TOC) SIF in estimating photosynthesis, Remote Sensing of Environment, 251, 112083, https://doi.org/10.1016/j.rse.2020.112083, 2020.

Madani, N., Parazoo, N. C., Kimball, J. S., Ballantyne, A. P., Reichle, R. H., Maneta, M., Saatchi, S., Palmer, P. I., Liu, Z., and Tagesson, T.: Recent Amplified Global Gross Primary Productivity Due to Temperature Increase Is Offset by Reduced Productivity Due to Water Constraints, AGU Advances, 1, https://doi.org/10.1029/2020AV000180, 2020.

Maguire, A. J., Eitel, J. U. H., Griffin, K. L., Magney, T. S., Long, R. A., Vierling, L. A., Schmiege, S. C., Jennewein, J. S., Weygint, W. A., Boelman, N. T., and Bruner, S. G.: On the Functional Relationship Between Fluorescence and Photochemical Yields in Complex Evergreen Needleleaf Canopies, Geophysical Research Letters, 47, https://doi.org/10.1029/2020GL087858, 2020.

Marrs, J. K., Reblin, J. S., Logan, B. A., Allen, D. W., Reinmann, A. B., Bombard, D. M., Tabachnik, D., and Hutyra, L. R.: Solar-Induced Fluorescence Does Not Track Photosynthetic Carbon Assimilation Following Induced Stomatal Closure, Geophys. Res. Lett., 47, https://doi.org/10.1029/2020GL087956, 2020.

Mengistu, A. G., Tsidu, G. M., Koren, G., Kooreman, M. L., Boersma, F., Tagesson, T., Ardö, J., Nouvellon, Y., and Peters, W.: Sun-induced Fluorescence and Near Infrared Reflectance of vegetation track the seasonal dynamics of gross primary production over Africa, 23, 2020.

Mengistu, A. G., Mengistu Tsidu, G., Koren, G., Kooreman, M. L., Boersma, K. F., Tagesson, T., Ardö, J., Nouvellon, Y., and Peters, W.: Sun-induced fluorescence and near-infrared reflectance of vegetation track the seasonal dynamics of gross primary production over Africa, Biogeosciences, 18, 2843–2857, https://doi.org/10.5194/bg-18-2843-2021, 2021.

Meroni, M., Picchi, V., Rossini, M., Cogliati, S., Panigada, C., Nali, C., Lorenzini, G., and Colombo, R.: Leaf level early assessment of ozone injuries by passive fluorescence and photochemical reflectance index, International Journal of Remote Sensing, 29, 5409–5422, https://doi.org/10.1080/01431160802036292, 2008.

Miao, G., Guan, K., Yang, X., Bernacchi, C. J., Berry, J. A., DeLucia, E. H., Wu, J., Moore, C. E., Meacham, K., Cai, Y., Peng, B., Kimm, H., and Masters, M. D.: Sun-Induced Chlorophyll Fluorescence, Photosynthesis, and Light Use Efficiency of a Soybean Field from Seasonally Continuous Measurements, Journal of Geophysical Research: Biogeosciences, 123, 610–623, https://doi.org/10.1002/2017JG004180, 2018.

Mohammed, G. H., Colombo, R., Middleton, E. M., Rascher, U., van der Tol, C., Nedbal, L., Goulas, Y., Pérez-Priego, O., Damm, A., Meroni, M., Joiner, J., Cogliati, S., Verhoef, W., Malenovský, Z., Gastellu-Etchegorry, J.-P., Miller, J. R., Guanter, L., Moreno, J., Moya, I., Berry, J. A., Frankenberg, C., and Zarco-Tejada, P. J.: Remote sensing of solar-induced chlorophyll fluorescence (SIF) in vegetation: 50 years of progress, Remote Sensing of Environment, 231, 111177, https://doi.org/10.1016/j.rse.2019.04.030, 2019.

Moureaux, C., Bodson, B., and Aubinet, M.: Mesure des flux de CO2 et bilan carboné de grandes cultures: état de la question et méthodologie, Biotechnologie, Agronomie, Société et Environnement, 12, 303-315, 2008.

Nadeau, C. and Bengio, Y.: Inference for the Generalization Error, Machine Learning, 52, 239–281, https://doi.org/10.1023/A:1024068626366, 2003.

Pabon-Moreno, D. E., Migliavacca, M., Reichstein, M., and Mahecha, M. D.: On the potential of Sentinel-2 for estimating Gross Primary Production, IEEE Trans. Geosci. Remote Sensing, 1–1, https://doi.org/10.1109/TGRS.2022.3152272, 2022.

Paul-Limoges, E., Damm, A., Hueni, A., Liebisch, F., Eugster, W., Schaepman, M. E., and Buchmann, N.: Effect of environmental conditions on sun-induced fluorescence in a mixed forest and a cropland, Remote Sensing of Environment, 219, 310–323, https://doi.org/10.1016/j.rse.2018.10.018, 2018.

Porcar-Castell, A., Tyystjärvi, E., Atherton, J., van der Tol, C., Flexas, J., Pfündel, E. E., Moreno, J., Frankenberg, C., and Berry, J. A.: Linking chlorophyll a fluorescence to photosynthesis for remote sensing applications: mechanisms and challenges, Journal of Experimental Botany, 65, 4065–4095, https://doi.org/10.1093/jxb/eru191, 2014.

Running, S. W., Nemani, R. R., Heinsch, F. A., Zhao, M., Reeves, M., and Hashimoto, H.: A Continuous Satellite-Derived Measure of Global Terrestrial Primary Production, BioScience, 54, 547, https://doi.org/10.1641/0006-3568(2004)054 [0547: ACSMOG]2.0.CO;2, 2004.

Sippel, S., Reichstein, M., Ma, X., Mahecha, M. D., Lange, H., Flach, M., and Frank, D.: Drought, Heat, and the Carbon Cycle: a Review, Curr Clim Change Rep, 4, 266–286, https://doi.org/10.1007/s40641-018-0103-4, 2018.

Smith, W. K., Biederman, J. A., Scott, R. L., Moore, D. J. P., He, M., Kimball, J. S., Yan, D., Hudson, A., Barnes, M. L., MacBean, N., Fox, A. M., and Litvak, M. E.: Chlorophyll Fluorescence Better Captures Seasonal and Interannual Gross Primary Productivity Dynamics Across Dryland Ecosystems of Southwestern North America, Geophysical Research Letters, 45, 748–757, https://doi.org/10.1002/2017GL075922, 2018.

Soudani, K., Hmimina, G., Dufrêne, E., Berveiller, D., Delpierre, N., Ourcival, J.-M., Rambal, S., and Joffre, R.: Relationships between photochemical reflectance index and light-use efficiency in deciduous and evergreen broadleaf forests, Remote Sensing of Environment, 144, 73–84, https://doi.org/10.1016/j.rse.2014.01.017, 2014.

Sun, Y., Frankenberg, C., Jung, M., Joiner, J., Guanter, L., Köhler, P., and Magney, T.: Overview of Solar-Induced chlorophyll Fluorescence (SIF) from the Orbiting Carbon Observatory-2: Retrieval, cross-mission comparison, and global monitoring for GPP, Remote Sensing of Environment, 209, 808–823, https://doi.org/10.1016/j.rse.2018.02.016, 2018.

Tagliabue, G., Panigada, C., Dechant, B., Baret, F., Cogliati, S., Colombo, R., Migliavacca, M., Rademske, P., Schickling, A., Schüttemeyer, D., Verrelst, J., Rascher, U., Ryu, Y., and Rossini, M.: Exploring the spatial relationship between airborne-derived red and far-red sun-induced fluorescence and process-based GPP estimates in a forest ecosystem, Remote Sensing of Environment, 231, 111272, https://doi.org/10.1016/j.rse.2019.111272, 2019.

Toloşi, L. and Lengauer, T.: Classification with correlated features: unreliability of feature ranking and solutions, Bioinformatics, 27, 1986–1994, https://doi.org/10.1093/bioinformatics/btr300, 2011.

Tramontana, G., Jung, M., Schwalm, C. R., Ichii, K., Camps-Valls, G., Ráduly, B., Reichstein, M., Arain, M. A., Cescatti, A., Kiely, G., Merbold, L., Serrano-Ortiz, P., Sickert, S., Wolf, S., and Papale, D.: Predicting carbon dioxide and energy fluxes across global FLUXNET sites withregression algorithms, Biogeosciences, 13, 4291–4313, https://doi.org/10.5194/bg-13-4291-2016, 2016.

Tucker, C. J.: Red and photographic infrared linear combinations for monitoring vegetation, Remote Sensing of Environment, 8, 127–150, 1979.

Vermote, P. E. F., Roger, J. C., and Ray, J. P.: MODIS Land Surface Reflectance Science Computing Facility Principal Investigator: Dr. Eric F. Vermote Web site: http://modis-sr.ltdri.org Correspondence e-mail address: mod09@ltdri.org, 35, 2015.

Wang, N., Suomalainen, J., Bartholomeus, H., Kooistra, L., Masiliūnas, D., and Clevers, J. G. P. W.: Diurnal variation of sun-induced chlorophyll fluorescence of agricultural crops observed from a point-based spectrometer on a UAV, International Journal of Applied Earth Observation and Geoinformation, 96, 102276, https://doi.org/10.1016/j.jag.2020.102276, 2021.

Wang, X., Chen, J. M., and Ju, W.: Photochemical reflectance index (PRI) can be used to improve the relationship between gross primary productivity (GPP) and sun-induced

chlorophyll fluorescence (SIF), Remote Sensing of Environment, 246, 111888, https://doi.org/10.1016/j.rse.2020.111888, 2020.

Wang, X., Biederman, J. A., Knowles, J. F., Scott, R. L., Turner, A. J., Dannenberg, M. P., Köhler, P., Frankenberg, C., Litvak, M. E., Flerchinger, G. N., Law, B. E., Kwon, H., Reed, S. C., Parton, W. J., Barron-Gafford, G. A., and Smith, W. K.: Satellite solar-induced chlorophyll fluorescence and near-infrared reflectance capture complementary aspects of dryland vegetation productivity dynamics, Remote Sensing of Environment, 270, 112858, https://doi.org/10.1016/j.rse.2021.112858, 2022.

Wieneke, S., Ahrends, H., Damm, A., Pinto, F., Stadler, A., Rossini, M., and Rascher, U.: Airborne based spectroscopy of red and far-red sun-induced chlorophyll fluorescence: Implications for improved estimates of gross primary productivity, Remote Sensing of Environment, 184, 654–667, https://doi.org/10.1016/j.rse.2016.07.025, 2016.

Wieneke, S., Burkart, A., Cendrero-Mateo, M. P., Julitta, T., Rossini, M., Schickling, A., Schmidt, M., and Rascher, U.: Linking photosynthesis and sun-induced fluorescence at sub-daily to seasonal scales, Remote Sensing of Environment, 219, 247–258, https://doi.org/10.1016/j.rse.2018.10.019, 2018.

Wolanin, A., Camps-Valls, G., Gómez-Chova, L., Mateo-García, G., van der Tol, C., Zhang, Y., and Guanter, L.: Estimating crop primary productivity with Sentinel-2 and Landsat 8 using machine learning methods trained with radiative transfer simulations, Remote Sensing of Environment, 225, 441–457, https://doi.org/10.1016/j.rse.2019.03.002, 2019.

Wood, J. D., Griffis, T. J., Baker, J. M., Frankenberg, C., Verma, M., and Yuen, K.: Multiscale analyses of solar-induced florescence and gross primary production: Multiscale GPP-SIF RELATIONS, Geophys. Res. Lett., 44, 533–541, https://doi.org/10.1002/2016GL070775, 2017.

Wu, G., Guan, K., Jiang, C., Peng, B., Kimm, H., Chen, M., Yang, X., Wang, S., Suyker, A. E., Bernacchi, C. J., Moore, C. E., Zeng, Y., Berry, J. A., and Cendrero-Mateo, M. P.: Radiance-based NIR $_{v}$ as a proxy for GPP of corn and soybean, Environ. Res. Lett., 15, 034009, https://doi.org/10.1088/1748-9326/ab65cc, 2020.

Xiao, J., Chevallier, F., Gomez, C., Guanter, L., Hicke, J. A., Huete, A. R., Ichii, K., Ni, W., Pang, Y., Rahman, A. F., Sun, G., Yuan, W., Zhang, L., and Zhang, X.: Remote sensing of the terrestrial carbon cycle: A review of advances over 50 years, Remote Sensing of Environment, 233, 111383, https://doi.org/10.1016/j.rse.2019.111383, 2019.

Xiao, X.: Modeling gross primary production of temperate deciduous broadleaf forest using satellite images and climate data, Remote Sensing of Environment, 91, 256–270, https://doi.org/10.1016/j.rse.2004.03.010, 2004.

Yang, H., Yang, X., Zhang, Y., Heskel, M. A., Lu, X., Munger, J. W., Sun, S., and Tang, J.: Chlorophyll fluorescence tracks seasonal variations of photosynthesis from leaf to canopy in a temperate forest, Global Change Biology, 23, 2874–2886, https://doi.org/10.1111/gcb.13590, 2017.

Yang, P., van der Tol, C., Campbell, P. K. E., and Middleton, E. M.: Fluorescence Correction Vegetation Index (FCVI): A physically based reflectance index to separate physiological and non-physiological information in far-red sun-induced chlorophyll fluorescence, Remote Sensing of Environment, 240, 111676, https://doi.org/10.1016/j.rse.2020.111676, 2020a.

Yang, P., Van der Tol, C., Campbell, P. K. E., and Middleton, E. M.: Unravelling the physical and physiological basis for the solar-inducedchlorophyll fluorescence and photosynthesis relationship, Biodiversity and Ecosystem Function: Terrestrial, https://doi.org/10.5194/bg-2020-323, 2020b.

Yang, P., van der Tol, C., Campbell, P. K. E., and Middleton, E. M.: Unraveling the physical and physiological basis for the solar- induced chlorophyll fluorescence and photosynthesis relationship using continuous leaf and canopy measurements of a corn crop, Biogeosciences, 18, 441–465, https://doi.org/10.5194/bg-18-441-2021, 2021.

Yang, X., Tang, J., Mustard, J. F., Lee, J.-E., Rossini, M., Joiner, J., Munger, J. W., Kornfeld, A., and Richardson, A. D.: Solar-induced chlorophyll fluorescence that correlates with canopy photosynthesis on diurnal and seasonal scales in a temperate deciduous forest: Fluorescence and photosynthesis, Geophysical Research Letters, 42, 2977–2987, https://doi.org/10.1002/2015GL063201, 2015.

Yazbeck, T., Bohrer, G., Gentine, P., Ye, L., Arriga, N., Bernhofer, C., Blanken, P. D., Desai, A. R., Durden, D., Knohl, A., Kowalska, N., Metzger, S., Mölder, M., Noormets, A., Novick, K., Scott, R. L., Šigut, L., Soudani, K., Ueyama, M., and Varlagin, A.: Site Characteristics Mediate the Relationship Between Forest Productivity and Satellite Measured Solar Induced Fluorescence, Front. For. Glob. Change, 4, 695269, https://doi.org/10.3389/ffgc.2021.695269, 2021.

Zeng, Y., Badgley, G., Dechant, B., Ryu, Y., Chen, M., and Berry, J. A.: A practical approach for estimating the escape ratio of near-infrared solar-induced chlorophyll fluorescence, Remote Sensing of Environment, 232, 111209, https://doi.org/10.1016/j.rse.2019.05.028, 2019.

Zhang, J., Xiao, J., Tong, X., Zhang, J., Meng, P., Li, J., Liu, P., and Yu, P.: NIRv and SIF better estimate phenology than NDVI and EVI: Effects of spring and autumn phenology on ecosystem production of planted forests, Agricultural and Forest Meteorology, 315, 108819, https://doi.org/10.1016/j.agrformet.2022.108819, 2022.

Zhang, Y., Xiao, X., Wu, X., Zhou, S., Zhang, G., Qin, Y., and Dong, J.: A global moderate resolution dataset of gross primary production of vegetation for 2000–2016, Sci Data, 4, 170165, https://doi.org/10.1038/sdata.2017.165, 2017.

Zhang, Y., Xiao, X., Zhang, Y., Wolf, S., Zhou, S., Joiner, J., Guanter, L., Verma, M., Sun, Y., Yang, X., Paul-Limoges, E., Gough, C. M., Wohlfahrt, G., Gioli, B., van der Tol, C., Yann, N., Lund, M., and de Grandcourt, A.: On the relationship between sub-daily instantaneous and daily total gross primary production: Implications for interpreting satellite-based SIF retrievals, Remote Sensing of Environment, 205, 276–289, https://doi.org/10.1016/j.rse.2017.12.009, 2018.

Zhang, Y., Migliavacca, M., Penuelas, J., and Ju, W.: Advances in hyperspectral remote sensing of vegetation traits and functions, Remote Sensing of Environment, 252, 112121, https://doi.org/10.1016/j.rse.2020.112121, 2021a.

Zhang, Y., Zhang, Q., Liu, L., Zhang, Y., Wang, S., Ju, W., Zhou, G., Zhou, L., Tang, J., Zhu, X., Wang, F., Huang, Y., Zhang, Z., Qiu, B., Zhang, X., Wang, S., Huang, C., Tang, X., and Zhang, J.: ChinaSpec: a Network for Long-term Ground-based Measurements of Solar-induced Fluorescence in China, J Geophys Res Biogeosci, https://doi.org/10.1029/2020JG006042, 2021b.

Zhang, Z., Zhang, Y., Porcar-Castell, A., Joiner, J., Guanter, L., Yang, X., Migliavacca, M., Ju, W., Sun, Z., Chen, S., Martini, D., Zhang, Q., Li, Z., Cleverly, J., Wang, H., and Goulas, Y.: Reduction of structural impacts and distinction of photosynthetic pathways in a global estimation of GPP from space-borne solar-induced chlorophyll fluorescence, Remote Sensing of Environment, 240, 111722, https://doi.org/10.1016/j.rse.2020.111722, 2020.

Drought 2018 Team and ICOS Ecosystem Thematic Centre: Drought-2018 ecosystem eddy covariance flux product for 52 stations in FLUXNET-Archive format, doi:10.18160/YVR0-4898, 2020. Last acces: 12/21/2021

ICOS RI. Ecosystem final quality (L2) product in ETC-Archive format - release 2022-1. https://doi.org/10.18160/PAD9-HQHU, 2022. Last acces: 12/21/2021

Dataset Provider: NASA LP DAAC at the USGS EROS Center. MODIS Terra : https://doi.org/10.5067/MODIS/MOD09GA.006, 2002. MODIS Aqua: https://doi.org/10.5067/MODIS/MYD09GQ.006, 2002. Last access: 10/18/2021.

Philipp Koehler, & Christian Frankenberg. (2020). Ungridded TROPOMI SIF (at 740nm) (1.0) [Data set]. CaltechDATA. https://doi.org/10.22002/D1.1347. Last access: 6/14/2021.

References Chapter 4: Data-based investigation of the effects of canopy structure and shadows on chlorophyll fluorescence in a deciduous oak forest

Aasen, Van Wittenberghe, Medina, Damm, Goulas, Wieneke, Hueni, Malenovský, Alonso, Pacheco-Labrador, Cendrero-Mateo, Tomelleri, Burkart, Cogliati, Rascher, and Arthur: Sun-Induced Chlorophyll Fluorescence II: Review of Passive Measurement Setups, Protocols, and Their Application at the Leaf to Canopy Level, Remote Sensing, 11, 927, https://doi.org/10.3390/rs11080927, 2019.

Badgley, G., Field, C. B., and Berry, J. A.: Canopy near-infrared reflectance and terrestrial photosynthesis, Science Advances, 3, e1602244, https://doi.org/10.1126/sciadv.1602244, 2017.

Baker, N. R.: Chlorophyll Fluorescence: A Probe of Photosynthesis In Vivo, Annual Review of Plant Biology, 59, 89–113, https://doi.org/10.1146/annurev.arplant.59.032607.092759, 2008.

Balde, H., Hmimina, G., Goulas, Y., Latouche, G., and Soudani, K.: Synergy between TROPOMI sun-induced chlorophyll fluorescence and MODIS spectral reflectance for understanding the dynamics of gross primary productivity at Integrated Carbon Observatory System (ICOS) ecosystem flux sites, Biogeosciences, 20, 1473–1490, https://doi.org/10.5194/bg-20-1473-2023, 2023.

Biriukova, K., Pacheco-Labrador, J., Migliavacca, M., Mahecha, M. D., Gonzalez-Cascon, R., Martín, M. P., and Rossini, M.: Performance of Singular Spectrum Analysis in Separating Seasonal and Fast Physiological Dynamics of Solar-Induced Chlorophyll Fluorescence and PRI Optical Signals, Journal of Geophysical Research: Biogeosciences, 126, e2020JG006158, https://doi.org/10.1029/2020JG006158, 2021.

Breiman, L.: Random Forests, Machine Learning, 45, 5–32, https://doi.org/10.1023/A:1010933404324, 2001.

Campbell, P., Huemmrich, K., Middleton, E., Ward, L., Julitta, T., Daughtry, C., Burkart, A., Russ, A., and Kustas, W.: Diurnal and Seasonal Variations in Chlorophyll Fluorescence Associated with Photosynthesis at Leaf and Canopy Scales, Remote Sensing, 11, 488, https://doi.org/10.3390/rs11050488, 2019.

Chang, C. Y., Wen, J., Han, J., Kira, O., LeVonne, J., Melkonian, J., Riha, S. J., Skovira, J., Ng, S., Gu, L., Wood, J. D., Näthe, P., and Sun, Y.: Unpacking the drivers of diurnal dynamics of sun-induced chlorophyll fluorescence (SIF): Canopy structure, plant physiology, instrument configuration and retrieval methods, Remote Sensing of Environment, 265, 112672, https://doi.org/10.1016/j.rse.2021.112672, 2021.

Cogliati, S., Verhoef, W., Kraft, S., Sabater, N., Alonso, L., Vicent, J., Moreno, J., Drusch, M., and Colombo, R.: Retrieval of sun-induced fluorescence using advanced spectral fitting methods, Remote Sensing of Environment, 169, 344–357, https://doi.org/10.1016/j.rse.2015.08.022, 2015.

Damm, A., Guanter, L., Paul-Limoges, E., van der Tol, C., Hueni, A., Buchmann, N., Eugster, W., Ammann, C., and Schaepman, M. E.: Far-red sun-induced chlorophyll fluorescence shows ecosystem-specific relationships to gross primary production: An assessment based on observational and modeling approaches, Remote Sensing of Environment, 166, 91–105, https://doi.org/10.1016/j.rse.2015.06.004, 2015.

Daumard, F., Goulas, Y., Champagne, S., Fournier, A., Ounis, A., Olioso, A., and Moya, I.: Continuous Monitoring of Canopy Level Sun-Induced Chlorophyll Fluorescence During the Growth of a Sorghum Field, IEEE Transactions on Geoscience and Remote Sensing, 50, 4292–4300, https://doi.org/10.1109/TGRS.2012.2193131, 2012.

De Cannière, S., Vereecken, H., Defourny, P., and Jonard, F.: Remote Sensing of Instantaneous Drought Stress at Canopy Level Using Sun-Induced Chlorophyll Fluorescence and Canopy Reflectance, Remote Sensing, 14, 2642, https://doi.org/10.3390/rs14112642, 2022.

Dechant, B., Ryu, Y., Badgley, G., Zeng, Y., Berry, J. A., Zhang, Y., Goulas, Y., Li, Z., Zhang, Q., Kang, M., Li, J., and Moya, I.: Canopy structure explains the relationship between photosynthesis and sun-induced chlorophyll fluorescence in crops, Remote Sensing of Environment, 241, 111733, https://doi.org/10.1016/j.rse.2020.111733, 2020.

Dechant, B., Ryu, Y., Badgley, G., Köhler, P., Rascher, U., Migliavacca, M., Zhang, Y., Tagliabue, G., Guan, K., Rossini, M., Goulas, Y., Zeng, Y., Frankenberg, C., and Berry, J. A.: NIRVP: A robust structural proxy for sun-induced chlorophyll fluorescence and photosynthesis across scales, Remote Sensing of Environment, 268, 112763, https://doi.org/10.1016/j.rse.2021.112763, 2022.

Delpierre, N., Berveiller, D., Granda, E., and Dufrêne, E.: Wood phenology, not carbon input, controls the interannual variability of wood growth in a temperate oak forest, New Phytologist, 210, 459–470, https://doi.org/10.1111/nph.13771, 2016.

Drusch, M., Moreno, J., Del Bello, U., Franco, R., Goulas, Y., Huth, A., Kraft, S., Middleton, E. M., Miglietta, F., Mohammed, G., Nedbal, L., Rascher, U., Schuttemeyer, D., and Verhoef, W.: The FLuorescence EXplorer Mission Concept—ESA's Earth Explorer 8, IEEE Trans. Geosci. Remote Sensing, 55, 1273–1284, https://doi.org/10.1109/TGRS.2016.2621820, 2017.

Frankenberg, C., Fisher, J. B., Worden, J., Badgley, G., Saatchi, S. S., Lee, J.-E., Toon, G. C., Butz, A., Jung, M., Kuze, A., and Yokota, T.: New global observations of the terrestrial carbon cycle from GOSAT: Patterns of plant fluorescence with gross primary productivity: CHLOROPHYLL FLUORESCENCE FROM SPACE, Geophysical Research Letters, 38, n/a-n/a, https://doi.org/10.1029/2011GL048738, 2011.

Gao, S., Huete, A., Kobayashi, H., Doody, T. M., Liu, W., Wang, Y., Zhang, Y., and Lu, X.: Simulation of solar-induced chlorophyll fluorescence in a heterogeneous forest using 3-D radiative transfer modelling and airborne LiDAR, ISPRS Journal of Photogrammetry and Remote Sensing, 191, 1–17, https://doi.org/10.1016/j.isprsjprs.2022.07.004, 2022.

Goulas, Y., Fournier, A., Daumard, F., Champagne, S., Ounis, A., Marloie, O., and Moya, I.: Gross Primary Production of a Wheat Canopy Relates Stronger to Far Red Than to Red Solar-Induced Chlorophyll Fluorescence, Remote Sensing, 9, 97, https://doi.org/10.3390/rs9010097, 2017.

Guanter, L., Zhang, Y., Jung, M., Joiner, J., Voigt, M., Berry, J. A., Frankenberg, C., Huete, A. R., Zarco-Tejada, P., Lee, J.-E., Moran, M. S., Ponce-Campos, G., Beer, C., Camps-Valls, G., Buchmann, N., Gianelle, D., Klumpp, K., Cescatti, A., Baker, J. M., and Griffis, T. J.: Global and time-resolved monitoring of crop photosynthesis with chlorophyll fluorescence, Proc. Natl. Acad. Sci. U.S.A., 111, https://doi.org/10.1073/pnas.1320008111, 2014.

He, L., Magney, T., Dutta, D., Yin, Y., Köhler, P., Grossmann, K., Stutz, J., Dold, C., Hatfield, J., Guan, K., Peng, B., and Frankenberg, C.: From the Ground to Space: Using Solar-Induced Chlorophyll Fluorescence to Estimate Crop Productivity, Geophysical Research Letters, 47, https://doi.org/10.1029/2020GL087474, 2020.

Jonard, F., De Cannière, S., Brüggemann, N., Gentine, P., Short Gianotti, D. J., Lobet, G., Miralles, D. G., Montzka, C., Pagán, B. R., Rascher, U., and Vereecken, H.: Value of sun-induced chlorophyll fluorescence for quantifying hydrological states and fluxes: Current status and challenges, Agricultural and Forest Meteorology, 291, 108088, https://doi.org/10.1016/j.agrformet.2020.108088, 2020.

Li, X. and Xiao, J.: TROPOMI observations allow for robust exploration of the relationship between solar-induced chlorophyll fluorescence and terrestrial gross primary production, Remote Sensing of Environment, 268, 112748, https://doi.org/10.1016/j.rse.2021.112748, 2022.

Li, Z., Zhang, Q., Li, J., Yang, X., Wu, Y., Zhang, Z., Wang, S., Wang, H., and Zhang, Y.: Solar-induced chlorophyll fluorescence and its link to canopy photosynthesis in maize from continuous ground measurements, Remote Sensing of Environment, 236, 111420, https://doi.org/10.1016/j.rse.2019.111420, 2020.

Lin, J., Shen, Q., Wu, J., Zhao, W., and Liu, L.: Assessing the Potential of Downscaled Far Red Solar-Induced Chlorophyll Fluorescence from the Canopy to Leaf Level for Drought Monitoring in Winter Wheat, Remote Sensing, 14, 1357, https://doi.org/10.3390/rs14061357, 2022.

Liu, Y., Chen, J. M., He, L., Zhang, Z., Wang, R., Rogers, C., Fan, W., de Oliveira, G., and Xie, X.: Non-linearity between gross primary productivity and far-red solar-induced chlorophyll fluorescence emitted from canopies of major biomes, Remote Sensing of Environment, 271, 112896, https://doi.org/10.1016/j.rse.2022.112896, 2022.

Loayza, H., Moya, I., Quiroz, R., Ounis, A., and Goulas, Y.: Active and passive chlorophyll fluorescence measurements at canopy level on potato crops. Evidence of similitude of diurnal cycles of apparent fluorescence yields, Photosynth Res, 155, 271–288, https://doi.org/10.1007/s11120-022-00995-8, 2023.

Lopez Gonzalez, M. d. l. L. (2015), Seguimiento del estrés hídrico en la vid mediante técnicas de fluorescencia de la clorofila y otros métodos ópticos, Thesis, Universidad de Castilla-La-Mancha, Albacete.

Lu, X., Liu, Z., Zhao, F., and Tang, J.: Comparison of total emitted solar-induced chlorophyll fluorescence (SIF) and top-of-canopy (TOC) SIF in estimating photosynthesis, Remote Sensing of Environment, 251, 112083, https://doi.org/10.1016/j.rse.2020.112083, 2020.

Magney, T. S., Frankenberg, C., Fisher, J. B., Sun, Y., North, G. B., Davis, T. S., Kornfeld, A., and Siebke, K.: Connecting active to passive fluorescence with photosynthesis: a method for evaluating remote sensing measurements of Chl fluorescence, New Phytologist, 215, 1594–1608, https://doi.org/10.1111/nph.14662, 2017.

Maysonnave, J., Delpierre, N., François, C., Jourdan, M., Cornut, I., Bazot, S., Vincent, G., Morfin, A., and Berveiller, D.: Contribution of deep soil layers to the transpiration of a temperate deciduous forest: quantification and implications for the modelling of productivity, Ecology, https://doi.org/10.1101/2022.02.14.480025, 2022.

Mengistu, A. G., Mengistu Tsidu, G., Koren, G., Kooreman, M. L., Boersma, K. F., Tagesson, T., Ardö, J., Nouvellon, Y., and Peters, W.: Sun-induced fluorescence and near-infrared reflectance of vegetation track the seasonal dynamics of gross primary production over Africa, Biogeosciences, 18, 2843–2857, https://doi.org/10.5194/bg-18-2843-2021, 2021.

Meroni, M., Rossini, M., Guanter, L., Alonso, L., Rascher, U., Colombo, R., and Moreno, J.: Remote sensing of solar-induced chlorophyll fluorescence: Review of methods and applications, Remote Sensing of Environment, 113, 2037–2051, https://doi.org/10.1016/j.rse.2009.05.003, 2009.

Miao, G., Guan, K., Suyker, A. E., Yang, X., Arkebauer, T. J., Walter-Shea, E. A., Kimm, H., Hmimina, G. Y., Gamon, J. A., Franz, T. E., Frankenberg, C., Berry, J. A., and Wu, G.: Varying Contributions of Drivers to the Relationship Between Canopy Photosynthesis and Far-Red Sun-Induced Fluorescence for Two Maize Sites at Different Temporal Scales, Journal of Geophysical Research: Biogeosciences, 125, https://doi.org/10.1029/2019JG005051, 2020.

Mohammed, G. H., Colombo, R., Middleton, E. M., Rascher, U., van der Tol, C., Nedbal, L., Goulas, Y., Pérez-Priego, O., Damm, A., Meroni, M., Joiner, J., Cogliati, S., Verhoef, W., Malenovský, Z., Gastellu-Etchegorry, J.-P., Miller, J. R., Guanter, L., Moreno, J., Moya, I., Berry, J. A., Frankenberg, C., and Zarco-Tejada, P. J.: Remote sensing of solar-induced chlorophyll fluorescence (SIF) in vegetation: 50 years of progress, Remote Sensing of Environment, 231, 111177, https://doi.org/10.1016/j.rse.2019.04.030, 2019.

Morozumi, T., Kato, T., Kobayashi, H., Sakai, Y., Tsujimoto, K., Nakashima, N., Buareal, K., Lan, W., and Ninomiya, H.: Row orientation influences the diurnal cycle of solar-induced chlorophyll fluorescence emission from wheat canopy, as demonstrated by radiative transfer modeling, Agricultural and Forest Meteorology, 339, 109576, https://doi.org/10.1016/j.agrformet.2023.109576, 2023.

Moya, I., Loayza, H., López, M. L., Quiroz, R., Ounis, A., and Goulas, Y.: Canopy chlorophyll fluorescence applied to stress detection using an easy-to-build micro-lidar, Photosynthesis Research, 142, 1–15, https://doi.org/10.1007/s11120-019-00642-9, 2019.

Nichol, C. J., Drolet, G., Porcar-Castell, A., Wade, T., Sabater, N., Middleton, E. M., MacLellan, C., Levula, J., Mammarella, I., Vesala, T., and Atherton, J.: Diurnal and Seasonal Solar Induced Chlorophyll Fluorescence and Photosynthesis in a Boreal Scots Pine Canopy, Remote Sensing, 11, 273, https://doi.org/10.3390/rs11030273, 2019.

Ounis, A., Evain, S., Flexas, J., Tosti, S., and Moya, I.: Adaptation of a PAM-fluorometer for remote sensing of chlorophyll fluorescence, Photosynthesis Research, 68, 113–120, https://doi.org/10.1023/A:1011843131298, 2001.

Ounis, A., Bach, J., Mahjoub, A., Daumard, F., Moya, I., and Goulas, Y.: Combined use of LIDAR and hyperspectral measurements for remote sensing of fluorescence and vertical profile of canopies, Rev. Teledetec., 87, https://doi.org/10.4995/raet.2015.3982, 2016.

Paul-Limoges, E., Damm, A., Hueni, A., Liebisch, F., Eugster, W., Schaepman, M. E., and Buchmann, N.: Effect of environmental conditions on sun-induced fluorescence in a mixed forest and a cropland, Remote Sensing of Environment, 219, 310–323, https://doi.org/10.1016/j.rse.2018.10.018, 2018.

Porcar-Castell, A., Tyystjärvi, E., Atherton, J., van der Tol, C., Flexas, J., Pfündel, E. E., Moreno, J., Frankenberg, C., and Berry, J. A.: Linking chlorophyll a fluorescence to photosynthesis for remote sensing applications: mechanisms and challenges, Journal of Experimental Botany, 65, 4065–4095, https://doi.org/10.1093/jxb/eru191, 2014.

Rascher, U., Alonso, L., Burkart, A., Cilia, C., Cogliati, S., Colombo, R., Damm, A., Drusch, M., Guanter, L., Hanus, J., Hyvärinen, T., Julitta, T., Jussila, J., Kataja, K., Kokkalis, P., Kraft, S., Kraska, T., Matveeva, M., Moreno, J., Muller, O., Panigada, C., Pikl, M., Pinto, F., Prey, L., Pude, R., Rossini, M., Schickling, A., Schurr, U., Schüttemeyer, D., Verrelst, J., and Zemek, F.: Sun-induced fluorescence - a new probe of photosynthesis: First maps from the imaging spectrometer *HyPlant*, Glob Change Biol, 21, 4673–4684, https://doi.org/10.1111/gcb.13017, 2015.

Soudani, K., Hmimina, G., Dufrêne, E., Berveiller, D., Delpierre, N., Ourcival, J.-M., Rambal, S., and Joffre, R.: Relationships between photochemical reflectance index and light-use efficiency in deciduous and evergreen broadleaf forests, Remote Sensing of Environment, 144, 73–84, https://doi.org/10.1016/j.rse.2014.01.017, 2014.

Soudani, K., Delpierre, N., Berveiller, D., Hmimina, G., Pontailler, J.-Y., Seureau, L., Vincent, G., and Dufrêne, É.: A survey of proximal methods for monitoring leaf phenology in temperate deciduous forests, Biogeosciences, 18, 3391–3408, https://doi.org/10.5194/bg-18-3391-2021, 2021.

Sun, Y., Gu, L., Wen, J., van der Tol, C., Porcar-Castell, A., Joiner, J., Chang, C. Y., Magney, T., Wang, L., Hu, L., Rascher, U., Zarco-Tejada, P., Barrett, C. B., Lai, J., Han, J., and Luo, Z.: From remotely sensed solar-induced chlorophyll fluorescence to ecosystem structure, function, and service: Part I—Harnessing theory, Global Change Biology, 29, 2926–2952, https://doi.org/10.1111/gcb.16634, 2023a.

Sun, Y., Wen, J., Gu, L., Joiner, J., Chang, C. Y., van der Tol, C., Porcar-Castell, A., Magney, T., Wang, L., Hu, L., Rascher, U., Zarco-Tejada, P., Barrett, C. B., Lai, J., Han, J., and Luo, Z.: From remotely-sensed solar-induced chlorophyll fluorescence to ecosystem structure, function, and service: Part II—Harnessing data, Global Change Biology, 29, 2893–2925, https://doi.org/10.1111/gcb.16646, 2023b.

Ustin, S. L. and Middleton, E. M.: Current and near-term advances in Earth observation for ecological applications, Ecol Process, 10, 1, https://doi.org/10.1186/s13717-020-00255-4, 2021.

Verma, M., Schimel, D., Evans, B., Frankenberg, C., Beringer, J., Drewry, D. T., Magney, T., Marang, I., Hutley, L., Moore, C., and Eldering, A.: Effect of environmental conditions on the relationship between solar-induced fluorescence and gross primary productivity at an OzFlux grassland site: OCO SIF, MODIS, and GPP, Journal of Geophysical Research: Biogeosciences, 122, 716–733, https://doi.org/10.1002/2016JG003580, 2017.

Wang, N., Suomalainen, J., Bartholomeus, H., Kooistra, L., Masiliūnas, D., and Clevers, J. G. P. W.: Diurnal variation of sun-induced chlorophyll fluorescence of agricultural crops observed from a point-based spectrometer on a UAV, International Journal of Applied Earth Observation and Geoinformation, 96, 102276, https://doi.org/10.1016/j.jag.2020.102276, 2021.

Wang, X., Biederman, J. A., Knowles, J. F., Scott, R. L., Turner, A. J., Dannenberg, M. P., Köhler, P., Frankenberg, C., Litvak, M. E., Flerchinger, G. N., Law, B. E., Kwon, H., Reed, S. C., Parton, W. J., Barron-Gafford, G. A., and Smith, W. K.: Satellite solar-induced chlorophyll fluorescence and near-infrared reflectance capture complementary aspects of dryland vegetation productivity dynamics, Remote Sensing of Environment, 270, 112858, https://doi.org/10.1016/j.rse.2021.112858, 2022.

Wood, J. D., Griffis, T. J., Baker, J. M., Frankenberg, C., Verma, M., and Yuen, K.: Multiscale analyses of solar-induced florescence and gross primary production: Multiscale GPP-SIF RELATIONS, Geophys. Res. Lett., 44, 533–541, https://doi.org/10.1002/2016GL070775, 2017.

Xu, S., Atherton, J., Riikonen, A., Zhang, C., Oivukkamäki, J., MacArthur, A., Honkavaara, E., Hakala, T., Koivumäki, N., Liu, Z., and Porcar-Castell, A.: Structural and photosynthetic dynamics mediate the response of SIF to water stress in a potato crop, Remote Sensing of Environment, 263, 112555, https://doi.org/10.1016/j.rse.2021.112555, 2021.

Yang, H., Yang, X., Zhang, Y., Heskel, M. A., Lu, X., Munger, J. W., Sun, S., and Tang, J.: Chlorophyll fluorescence tracks seasonal variations of photosynthesis from leaf to canopy in a temperate forest, Global Change Biology, 23, 2874–2886, https://doi.org/10.1111/gcb.13590, 2017.

Yang, P. and van der Tol, C.: Linking canopy scattering of far-red sun-induced chlorophyll fluorescence with reflectance, Remote Sensing of Environment, 209, 456–467, https://doi.org/10.1016/j.rse.2018.02.029, 2018.

Yang, P., van der Tol, C., Campbell, P. K. E., and Middleton, E. M.: Fluorescence Correction Vegetation Index (FCVI): A physically based reflectance index to separate physiological and non-physiological information in far-red sun-induced chlorophyll fluorescence, Remote Sensing of Environment, 240, 111676, https://doi.org/10.1016/j.rse.2020.111676, 2020.

Yazbeck, T., Bohrer, G., Gentine, P., Ye, L., Arriga, N., Bernhofer, C., Blanken, P. D., Desai, A. R., Durden, D., Knohl, A., Kowalska, N., Metzger, S., Mölder, M., Noormets, A., Novick, K., Scott, R. L., Šigut, L., Soudani, K., Ueyama, M., and Varlagin, A.: Site Characteristics Mediate the Relationship Between Forest Productivity and Satellite Measured Solar Induced Fluorescence, Front. For. Glob. Change, 4, 695269, https://doi.org/10.3389/ffgc.2021.695269, 2021.

Zeng, Y., Badgley, G., Dechant, B., Ryu, Y., Chen, M., and Berry, J. A.: A practical approach for estimating the escape ratio of near-infrared solar-induced chlorophyll fluorescence, Remote Sensing of Environment, 232, 111209, https://doi.org/10.1016/j.rse.2019.05.028, 2019.

Zeng, Y., Chen, M., Hao, D., Damm, A., Badgley, G., Rascher, U., Johnson, J. E., Dechant, B., Siegmann, B., Ryu, Y., Qiu, H., Krieger, V., Panigada, C., Celesti, M., Miglietta, F., Yang, X., and Berry, J. A.: Combining near-infrared radiance of vegetation and fluorescence spectroscopy to detect effects of abiotic changes and stresses, Remote Sensing of Environment, 270, 112856, https://doi.org/10.1016/j.rse.2021.112856, 2022a.

Zeng, Y., Hao, D., Huete, A., Dechant, B., Berry, J., Chen, J. M., Joiner, J., Frankenberg, C., Bond-Lamberty, B., Ryu, Y., Xiao, J., Asrar, G. R., and Chen, M.: Optical vegetation indices for monitoring terrestrial ecosystems globally, Nat Rev Earth Environ, 3, 477–493, https://doi.org/10.1038/s43017-022-00298-5, 2022b.

Zhang, Y., Zhang, Q., Liu, L., Zhang, Y., Wang, S., Ju, W., Zhou, G., Zhou, L., Tang, J., Zhu, X., Wang, F., Huang, Y., Zhang, Z., Qiu, B., Zhang, X., Wang, S., Huang, C., Tang, X., and Zhang, J.: ChinaSpec: a Network for Long-term Ground-based Measurements of Solar-induced Fluorescence in China, J Geophys Res Biogeosci, https://doi.org/10.1029/2020JG006042, 2021.

Zhang, Z. and Zhang, Y.: Solar angle matters: Diurnal pattern of solar-induced chlorophyll fluorescence from OCO-3 and TROPOMI, Remote Sensing of Environment, 285, 113380, https://doi.org/10.1016/j.rse.2022.113380, 2023.

References Chapter 5: Investigating the responses of sun-induced chlorophyll fluorescence, gross primary production and of the relation between the two to abiotic factors in a temperate deciduous forest

Badgley, G., Field, C. B., and Berry, J. A.: Canopy near-infrared reflectance and terrestrial photosynthesis, Science Advances, 3, e1602244, https://doi.org/10.1126/sciadv.1602244, 2017.

Balde, H., Hmimina, G., Goulas, Y., Latouche, G., and Soudani, K.: Synergy between TROPOMI sun-induced chlorophyll fluorescence and MODIS spectral reflectance for understanding the dynamics of gross primary productivity at Integrated Carbon Observatory System (ICOS) ecosystem flux sites, Biogeosciences, 20, 1473–1490, https://doi.org/10.5194/bg-20-1473-2023, 2023.

Berger, K., Machwitz, M., Kycko, M., Kefauver, S. C., Van Wittenberghe, S., Gerhards, M., Verrelst, J., Atzberger, C., van der Tol, C., Damm, A., Rascher, U., Herrmann, I., Paz, V. S., Fahrner, S., Pieruschka, R., Prikaziuk, E., Buchaillot, Ma. L., Halabuk, A., Celesti, M., Koren, G., Gormus, E. T., Rossini, M., Foerster, M., Siegmann, B., Abdelbaki, A., Tagliabue, G., Hank, T., Darvishzadeh, R., Aasen, H., Garcia, M., Pôças,

I., Bandopadhyay, S., Sulis, M., Tomelleri, E., Rozenstein, O., Filchev, L., Stancile, G., and Schlerf, M.: Multi-sensor spectral synergies for crop stress detection and monitoring in the optical domain: A review, Remote Sensing of Environment, 280, 113198, https://doi.org/10.1016/j.rse.2022.113198, 2022.

Breiman, L.: Random Forests, Machine Learning, 45, 5–32, https://doi.org/10.1023/A:1010933404324, 2001.

Cendrero-Mateo, Wieneke, Damm, Alonso, Pinto, Moreno, Guanter, Celesti, Rossini, Sabater, Cogliati, Julitta, Rascher, Goulas, Aasen, Pacheco-Labrador, and Arthur: Sun-Induced Chlorophyll Fluorescence III: Benchmarking Retrieval Methods and Sensor Characteristics for Proximal Sensing, Remote Sensing, 11, 962, https://doi.org/10.3390/rs11080962, 2019.

Cheng, X., Hu, M., Zhou, Y., Wang, F., Liu, L., Wang, Y., Huang, H., and Zhang, J.: The divergence of micrometeorology sensitivity leads to changes in GPP/SIF between cork oak and poplar, Agricultural and Forest Meteorology, 326, 109189, https://doi.org/10.1016/j.agrformet.2022.109189, 2022.

Damm, A., Guanter, L., Paul-Limoges, E., van der Tol, C., Hueni, A., Buchmann, N., Eugster, W., Ammann, C., and Schaepman, M. E.: Far-red sun-induced chlorophyll fluorescence shows ecosystem-specific relationships to gross primary production: An assessment based on observational and modeling approaches, Remote Sensing of Environment, 166, 91–105, https://doi.org/10.1016/j.rse.2015.06.004, 2015.

Daumard, F., Goulas, Y., Champagne, S., Fournier, A., Ounis, A., Olioso, A., and Moya, I.: Continuous Monitoring of Canopy Level Sun-Induced Chlorophyll Fluorescence During the Growth of a Sorghum Field, IEEE Transactions on Geoscience and Remote Sensing, 50, 4292–4300, https://doi.org/10.1109/TGRS.2012.2193131, 2012.

De Cannière, S., Vereecken, H., Defourny, P., and Jonard, F.: Remote Sensing of Instantaneous Drought Stress at Canopy Level Using Sun-Induced Chlorophyll Fluorescence and Canopy Reflectance, Remote Sensing, 14, 2642, https://doi.org/10.3390/rs14112642, 2022.

Delpierre, N., Berveiller, D., Granda, E., and Dufrêne, E.: Wood phenology, not carbon input, controls the interannual variability of wood growth in a temperate oak forest, New Phytologist, 210, 459–470, https://doi.org/10.1111/nph.13771, 2016.

Durand, M., Murchie, E. H., Lindfors, A. V., Urban, O., Aphalo, P. J., and Robson, T. M.: Diffuse solar radiation and canopy photosynthesis in a changing environment, Agricultural and Forest Meteorology, 311, 108684, https://doi.org/10.1016/j.agrformet.2021.108684, 2021.

Frankenberg, C., Fisher, J. B., Worden, J., Badgley, G., Saatchi, S. S., Lee, J.-E., Toon, G. C., Butz, A., Jung, M., Kuze, A., and Yokota, T.: New global observations of the terrestrial carbon cycle from GOSAT: Patterns of plant fluorescence with gross primary productivity: CHLOROPHYLL FLUORESCENCE FROM SPACE, Geophysical Research Letters, 38, n/a-n/a, https://doi.org/10.1029/2011GL048738, 2011.

Gamon, J. A., Serrano, L., and Surfus, J. S.: The photochemical reflectance index: an optical indicator of photosynthetic radiation use efficiency across species, functional types, and nutrient levels, Oecologia, 112, 492–501, https://doi.org/10.1007/s004420050337, 1997.

Goulas, Y., Fournier, A., Daumard, F., Champagne, S., Ounis, A., Marloie, O., and Moya, I.: Gross Primary Production of a Wheat Canopy Relates Stronger to Far Red Than to Red Solar-Induced Chlorophyll Fluorescence, Remote Sensing, 9, 97, https://doi.org/10.3390/rs9010097, 2017.

Helm, L. T., Shi, H., Lerdau, M. T., and Yang, X.: Solar-induced chlorophyll fluorescence and short-term photosynthetic response to drought, Ecological Applications, 30, https://doi.org/10.1002/eap.2101, 2020.

Hmimina, G., Dufrêne, E., and Soudani, K.: Relationship between photochemical reflectance index and leaf ecophysiological and biochemical parameters under two different water statuses: towards a rapid and efficient correction method using real-time measurements: Disentangling PRI variability, Plant Cell Environ, 37, 473–487, https://doi.org/10.1111/pce.12171, 2014.

Hu, M., Cheng, X., Zhang, J., Huang, H., Zhou, Y., Wang, X., Pan, Q., and Guan, C.: Temporal Variation in Tower-Based Solar-Induced Chlorophyll Fluorescence and Its Environmental Response in a Chinese Cork Oak Plantation, Remote Sensing, 15, 3568, https://doi.org/10.3390/rs15143568, 2023.

Intergovernmental Panel On Climate Change: Climate Change and Land: IPCC Special Report on Climate Change, Desertification, Land Degradation, Sustainable Land Management, Food Security, and Greenhouse Gas Fluxes in Terrestrial Ecosystems, 1st ed., Cambridge University Press, https://doi.org/10.1017/9781009157988, 2022.

Jonard, F., De Cannière, S., Brüggemann, N., Gentine, P., Short Gianotti, D. J., Lobet, G., Miralles, D. G., Montzka, C., Pagán, B. R., Rascher, U., and Vereecken, H.: Value of sun-induced chlorophyll fluorescence for quantifying hydrological states and fluxes: Current status and challenges, Agricultural and Forest Meteorology, 291, 108088, https://doi.org/10.1016/j.agrformet.2020.108088, 2020.

Kim, J., Ryu, Y., Dechant, B., Lee, H., Kim, H. S., Kornfeld, A., and Berry, J. A.: Solar-induced chlorophyll fluorescence is non-linearly related to canopy photosynthesis in a temperate evergreen needleleaf forest during the fall transition, Remote Sensing of Environment, 258, 112362, https://doi.org/10.1016/j.rse.2021.112362, 2021.

Kováč, D., Ač, A., Šigut, L., Peñuelas, J., Grace, J., and Urban, O.: Combining NDVI, PRI and the quantum yield of solar-induced fluorescence improves estimations of carbon fluxes in deciduous and evergreen forests, Science of The Total Environment, 829, 154681, https://doi.org/10.1016/j.scitotenv.2022.154681, 2022.

Li, Y.-T., Gao, H.-Y., and Zhang, Z.-S.: Effects of Environmental and Non-Environmental Factors on Dynamic Photosynthetic Carbon Assimilation in Leaves under Changing Light, Plants, 12, 2015, https://doi.org/10.3390/plants12102015, 2023.

Lu, X., Liu, Z., Zhao, F., and Tang, J.: Comparison of total emitted solar-induced chlorophyll fluorescence (SIF) and top-of-canopy (TOC) SIF in estimating photosynthesis, Remote Sensing of Environment, 251, 112083, https://doi.org/10.1016/j.rse.2020.112083, 2020.

Magney, T. S., Barnes, M. L., and Yang, X.: On the Covariation of Chlorophyll Fluorescence and Photosynthesis Across Scales, Geophysical Research Letters, 47, https://doi.org/10.1029/2020GL091098, 2020.

Marrs, J. K., Reblin, J. S., Logan, B. A., Allen, D. W., Reinmann, A. B., Bombard, D. M., Tabachnik, D., and Hutyra, L. R.: Solar-Induced Fluorescence Does Not Track Photosynthetic Carbon Assimilation Following Induced Stomatal Closure, Geophysical Research Letters, 47, https://doi.org/e2020GL087956 10.1029/2020gl087956, 2020.

Martini, D., Sakowska, K., Wohlfahrt, G., Pacheco-Labrador, J., van der Tol, C., Porcar-Castell, A., Magney, T. S., Carrara, A., Colombo, R., El-Madany, T. S., Gonzalez-Cascon, R., Martín, M. P., Julitta, T., Moreno, G., Rascher, U., Reichstein, M., Rossini, M., and Migliavacca, M.: Heatwave breaks down the linearity between sun-induced fluorescence and gross primary production, New Phytologist, 233, 2415–2428, https://doi.org/10.1111/nph.17920, 2022.

Maysonnave, J., Delpierre, N., François, C., Jourdan, M., Cornut, I., Bazot, S., Vincent, G., Morfin, A., and Berveiller, D.: Contribution of deep soil layers to the transpiration of a temperate deciduous forest: quantification and implications for the modelling of productivity, Ecology, https://doi.org/10.1101/2022.02.14.480025, 2022.

Miao, G., Guan, K., Suyker, A. E., Yang, X., Arkebauer, T. J., Walter-Shea, E. A., Kimm, H., Hmimina, G. Y., Gamon, J. A., Franz, T. E., Frankenberg, C., Berry, J. A., and Wu, G.: Varying Contributions of Drivers to the Relationship Between Canopy Photosynthesis and Far-Red Sun-Induced Fluorescence for Two Maize Sites at Different Temporal Scales, Journal of Geophysical Research: Biogeosciences, 125, https://doi.org/10.1029/2019JG005051, 2020.

Mohammed, G. H., Colombo, R., Middleton, E. M., Rascher, U., van der Tol, C., Nedbal, L., Goulas, Y., Pérez-Priego, O., Damm, A., Meroni, M., Joiner, J., Cogliati, S., Verhoef, W., Malenovský, Z., Gastellu-Etchegorry, J.-P., Miller, J. R., Guanter, L., Moreno, J., Moya, I., Berry, J. A., Frankenberg, C., and Zarco-Tejada, P. J.: Remote sensing of solar-induced chlorophyll fluorescence (SIF) in vegetation: 50 years of progress, Remote Sensing of Environment, 231, 111177, https://doi.org/10.1016/j.rse.2019.04.030, 2019.

Monteith, J. L.: Solar radiation and productivity in tropical ecosystems, Journal of Applied Ecology, 9, 747–766, 1972.

Pierrat, Z., Magney, T., Parazoo, N. C., Grossmann, K., Bowling, D. R., Seibt, U., Johnson, B., Helgason, W., Barr, A., Bortnik, J., Norton, A., Maguire, A., Frankenberg, C., and Stutz, J.: Diurnal and Seasonal Dynamics of Solar-Induced Chlorophyll Fluorescence, Vegetation Indices, and Gross Primary Productivity in the Boreal Forest, Journal of Geophysical Research: Biogeosciences, 127, e2021JG006588, https://doi.org/10.1029/2021JG006588, 2022a.

Pierrat, Z. A., Bortnik, J., Johnson, B., Barr, A., Magney, T., Bowling, D. R., Parazoo, N., Frankenberg, C., Seibt, U., and Stutz, J.: Forests for forests: combining vegetation indices with solar-induced chlorophyll fluorescence in random forest models improves gross primary productivity prediction in the boreal forest, Environ. Res. Lett., 17, 125006, https://doi.org/10.1088/1748-9326/aca5a0, 2022b.

Porcar-Castell, A., Tyystjärvi, E., Atherton, J., van der Tol, C., Flexas, J., Pfündel, E. E., Moreno, J., Frankenberg, C., and Berry, J. A.: Linking chlorophyll a fluorescence to photosynthesis for remote sensing applications: mechanisms and challenges, Journal of Experimental Botany, 65, 4065–4095, https://doi.org/10.1093/jxb/eru191, 2014.

Soudani, K., Hmimina, G., Dufrêne, E., Berveiller, D., Delpierre, N., Ourcival, J.-M., Rambal, S., and Joffre, R.: Relationships between photochemical reflectance index and light-use efficiency in deciduous and evergreen broadleaf forests, Remote Sensing of Environment, 144, 73–84, https://doi.org/10.1016/j.rse.2014.01.017, 2014.

Soudani, K., Delpierre, N., Berveiller, D., Hmimina, G., Pontailler, J.-Y., Seureau, L., Vincent, G., and Dufrêne, É.: A survey of proximal methods for monitoring leaf phenology in temperate deciduous forests, Biogeosciences, 18, 3391–3408, https://doi.org/10.5194/bg-18-3391-2021, 2021.

Sukhova, E., Yudina, L., Kior, A., Kior, D., Popova, A., Zolin, Y., Gromova, E., and Sukhov, V.: Modified Photochemical Reflectance Indices as New Tool for Revealing Influence of Drought and Heat on Pea and Wheat Plants, Plants, 11, 1308, https://doi.org/10.3390/plants11101308, 2022.

Sun, Y., Gu, L., Wen, J., van der Tol, C., Porcar-Castell, A., Joiner, J., Chang, C. Y., Magney, T., Wang, L., Hu, L., Rascher, U., Zarco-Tejada, P., Barrett, C. B., Lai, J., Han, J., and Luo, Z.: From remotely sensed solar-induced chlorophyll fluorescence to ecosystem structure, function, and service: Part I—Harnessing theory, Global Change Biology, 29, 2926–2952, https://doi.org/10.1111/gcb.16634, 2023a.

Sun, Y., Wen, J., Gu, L., Joiner, J., Chang, C. Y., van der Tol, C., Porcar-Castell, A., Magney, T., Wang, L., Hu, L., Rascher, U., Zarco-Tejada, P., Barrett, C. B., Lai, J., Han, J., and Luo, Z.: From remotely-sensed solar-induced chlorophyll fluorescence to ecosystem structure, function, and service: Part II—Harnessing data, Global Change Biology, 29, 2893–2925, https://doi.org/10.1111/gcb.16646, 2023b.

Tucker, C. J.: Red and photographic infrared linear combinations for monitoring vegetation, Remote Sensing of Environment, 8, 127–150, https://doi.org/10.1016/0034-4257(79)90013-0, 1979.

Wang, N., Clevers, J. G. P. W., Wieneke, S., Bartholomeus, H., and Kooistra, L.: Potential of UAV-based sun-induced chlorophyll fluorescence to detect water stress in sugar beet, Agricultural and Forest Meteorology, 323, 109033, https://doi.org/10.1016/j.agrformet.2022.109033, 2022.

Wang, X., Chen, J. M., and Ju, W.: Photochemical reflectance index (PRI) can be used to improve the relationship between gross primary productivity (GPP) and sun-induced

chlorophyll fluorescence (SIF), Remote Sensing of Environment, 246, 111888, https://doi.org/10.1016/j.rse.2020.111888, 2020.

Xiao, J., Chevallier, F., Gomez, C., Guanter, L., Hicke, J. A., Huete, A. R., Ichii, K., Ni, W., Pang, Y., Rahman, A. F., Sun, G., Yuan, W., Zhang, L., and Zhang, X.: Remote sensing of the terrestrial carbon cycle: A review of advances over 50 years, Remote Sensing of Environment, 233, 111383, https://doi.org/10.1016/j.rse.2019.111383, 2019.

Xiao, J., Fisher, J. B., Hashimoto, H., Ichii, K., and Parazoo, N. C.: Emerging satellite observations for diurnal cycling of ecosystem processes, Nat. Plants, 7, 877–887, https://doi.org/10.1038/s41477-021-00952-8, 2021.

Xu, S., Atherton, J., Riikonen, A., Zhang, C., Oivukkamäki, J., MacArthur, A., Honkavaara, E., Hakala, T., Koivumäki, N., Liu, Z., and Porcar-Castell, A.: Structural and photosynthetic dynamics mediate the response of SIF to water stress in a potato crop, Remote Sensing of Environment, 263, 112555, https://doi.org/10.1016/j.rse.2021.112555, 2021.

Zanotelli, D., Asensio, D., Schwarz, M., Benyahia, F., Hammerle, A., Abdelkader, A. B., Campos, F. B., Callesen, T., Andreotti, C., Montagnani, L., Tagliavini, M., and Wohlfahrt, G.: Vineyard water and carbon dioxide exchange during a heat wave, Copernicus Meetings, https://doi.org/10.5194/egusphere-egu23-10124, 2023.

Zeng, Y., Hao, D., Huete, A., Dechant, B., Berry, J., Chen, J. M., Joiner, J., Frankenberg, C., Bond-Lamberty, B., Ryu, Y., Xiao, J., Asrar, G. R., and Chen, M.: Optical vegetation indices for monitoring terrestrial ecosystems globally, Nat Rev Earth Environ, 3, 477–493, https://doi.org/10.1038/s43017-022-00298-5, 2022.

Zhang, J., Xiao, J., Tong, X., Zhang, J., Meng, P., Li, J., Liu, P., and Yu, P.: NIRv and SIF better estimate phenology than NDVI and EVI: Effects of spring and autumn phenology on ecosystem production of planted forests, Agricultural and Forest Meteorology, 315, 108819, https://doi.org/10.1016/j.agrformet.2022.108819, 2022.

Zhang, Z., Chen, J. M., Zhang, Y., and Li, M.: Improving the ability of solar-induced chlorophyll fluorescence to track gross primary production through differentiating sunlit and shaded leaves, Agricultural and Forest Meteorology, 341, 109658, https://doi.org/10.1016/j.agrformet.2023.109658, 2023.

References Chapter 6: General conclusions, discussion and perspectives

Ač, A., Malenovský, Z., Olejníčková, J., Gallé, A., Rascher, U., and Mohammed, G.: Meta-analysis assessing potential of steady-state chlorophyll fluorescence for remote sensing detection of plant water, temperature and nitrogen stress, Remote Sensing of Environment, 168, 420–436, https://doi.org/10.1016/j.rse.2015.07.022, 2015.

Balde, H., Hmimina, G., Goulas, Y., Latouche, G., and Soudani, K.: Synergy between TROPOMI sun-induced chlorophyll fluorescence and MODIS spectral reflectance for understanding the dynamics of gross primary productivity at Integrated Carbon Observatory System (ICOS) ecosystem flux sites, Biogeosciences, 20, 1473–1490, https://doi.org/10.5194/bg-20-1473-2023, 2023.

Berger, K., Machwitz, M., Kycko, M., Kefauver, S. C., Van Wittenberghe, S., Gerhards, M., Verrelst, J., Atzberger, C., van der Tol, C., Damm, A., Rascher, U., Herrmann, I., Paz, V. S., Fahrner, S., Pieruschka, R., Prikaziuk, E., Buchaillot, Ma. L., Halabuk, A., Celesti, M., Koren, G., Gormus, E. T., Rossini, M., Foerster, M., Siegmann, B., Abdelbaki, A., Tagliabue, G., Hank, T., Darvishzadeh, R., Aasen, H., Garcia, M., Pôças, I., Bandopadhyay, S., Sulis, M., Tomelleri, E., Rozenstein, O., Filchev, L., Stancile, G., and Schlerf, M.: Multi-sensor spectral synergies for crop stress detection and monitoring in the optical domain: A review, Remote Sensing of Environment, 280, 113198, https://doi.org/10.1016/j.rse.2022.113198, 2022.

Campbell, P., Huemmrich, K., Middleton, E., Ward, L., Julitta, T., Daughtry, C., Burkart, A., Russ, A., and Kustas, W.: Diurnal and Seasonal Variations in Chlorophyll Fluorescence Associated with Photosynthesis at Leaf and Canopy Scales, Remote Sensing, 11, 488, https://doi.org/10.3390/rs11050488, 2019.

Chang, C. Y., Wen, J., Han, J., Kira, O., LeVonne, J., Melkonian, J., Riha, S. J., Skovira, J., Ng, S., Gu, L., Wood, J. D., Näthe, P., and Sun, Y.: Unpacking the drivers of diurnal dynamics of sun-induced chlorophyll fluorescence (SIF): Canopy structure, plant physiology, instrument configuration and retrieval methods, Remote Sensing of Environment, 265, 112672, https://doi.org/10.1016/j.rse.2021.112672, 2021.

Chen, J., Liu, X., Du, S., Ma, Y., and Liu, L.: Integrating SIF and Clearness Index to Improve Maize GPP Estimation Using Continuous Tower-Based Observations, Sensors, 20, 2493, https://doi.org/10.3390/s20092493, 2020.

Cho, S., Kang, M., Ichii, K., Kim, J., Lim, J.-H., Chun, J.-H., Park, C.-W., Kim, H. S., Choi, S.-W., Lee, S.-H., Indrawati, Y. M., and Kim, J.: Evaluation of forest carbon uptake in South Korea using the national flux tower network, remote sensing, and data-driven technology, Agricultural and Forest Meteorology, 311, 108653, https://doi.org/10.1016/j.agrformet.2021.108653, 2021.

Damm, A., Guanter, L., Paul-Limoges, E., van der Tol, C., Hueni, A., Buchmann, N., Eugster, W., Ammann, C., and Schaepman, M. E.: Far-red sun-induced chlorophyll fluorescence shows ecosystem-specific relationships to gross primary production: An assessment based on observational and modeling approaches, Remote Sensing of Environment, 166, 91–105, https://doi.org/10.1016/j.rse.2015.06.004, 2015.

Damm, A., Haghighi, E., Paul-Limoges, E., and van der Tol, C.: On the seasonal relation of sun-induced chlorophyll fluorescence and transpiration in a temperate mixed forest, Agricultural and Forest Meteorology, 304–305, 108386, https://doi.org/10.1016/j.agrformet.2021.108386, 2021.

De Cannière, S., Vereecken, H., Defourny, P., and Jonard, F.: Remote Sensing of Instantaneous Drought Stress at Canopy Level Using Sun-Induced Chlorophyll Fluorescence and

Canopy Reflectance, Remote Sensing, 14, 2642, https://doi.org/10.3390/rs14112642, 2022.

Drusch, M., Moreno, J., Del Bello, U., Franco, R., Goulas, Y., Huth, A., Kraft, S., Middleton, E. M., Miglietta, F., Mohammed, G., Nedbal, L., Rascher, U., Schuttemeyer, D., and Verhoef, W.: The FLuorescence EXplorer Mission Concept—ESA's Earth Explorer 8, IEEE Trans. Geosci. Remote Sensing, 55, 1273–1284, https://doi.org/10.1109/TGRS.2016.2621820, 2017.

Feng, W., Yao, X., Tian, Y., Cao, W., Zhu, Y., Feng, W., Yao, X., Tian, Y., Cao, W., and Zhu, Y.: Monitoring leaf pigment status with hyperspectral remote sensing in wheat, Aust. J. Agric. Res., 59, 748–760, https://doi.org/10.1071/AR07282, 2008.

Frankenberg, C. and Berry, J.: Solar Induced Chlorophyll Fluorescence: Origins, Relation to Photosynthesis and Retrieval, in: Comprehensive Remote Sensing, Elsevier, 143–162, https://doi.org/10.1016/B978-0-12-409548-9.10632-3, 2018.

Gastellu-Etchegorry, J. P., Martin, E., and Gascon, F.: DART: a 3D model for simulating satellite images and studying surface radiation budget, International Journal of Remote Sensing, 25, 73–96, https://doi.org/10.1080/0143116031000115166, 2004.

Goulas, Y., Fournier, A., Daumard, F., Champagne, S., Ounis, A., Marloie, O., and Moya, I.: Gross Primary Production of a Wheat Canopy Relates Stronger to Far Red Than to Red Solar-Induced Chlorophyll Fluorescence, Remote Sensing, 9, 97, https://doi.org/10.3390/rs9010097, 2017.

Grotti, M., Calders, K., Origo, N., Puletti, N., Alivernini, A., Ferrara, C., and Chianucci, F.: An intensity, image-based method to estimate gap fraction, canopy openness and effective leaf area index from phase-shift terrestrial laser scanning, Agricultural and Forest Meteorology, 280, 107766, https://doi.org/10.1016/j.agrformet.2019.107766, 2020.

Gu, L., Han, J., Wood, J. D., Chang, C. Y., and Sun, Y.: Sun-induced Chl fluorescence and its importance for biophysical modeling of photosynthesis based on light reactions, New Phytologist, 223, 1179–1191, https://doi.org/10.1111/nph.15796, 2019.

Guanter, L., Frankenberg, C., Dudhia, A., Lewis, P. E., Gómez-Dans, J., Kuze, A., Suto, H., and Grainger, R. G.: Retrieval and global assessment of terrestrial chlorophyll fluorescence from GOSAT space measurements, Remote Sensing of Environment, 121, 236–251, https://doi.org/10.1016/j.rse.2012.02.006, 2012.

He, L., Magney, T., Dutta, D., Yin, Y., Köhler, P., Grossmann, K., Stutz, J., Dold, C., Hatfield, J., Guan, K., Peng, B., and Frankenberg, C.: From the Ground to Space: Using Solar-Induced Chlorophyll Fluorescence to Estimate Crop Productivity, Geophysical Research Letters, 47, https://doi.org/10.1029/2020GL087474, 2020.

Helm, L. T., Shi, H., Lerdau, M. T., and Yang, X.: Solar-induced chlorophyll fluorescence and short-term photosynthetic response to drought, Ecological Applications, 30, https://doi.org/10.1002/eap.2101, 2020.

Jonard, F., De Cannière, S., Brüggemann, N., Gentine, P., Short Gianotti, D. J., Lobet, G., Miralles, D. G., Montzka, C., Pagán, B. R., Rascher, U., and Vereecken, H.: Value of sun-induced chlorophyll fluorescence for quantifying hydrological states and fluxes: Current status and challenges, Agricultural and Forest Meteorology, 291, 108088, https://doi.org/10.1016/j.agrformet.2020.108088, 2020.

Kim, J., Ryu, Y., Dechant, B., Lee, H., Kim, H. S., Kornfeld, A., and Berry, J. A.: Solar-induced chlorophyll fluorescence is non-linearly related to canopy photosynthesis in a temperate evergreen needleleaf forest during the fall transition, Remote Sensing of Environment, 258, 112362, https://doi.org/10.1016/j.rse.2021.112362, 2021.

Kimm, H., Guan, K., Jiang, C., Miao, G., Wu, G., Suyker, A. E., Ainsworth, E. A., Bernacchi, C. J., Montes, C. M., Berry, J. A., Yang, X., Frankenberg, C., Chen, M., and Köhler, P.: A physiological signal derived from sun-induced chlorophyll fluorescence quantifies crop physiological response to environmental stresses in the U.S. Corn Belt, Environ. Res. Lett., 16, 124051, https://doi.org/10.1088/1748-9326/ac3b16, 2021.

Kira, O., Y-Y. Chang, C., Gu, L., Wen, J., Hong, Z., and Sun, Y.: Partitioning Net Ecosystem Exchange (NEE) of CO2 Using Solar-Induced Chlorophyll Fluorescence (SIF), Geophysical Research Letters, 48, e2020GL091247, https://doi.org/10.1029/2020GL091247, 2021.

Li, X. and Xiao, J.: TROPOMI observations allow for robust exploration of the relationship between solar-induced chlorophyll fluorescence and terrestrial gross primary production, Remote Sensing of Environment, 268, 112748, https://doi.org/10.1016/j.rse.2021.112748, 2022.

Li, X., Liu, L., Yang, H., and Li, Y.: Relationships between carbon fluxes and environmental factors in a drip-irrigated, film-mulched cotton field in arid region, PLOS ONE, 13, e0192467, https://doi.org/10.1371/journal.pone.0192467, 2018.

Liu, Z., Zhao, F., Liu, X., Yu, Q., Wang, Y., Peng, X., Cai, H., and Lu, X.: Direct estimation of photosynthetic CO2 assimilation from solar-induced chlorophyll fluorescence (SIF), Remote Sensing of Environment, 271, 112893, https://doi.org/10.1016/j.rse.2022.112893, 2022.

Loayza, H., Moya, I., Quiroz, R., Ounis, A., and Goulas, Y.: Active and passive chlorophyll fluorescence measurements at canopy level on potato crops. Evidence of similitude of diurnal cycles of apparent fluorescence yields, Photosynth Res, 155, 271–288, https://doi.org/10.1007/s11120-022-00995-8, 2023.

Lu, X., Liu, Z., An, S., Miralles, D. G., Maes, W., Liu, Y., and Tang, J.: Potential of solar-induced chlorophyll fluorescence to estimate transpiration in a temperate forest, Agricultural and Forest Meteorology, 252, 75–87, https://doi.org/10.1016/j.agrformet.2018.01.017, 2018.

Lu, X., Liu, Z., Zhao, F., and Tang, J.: Comparison of total emitted solar-induced chlorophyll fluorescence (SIF) and top-of-canopy (TOC) SIF in estimating photosynthesis, Remote Sensing of Environment, 251, 112083, https://doi.org/10.1016/j.rse.2020.112083, 2020a.

Lu, X., Liu, Z., Zhao, F., and Tang, J.: Comparison of total emitted solar-induced chlorophyll fluorescence (SIF) and top-of-canopy (TOC) SIF in estimating photosynthesis, Remote Sensing of Environment, 251, 112083, https://doi.org/10.1016/j.rse.2020.112083, 2020b.

Maes, W. H., Pagán, B. R., Martens, B., Gentine, P., Guanter, L., Steppe, K., Verhoest, N. E. C., Dorigo, W., Li, X., Xiao, J., and Miralles, D. G.: Sun-induced fluorescence closely linked to ecosystem transpiration as evidenced by satellite data and radiative transfer models, Remote Sensing of Environment, 249, 112030, https://doi.org/10.1016/j.rse.2020.112030, 2020.

Magney, T. S., Bowling, D. R., Logan, B. A., Grossmann, K., Stutz, J., Blanken, P. D., Burns, S. P., Cheng, R., Garcia, M. A., Köhler, P., Lopez, S., Parazoo, N. C., Raczka, B., Schimel, D., and Frankenberg, C.: Mechanistic evidence for tracking the seasonality of photosynthesis with solar-induced fluorescence, Proceedings of the National Academy of Sciences, 116, 11640–11645, https://doi.org/10.1073/pnas.1900278116, 2019.

Magney, T. S., Barnes, M. L., and Yang, X.: On the Covariation of Chlorophyll Fluorescence and Photosynthesis Across Scales, Geophysical Research Letters, 47, https://doi.org/10.1029/2020GL091098, 2020.

le Maire, G., François, C., Soudani, K., Berveiller, D., Pontailler, J.-Y., Bréda, N., Genet, H., Davi, H., and Dufrêne, E.: Calibration and validation of hyperspectral indices for the estimation of broadleaved forest leaf chlorophyll content, leaf mass per area, leaf area index and leaf canopy biomass, Remote Sensing of Environment, 112, 3846–3864, https://doi.org/10.1016/j.rse.2008.06.005, 2008.

Man, Q., Dong, P., Guo, H., Liu, G., and Shi, R.: Light detection and ranging and hyperspectral data for estimation of forest biomass: a review, JARS, 8, 081598, https://doi.org/10.1117/1.JRS.8.081598, 2014.

Marrs, J. K., Reblin, J. S., Logan, B. A., Allen, D. W., Reinmann, A. B., Bombard, D. M., Tabachnik, D., and Hutyra, L. R.: Solar-Induced Fluorescence Does Not Track Photosynthetic Carbon Assimilation Following Induced Stomatal Closure, Geophys. Res. Lett., 47, https://doi.org/10.1029/2020GL087956, 2020.

Martini, D., Sakowska, K., Wohlfahrt, G., Pacheco-Labrador, J., van der Tol, C., Porcar-Castell, A., Magney, T. S., Carrara, A., Colombo, R., El-Madany, T. S., Gonzalez-Cascon, R., Martín, M. P., Julitta, T., Moreno, G., Rascher, U., Reichstein, M., Rossini, M., and Migliavacca, M.: Heatwave breaks down the linearity between sun-induced fluorescence and gross primary production, New Phytologist, 233, 2415–2428, https://doi.org/10.1111/nph.17920, 2022.

Miao, G., Guan, K., Yang, X., Bernacchi, C. J., Berry, J. A., DeLucia, E. H., Wu, J., Moore, C. E., Meacham, K., Cai, Y., Peng, B., Kimm, H., and Masters, M. D.: Sun-Induced Chlorophyll Fluorescence, Photosynthesis, and Light Use Efficiency of a Soybean Field from Seasonally Continuous Measurements, Journal of Geophysical Research: Biogeosciences, 123, 610–623, https://doi.org/10.1002/2017JG004180, 2018.

Moya, I., Loayza, H., López, M. L., Quiroz, R., Ounis, A., and Goulas, Y.: Canopy chlorophyll fluorescence applied to stress detection using an easy-to-build micro-lidar, Photosynthesis Research, 142, 1–15, https://doi.org/10.1007/s11120-019-00642-9, 2019.

Noda, H. M., Muraoka, H., and Nasahara, K. N.: Plant ecophysiological processes in spectral profiles: perspective from a deciduous broadleaf forest, J Plant Res, 134, 737–751, https://doi.org/10.1007/s10265-021-01302-7, 2021.

Pasqualotto, N., Delegido, J., Van Wittenberghe, S., Verrelst, J., Rivera, J. P., and Moreno, J.: Retrieval of canopy water content of different crop types with two new hyperspectral indices: Water Absorption Area Index and Depth Water Index, International Journal of Applied Earth Observation and Geoinformation, 67, 69–78, https://doi.org/10.1016/j.jag.2018.01.002, 2018.

Paul-Limoges, E., Damm, A., Hueni, A., Liebisch, F., Eugster, W., Schaepman, M. E., and Buchmann, N.: Effect of environmental conditions on sun-induced fluorescence in a mixed forest and a cropland, Remote Sensing of Environment, 219, 310–323, https://doi.org/10.1016/j.rse.2018.10.018, 2018.

Pierrat, Z., Magney, T., Parazoo, N. C., Grossmann, K., Bowling, D. R., Seibt, U., Johnson, B., Helgason, W., Barr, A., Bortnik, J., Norton, A., Maguire, A., Frankenberg, C., and Stutz, J.: Diurnal and Seasonal Dynamics of Solar-Induced Chlorophyll Fluorescence, Vegetation Indices, and Gross Primary Productivity in the Boreal Forest, Journal of Geophysical Research: Biogeosciences, 127, e2021JG006588, https://doi.org/10.1029/2021JG006588, 2022.

Pinto, F., Celesti, M., Acebron, K., Alberti, G., Cogliati, S., Colombo, R., Juszczak, R., Matsubara, S., Miglietta, F., Palombo, A., Panigada, C., Pignatti, S., Rossini, M., Sakowska, K., Schickling, A., Schüttemeyer, D., Stróżecki, M., Tudoroiu, M., and Rascher, U.: Dynamics of sun-induced chlorophyll fluorescence and reflectance to detect stress-induced variations in canopy photosynthesis, Plant Cell Environ, 43, 1637–1654, https://doi.org/10.1111/pce.13754, 2020.

Porcar-Castell, A., Malenovský, Z., Magney, T., Van Wittenberghe, S., Fernández-Marín, B., Maignan, F., Zhang, Y., Maseyk, K., Atherton, J., Albert, L. P., Robson, T. M., Zhao, F., Garcia-Plazaola, J.-I., Ensminger, I., Rajewicz, P. A., Grebe, S., Tikkanen, M., Kellner, J. R., Ihalainen, J. A., Rascher, U., and Logan, B.: Chlorophyll a fluorescence illuminates a path connecting plant molecular biology to Earth-system science, Nat. Plants, 7, 998–1009, https://doi.org/10.1038/s41477-021-00980-4, 2021.

Rascher, U., Alonso, L., Burkart, A., Cilia, C., Cogliati, S., Colombo, R., Damm, A., Drusch, M., Guanter, L., Hanus, J., Hyvärinen, T., Julitta, T., Jussila, J., Kataja, K., Kokkalis, P., Kraft, S., Kraska, T., Matveeva, M., Moreno, J., Muller, O., Panigada, C., Pikl, M., Pinto, F., Prey, L., Pude, R., Rossini, M., Schickling, A., Schurr, U., Schüttemeyer, D., Verrelst, J., and Zemek, F.: Sun-induced fluorescence - a new probe of photosynthesis: First maps from the imaging spectrometer *HyPlant*, Glob Change Biol, 21, 4673–4684, https://doi.org/10.1111/gcb.13017, 2015.

Regaieg, O., Wang, Y., Malenovský, Z., Yin, T., Kallel, A., Duran N., J., Delavois, A., Qi, J., Chavanon, E., Lauret, N., Guilleux, J., Cook, B., Morton, D., and Gastellu-Etchegorry, J. P.: Simulation of Solar-Induced Chlorophyll Fluorescence from 3D Canopies with the Dart Model, in: IGARSS 2020 - 2020 IEEE International Geoscience and Remote Sensing Symposium, IGARSS 2020 - 2020 IEEE International Geoscience and Remote Sensing Symposium, 4846–4849, https://doi.org/10.1109/IGARSS39084.2020.9323616, 2020.

Rossini, M., Nedbal, L., Guanter, L., Ač, A., Alonso, L., Burkart, A., Cogliati, S., Colombo, R., Damm, A., Drusch, M., Hanus, J., Janoutova, R., Julitta, T., Kokkalis, P., Moreno, J., Novotny, J., Panigada, C., Pinto, F., Schickling, A., Schüttemeyer, D., Zemek, F., and Rascher, U.: Red and far red Sun-induced chlorophyll fluorescence as a measure of plant photosynthesis, Geophys. Res. Lett., 42, 1632–1639, https://doi.org/10.1002/2014GL062943, 2015.

Song, J., Zhu, X., Qi, J., Pang, Y., Yang, L., and Yu, L.: A Method for Quantifying Understory Leaf Area Index in a Temperate Forest through Combining Small Footprint Full-Waveform and Point Cloud LiDAR Data, Remote Sensing, 13, 3036, https://doi.org/10.3390/rs13153036, 2021.

Sun, Y., Gu, L., Wen, J., van der Tol, C., Porcar-Castell, A., Joiner, J., Chang, C. Y., Magney, T., Wang, L., Hu, L., Rascher, U., Zarco-Tejada, P., Barrett, C. B., Lai, J., Han, J., and Luo, Z.: From remotely sensed solar-induced chlorophyll fluorescence to ecosystem structure, function, and service: Part I—Harnessing theory, Global Change Biology, 29, 2926–2952, https://doi.org/10.1111/gcb.16634, 2023a.

Sun, Y., Wen, J., Gu, L., Joiner, J., Chang, C. Y., van der Tol, C., Porcar-Castell, A., Magney, T., Wang, L., Hu, L., Rascher, U., Zarco-Tejada, P., Barrett, C. B., Lai, J., Han, J., and Luo, Z.: From remotely-sensed solar-induced chlorophyll fluorescence to ecosystem structure, function, and service: Part II—Harnessing data, Global Change Biology, 29, 2893–2925, https://doi.org/10.1111/gcb.16646, 2023b.

Tagliabue, G., Panigada, C., Dechant, B., Baret, F., Cogliati, S., Colombo, R., Migliavacca, M., Rademske, P., Schickling, A., Schüttemeyer, D., Verrelst, J., Rascher, U., Ryu, Y., and Rossini, M.: Exploring the spatial relationship between airborne-derived red and far-red sun-induced fluorescence and process-based GPP estimates in a forest ecosystem, Remote Sensing of Environment, 231, 111272, https://doi.org/10.1016/j.rse.2019.111272, 2019.

Verma, M., Schimel, D., Evans, B., Frankenberg, C., Beringer, J., Drewry, D. T., Magney, T., Marang, I., Hutley, L., Moore, C., and Eldering, A.: Effect of environmental conditions on the relationship between solar-induced fluorescence and gross primary productivity at an OzFlux grassland site: OCO SIF, MODIS, and GPP, Journal of Geophysical Research: Biogeosciences, 122, 716–733, https://doi.org/10.1002/2016JG003580, 2017.

Wang, N., Yang, P., Clevers, J. G. P. W., Wieneke, S., and Kooistra, L.: Decoupling physiological and non-physiological responses of sugar beet to water stress from sun-induced chlorophyll fluorescence, Remote Sensing of Environment, 286, 113445, https://doi.org/10.1016/j.rse.2022.113445, 2023.

Wieneke, S., Burkart, A., Cendrero-Mateo, M. P., Julitta, T., Rossini, M., Schickling, A., Schmidt, M., and Rascher, U.: Linking photosynthesis and sun-induced fluorescence at sub-daily to seasonal scales, Remote Sensing of Environment, 219, 247–258, https://doi.org/10.1016/j.rse.2018.10.019, 2018.

Wohlfahrt, G., Gerdel, K., Migliavacca, M., Rotenberg, E., Tatarinov, F., Müller, J., Hammerle, A., Julitta, T., Spielmann, F. M., and Yakir, D.: Sun-induced fluorescence and gross primary productivity during a heat wave, Scientific Reports, 8, https://doi.org/10.1038/s41598-018-32602-z, 2018.

Wu, G., Guan, K., Jiang, C., Peng, B., Kimm, H., Chen, M., Yang, X., Wang, S., Suyker, A. E., Bernacchi, C. J., Moore, C. E., Zeng, Y., Berry, J. A., and Cendrero-Mateo, M. P.: Radiance-based NIR $_{v}$ as a proxy for GPP of corn and soybean, Environ. Res. Lett., 15, 034009, https://doi.org/10.1088/1748-9326/ab65cc, 2020.

Wu, G., Guan, K., Jiang, C., Kimm, H., Miao, G., Bernacchi, C. J., Moore, C. E., Ainsworth, E. A., Yang, X., Berry, J. A., Frankenberg, C., and Chen, M.: Attributing differences of solar-induced chlorophyll fluorescence (SIF)-gross primary production (GPP) relationships between two C4 crops: corn and miscanthus, Agricultural and Forest Meteorology, 323, 109046, https://doi.org/10.1016/j.agrformet.2022.109046, 2022.

Yang, P., van der Tol, C., Verhoef, W., Damm, A., Schickling, A., Kraska, T., Muller, O., and Rascher, U.: Using reflectance to explain vegetation biochemical and structural effects on sun-induced chlorophyll fluorescence, Remote Sensing of Environment, 231, 110996, https://doi.org/10.1016/j.rse.2018.11.039, 2019.

Yang, P., van der Tol, C., Campbell, P. K. E., and Middleton, E. M.: Unraveling the physical and physiological basis for the solar- induced chlorophyll fluorescence and photosynthesis relationship using continuous leaf and canopy measurements of a corn crop, Biogeosciences, 18, 441–465, https://doi.org/10.5194/bg-18-441-2021, 2021.

Yang, X., Tang, J., Mustard, J. F., Lee, J.-E., Rossini, M., Joiner, J., Munger, J. W., Kornfeld, A., and Richardson, A. D.: Solar-induced chlorophyll fluorescence that correlates with canopy photosynthesis on diurnal and seasonal scales in a temperate deciduous forest: Fluorescence and photosynthesis, Geophysical Research Letters, 42, 2977–2987, https://doi.org/10.1002/2015GL063201, 2015.

Zeng, Y., Badgley, G., Dechant, B., Ryu, Y., Chen, M., and Berry, J. A.: A practical approach for estimating the escape ratio of near-infrared solar-induced chlorophyll fluorescence, Remote Sensing of Environment, 232, 111209, https://doi.org/10.1016/j.rse.2019.05.028, 2019.

Zeng, Y., Hao, D., Huete, A., Dechant, B., Berry, J., Chen, J. M., Joiner, J., Frankenberg, C., Bond-Lamberty, B., Ryu, Y., Xiao, J., Asrar, G. R., and Chen, M.: Optical vegetation indices for monitoring terrestrial ecosystems globally, Nat Rev Earth Environ, 3, 477–493, https://doi.org/10.1038/s43017-022-00298-5, 2022.

Zhan, W., Yang, X., Ryu, Y., Dechant, B., Huang, Y., Goulas, Y., Kang, M., and Gentine, P.: Two for one: Partitioning CO2 fluxes and understanding the relationship between solar-induced chlorophyll fluorescence and gross primary productivity using machine

learning, Agricultural and Forest Meteorology, 321, 108980, https://doi.org/10.1016/j.agrformet.2022.108980, 2022.

Zhang, J., Gonsamo, A., Tong, X., Xiao, J., Rogers, C. A., Qin, S., Liu, P., Yu, P., and Ma, P.: Solar-induced chlorophyll fluorescence captures photosynthetic phenology better than traditional vegetation indices, ISPRS Journal of Photogrammetry and Remote Sensing, 203, 183–198, https://doi.org/10.1016/j.isprsjprs.2023.07.021, 2023a.

Zhang, R., Zhou, Y., Hu, T., Sun, W., Zhang, S., Wu, J., and Wang, H.: Detecting the Spatiotemporal Variation of Vegetation Phenology in Northeastern China Based on MODIS NDVI and Solar-Induced Chlorophyll Fluorescence Dataset, Sustainability, 15, 6012, https://doi.org/10.3390/su15076012, 2023b.

Annexes

Annexe Chapter 3. Synergy between TROPOMI sun-induced chlorophyll fluorescence and MODIS spectral reflectance for understanding the dynamics of gross primary productivity at Integrated Carbon Observatory System (ICOS) ecosystem flux sites

Tab S3.1. Information on the sites used in this study from the ICOS release 2018 and 2021. The PFT represents the plant functional type corresponding to each site: MF (mixed forests), CRO (croplands), DBF (deciduous broadleaf forests), EBF (evergreen broadleaf forests), ENF (evergreen needleleaf forests), GRA (grasslands), OSH (open shrublands), and WET (wetlands). Years denote the year of data flux available for each site.

Site ID	Site name	Latitude (°)	Longitude (°)	PFT	Years
BE-Bra	Brasschaat	51.307617	4.519844	MF	2018
BE-Lcr	Lochristi	51.112184	3.850433	CRO	2019, 2020
BE-Lon	Lonzee	50.551586	4.7461305	CRO	2019, 2020
BE-Vie	Vielsalm	50.305068	5.998052	ENF	2018
CH-Dav	Davos	46.815283	9.855009	ENF	2018, 2019, 2020
CZ-BK1	Bily Kriz forest	49.50213	18.53685	ENF	2018
CZ-Lnz	Lanzhot	48.681611	16.946416	MF	2018
CZ-Wet	Trebon	49.024657	14.7703419	WET	2018
DE-Geb	Gebesee	51.099714	10.914629	CRO	2018
DE-Gri	Grillenburg	50.950046	13.512681	GRA	2018, 2019, 2020
DE-Hai	Hainich	51.079189	10.452336	DBF	2018, 2019, 2020
DE_HoH	Hohes Holz	52.086484	11.222468	DBF	2018, 2019, 2020
DE-Hzd	Hetzdorf	50.963566	13.490172	DBF	2018
DE-Kli	Klingenberg	50.892881	13.5225056	CRO	2018, 2019, 2020
DE-RuR	Rollesbroich	50.621914	6.3041256	GRA	2018
DE-RuS	Selhausen Juelich	50.865912	6.4471689	CRO	2018, 2019, 2020
DE-RuW	Wustebach	50.504907	6.33101886	ENF	2018
DE-Tha	Tharandt	50.962631	13.565225	ENF	2018
DK-Sor	Soroe	55.485869	11.644644	DBF	2018

FI-Hyy	Hyytiala	61.84741	24.29477	ENF	2018, 2020
FI-Sii	Siikaneva	61.832683	24.19278333	WET	2018, 2019, 2020
FI-Var	Varrio	67.7549	29.61	ENF	2018, 2019, 2020
FR-Aur	Aurade	43.54965	1.10615	CRO	2019, 2020
FR-Bil	Bilos - Salles	44.49389	-0.95592	ENF	2018, 2019, 2020
FR-EM2	Estrees-Mons A28	49.872108	3.02065	CRO	2018, 2019, 2020
FR-Fon	Fontainebleau-Barbeau	48.476339	2.780136	DBF	2018, 2019, 2020
FR-Hes	Hesse	48.84415	1.951910019	DBF	2018
FR-LGt	La Guette	48.67416	7.06461667	WET	2018, 2019, 2020
FR-Mej	Mejusseaume	48.117707	-1.798283	CRO	2019, 2020
GF-Guy	Guyaflux	5.2787	-52.9248	EBF	2018, 2019, 2020
IT-BCi	Borgo Cioffi	40.52375	14.957444	CRO	2018
IT-Cp2	Castelporziano2	41.704267	12.357293	EBF	2018
IT-Lsn	Lison	45.740481	12.750297	OSH	2018, 2019, 2020
IT-SR2	San Rossore 2	43.73203	10.29095	ENF	2018, 2019, 2020
IT-Tor	Torgnon	45.844444	7.578055556	GRA	2018, 2019, 2020
NL-Loo	Loobos	52.16648	5.74355	ENF	2018
SE-Deg	Degero	64.182	19.556694	WET	2018, 2020
SE-Htm	Hyltemossa	56.09763	13.41897	ENF	2018, 2019, 2020
SE-Nor	Norunda	60.086441	17.479455	ENF	2018, 2019, 2020
SE-Svb	Svartberget	64.256097	19.77451111	ENF	2018, 2019, 2020

Tab S3.2. MODIS Terra and Aqua surface spectral reflectance bands. NIR denotes near-infrared, SWNIR for shortwave near-infrared, SWIR shortwave infrared, and VNIR visible near-infrared.

Acronym	Full Name	Wavelengths (nm)	Band name	Spatial Resolution
B_1	Surface Reflectance for B_1	620-670	Red	500 m
B_2	Surface Reflectance for B_2	841-876	NIR	
B_3	Surface Reflectance for B_3	459-479	Blue	
B_4	Surface Reflectance for B_4	545-565	Green	
B_5	Surface Reflectance for B_5	1230-1250	SWNIR	
B_6	Surface Reflectance for B_6	1628-1652	SWIR	
B_7	Surface Reflectance for B_7	2105-2155	SWIR	
B_8	Surface Reflectance for B_8	405-420	Blue	1 km
B_9	Surface Reflectance for B_9	438-448	Blue	
B_{10}	Surface Reflectance for B_{10}	483-493	Blue	
B_{11}	Surface Reflectance for B_{11}	526-536	Green	

B_{12}	Surface Reflectance for B_{12}	546-556	Green
B_{13}	Surface Reflectance for B_{13}	662-672	Red
B_{14}	Surface Reflectance for B_{14}	673-683	VNIR
B_{15}	Surface Reflectance for B_{15}	743-753	VNIR
B_{16}	Surface Reflectance for B_{16}	862-877	NIR

Tab S3.3. Detailed results and statistics of the site-specific hyperbolic relationships between GPP and SIF_d. R^2 denotes the coefficient of determination. The unit of RMSE (Root Mean Squared Error) is in (gC m^{-2} d^{-1}). PFT represents the plant functional type of each site: MF (mixed forests), CRO (croplands), DBF (deciduous broadleaf forests), EBF (evergreen broadleaf forests), ENF (evergreen needleleaf forests), GRA (grasslands), OSH (open shrublands), and WET (wetlands). All pairwise hyperbolic relationships between GPP and SIF_d were statistically significant with $p<0.0001$, except for IT-Cp2, Guy and FR-Mej sites. a and b denote the fitted parameters from the hyperbolic model.

Site ID	R^2	a	b	RMSE	N	PFT
BE-Bra	0.64	16.15	0.37	1.92	288	MF
BE-Lcr	0.24	14.12	0.28	4.03	618	CRO
BE-Lon	0.37	79.75	4.36	6.16	572	CRO
BE-Vie	0.28	8.60	0.07	2.42	220	ENF
CH-Dav	0.21	4.87	0.05	1.76	350	ENF
CZ-BK1	0.34	12.23	0.04	3.62	160	ENF
CZ-Lnz	0.46	16.31	0.28	3.28	332	MF
CZ-Wet	0.28	13.11	0.31	3.66	292	WET
DE-Geb	0.56	19.49	0.63	3.44	236	CRO
DE-Gri	0.34	12.66	0.33	3.34	818	GRA
DE-Hai	0.57	21.80	1.12	2.94	802	DBF
DE-HoH	0.43	19.63	0.67	4.36	944	DBF
DE-Hzd	0.50	16.20	0.63	2.87	248	DBF
DE-Kli	0.35	28.94	1.90	3.88	850	CRO
DE-RuR	0.22	11.02	0.15	3.88	274	GRA
DE-RuS	0.28	31.74	0.97	6.30	678	CRO
DE-RuW	0.10	8.94	0.02	2.62	216	ENF
DE-Tha	0.74	10.40	0.21	1.79	268	ENF
DK-Sor	0.87	74.20	3.51	2.71	298	DBF
FI-Hyy	0.36	9.14	0.13	2.54	498	ENF
FI-Sii	0.37	4.36	0.23	1.10	766	WET
FI-Var	0.12	4.83	0.02	2.08	560	ENF
FR-Aur	0.22	16.48	1.05	3.74	854	CRO
FR-Bil	0.19	8.02	0.07	3.32	836	ENF
FR-EM2	0.13	9.22	0.25	4.99	762	CRO
FR-Fon	0.75	23.71	0.77	2.72	932	DBF
FR-Hes	0.56	27.10	0.94	3.80	342	DBF
FR-LGt	0.44	11.10	0.40	2.22	1050	WET

FR-Mej	0.07	9.75	0.18	5.17	668	CRO
GF-Guy	0.012	12.36	0.02	2.65	774	EBF
IT-BCi	0.19	18.71	0.27	6.18	300	CRO
IT-Cp2	0.002	9.56	0.00	2.01	182	EBF
IT-Lsn	0.61	13.44	0.50	2.10	1510	OSH
IT-SR2	0.30	10.43	0.07	2.99	750	ENF
IT-Tor	0.50	11.99	0.25	2.91	566	GRA
NL-Loo	0.40	9.67	0.05	1.98	234	ENF
SE-Deg	0.42	2.16	0.18	0.55	602	WET
SE-Htm	0.35	9.91	0.10	2.91	808	ENF
SE-Nor	0.68	12.16	0.23	2.12	640	ENF
SE-Svb	0.18	7.00	0.03	2.70	900	ENF

Tab S3.4. Detailed results and statistics of the site-specific linear relationships between GPP and SIF_d. The sign ± denotes the 95% confidence interval on the slope and on the intercept for each relationship. R^2 denotes the coefficient of determination. The units are for the slope in (gC m^{-2} d^{-1}/(mW m^{-2} sr^{-1} nm^{-1})), intercept in (gC m^{-2} d^{-1}), and RMSE (Root Mean Squared Error) in (gC m^{-2} d^{-1}). PFT represents the plant functional type of each site: MF (mixed forests), CRO (croplands), DBF (deciduous broadleaf forests), EBF (evergreen broadleaf forests), ENF (evergreen needleleaf forests), GRA (grasslands), OSH (open shrublands), and WET (wetlands). All pairwise linear relationships between GPP and SIF_d were statistically significant with $p<0.0001$, except the IT-Cp2 site ($p<0.604$).

Relatively moderate and strong relationships were found at DK-Sor, FR-Fon, BE-Bra, DE-Hai, DE-Tha, and IT-Lsn, which are DBF, MF, ENF and OSH vegetation type sites, with R^2 values being between 0.54 and 0.81 ($p<0.0001$). The weakest relationships were recorded at FI-Var, FR-EM2 and FR-Mej sites, and no significant relationship was found at GF-Guy and IT-Cp2.

Site ID	R^2	Slope	Intercept	RMSE	N	PFT
BE-Bra	0.59	11.27±1.07	3.33±0.45	2.00	300	MF
BE-Lcr	0.20	9.02±1.39	4.06±0.66	4.06	630	CRO
BE-Lon	0.27	12.33±1.64	2.1±0.89	6.05	582	CRO
BE-Vie	0.20	4.75±1.24	4.84±0.60	2.44	228	ENF
CH-Dav	0.15	4.17±0.96	2.67±0.26	1.74	406	ENF
CZ-BK1	0.35	18±3.62	5.92±0.79	3.38	178	ENF
CZ-Lnz	0.42	9.98±1.25	4.76±0.60	3.18	346	MF
CZ-Wet	0.20	9.46±2.16	3.12±0.71	3.68	306	WET
DE-Geb	0.53	10.04±1.18	2.12±0.68	3.80	254	CRO
DE-Gri	0.28	8.58±0.94	2.89±0.38	3.26	842	GRA
DE-Hai	0.57	9.23±0.54	1.40±0.32	2.91	852	DBF
DE-HoH	0.35	9.29±0.79	3.04±0.41	4.14	1002	DBF
DE-Hzd	0.41	8.56±1.25	2.40±0.57	2.73	260	DBF
DE-Kli	0.31	9.05±0.89	1.18±0.40	3.85	886	CRO
DE-RuR	0.17	6.87±1.76	4.59±0.87	3.80	280	GRA
DE-RuS	0.29	17.04±1.97	1.81±0.80	6.22	708	CRO
DE-RuW	0.16	5.02±1.51	6.42±0.57	2.61	230	ENF
DE-Tha	0.56	6.43±0.68	3.54±0.31	1.61	280	ENF

DK-Sor	0.81	14.06±0.77	2.09±0.56	2.73	310	DBF
FI-Hyy	0.27	8.05±1.10	3.33±0.34	2.68	554	ENF
FI-Sii	0.32	4.01±0.40	1.06±0.12	1.10	850	WET
FI-Var	0.13	4.73±0.92	3.23±0.20	2.00	690	ENF
FR-Aur	0.23	7.98±0.97	1.08±0.41	3.65	908	CRO
FR-Bil	0.17	6.47±0.95	3.98±0.32	3.13	884	ENF
FR-EM2	0.11	5.10±1.02	2.99±0.59	4.85	780	CRO
FR-Fon	0.66	11.91±0.53	2.48±0.27	2.71	986	DBF
FR-Hes	0.50	12.12±1.28	2.55±0.66	3.78	352	DBF
FR-LGt	0.43	8.02±0.55	1.76±0.22	2.29	1114	WET
FR-Mej	0.04	4.72±1.65	4.40±0.84	5.22	672	CRO
GF-Guy	0.02	1.86±0.91	10.79±0.57	2.63	774	EBF
IT-BCi	0.16	13.43±3.5	5.10±1.39	6.11	306	CRO
IT-Cp2	0.001	0.36±1.37	9.37±0.54	2.01	190	EBF
IT-Lsn	0.54	8±0.36	2.17±0.17	2.10	1594	OSH
IT-SR2	0.21	6.78±0.94	5.78±0.36	2.95	774	ENF
IT-Tor	0.42	11.31±1.02	2.30±0.30	2.83	646	GRA
NL-Loo	0.24	5.36±1.22	5.96±0.48	2.19	242	ENF
SE-Deg	0.35	2.04±0.21	0.61±0.06	0.54	680	WET
SE-Htm	0.29	6.34±0.66	4.70±0.30	2.72	860	ENF
SE-Nor	0.51	8.35±0.62	3.53±0.25	2.14	684	ENF
SE-Svb	0.20	7.61±0.93	3.88±0.24	2.75	1056	ENF

Tab S3.5. Summary statistics of plant functional type-specific linear relationship between GPP and SIF_d in eight major PFT. All pairwise linear relationships between GPP and SIF_d were statistically significant with $p<0.0001$. The units are for the slope in (gC m^{-2} d^{-1}/ (mW m^{-2} sr^{-1} nm^{-1})), intercept in (gC m^{-2} d^{-1}), and RMSE in (gC m^{-2} d^{-1}). The sign ± denotes the 95% confidence interval on the slope and intercept of the relationships between SIF_d and GPP. Relatively moderate and goodness of fit were found in MF, DBF and OSH biomes, and the lowest in EBF and CRO vegetation types.

PFT	Sites	R^2	Slope	Intercept	RMSE	N
CRO	9	0.18	8.93±0.49	2.61±0.24	5.24	5726
DBF	6	0.52	10.75±0.33	2.32±0.18	3.50	3762
EBF	2	0.07	3.08±0.72	9.76±0.42	2.62	964
ENF	13	0.26	7.28±0.28	4.07±0.10	2.85	7066
GRA	3	0.33	9.39±0.62	2.79±0.24	3.24	1768
MF	2	0.47	10.53±0.87	4.10±0.39	2.74	646
OSH	1	0.54	8.00±0.36	2.17±0.17	2.10	1594
WET	4	0.29	7.14±0.40	1.15±0.14	2.44	2950
ALL	40	0.30	9.12±0.17	2.87±0.08	3.82	24476

Tab S3.6. The Generalized Linear Model (GLM) results statistics. The following equation was fitted to investigate the effects of the site, year, and PFT and their interactions on the seasonal and interannual variations of SIF_d and its relationship with GPP. SIF_d = 1 + Year + Site + PFT + GPP + Year ×GPP + Site×GPP + PFT×GPP. All pairwise relationships between GPP and SIF_d were statistically significant with $p<0.001$, except for Site×GPP interaction ($p<0.896$).

Parameters	Estimate	Std. Error	p-value

Intercept	-3.01E+01	5.79E+00	2.00E-07
Year	1.50E-02	2.87E-03	1.66E-07
Site	-1.06E-03	2.49E-04	2.13E-05
PFT	-1.31E-02	1.02E-03	< 2e-16
GPP	3.09E+00	7.60E-01	4.83E-05
Year×GPP	-1.52E-03	3.76E-04	5.70E-05
Site×GPP	-4.17E-06	3.19E-05	0.896
PFT×GPP	1.88E-03	1.59E-04	< 2e-16

Tab S3.7. Detailed results and statistics of the site-specific comparison between tower-based observed GPP against the RF predicted GPP. PFT denotes plant functional type of each site, including MF (mixed forests), CRO (croplands), DBF (deciduous broadleaf forests), EBF (evergreen broadleaf forests), ENF (evergreen needleleaf forests), GRA (grasslands), OSH (open shrublands), and WET (wetlands). The adj. R2 denotes the adjusted coefficient of determination. The units are for the slope in (gC m-2 d-1/(mW m-2 sr-1 nm-1)), intercept in (gC m-2 d-1), and RMSE (Root Mean Squared Error) in (gC m-2 d-1). The sign ± denotes the confidence interval at 95% probability level on the slope and on the intercept for each relationship. RF-R model includes only surface spectral reflectance as explanatory variables, RF-SIF-R uses SIFd and spectral bands inputs to predict GPP, RF-SIF-VI explores SIFd and VIs as inputs, and RF-SIF-PFT establishes based on SIFd, spectral bands and vegetation type as categorial variable to estimate GPP.

			RF-R				**RF-SIF-R**			
Site ID	PFT	N	adj. R^2	Slope	Intercept	RMSE	adj. R^2	Slope	Intercept	RMSE
BE-Bra	MF	55	0.62	0.84±0.18	1.29±1.43	1.70	0.71	0.98±0.17	0.15±1.37	1.49
BE-Lcr	CRO	124	0.92	1.03±0.05	-0.14±0.47	1.26	0.9	1.06±0.06	-0.39±0.54	1.40
BE-Lon	CRO	111	0.91	1.03±0.06	-0.24±0.55	1.93	0.88	1.09±0.07	-0.45±0.65	2.22
BE-Vie	ENF	41	0.81	1.02±0.16	-0.07±1.04	1.08	0.70	1 .00±0.21	-0.20±1.43	1.37
CH-Dav	ENF	95	0.84	0.95±0.09	-0.01±0.34	0.79	0.75	0.87±0.10	0.04±0.43	0.98
CZ-BK1	ENF	23	0.63	0.96±0.32	0.86±3.03	2.28	0.70	1.31±0.37	-1.22±3.16	2.04
CZ-Lnz	MF	62	0.93	1.13±0.08	-0.81±0.78	1.12	0.87	1.15±0.12	-0.67±1.08	1.53
CZ-Wet	WET	54	0.88	0.98±0.10	-0.02±0.74	1.48	0.79	1.09±0.16	-0.52±1.09	1.97
DE-Geb	CRO	48	0.83	1.06±0.14	-0.14±1.11	2.23	0.87	1.05±0.12	0.11±0.93	1.95
DE-Gri	GRA	169	0.81	1.09±0.08	-0.49±0.52	1.58	0.77	1.12±0.09	-0.61±0.60	1.74
DE-Hai	DBF	161	0.90	1.01±0.05	-0.26±0.38	1.46	0.87	1.01±0.06	-0.57±0.46	1.66
DE-HoH	DBF	183	0.94	1.00±0.04	-0.06±0.33	1.28	0.90	1.04±0.05	-0.29±0.43	1.61
DE-Hzd	DBF	61	0.84	1.03±0.12	0.02±0.74	1.43	0.84	1.14±0.13	-0.83±0.83	1.44
DE-Kli	CRO	177	0.88	1.02±0.06	-0.58±0.35	1.59	0.83	1.08±0.07	-1.12±0.47	1.93
DE-RuR	GRA	61	0.75	0.95±0.14	0.66±1.14	1.82	0.59	1.05±0.23	0.19±1.71	2.33
DE-RuS	CRO	148	0.79	0.98±0.08	0.68±0.77	3.13	0.74	0.98±0.09	0.82±0.87	3.50
DE-RuW	ENF	46	0.81	0.96±0.14	0.38±1.13	1.14	0.54	0.94±0.26	0.78±2.03	1.78
DE-Tha	ENF	52	0.77	0.93±0.14	0.61±0.90	1.14	0.67	0.85±0.17	0.85±1.10	1.38
DK-Sor	DBF	59	0.94	1.05±0.07	0.15±0.88	1.56	0.93	1.04±0.08	0.39±0.96	1.73
FI-Hyy	ENF	104	0.92	1.02±0.06	-0.15±0.37	0.91	0.81	1.05±0.10	-0.23±0.61	1.41
FI-Sii	WET	163	0.86	0.91±0.06	0.01±0.15	0.49	0.69	0.68±0.08	0.30±0.21	0.72
FI-Var	ENF	139	0.79	0.97±0.08	0.13±0.38	1.05	0.74	0.96±0.10	0.12±0.43	1.16
FR-Aur	CRO	205	0.86	1.00±0.06	-0.14±0.28	1.45	0.83	1 .00±0.06	-0.10±0.32	1.61
FR-Bil	ENF	168	0.89	1.05±0.06	-0.13±0.35	1.15	0.82	1.09±0.08	-0.35±0.48	1.48

FR-EM2	CRO	169	0.62	0.94±0.11	0.62±0.75	2.97	0.59	0.86±0.11	1.03±0.74	3.08
FR-Fon	DBF	210	0.95	1.01±0.03	-0.20±0.25	0.97	0.95	1.02±0.03	-0.34±0.28	1.06
FR-Hes	DBF	74	0.83	1.00±0.10	-0.70±0.98	2.07	0.80	1.08±0.12	-1.43±1.14	2.24
FR-LGt	WET	239	0.93	1.03±0.04	-0.34±0.19	0.82	0.85	1.01±0.05	-0.45±0.28	1.15
FR-Mej	CRO	120	0.81	0.98±0.09	0.21±0.74	2.44	0.74	1.09±0.12	-0.34±0.95	2.89
GF-Guy	EBF	146	0.80	0.99±0.53	0.21±0.96	1.18	0.71	1.00±0.10	0.35±1.20	1.42
IT-BCi	CRO	69	0.21	1.16±0.53	0.94±5.08	5.98	0.21	0.61±0.28	5.31±3.23	5.98
IT-Cp2	EBF	42	0.36	0.65±0.27	3.89±2.51	1.25	0.25	0.58±0.31	4.85±2.73	1.36
IT-Lsn	OSH	317	0.91	1.02±0.04	-0.09±0.22	0.99	0.88	1.01±0.04	0.01±0.24	1.10
IT-SR2	ENF	160	0.60	0.96±0.12	0.55±1.02	2.04	0.56	1.08±0.15	-0.08±1.18	2.12
IT-Tor	GRA	134	0.79	0.97±0.09	0.19±0.43	1.60	0.75	1.00±0.10	0.13±0.49	1.74
NL-Loo	ENF	47	0.77	1.11±0.18	-0.46±1.32	1.30	0.66	1.19±0.25	-0.55±1.73	1.58
SE-Deg	WET	143	0.38	0.37±0.08	0.56±0.13	0.53	0.41	0.34±0.07	0.49±0.14	0.52
SE-Htm	ENF	167	0.78	1.02±0.08	-0.03±0.63	1.52	0.70	1.04±0.10	-0.17±0.78	1.77
SE-Nor	ENF	144	0.87	0.97±0.06	0.15±0.41	1.05	0.79	0.99±0.09	0.16±0.55	1.33
SE-Svb	ENF	199	0.92	1.01±0.04	0.00±0.02	0.91	0.86	1.05±0.06	-0.21±0.34	1.15
			RF-SIF-VI				**RF-SIF-R-PFT**			
Site ID	PFT	N	adj. R^2	Slope	Intercept	RMSE	adj. R^2	Slope	Intercept	RMSE
BE-Bra	MF	55	0.59	0.85±0.19	1.18±1.53	1.76	0.72	0.97±0.16	0.14±1.34	1.47
BE-Lcr	CRO	124	0.85	1.08±0.08	-0.13±0.68	1.77	0.91	1.05±0.06	-0.33±0.53	1.39
BE-Lon	CRO	111	0.83	1.12±0.10	-0.54±0.82	2.72	0.88	1.08±0.07	-0.36±0.65	2.22
BE-Vie	ENF	41	0.67	0.95±0.21	0.13±1.45	1.42	0.75	1.05±0.19	-0.61±1.32	1.23
CH-Dav	ENF	95	0.71	0.85±0.11	0.16±0.46	1.05	0.76	0.88±0.10	0.02±0.42	0.96
CZ-BK1	ENF	23	0.40	1.04±0.55	1.68±4.24	2.90	0.67	1.30±0.40	-1.21±3.40	2.15
CZ-Lnz	MF	62	0.75	1.11±0.16	-0.34±1.54	2.11	0.86	1.16±0.12	-0.90±1.12	1.55
CZ-Wet	WET	54	0.68	1.13±0.21	-0.59±1.42	2.42	0.82	1.11±0.14	-0.34±0.96	1.81
DE-Geb	CRO	48	0.8	0.99±0.14	0.31±1.15	2.40	0.87	1.05±0.12	0.15±0.92	1.92
DE-Gri	GRA	169	0.65	1.03±0.12	-0.37±0.77	2.16	0.78	1.13±0.09	-0.84±0.59	1.69
DE-Hai	DBF	161	0.82	0.99±0.07	-0.72±0.54	1.91	0.88	1.02±0.06	-0.48±0.43	1.58
DE-HoH	DBF	183	0.87	1.09±0.06	-0.52±0.52	1.88	0.90	1.03±0.05	-0.17±0.43	1.61
DE-Hzd	DBF	61	0.74	1.07±0.16	-0.67±1.06	1.81	0.86	1.09±0.11	-0.34±0.71	1.34
DE-Kli	CRO	177	0.71	1.03±0.10	-1.15±0.63	2.49	0.84	1.07±0.07	-1.07±0.44	1.84
DE-RuR	GRA	61	0.57	0.97±0.22	-0.01±1.81	2.37	0.60	1.07±0.22	0.02±1.69	2.28
DE-RuS	CRO	148	0.72	1.05±0.11	0.77±0.91	3.62	0.75	0.98±0.09	0.84±0.85	3.45
DE-RuW	ENF	46	0.35	0.74±0.30	2.53±2.24	2.12	0.56	0.97±0.26	0.54±2.00	1.74
DE-Tha	ENF	52	0.54	0.74±0.19	1.32±1.31	1.63	0.69	0.93±0.18	0.34±1.16	1.35
DK-Sor	DBF	59	0.90	1.06±0.09	0.58±1.10	1.98	0.93	1.04±0.08	0.34±0.95	1.71
FI-Hyy	ENF	104	0.74	1.06±0.12	-0.17±0.73	1.65	0.81	1.06±0.10	-0.35±0.62	1.41
FI-Sii	WET	163	0.68	0.64±0.07	0.27±0.21	0.73	0.78	0.89±0.07	0.10±0.18	0.60
FI-Var	ENF	139	0.66	0.90±0.11	0.28±0.50	1.32	0.73	0.94±0.10	0.14±0.44	1.18
FR-Aur	CRO	205	0.79	0.99±0.07	-0.18±0.36	1.80	0.83	0.99±0.06	-0.06±0.32	1.62
FR-Bil	ENF	168	0.71	1.05±0.10	-0.05±0.62	1.87	0.82	1.10±0.08	-0.57±0.49	1.47
FR-EM2	CRO	169	0.55	0.85±0.12	1.09±0.80	3.25	0.60	0.86±0.11	1.05±0.74	3.07
FR-Fon	DBF	210	0.87	1.00±0.05	-0.22±0.44	1.63	0.95	1.02±0.03	-0.29±0.27	1.03
FR-Hes	DBF	74	0.60	1.01±0.19	-0.87±1.72	3.18	0.81	1.07±0.12	-1.24±1.12	2.22
FR-LGt	WET	239	0.74	0.90±0.07	-0.38±0.40	1.53	0.88	1.06±0.05	-0.39±0.25	1.05

FR-Mej	CRO	120	0.68	1.07±0.13	-0.37±1.09	3.20	0.75	1.08±0.11	-0.28±0.92	2.81
GF-Guy	EBF	146	0.53	0.89±0.14	2.07±1.51	1.81	0.75	1.05±0.10	-0.36±1.17	1.33
IT-BCi	CRO	69	0.21	0.63±0.29	5.16±3.33	6.00	0.20	0.60±0.28	5.46±3.24	6.02
IT-Cp2	EBF	42	0.10	0.35±0.29	7.13±2.42	1.49	0.3	0.65±0.31	3.95±2.84	1.31
IT-Lsn	OSH	317	0.83	0.98±0.05	0.21±0.29	1.33	0.89	1.02±0.04	-0.06±0.24	1.08
IT-SR2	ENF	160	0.38	1.02±0.20	0.80±1.51	2.52	0.58	1.11±0.15	-0.34±1.16	2.07
IT-Tor	GRA	134	0.71	0.98±0.11	0.19±0.53	1.88	0.75	0.99±0.10	0.08±0.49	1.74
NL-Loo	ENF	47	0.47	1.05±0.33	0.61±2.14	1.96	0.69	1.22±0.24	-0.98±1.70	1.51
SE-Deg	WET	143	0.38	0.22±0.05	0.54±0.14	0.53	0.55	0.50±0.07	0.34±0.13	0.45
SE-Htm	ENF	167	0.56	0.98±0.13	0.27±0.99	2.15	0.72	1.08±0.10	-0.44±0.77	1.71
SE-Nor	ENF	144	0.70	0.94±0.10	0.61±0.63	1.57	0.81	1.02±0.08	-0.14±0.52	1.24
SE-Svb	ENF	199	0.68	0.99±0.09	0.16±0.55	1.76	0.87	1.04±0.06	-0.26±0.35	1.15

Figure S3.1. Site-specific linear relationships tower-based GPP and SIF_d at daily timescale. The R^2 represents the coefficient of determination of the relationship between GPP and SIF_d for each site. The color code represents the eight different plant functional types encountered in the study sites: Red color stands for CRO (croplands), green for DBF (deciduous broadleaf forests), yellow for EBF (evergreen broadleaf forests), magenta for ENF (evergreen needleleaf forests), blue for GRA (grasslands), Cyan for MF (mixed forests), lime for OSH (open shrubland), and dimgrey for WET (wetland). The shaded area depicted in each line is the 95% confidence interval of the linear relationship between GPP and SIF_d.

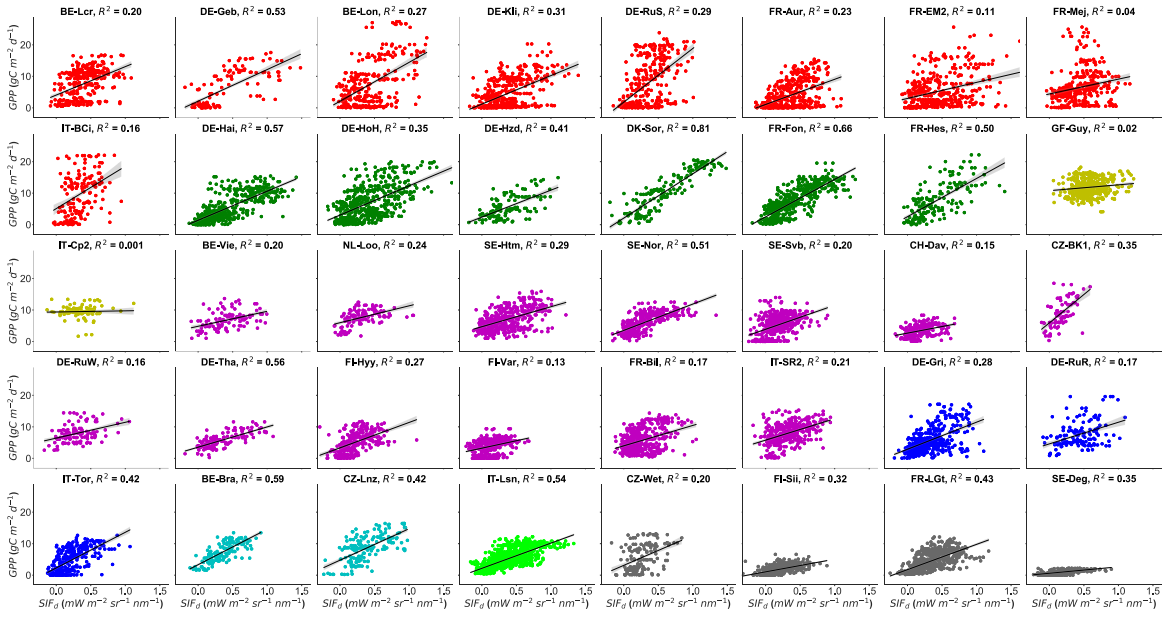

Figure S3.2. Linear relationships between tower-based GPP and SIF_d in eight plant functional types: MF, CRO, ENF, DBF, EBF, GRA, OSH, and WET at daily timescale. The R^2 represents the coefficient of determination of the relationship between GPP and SIF_d. p is the probability value of the linear model. The shaded area depicted in each line is the 95% confidence interval of the linear relationships between GPP and SIF_d.

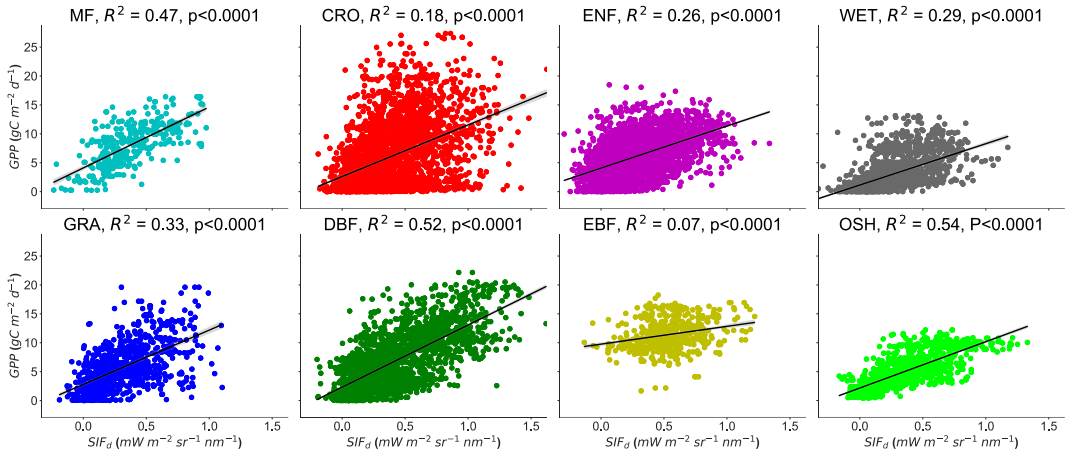

Figure S3.3. Scatterplots of the linear relationships between tower-based GPP and SIF_d in eight PFT pooled together across all sites. The shaded area depicted in each line is the 95% confidence interval of the linear relationships between GPP and SIF_d.

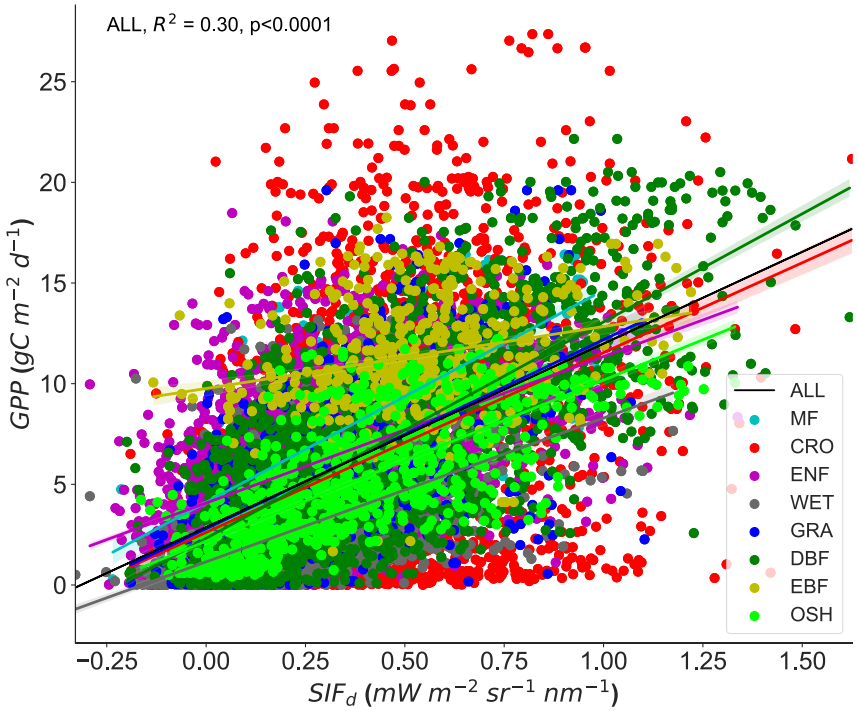

Figure S3.4. Correlation matrix between variables. B_1 to B_{16} denote the spectral reflectance of MODIS bands, SIF_d is the daily TROPOMI sun-induced chlorophyll fluorescence, GPP is the tower-based daily gross primary production, NDVI (normalized difference vegetation index), NIRv (near infrared reflectance of vegetation index), and PRI (photochemical reflectance index). The correlation matrix shows strong relations between variables. Based on these observations B_{10}, B_{12} and B_{14} were excluded from the explanatory variables for establishing the RF regression models. Furthermore, B_{15} and B_{16} were excluded from the analyses due to many missing values that they contained.

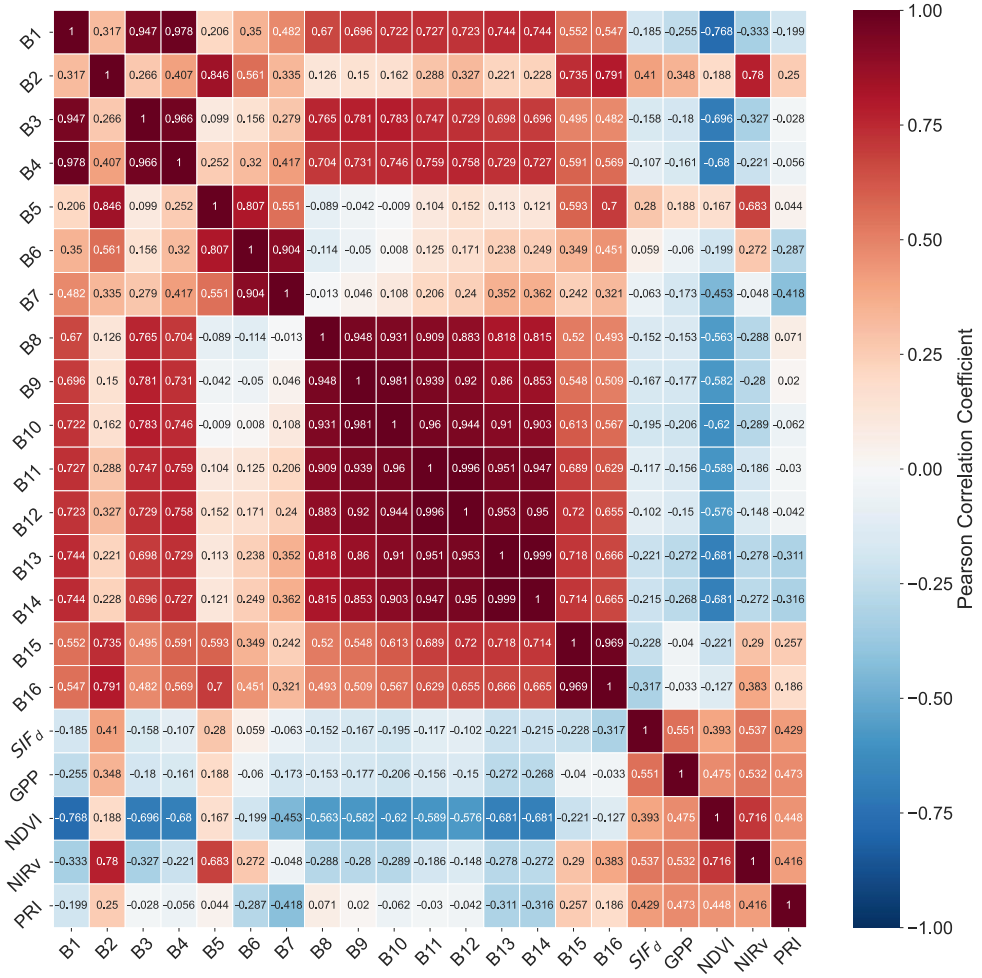
B1 1 0.317 0.947 0.978 0.206 0.35 0.482 0.67 0.696 0.722 0.727 0.723 0.744 0.744 0.552 0.547 -0.185 -0.255 -0.768 -0.333 -0.199
B2 0.317 1 0.266 0.407 0.846 0.561 0.335 0.126 0.15 0.162 0.288 0.327 0.221 0.228 0.735 0.791 0.41 0.348 0.188 0.78 0.25
B3 0.947 0.266 1 0.966 0.099 0.156 0.279 0.765 0.781 0.783 0.747 0.729 0.698 0.696 0.495 0.482 -0.158 -0.18 -0.696 -0.327 -0.028
B4 0.978 0.407 0.966 1 0.252 0.32 0.417 0.704 0.731 0.746 0.759 0.758 0.729 0.727 0.591 0.569 -0.107 -0.161 -0.68 -0.221 -0.056
B5 0.206 0.846 0.099 0.252 1 0.807 0.551 -0.089 -0.042 -0.009 0.104 0.152 0.113 0.121 0.593 0.7 0.28 0.188 0.167 0.683 0.044
B6 0.35 0.561 0.156 0.32 0.807 1 0.904 -0.114 -0.05 0.008 0.125 0.171 0.238 0.249 0.349 0.451 0.059 -0.06 -0.199 0.272 -0.287
B7 0.482 0.335 0.279 0.417 0.551 0.904 1 -0.013 0.046 0.108 0.206 0.24 0.352 0.362 0.242 0.321 -0.063 -0.173 -0.453 -0.048 -0.418
B8 0.67 0.126 0.765 0.704 -0.089 -0.114 -0.013 1 0.948 0.931 0.909 0.883 0.818 0.815 0.52 0.493 -0.152 -0.153 -0.563 -0.288 0.071
B9 0.696 0.15 0.781 0.731 -0.042 -0.05 0.046 0.948 1 0.981 0.939 0.92 0.86 0.853 0.548 0.509 -0.167 -0.177 -0.582 -0.28 0.02
B10 0.722 0.162 0.783 0.746 -0.009 0.008 0.108 0.931 0.981 1 0.96 0.944 0.91 0.903 0.613 0.567 -0.195 -0.206 -0.62 -0.289 -0.062
B11 0.727 0.288 0.747 0.759 0.104 0.125 0.206 0.909 0.939 0.96 1 0.996 0.951 0.947 0.689 0.629 -0.117 -0.156 -0.589 -0.186 -0.03
B12 0.723 0.327 0.729 0.758 0.152 0.171 0.24 0.883 0.92 0.944 0.996 1 0.953 0.95 0.72 0.655 -0.102 -0.15 -0.576 -0.148 -0.042
B13 0.744 0.221 0.698 0.729 0.113 0.238 0.352 0.818 0.86 0.91 0.951 0.953 1 0.999 0.718 0.666 -0.221 -0.272 -0.681 -0.278 -0.311
B14 0.744 0.228 0.696 0.727 0.121 0.249 0.362 0.815 0.853 0.903 0.947 0.95 0.999 1 0.714 0.665 -0.215 -0.268 -0.681 -0.272 -0.316
B15 0.552 0.735 0.495 0.591 0.593 0.349 0.242 0.52 0.548 0.613 0.689 0.72 0.718 0.714 1 0.969 -0.228 -0.04 -0.221 0.29 0.257
B16 0.547 0.791 0.482 0.569 0.7 0.451 0.321 0.493 0.509 0.567 0.629 0.655 0.666 0.665 0.969 1 -0.317 -0.033 -0.127 0.383 0.186
SIF d -0.185 0.41 -0.158 -0.107 0.28 0.059 -0.063 -0.152 -0.167 -0.195 -0.117 -0.102 -0.221 -0.215 -0.228 -0.317 1 0.551 0.393 0.537 0.429
GPP -0.255 0.348 -0.18 -0.161 0.188 -0.06 -0.173 -0.153 -0.177 -0.206 -0.156 -0.15 -0.272 -0.268 -0.04 -0.033 0.551 1 0.475 0.532 0.473
NDVI -0.768 0.188 -0.696 -0.68 0.167 -0.199 -0.453 -0.563 -0.582 -0.62 -0.589 -0.576 -0.681 -0.681 -0.221 -0.127 0.393 0.475 1 0.716 0.448
NIRv -0.333 0.78 -0.327 -0.221 0.683 0.272 -0.048 -0.288 -0.28 -0.289 -0.186 -0.148 -0.278 -0.272 0.29 0.383 0.537 0.532 0.716 1 0.416
PRI -0.199 0.25 -0.028 -0.056 0.044 -0.287 -0.418 0.071 0.02 -0.062 -0.03 -0.042 -0.311 -0.316 0.257 0.186 0.429 0.473 0.448 0.416 1
B1 B2 B3 B4 B5 B6 B7 B8 B9 B10 B11 B12 B13 B14 B15 B16 SIF d GPP NDVI NIRv PRI
1.00
0.75
0.50
0.25
0.00
−0.25
−0.50
−0.75
−1.00
Pearson Correlation Coefficient

Figure S3.5. Comparison between RF models estimated GPP and observed tower-based GPP across all ICOS flux tower sites. Overall, our RF models show a high explanation of GPP variability across different vegetation types. However, the RF-SIF-VI shows some limits in some sites in predicting tower-based GPP as it overestimates (for instance at *SE-Deg*) and underestimates (for instance at *IT-Cp2*) tower-based GPP. The color code represents the different RF GPP predictions and the observed GPP: Red color stands for RF-SIF-R, green for RF-SIF-R-PFT, blue for RF-R, Cyan for RF-SIF-VI, and black for the observed tower-based GPP.

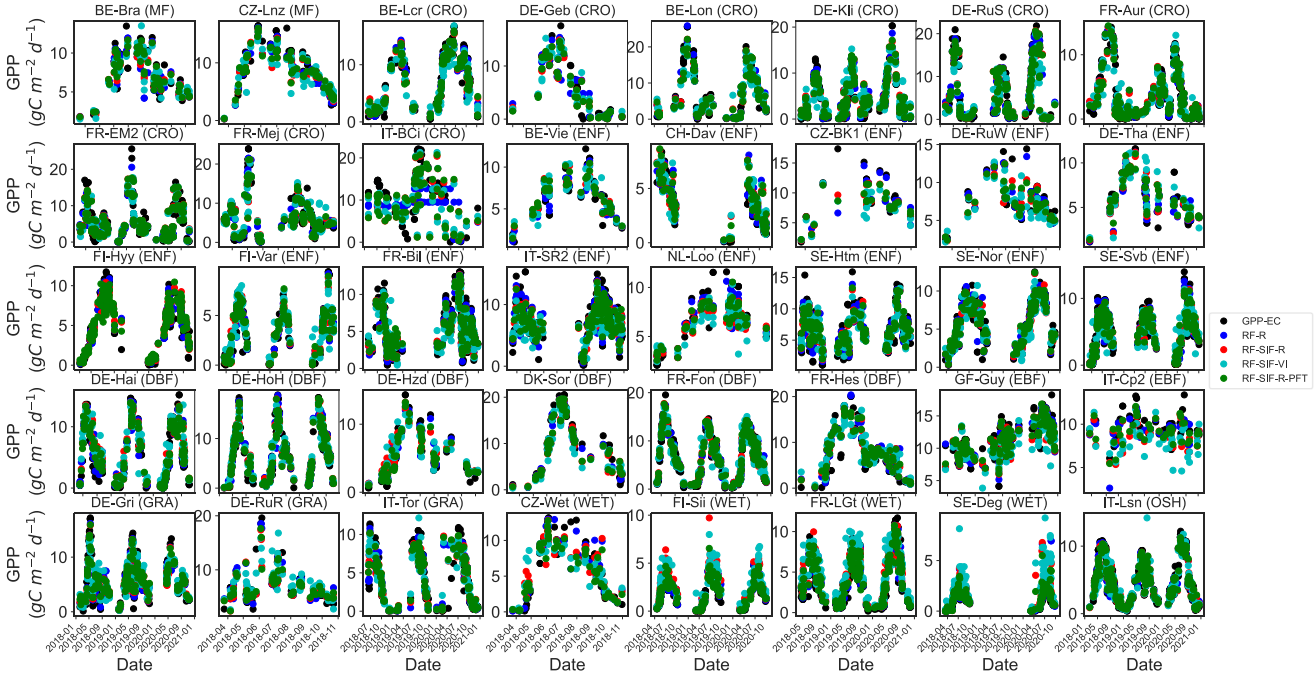

Figure S3.6a RF-R. Scatterplots between tower-based GPP and RF-R predicted GPP of each site. The adj. R^2 represents the adjusted coefficient of determination of the relationships between observed GPP and predicted GPP. The color code represents the eight different plant functional types encountered in the study sites: Red color stands for CRO (croplands), green for DBF (deciduous broadleaf forests), yellow for EBF (evergreen broadleaf forests), magenta for ENF (evergreen needleleaf forests), blue for GRA (grasslands), Cyan for MF (mixed forests), lime for OSH (open shrubland), and dimgrey for WET (wetland). The shaded area depicted in each line is the 95% confidence interval of the relationships between predicted GPP and observed GPP.

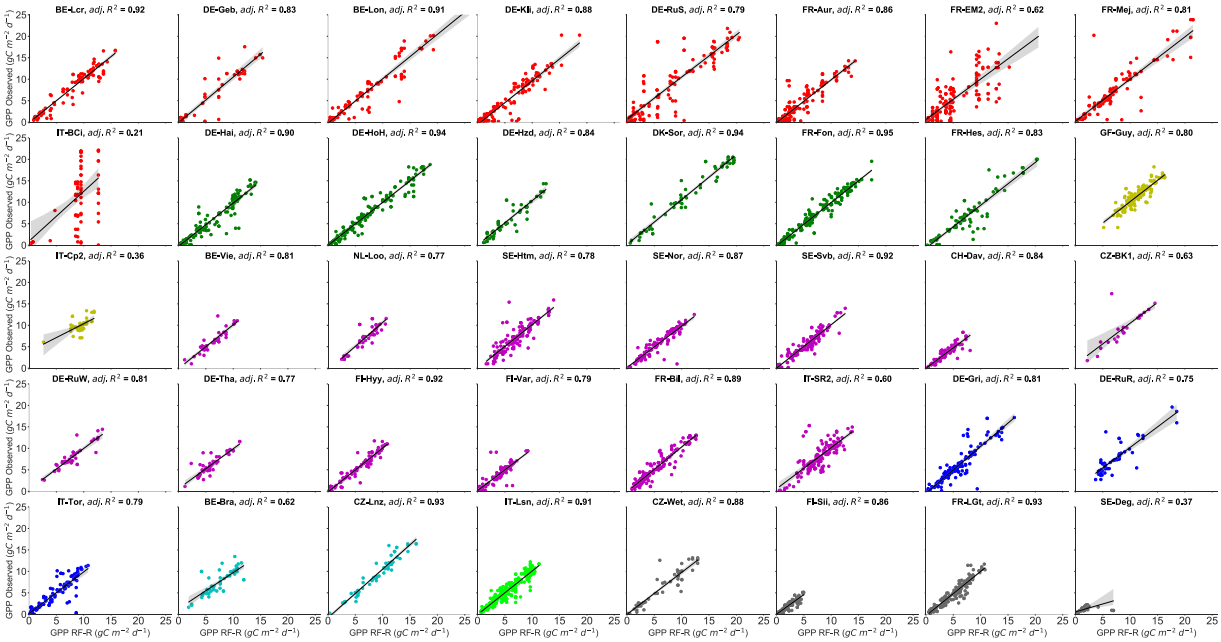

Figure S3.6b RF-R. Scatterplots of the tower-based GPP against RF-R predicted GPP based on each PFT: mixed forests (MF), croplands (CRO), evergreen needleleaf forests (ENF), deciduous broadleaf forests (DBF), evergreen broadleaf forests (EBF), grasslands (GRA), open shrublands (OSH), and wetlands (WET) at daily timescale. The adj. R^2 represents the adjusted coefficient of determination of the relationship between observed GPP and predicted GPP. p denotes the statistically significant level of the relationships. The shaded area depicted in each line is the 95% confidence interval of the relationships between predicted GPP and observed GPP.

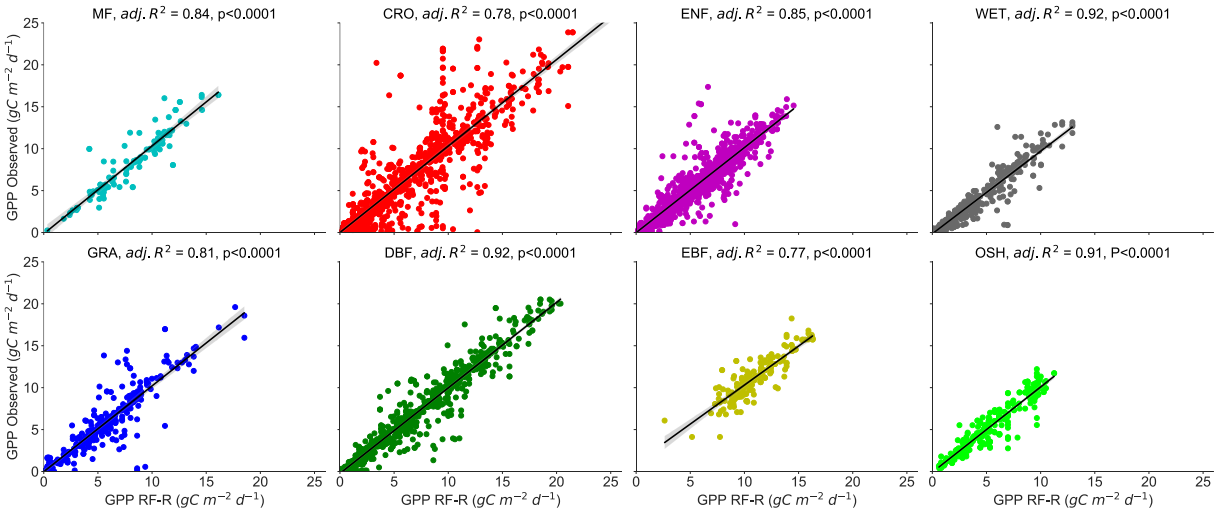

Figure S3.7a RF-SIF-VI. Scatterplots between tower-based GPP and RF-SIF-VI predicted GPP for each site. The adj. R^2 represents the adjusted coefficient of determination of the relationships between observed GPP and predicted GPP. The color code represents the eight different vegetation types encountered in the study sites: Red color stands for CRO (croplands), green for DBF (deciduous broadleaf forests), yellow for EBF (evergreen broadleaf forests), magenta for ENF (evergreen needleleaf forests), blue for GRA (grasslands), Cyan for MF (mixed forests), lime for OSH (open shrubland), and dimgrey for WET (wetland). The shaded area depicted in each line is the 95% confidence interval of the relationships between predicted GPP and observed GPP.

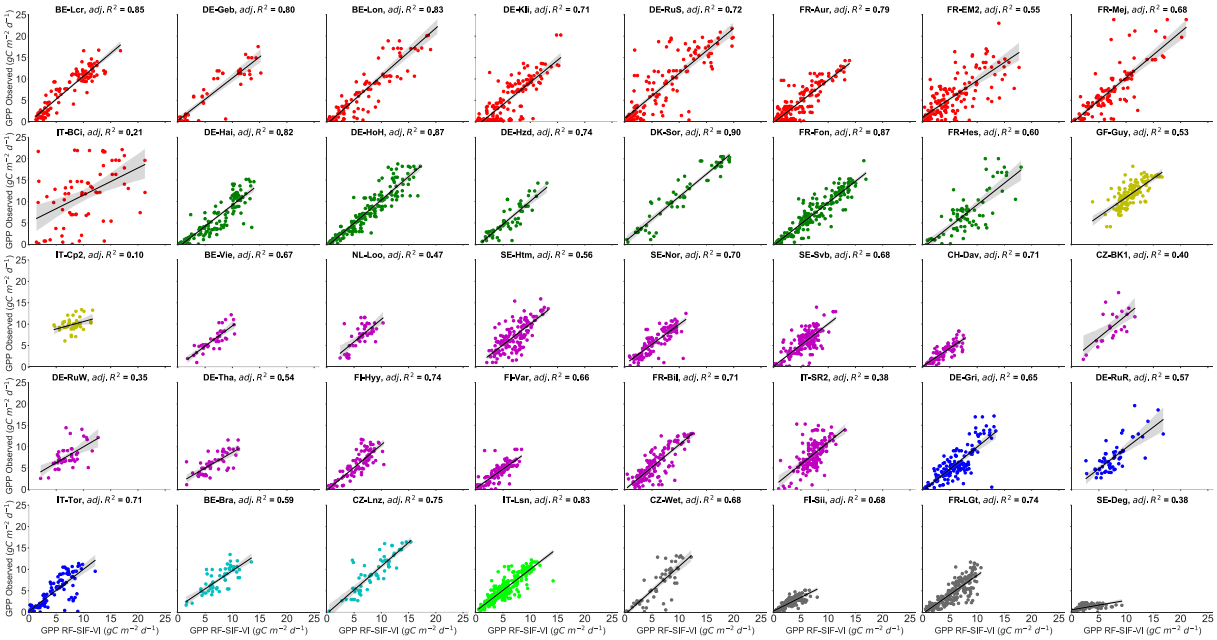

Figure S3.7b RF-SIF-VI. Scatterplots of the tower-based GPP against RF-SIF-VI predicted GPP for each plant functional types: mixed forests (MF), croplands (CRO), evergreen needleleaf forests (ENF), deciduous broadleaf forests (DBF), evergreen broadleaf forests (EBF), grasslands (GRA), open shrublands (OSH), and wetlands (WET) at daily timescale. The adj. R^2 represents the adjusted coefficient of determination of the relationship between observed GPP and predicted GPP. p denotes the statistically significant level of the relationships. The shaded area depicted in each line is the 95% confidence interval of the relationships between predicted GPP and observed GPP. The strongest correlations between observed and predicted GPP are observed in DBF and OSH vegetation types, while the lowest are recorded in EBF and ENF.

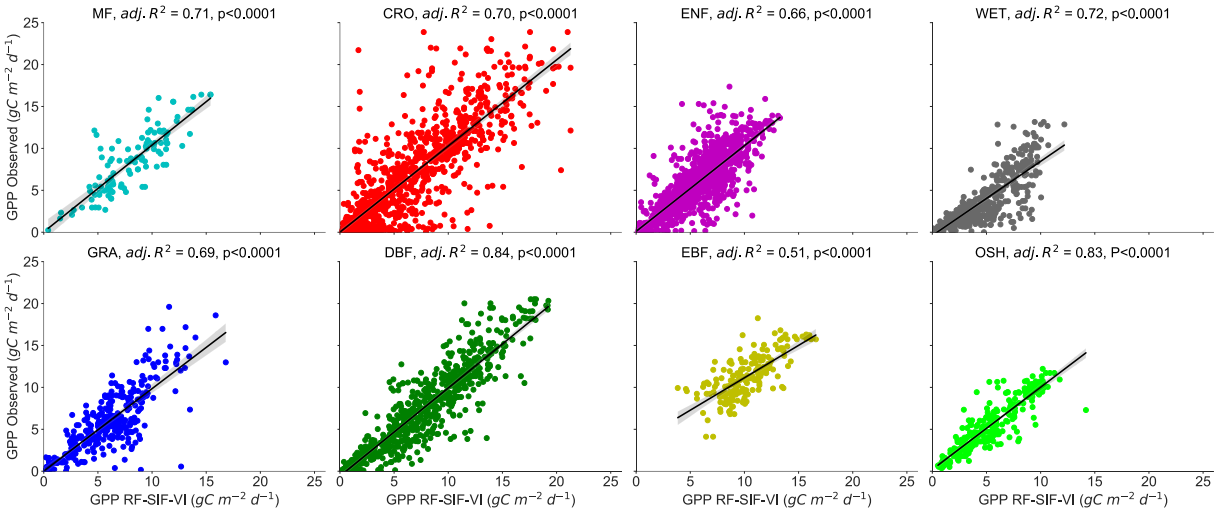

Figure S3.8a RF-SIF-R-PFT. Scatterplots between tower-based GPP and RF-SIF-R-PFT predicted GPP for each site. The adj. R^2 represents the adjusted coefficient of determination of the agreement between predicted GPP and observed GPP. The color code represents the eight different vegetation types encountered in the study sites: Red color stands for CRO (croplands), green for DBF (deciduous broadleaf forests), yellow for EBF (evergreen broadleaf forests), magenta for ENF (evergreen needleleaf forests), blue for GRA (grasslands), Cyan for MF (mixed forests), lime for OSH (open shrubland), and dimgrey for WET (wetland). The shaded area depicted in each line is the 95% confidence interval of relationships between predicted GPP and observed GPP.

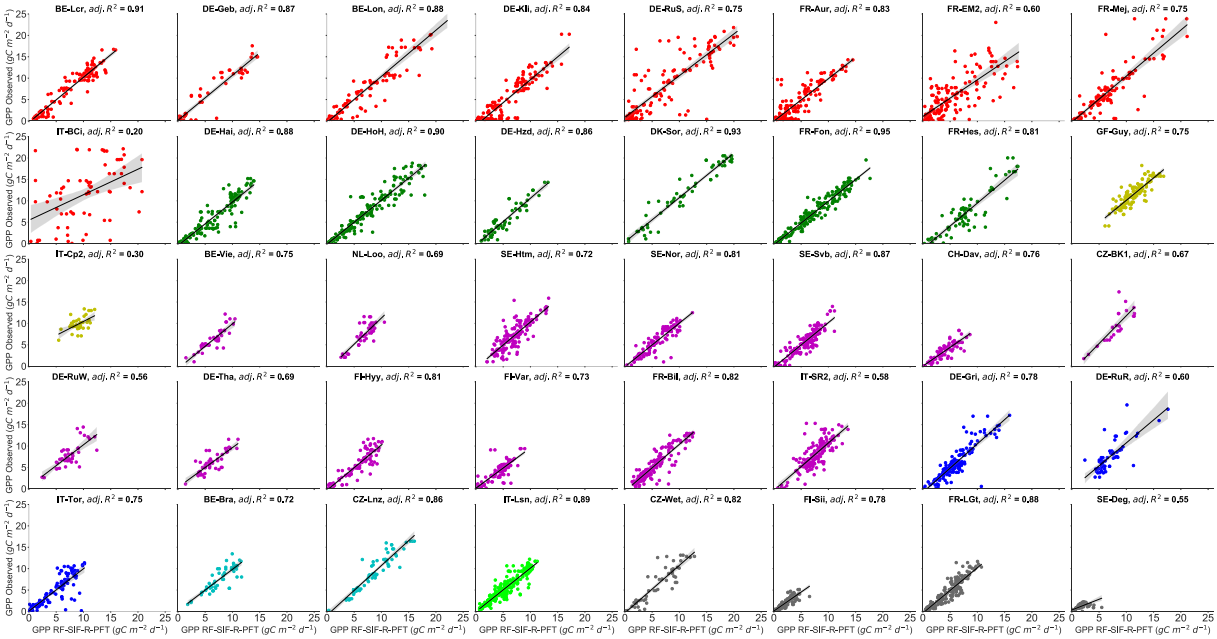

Figure S3.8b RF-SIF-R-PFT: Scatterplots of the ICOS tower-based GPP against RF-SIF-R-PFT predicted GPP for each plant functional type: mixed forests (MF), croplands (CRO), evergreen needleleaf forests (ENF), deciduous broadleaf forests (DBF), evergreen broadleaf forests (EBF), grasslands (GRA), open shrublands (OSH), and wetlands (WET) at daily timescale. The adj. R^2 represents the adjusted coefficient of determination of the relationship between observed GPP and predicted GPP. p denotes the statistically significant level of the relationships. The shaded area depicted in each line is the 95% confidence interval of the relationships between GPP predicted and GPP observed.

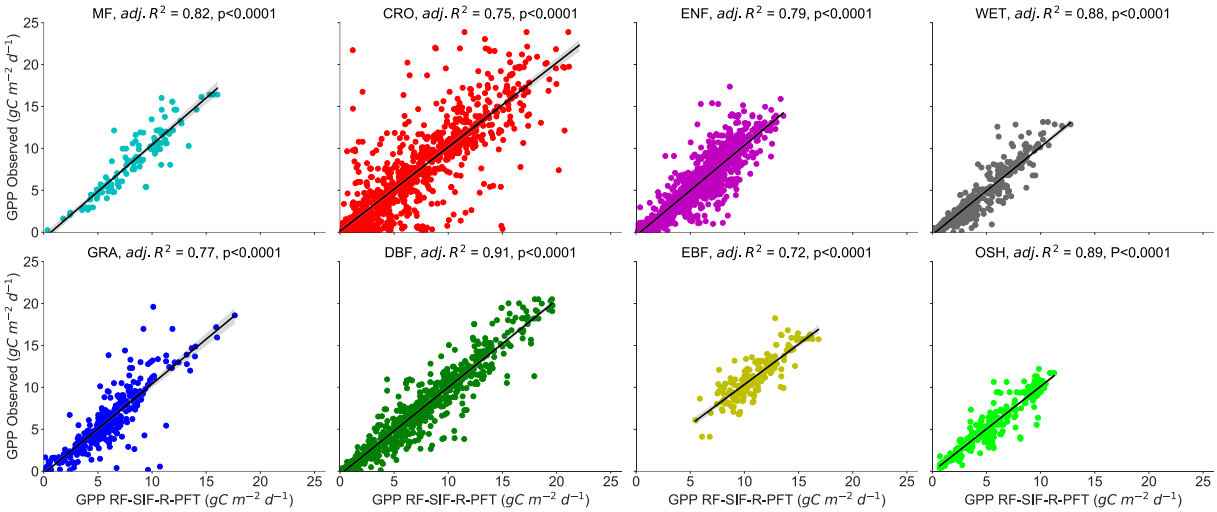
MF, adj. R^2 = 0.82, p<0.0001
CRO, adj. R^2 = 0.75, p<0.0001
ENF, adj. R^2 = 0.79, p<0.0001
WET, adj. R^2 = 0.88, p<0.0001
GRA, adj. R^2 = 0.77, p<0.0001
DBF, adj. R^2 = 0.91, p<0.0001
EBF, adj. R^2 = 0.72, p<0.0001
OSH, adj. R^2 = 0.89, P<0.0001
GPP Observed ($gC\ m^{-2}\ d^{-1}$)
GPP RF-SIF-R-PFT ($gC\ m^{-2}\ d^{-1}$)
0
5
10
15
20
25

Annexe Chapter 4. Data-based investigation of the effects of canopy structure and shadows on sun-induced chlorophyll fluorescence in a deciduous oak forest

Figure S4.1. The SIF3 and the active fluorometer instrument (LIF) setups at the top of the tower of the Fontainebleau-Barbeau forest ICOS site with a dominant stand of sessile oak (height of about 25 m) and a hornbeam understory. SIF3 and LIF instruments were set above the canopy.

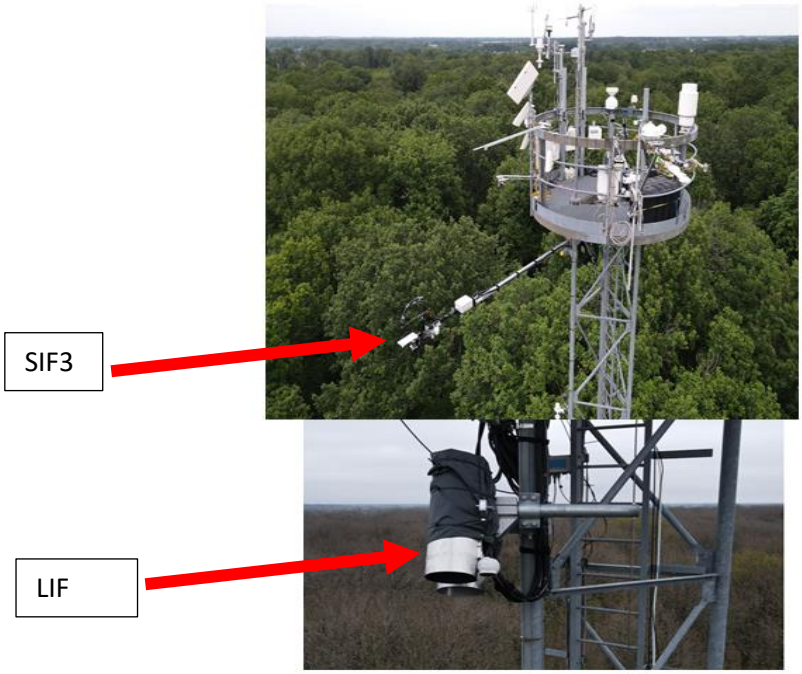

Figure S4.2. Correlation matrix between spectral reflectance bands of the canopy measured by SIF3. The data show strong relations between variables reflectance in the blue and the reflectance in the red, perhaps due to their strong light absorption, and between reflectance in the red-edge and reflectance in the near-infrared. Based on these observations all reflectance bands were not used for establishing the random forest models, but specific and low correlated bands were chosen in the blue, red, red-edge, and near-infrared regions as mentioned in Table 1.

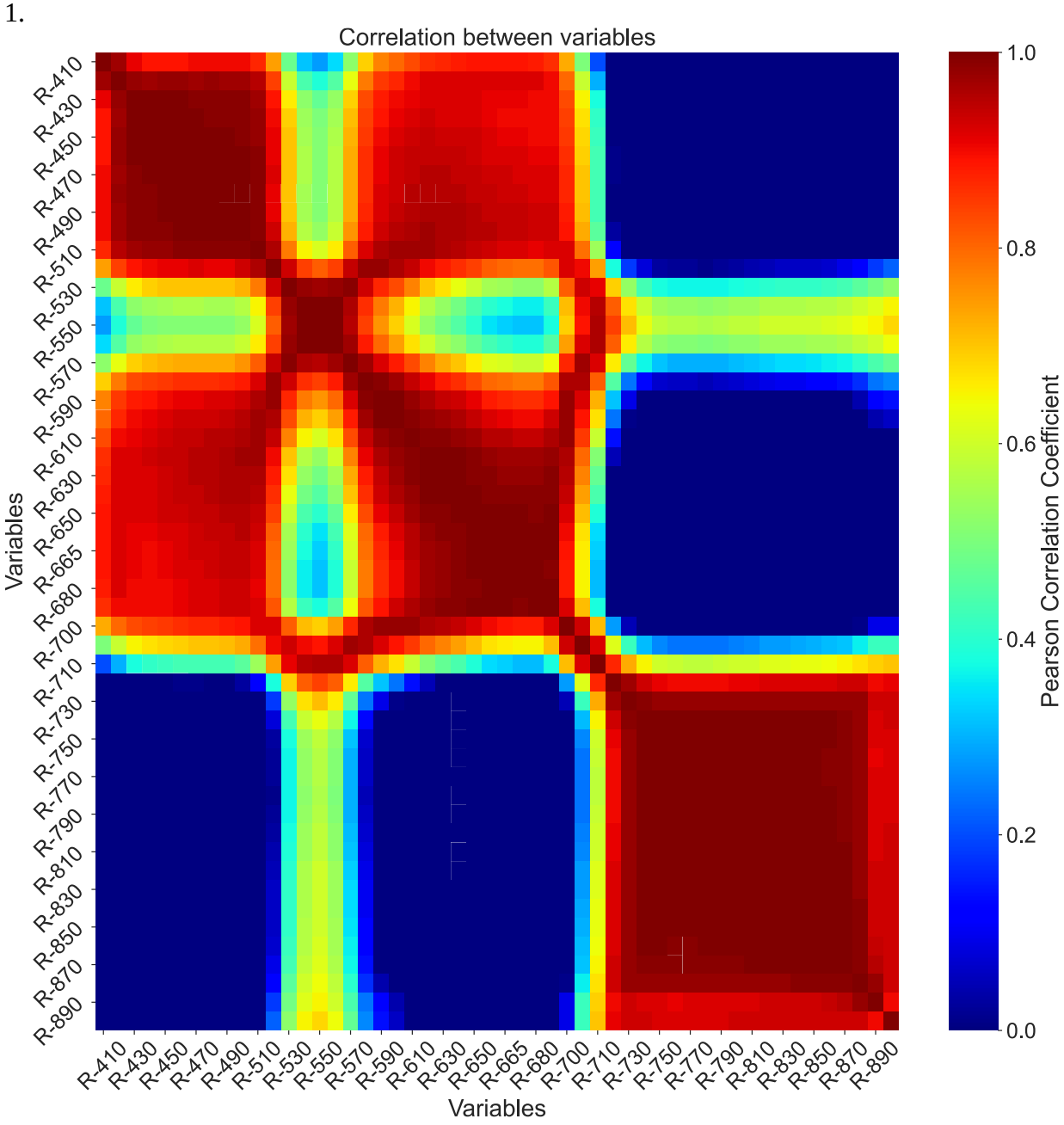

Figure S4.3. Correlation matrix between variables used for establishing the random forest models to predict $F_{yieldLIF}$ and Φ_k. The data show low correlations between variables than previously in Figure S4.2.

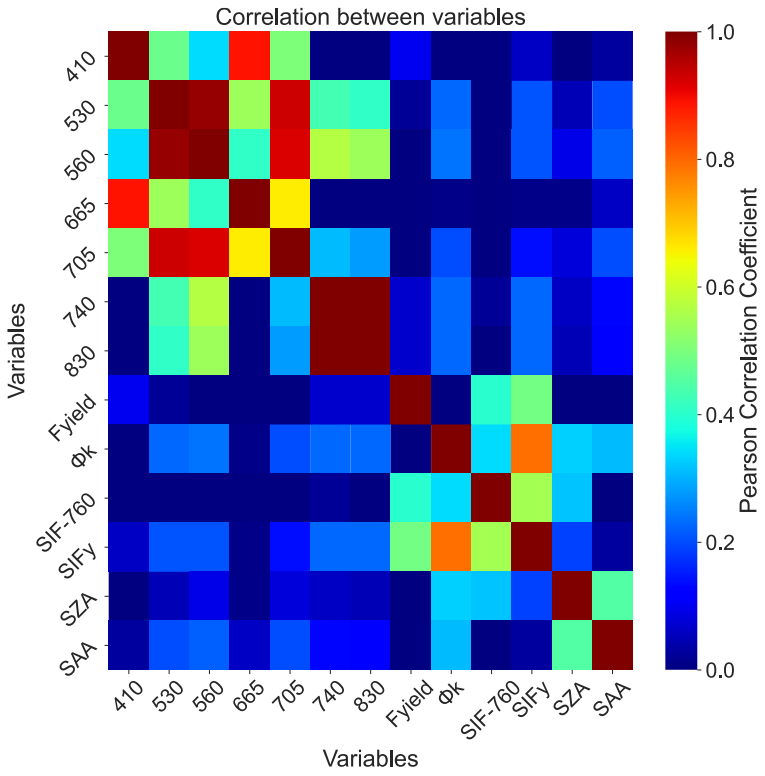

Figure S4.4. shows the coefficient of determination (R^2) of the relationship between SIF_y and $F_{yieldLIF}$ at hourly timescale. The results show improved correlations between SIF_y and $F_{yieldLIF}$ compared to the same analysis at the daily timescale (Figure 4.1).

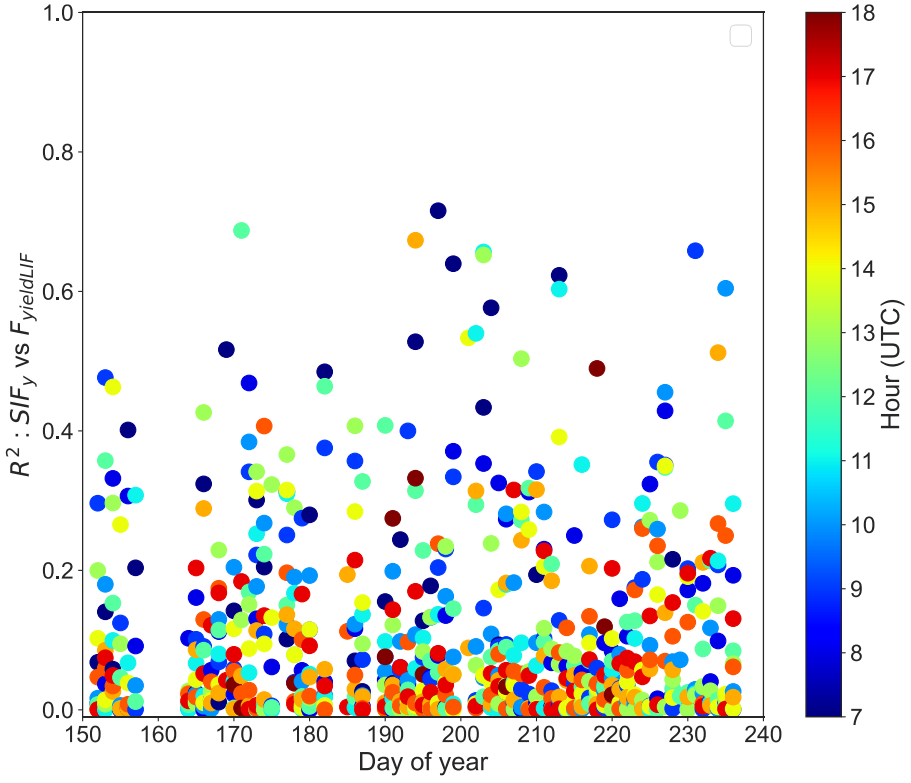

Figure S4.5. depicts, during the clear sky day, the sun fraction of the field of view (FOV) of SIF3 and the sun elevation angle as observed in the temperate deciduous forest of Barbeau. The sun fraction was estimated from randomly taken RGB images of the FOV of SIF3 from July to September 2022. The sun elevation angle showed a well-known trend, with its peaks at noon and low values recorded in the morning and late afternoon hours. As expected, the sun fraction revealed its lowest values in the morning and late afternoon and peak values at noon. However, the decline observed in the sun fraction between 9 and around 12 am shows the impact of the vegetation structure and sun-canopy geometry.

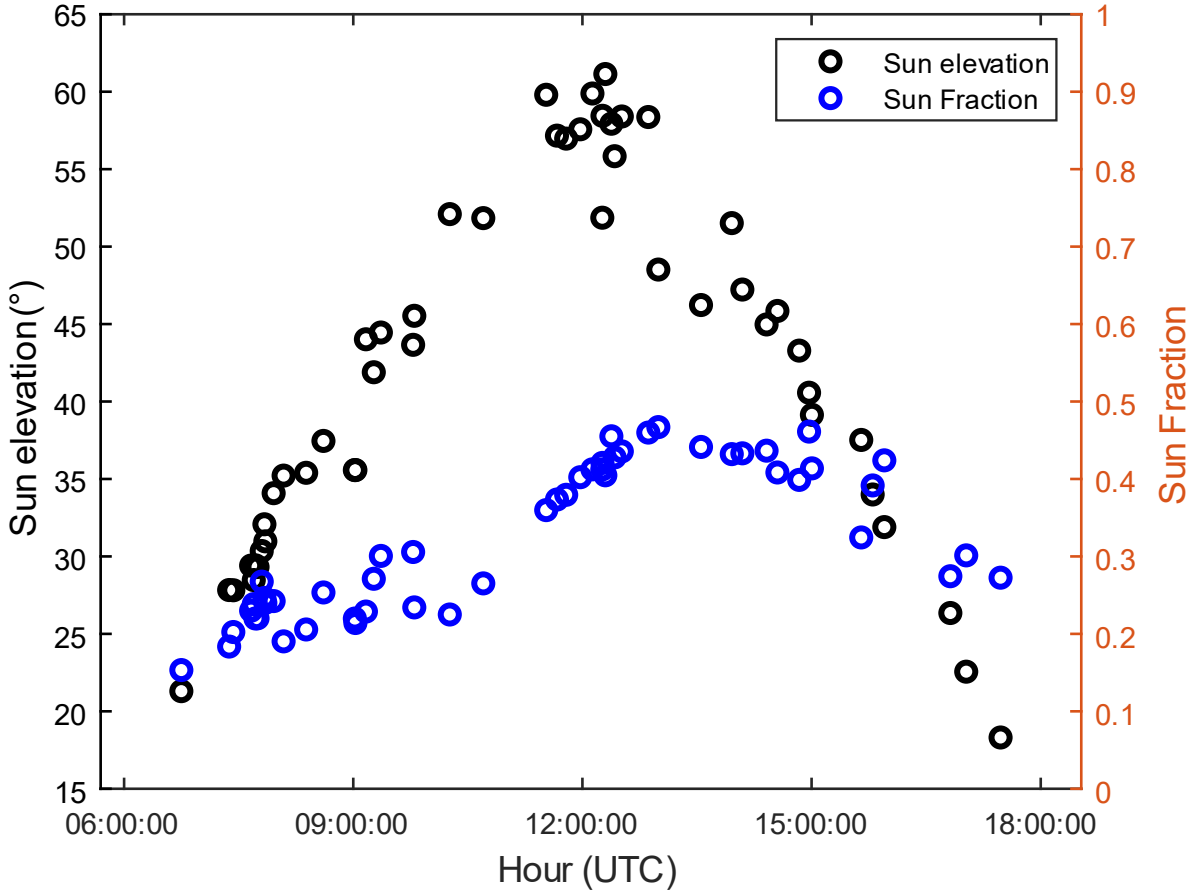

Figure S4.6. depicts the shadows on the FOV of SIF3 observed on an RGB image captured on August, 6th, 2022, at 10:15 am (UTC). The cycle inside the left pink image showed the FOV of SIF3, which showed a shadowed canopy with only a small portion in the sun. The black and white image on the right showed the sun fraction (white), and the value of the sun fraction in the FOV of SIF3: 22.91%. This result indicates that more than 75% of the FOV of SIF3 was in the shade at this time of the day.

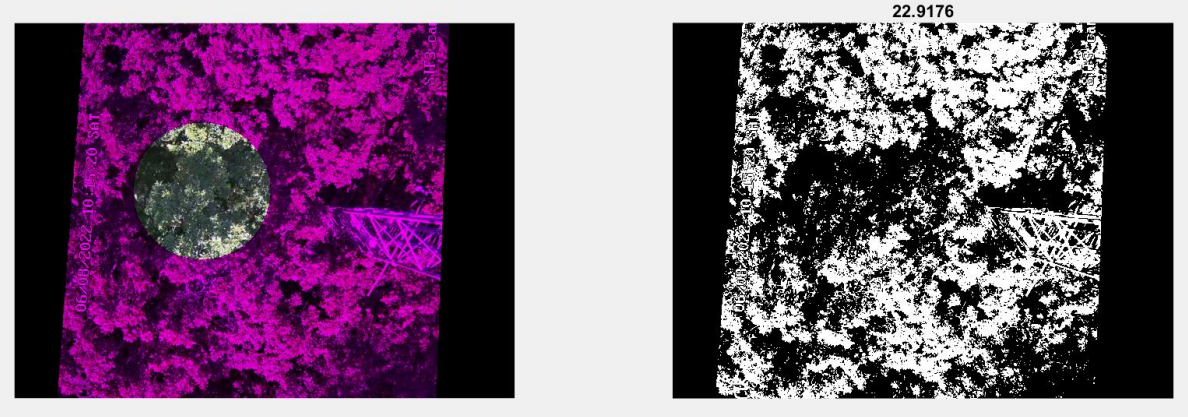

Figure S4.7. show the full diurnal cycles of $F_{yieldLIF}$ and photosynthetically active radiation (PAR) measured in June 17th, and 18th, 2022 in the deciduous oak temperate forest of Barbeau. The diurnal cycles of PAR showed that the two days were totally clear and sunny. It can be seen that when the first light beams hit the canopy a peak of $F_{yieldLIF}$ appeared, followed by a rapid decrease. It was the case for all recorded diurnal cycles. Further, $F_{yieldLIF}$ showed different diurnal patterns and responded to the incident PAR. For clear sunny days, like here, $F_{yieldLIF}$ significantly increased after sunrise and reached a maximum value when the PAR reached around 600 µmol photons m^{-2} s^{-1}. Afterwards, $F_{yieldLIF}$ drastically declined while PAR continued to increase until $F_{yieldLIF}$ reached a minimum value in the afternoon, from where $F_{yieldLIF}$ slightly increased during the night. This suggests that the decrease of $F_{yieldLIF}$ can be attributed to the activation of the non-photochemical quenching for the dissipation of the excess light energy induced by the high level of incoming radiation and hence avoiding the photodamage of the plant.

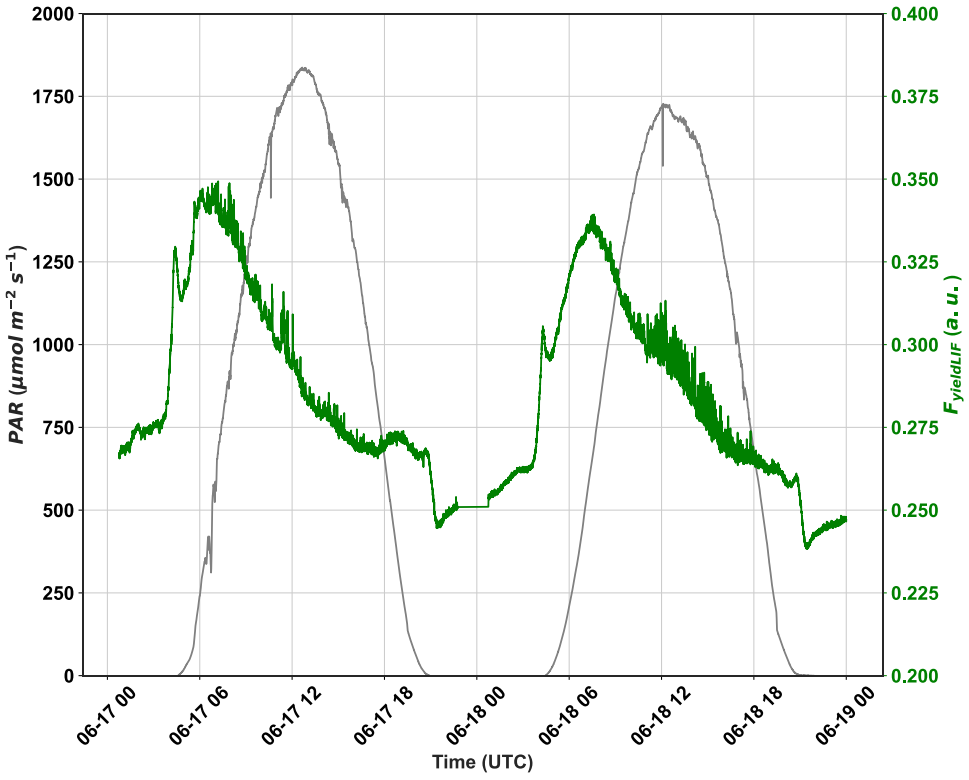

Figure S4.8. Figure S4.8a exhibits the inter-daily variations of the coefficient of determination (R^2) of the relationships between the reflectance at near-infrared band (R-NIR) and the Φ_k at instantaneous scale, as a function of the ratio between diffuse and total PAR. Figure S4.8b presents the seasonal relationships between daily means $\overline{R-NIR}$ and $\overline{\Phi_k}$ as a function of the ratio between diffuse and total PAR. And Figure S4.8c shows the seasonal dynamics in $\overline{R-NIR}$ and $\overline{\Phi_k}$. The shaded area indicates the 95% confidence interval. The asterisks stand for the statistical significance level (** = P≤0.01). The data show some strong correlations between R-NIR and Φ_k-760 at the daily timescale, while this relation was weak at the seasonal scale. These results are similar to the ones we obtained by studying the relationship between NIR_v and Φ_k, suggesting that spectral reflectance at the near-infrared had the same relation with Φ_k, and hence may be also relevant in capturing changes in fAPAR and f_{esc} at canopy scale.

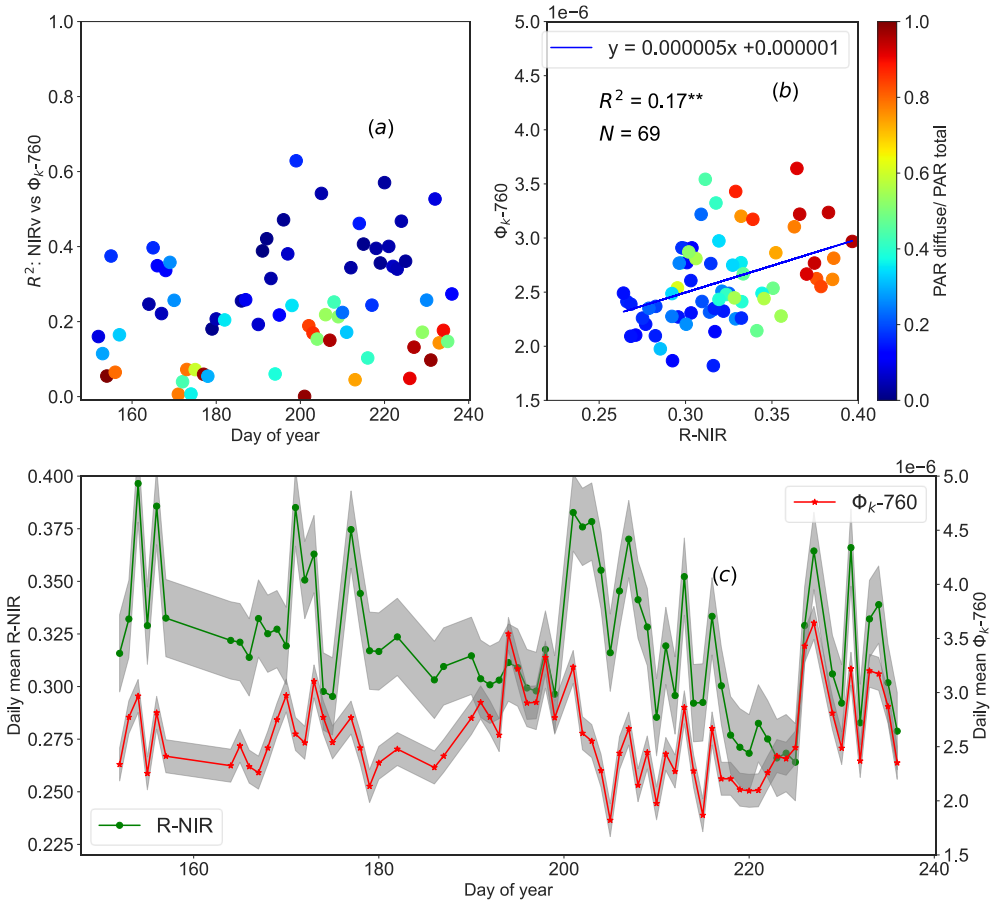

Figure S4.9. Random forest (RF) model outputs: Figure S4.9a presents FY-R model performance between observed and predicted $F_{yieldLIF}$, Figure S4.9b shows predictor importance estimates for FY-R model, Figure S4.9c represents FY-R-SIF model performance between observed and predicted $F_{yieldLIF}$, Figure S4.9d shows predictor importance estimates for FY-R-SIF model, and Figure S9e depicts FY-R-SIF_y model performance between observed and predicted $F_{yieldLIF}$, Figure S9f shows predictor importance estimates for FY-R-SIF_y model. *N* denotes the number of data points used for the RF model's testing, adj. R^2 represents the adjusted coefficient of determination of the relationship between the test dataset $F_{yieldLIF}$ and predicted $F_{yieldLIF}$, OOB R^2 is the model accuracy on the validation dataset (1/3 of the training set), and the RMSE is the root mean square error between observed $F_{yieldLIF}$ and RF model predicted $F_{yieldLIF}$. The dashed diagonal line depicts the 1:1 line. FY-*R* denotes $F_{yieldLIF}$

prediction using R, as inputs to predict $F_{yieldLIF}$; and FY-R-SIF includes *R* and SIF to predict $F_{yieldLIF}$, and FY-R-SIFy uses R and SIF_y to estimate $F_{yieldLIF}$. The data revealed that adding SIF or SIF_y as predictors did not improve the model performance compared to FY-R model. But the predictor importance estimates showed that SIF and SIF_y provide useful and impactful information in determining $F_{yieldLIF}$. This result indicates that even at high temporal resolution the contribution of SIF or SIF_y is important compared to each R band individually, but the combined effect of R bands could mitigate or hide the use of SIF as a vegetation physiological trait.

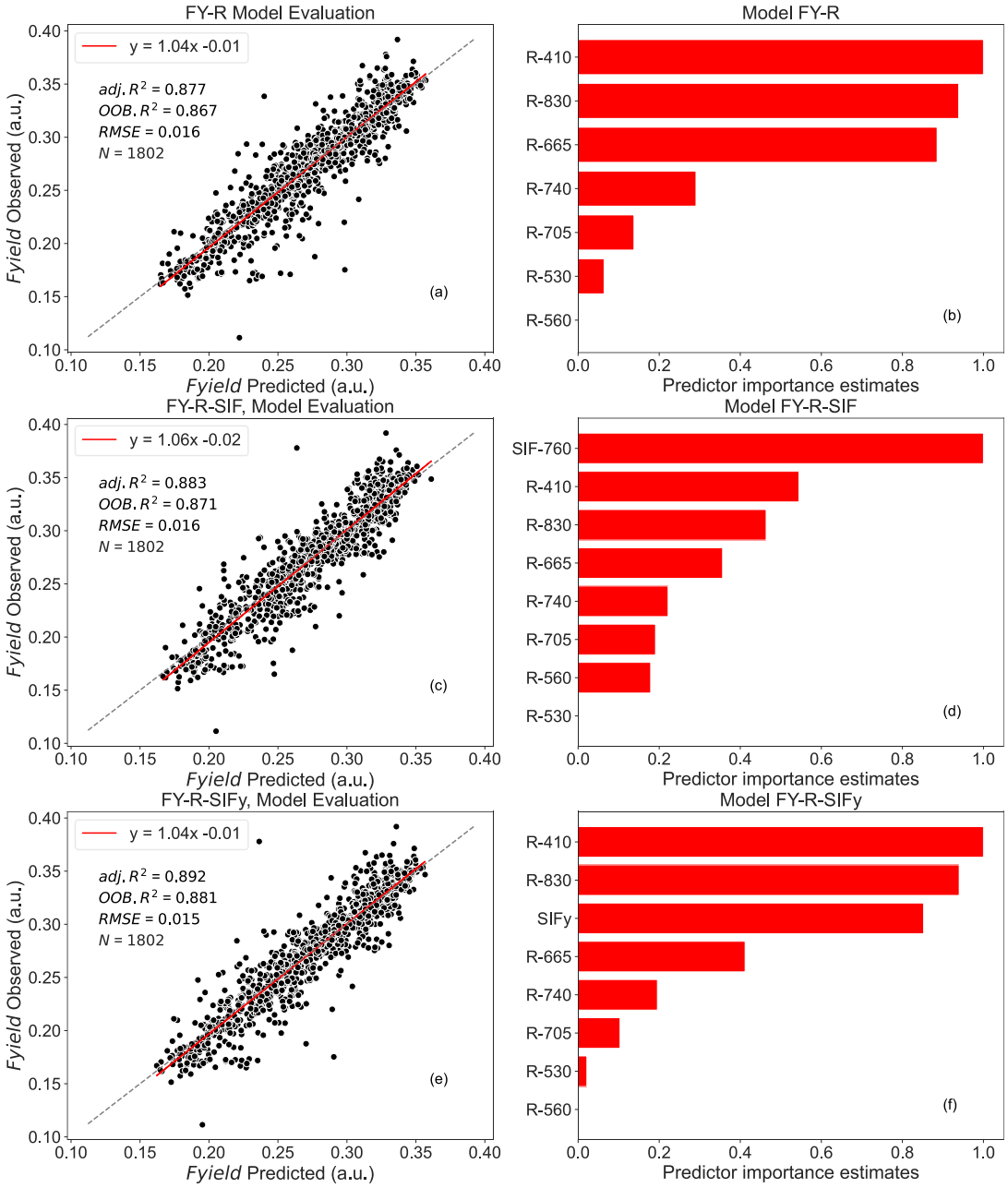

Annexe Chapter 5. Investigating the responses of sun-induced chlorophyll fluorescence, gross primary production and of the relation between the two to abiotic factors in a temperate deciduous forest

Figure S5.1. Figure S5.1a depicts SIF-ENV-SA model performance between observed and predicted SIF-760, Figure S5.1b represents predictor importance estimates for SIF-ENV-SA model, Figure S5.1c depicts GPP-ENV-SA model performance between observed and predicted GPP, Figure S5.1d represents predictor importance estimates for GPP-ENV-SA model. *N* denotes the number of data points used for the RF model evaluation, adj. R^2 represents the adjusted coefficient of determination of the relationship between data test and predicted SIF or GPP, OOB R^2 is the model accuracy on the validation data, and the RMSE is the root mean square error between observed SIF or GPP and RF model predicted SIF or GPP. The dashed diagonal line depicts the 1:1 line. Data under only sunny days at half-hourly timescale were used.

The RF regression of SIF on variables exhibited in Figure S5.1b explains approximately 94% of the total variance of far-red SIF (Figure S5.1a). SWC appears to be the most important variable, followed by SZA and SAA, and the contribution of VPD plays an insignificant role for SIF prediction (Figure S5.1b). For GPP, the RF model on variables represented in Figure S5.1d captures 70% of the variability in GPP (Figure S5.1c). VPD and SZA appear to be the most determinant variables, followed by SWC and the contribution of SAA was insignificant for GPP prediction.

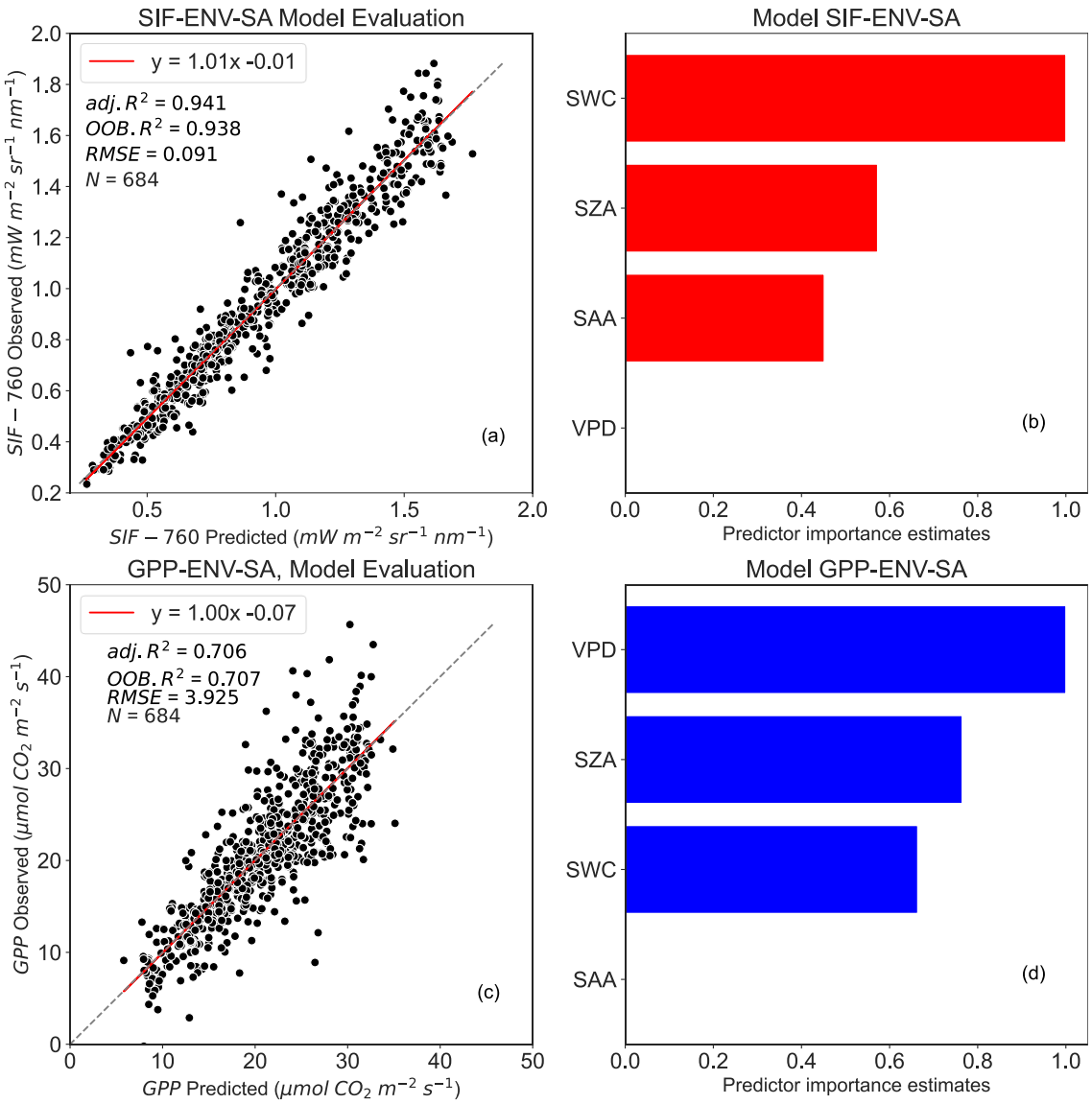

Figure S5.2. Partial dependence describing the marginal effect of each variable on far-red SIF variations under clear sky days at half-hourly timescale for the SIF-ENV-SA model.

The results in Figure S5.2 reveal a monotonic positive relationship between SIF and lower values of SWC (SWC < 3 $cm^3\ cm^{-3}$) and a saturation pattern is observed at high SWC values (SWC > 3 $cm^3\ cm^{-3}$). The relationship between SIF and SAA is also positive for values of SAA < 200 degrees, however, for values of SAA between 200 and 250 degrees, their relations become negative. SZA and VPD are negatively related to SIF.

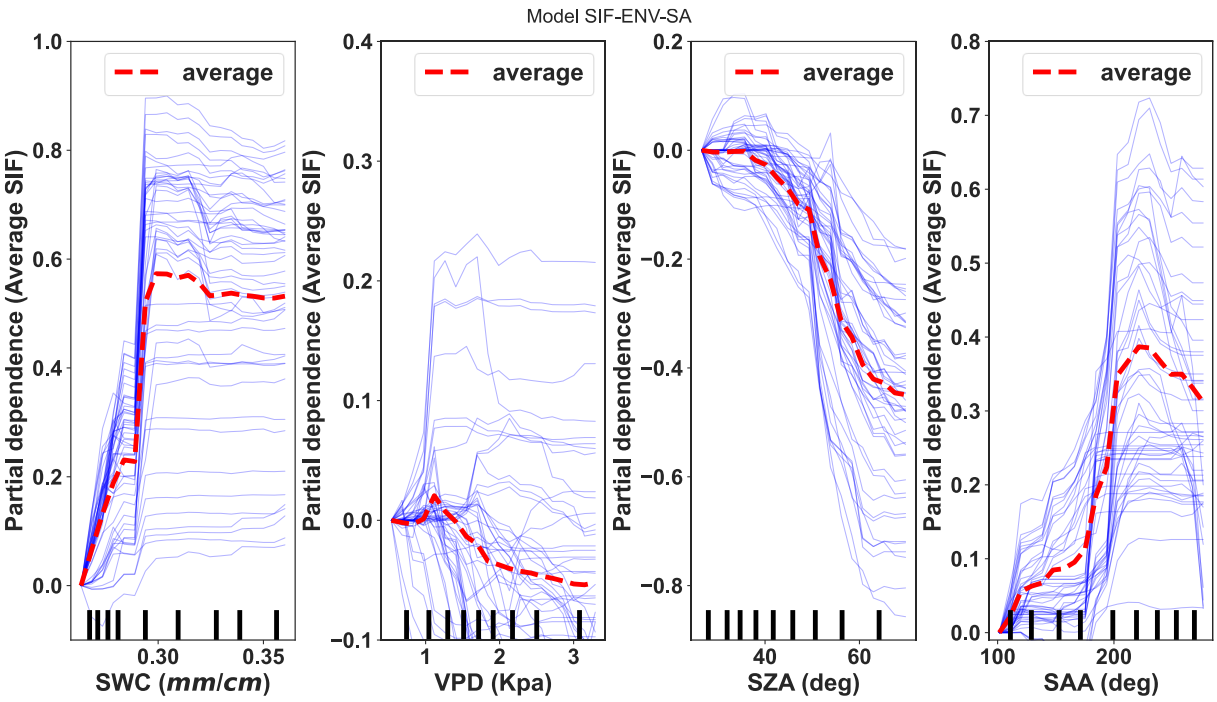

Figure S5.3. Partial dependence describing the marginal effect of each variable on GPP variations under clear sky days at half-hourly timescale for the GPP-ENV-SA model.

The results in Figure S5.3 show that SWC has a positive relationship with GPP, but their correlations stayed almost constant before becoming positive again. The relationship between GPP and VPD, between GPP and SZA, and between GPP and SAA are strongly negative.

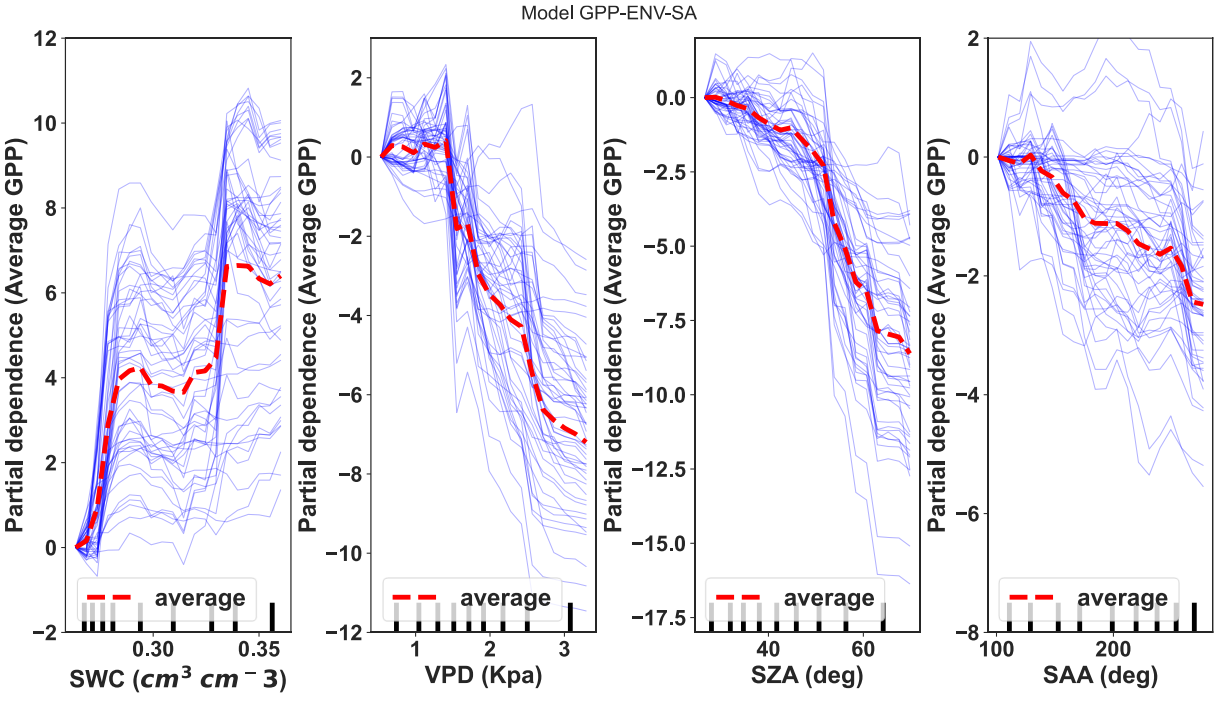

Télédétection de la fluorescence induite par laser et par le soleil pour l'étude du fonctionnement hydrique et carboné des écosystèmes terrestres

Résumé.

La fluorescence chlorophyllienne induite par le soleil (SIF) est désormais utilisée comme outil pour suivre la production primaire brute (GPP) du couvert végétal de différents écosystèmes. La SIF est importante pour comprendre le cycle global du carbone dans un contexte de changements climatiques. Cependant, l'usage de la SIF pour suivre les variations de la GPP est entravée par des facteurs confondants (propriétés biochimiques des feuilles, facteurs abiotiques, etc.). Dans cette thèse, on propose d'utiliser des observations à plusieurs échelles [satellitaires (TROPOMI et MODIS) et au sol] de la SIF, de réflectance, de la GPP et du rendement de la fluorescence chlorophyllienne par mesure active ($F_{yieldLIF}$), utile pour observer les variations physiologiques de la végétation, afin d'abord 1) d'évaluer la force des liens GPP-SIF et de prédire la GPP à l'aide de mesures spatiales ; ensuite, 2) d'examiner les liens $F_{yieldLIF}$-SIF_y (SIF normalisé par le rayonnement photosynthétiquement actif, PAR) et les effets de structure du couvert végétal sur la SIF; et enfin 3) d'explorer l'influence de la structure de la canopée et des facteurs abiotiques sur les variations de la SIF et de la GPP et sur leurs liens. On constate que la force et la nature des liens GPP-TROPOMI SIF sur 40 sites de tours à flux dépendent du site et du type de végétation, reflétant l'hétérogénéité spatiale et temporelle de la couverture végétale du pixel TROPOMI. En outre, les mesures satellitaires de la SIF et de la réflectance prédisent plus de 80 % des variations de la GPP. Toutefois, on remarque que les réflectances à différentes bandes prises ensemble prédisent mieux la GPP que TROPOMI SIF, mais l'importance relative montre que la SIF est la variable la plus importante pour prédire la GPP (SIF plus les indices de végétation (VIs) comme variables explicatives). Ce résultat soutient qu'à des échelles spatiales larges la réflectance pourrait être utilisée pour estimer la GPP et que l'usage de la SIF comme proxy de la GPP soulève la question de savoir si l'information physiologique liée à la photosynthèse issue de la SIF pourrait être détectée à cette échelle. Par ailleurs, à partir de mesures au sol effectuées à Fontainebleau-Barbeau, on montre que $F_{yieldLIF}$ n'est pas corrélé avec SIF_y à l'échelle diurne à cause des effets de géométrie d'éclairement. On constate aussi que les dynamiques diurnes de la SIF et du PAR décorrèlent lors des jours de ciel clair, montrant les effets de l'ombre sur la SIF. On montre aussi que la SIF et la réflectance peuvent être utilisées pour prédire $F_{yieldLIF}$, tandis Φ_k ($SIF_y/F_{yieldLIF}$) (indicateur de l'interaction structure-éclairement) est corrélé à la réflectance et à la géométrie de la canopée. On souligne que les liens GPP-SIF et leurs variations dépendent de l'échelle temporelle considérée. Particulièrement, à l'échelle saisonnière, on observe que les variations de GPP, SIF, SIF_y et $F_{yieldLIF}$ répondent au développement structurel et biochimique des canopées, ainsi qu'aux facteurs abiotiques. Lors des vaques de chaleurs, on constate que la SIF et les VIs (NDVI, NIRv et mNDI) d'une part et la SIF et le PAR d'autre part ne sont pas corrélés, tandis que GPP, SIF et $F_{yieldLIF}$ diminuent fortement. Ceci indique que SIF et $F_{yieldLIF}$ peuvent être utilisés pour suivre la photosynthèse du couvert en conditions de stress alors que les VIs ne peuvent pas. Cette réponse spécifique de la SIF et $F_{yieldLIF}$ comparée aux VIs souligne l'intérêt croissant de l'usage de la SIF comme proxy de la GPP dans des conditions climatiques

changeantes. Toutefois, à l'échelle diurne, les interactions entre structure de la canopée et géometrie d'éclairement contrôlent les variations de la SIF, de la GPP et de la relation GPP-SIF. On recommande l'usage de la synergie réflectance-SIF et des mesures actives pour mieux comprendre les variations de la SIF et son lien avec la GPP sur d'autres types de couverts végétaux.

Mots clés: fluorescence chlorophyllienne induite par le soleil, mesure active de la fluorescence chlorophyllienne, productivité primaire brute, structure de la canopée, et facteurs abiotiques.

Remote sensing of laser- and sun-induced chlorophyll fluorescence for studying water and carbon functioning in terrestrial ecosystems

Abstract.

Sun-Induced chlorophyll Fluorescence (SIF) is used as a tool to monitor Gross Primary Production (GPP) across different ecosystems. SIF is important to understand the global carbon cycle under changing climate conditions. However, the use of SIF to probe variations in GPP is challenged by confounding factors (canopy biochemical properties, abiotic factors, etc.). In this thesis, we proposed to use multiple scale measurements (spaceborne with the TROPOMI and MODIS sensors, and ground-based) of SIF, reflectance, GPP, and active chlorophyll fluorescence yield ($F_{yieldLIF}$), useful to observe the physiological variations of the vegetation. In order, first, to evaluate the strength and the nature of the relationship between GP-SIF and to predict GPP using remote sensing metrics; second, to examine the relationship between $F_{yieldLIF}$ and SIF_y (SIF normalized by the photosynthetically active radiation, PAR) and the effects of canopy structure and sun-canopy geometry on SIF signal, and third, to explore the influence of canopy structure, light intensity and abiotic factors on SIF and GPP variations and on their links. We found that the strength and the nature of the links between GPP and TROPOMI SIF, across forty flux sites, depend on sites and vegetation types. Further, combined use of SIF and reflectance from satellite observations predicted over 80% of GPP variations. However, we observed that daily surface reflectance at different bands when taken as a whole outperformed daily TROPOMI SIF in predicting GPP, but the relative importance of variables in the random forest model using SIF and VIs (NDVI, PRI and NIRv) as inputs to predict GPP shows that SIF is the most important variable for predicting GPP. This result indicates that at a broad spatial scale, reflectances could be used to predict GPP and the use of SIF as a proxy of GPP raises the question of whether the physiological information related to photosynthesis contained in SIF could be detected at this scale. Based on top-of-canopy measurements in Fontainebleau-Barbeau, we show that active $F_{yieldLIF}$ was not correlated with passive SIF_y at the diurnal timescale due to sun-canopy geometry effects. We also observed that the diurnal patterns in SIF and PAR did not match under clear sky conditions, underlining the effects of shadows on the measured canopy SIF. We also showed that the SIF and the reflectance can be used to predict $F_{yieldLIF}$, while $\Phi_k = SIF_y/F_{yieldLIF}$ (an indicator of the interaction between canopy structure and irradiance geometry) is strongly correlated with reflectance and sun-canopy geometry. The analyses show that the links between GPP and SIF and their variations, resulting from ground-based measurements, depend on the temporal scale considered. More specifically, at the

seasonal scale, we observed that variations in GPP, SIF, SIF_y and $F_{yieldLIF}$ respond to the structural and biochemical development of canopies and to variations in abiotic factors, especially during the heatwaves in 2022. During these extreme weather conditions, we observed that, on one hand, SIF and VIs (NDVI, NIRv and mNDI), and on the other hand, SIF and PAR are not correlated, while GPP, SIF and $F_{yieldLIF}$ strongly decreased. This indicates that SIF and $F_{yieldLIF}$ can be used to monitor impact on photosynthetic activity under stress conditions, while VIs cannot. This specific response of SIF and $F_{yieldLIF}$ compared to VIs highlights the growing interest in the use of SIF as a proxy of GPP under changing climate conditions. However, at the diurnal scale, the interactions between canopy structure and sun geometry, as well as the light intensity control the variations in SIF and GPP and their links. We strongly recommend the use of the synergy between reflectance, SIF and active fluorescence measurements to better understand the dynamics of SIF and its link to GPP in other vegetation types at the canopy scale.

Keywords: sun-induced chlorophyll fluorescence, active chlorophyll fluorescence, gross primary production, canopy structure, and abiotic factors.

Conferences and Workshops

Poster Presentations

- ✓ Journées des jeunes chercheur(es) de CNES; Oct. 2022, Toulouse, France; **Synergy between sun-induced chlorophyll fluorescence (SIF), surface spectral reflectance and reflectance-based indices on quantifying gross primary productivity (GPP).**

Oral Presentations

- ✓ **IWGGMS-19:** International Workshop on Greenhouse Gas Measurement from Space; Jul. 2023; Paris, France; **Synergy between sun-induced chlorophyll fluorescence (SIF), surface spectral reflectance and reflectance-based indices on quantifying gross primary productivity (GPP).**
- ✓ Jounée Scientifique et Technique de Barbeau ; March 2023 ; IDEEV, Gif-sur-Yvette, France ; **Les déterminants de la fluorescence de la chlorophylle à l'échelle du couvert végétal.**
- ✓ Workshop on SIF/Hyperspectral measurements; Sept. 2022; CESBIO/Toulouse, France; **Synergy between Sun-Induced chlorophyll Fluorescence (SIF), surface spectral reflectance and reflectance-based indices on quantifying Gross Primary Productivity (GPP); Tower-based laser- and sun-induced chlorophyll fluorescence in oak deciduous forest stands: shadow, reabsorption and scattering effects corrections at diurnal timescale.**
- ✓ SENSECO Final conference and MC5 meeting; Sept. 2022; Izmir, Turkiye**; Synergy between sun-induced chlorophyll fluorescence (SIF), surface spectral reflectance and reflectance-based indices on quantifying gross primary productivity (GPP)**
- ✓ SENSECO MC5 meeting; Feb. 2023; Barcelona, Spain; **Writing Guideline on "crop stress detection from UAVs: best practices and lessons learned for exploiting sensor synergies" paper submitted on: Precision Agriculture (PRAG) journal; Sept. 2023; Participated to the SENSECO spatial scaling challenge (paper writing in progress).**
- ✓ Journée thématique du PNTS May 2023 ; **Réalisation d'une vidéo pour Ma thèse depuis l'Espace en 180 seconds.**